Universität Bremen

Fachbereich 1, Physik und Elektrotechnik
Institut für Biophysik

THE DYNAMICS OF DORSAL ACTIN WAVES

Dipl.-Phys. Erik Bernitt

Dissertation zur Erlangung des akademischen Grades
Doktor der Naturwissenschaften
(Dr. rer. nat.)

Gutachter:
1. Prof. Dr. Hans-Günther Döbereiner
2. Prof. Dr. Karsten Kruse

Eingereicht am 14.10.2015
Verteidigt am 15.12.2015

Abstract

The polymerization of the structural protein actin from its monomeric to its filamentous state accounts for fundamental aspects of cellular morphodynamics and motility. In the latter two processes waves of actin polymerization are central, as has been shown throughout the last ten years.

This thesis is dedicated to deciphering of the propagation mechanism underlying actin waves known as Circular Dorsal Ruffles (CDRs). While these ring-shaped undulations on the dorsal cell side have been known to the biological community for several decades the mechanism underlying their formation and propagation has remained a puzzle. It is the hypothesis of this work that CDRs can be described as waves that form and propagate in an active medium that is constituted by the actin machinery of the cell. The identification of the corresponding functional elements is the aim of this work. For this, the structure, morphology and dynamics of CDRs are investigated in detail and with a view that is guided by the typical structure of models of active media. Throughout the whole thesis, the FitzHugh-Nagumo system serves as a prototype model for the explanation of the mechanisms underlying the phenomena observed for CDRs on an abstract level.

Novel results are presented regarding the identification of the processes of actin dynamics within CDRs and their compartmentalization. The systematic analysis of the dynamics of CDR wavefronts reveals that they exhibit a number of previously unknown phenomena, among them breathing modes, spiral waves, and collision annihilation. All these features are well founded in the framework of active media.

Since the dynamics of CDRs strongly depends on the cellular morphology, a novel method for their investigation is developed in which cells are forced into disc-shapes via microcontact printing for a quantitative analysis of data of identically shaped cells. On these cells, CDRs are constrained to one-dimensional propagation direction with periodic boundary conditions. Under these conditions, CDRs form repeatedly and propagate with constant velocities, forming distinct spatio-temporal patterns. This behaviour is fundamentally different from the dynamics that is normally associated with CDRs. However, it is expected from a theoretical point of view when one thinks of CDRs as waves in a noisy active medium. This is shown based on numerical studies of a noise-driven FitzHugh-Nagumo system. The geometrical properties of disc-shaped cells greatly facilitate the comparison of experimental data to results of simulations. This is used to explain the mechanisms underlying spatio-temporal pattern formation of CDR dynamics.

In combination with microfluidic technology, the well-defined wave patterns and comparability of data obtained on different cells open the door for experiments on the molecular mechanisms in CDRs. It is shown that the periods between successive wave events and the wave velocity can be controlled via the rate of actin depolymerization.

Contents

Acknowledgements

I would like to thank **Prof. Dr. Hans-Günther Döbereiner** for supervising my PhD project and many more things, among them: the freedom for development of own ideas and directions of my project, numerous discussions, the enthusiasm and the support of the development of my scientific profile.

I would like to thank **Prof. Dr. Karsten Kruse** for discussions and for being the second examiner of this thesis.

Special thanks go to **Prof. Dr. Nir Gov**. Several ideas behind the experiments go back to your input into the proposal underlying this project. Thank you also for the great hospitality, the long and numerous discussions, and the mediation of contacts to people who supported this project.

For the supply with the cell line NIH 3T3 X2 I would like to thank **Prof. Dr. Cheng-Gee Koh**. This line turned out to be essential for several of the experiments described in this thesis.

I am deeply thankful to my girlfriend **Kerstin Ringering** for all the discussions, the incredibly careful proofreading of this thesis and all the other support. Most of all, I am thankful for your understanding of all the effort I put into this project. My gratitude is way beyond of what I could express with words.

I like to thank **Robert Meißner** for proofreading of parts of this thesis, and discussions of my work. Especially I like to thank you for introducing me to the software XMDS, which was used for several of the theoretical studies in this thesis.

I am very thankful towards **Konstantin Finke** for proofreading parts of my thesis and for discussions on numerical solutions strategies for partial differential equations. Thanks a lot, Konne!

I like to thank **Richard Colmorn** for the writing sessions on Monday evenings at the Thalia coffeebar where each of us worked on our theses.

For discussions and proofreading of specific parts of this thesis I also would like to thank: **Christina Oettmeier**, **Julia Strübig**, **Anna Piorecka-Ecken**, **Jonghyun**

Lee and **Malte Ohmstede**. Thank you a lot!
Special thanks go to my brother **Lars Thomassen** for a quickly finished proofreading marathon.

I like to thank **Dr. Arik Yochelis** for helpful discussions in the scope of the idea of interpreting CDRs as waves in active media.

More special thanks go to:

Anja Bammann for her lab work, which is the basis for all the successful experiments due to her maintenance of the cell culture, supply with materials and preparation of samples. Thank you so much, Anja. This thesis would never have been possible without your support!

Alexander Seupt who was involved in several stages of this work. Thank you for your excellent work, Alex!

Sven Cordes for his great skills in 3-d modeling and for the many hours that we spent on the 3-d illustration of the morphology of CDRs (Figure 3.9).

I like to thank **Holger Doschke** for all his support regarding technical questions.

I like to thank **Eike Brauns**, **Melanie Kirsch** and the IMSAS for the production of the wafer that served as the master for production of microcontact stamps. Especially I would like to thank **Eike Brauns** for the good advice regarding the wafer design, the choice of software and various practical tips.

Furthermore I want to thank all my colleagues from the **Döbereiner lab** for the good time during my PhD. I much enjoyed working with you! Thank you for all the discussions and the support.

I would like to thank the German Research Foundation (**DFG**) for partial funding of the work described in this thesis. Further I am grateful for support from the Postgraduate International Programme (**PIP**) in physics and electrical engineering of the University of Bremen.

List of Figures

List of Tables

List of Symbols and Remarks on Notation

Only the most frequently used symbols and variables are listed here.

Symbol	**Description**
α	Tension energy density
β	Bending rigidity line density
c	Curve or contour, autocorrelation function, concentration
δ	Dirac's delta distribution, small increment
E_{ext}	External energy density
F	Free energy density
g	Radon transformation
$\mathcal{H}$	Energy functional
H	Spontaneous curvature of a protein species
I	Image intensity
K	Curvature
k	Kinetic reaction constant
κ	Bending modulus
L	Line
λ	CDR lifetime
N	Number
n_{cc}, n_{cw}	Occupation number of counter- , clockwise propagating CDRs
O	Object
p	Probability density
q	CDR configuration
$\vec{r}$	Spatial vector
ρ	Radius, radial coordinate
s	Arc length, spatial distance
T_{p}	Period between two wave pulses
T_{R}	Time for one revolution
t	Time
τ	Recovery time
Θ	Angle
$\vec{v}$	Velocity vector
x, y, z	Spatial variables

Temporal derivatives were abbreviated in the text flow and figures with dots. I.e. the temporal derivative of the variable x appears as $\dot{x}$ in the text and in figures.

The coordinate axes of plots of image data usually have an inverted y-axis in this thesis, with which a convention in image processing is followed [Burger and Burge, 2010].

The meaning of boxes and whiskers in box and whisker plots is given by the following schematic:

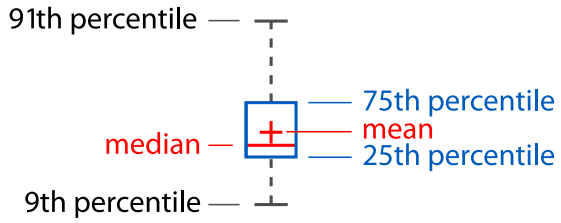

List of Abbreviations

The most frequently used abbreviations that are used in this thesis are listed here. Note that this list is not complete, as some abbreviations only appear in limited scopes. Especially, no protein names are listed below.

Abbreviations	**Full Name**
CDR	Circular Dorsal Ruffle
DIC	Differential Interference Contrast
FN	Fibronectin
FHN	FitzHugh-Nagumo
GAP	GTPase-Activating Protein
GEF	Guanine nucleotide Exchange Factors
GUI	Graphical User Interface
HAP	Hand fan-shaped Actin Particle
LSM	Laser Scanning Microscope
PBS	Phosphate Buffer Saline
PDGF	Platelet-Derived Growth Factor
PDMS	PolyDiMethylSiloxane
PEG	PolyEthylene Glycol
PBS	Phosphate Buffered Saline
ROI	Region Of Interest
SD	Standard Deviation
SE	Standard Error
SEM	Scanning Electron Microscopy
TIRF	Total Internal Reflection Fluorescence

Chapter 1

Introduction and Motivation

Eukaryotic cells such as fibroblasts appear static when observed under the microscope. In fact, however, their morphology is highly dynamic, albeit usually on time scales that are too slow for the human perception. In the mechanisms underlying the dynamics of cell shape one single protein plays an outstanding role, which is the structural protein actin.

Actin is the most abundant protein in nearly all eukaryotic cell types and fulfils a large number of different functions. Consequently, it belongs to the best-studied proteins and its research has a long and ongoing history [Alberts et al., 2005, 628 pp]. The variety of different functions of actin is due to its ability to form polar filaments out of monomeric units and its versatility in interaction with other proteins. Actin polymerization can form cellular protrusions, among others, and the counter-directional gliding movement of actin filaments, which is driven by molecular motors, can lead to cellular contractions [Bray, 2001, Blanchoin et al., 2014].

The ability to change their shapes is an essential property for the functionality of cells. Therefore, the dynamics of actin is highly regulated and maintained by a complex apparatus of numerous interacting proteins [Pollard and Borisy, 2003]. In the last years it became more and more evident that the spatio-temporal organization of cellular protrusions in form of propagating waves of actin polymerization constitutes a fundamental and conserved pattern among different cell types [Gerisch et al., 2004, Döbereiner et al., 2006, Weiner et al., 2007].

Circular Dorsal Ruffles (CDRs) are an especially explicit type of travelling wave of polymerizing actin. Figure 1.1 shows an example of a life course of a CDR (A), the actin nature of CDRs (B), and a close-up view on the morphology of the membrane enveloping a CDR (C). The figure reveals that the wavefronts of CDRs tend to take ring-shapes and form ruffles at the dorsal cell side, which explains the origin of their name. In fact, this choice of naming has historical reasons, as we[a] will see later. Today, it can be misleading, because the term "ruffle" is normally associated with upward-pointing

[a]This thesis uses the third person when including the reader, whereas the first person is used to represent the author.

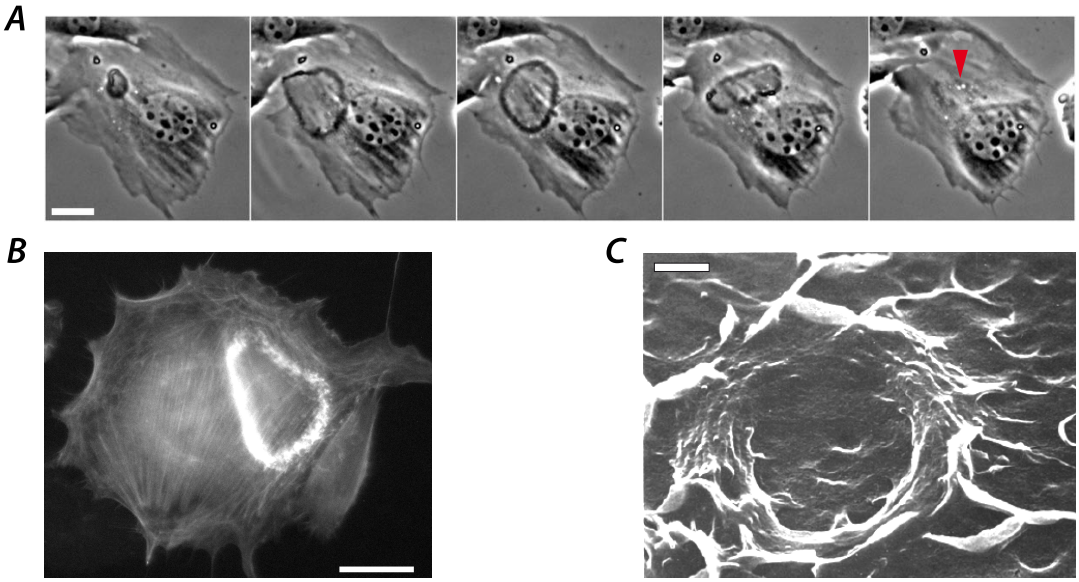

Figure 1.1: *Characteristics of CDRs*. *A*: Phase contrast time-lapse sequence showing the life course of a spontaneously formed CDR ($\Delta t = 8.9\,\mathrm{min}$). The red arrow highlights vesicles. *B*: A cell with stained filamentous actin (pLifeAct-TagRFP) exhibiting a CDR. *C*: close up scanning electron micrograph of a CDR showing ruffle-shaped protrusions. *C* was reprinted with permission from [Mellström et al., 1983] © Springer. Scale bars: *A* and *B*: $25\,\mu\mathrm{m}$, *C*: $2\,\mu\mathrm{m}$.

membrane protrusions close to the cell rim, as initially described by Abercrombie et al., rather than with actin waves [Abercrombie et al., 1970b]. Further, it will be shown later that CDRs do not always form ring-shaped wavefronts, which would favour a name such as "dorsal actin wave" over "circular dorsal ruffle". However, for the sake of coherence with the existing literature on the subject, we will stick to the existing naming convention throughout this whole thesis.

Even though CDRs have been known for several decades, the mechanisms leading to their formation and propagation are little understood to date. In this thesis the question of the wave mechanism underlying CDRs is addressed from a biophysical point of view. It is shown that CDRs behave like waves that propagate in an excitable medium. Guided by the well-known feedback schemes of excitable systems from a theoretical point of view, CDRs are investigated systematically in search for the corresponding modules mediating excitability, propagation of excitability, and the return to the non-excited state respectively.

In the further course of this introduction the history of the research on CDRs is summarized. The understanding of actin waves such as CDRs requires the convergence of different scientific fields such as biology, mathematics and physics. The resulting interdisciplinary perspective is built on a basis that comprises the non-linear theory of wave- and pattern formation as well as findings from the research on cell motility. The

respective fields are also briefly brought in historic perspective in the following. The actual biological details and the formalism for the description of actin waves is then introduced comprehensively in Chapter 2.

We start with a short overview about the research on cell morphodynamics and cell motility, as it is the basis for an understanding of the machinery underlying CDR formation.

1.1 From Early Research on Cell Motility to Models of Actin Waves

As CDRs form vertical outgrowths on the dorsal cell side, the understanding of the process of CDR formation requires some insight into the nature of the generation of cell protrusions. The motility module of protrusion is an essential process of cell locomotion [Blanchoin et al., 2014] and the history of the research on cell morphodynamics is therefore closely linked, or even identical, to the research on cell motility. The latter we define as a process in which the whole cell body translocates, i.e., exhibits a significant displacement of its center of mass, whereas the former refers to any kind of change in cell morphology. In this part of the introduction we will mainly focus on the history of the research on actin-based morphodynamics and motility, as the chapter on the theory of actin waves (Chapter 2) deals with the principles underlying actin-based cell motility comprehensively.

The research on cell protrusions dates back to the early work by Abercrombie et al., who were the first to systematically describe the structure and motion of the leading edge, called the lamellipodium, of motile fibroblasts using video- and electron microscopy [Abercrombie et al., 1970a, Abercrombie et al., 1971]. The research on the cell's lamellipodium is central to this thesis, because all available information indicate that actin within CDRs is organized in structures that are closely related to those underlying lamellipodia, as we will see later.

In the search for the origin of the driving force underlying lamellipodia protrusion it turned out that actin polymerization is the key player [Mitchison and Cramer, 1996]. Its capacity to polymerize into filaments which then are able to organize into meshworks provided the answer to the question on the driving mechanism underlying lamellipodia protrusion [Mogilner and Oster, 1996]. The understanding of this process required intensive research on actin, including the proteins that control actin polymerization [Carlier et al., 1999], and can be seen as one of the great success stories in the history of biology.

In the early 2000s the most important regulators of actin dynamics were identified and understood in broad outline in their interplay [Cameron et al., 2000]. This allowed to formulate minimal models of actin-based cell protrusion [Pollard and Borisy, 2003, Upadhyaya and van Oudenaarden, 2003]. With this basis established, the functionality of the motility apparatus of cells on higher levels could be tackled. Correspondingly, the ultimate goal of a complete understanding of the protein pathways involved in cellular motility came a step closer. Especially, a comprehension of the action of small

GTPases in the orchestrated protein interplay in protruding lamellipodia came into reach [Machacek et al., 2009].

For the understanding of the question how protein dynamics can lead to wave formation, their quantitative description via systems of partial differential equations has proven fruitful, which naturally drew the attention of the biophysical community towards this topic.

Indeed, the development of our current understanding of actin dynamics has seen considerable input from the physics community as the understanding of the physical properties of actin filaments [Mogilner and Oster, 1996, Mogilner and Oster, 2003], the gels formed by these filaments [Kruse et al., 2005], and their interactions with the cell membrane required this perspective [Tsekouras et al., 2011, Keren, 2011, Gauthier et al., 2012, Danuser et al., 2013]. In turn, the research on the cellular cytoskeleton inspired the physical community to develop generic theories of active polar gels [Kruse et al., 2003, Kruse et al., 2005, Marchetti et al., 2013]. These gels comprise a unique class of materials through which energy is constantly flowing supplied by the cellular fuel ATP. This means that active gels are inherently out of thermodynamic equilibrium. The activity is due to processes such as filament growth, filament shrinkage and the action of motor proteins that cause bidirectional sliding movement of filaments of anti parallel orientation.

Based on numerical studies, both, systems comprising motor proteins and systems without motor proteins, have been shown to be able to form waves [Kruse and Jülicher, 2003, Doubrovinski and Kruse, 2008]. These waves were indeed observed in various experimental systems for the study of actin dynamics comprising the slime mould *Dictyostelium discoideum* [Bretschneider et al., 2009], the lamellipodium of various spreading cell types [Döbereiner et al., 2006], the dorsal cell surface [Chen et al., 2009], or the leading edge of human neutrophils [Weiner et al., 2007]. To date the existence of actin waves is considered an essential feature of cellular morphodynamics and cell motility [Weiner et al., 2007, Allard and Mogilner, 2013].

Recently, the theories for actin waves have been extended to take into account the interactions between the dynamic cell shape and the wave-generating cell body towards modelling of cell motility [Doubrovinski and Kruse, 2011, Dreher et al., 2014, Camley et al., 2014].

1.2 Research on CDRs

Even though the wave nature of CDRs is obvious when video microscopy is employed, historically they were first recognized for their striking morphological features. This fact explains why the term "circular dorsal ruffle" reflects their morphological appearance, but not their wave character.

Already in the pioneering work by Abercrombie et al. the phenomenon of "ruffling" was described, i.e., the formation of lamellipodia-like protrusions into vertical direction away from the substrate [Abercrombie et al., 1970b]. The ruffling introduced by

Abercrombie et al. is, more specifically, termed peripheral ruffling today as it appears at, or close to, the frontal cell periphery. Some years later similar structures were observed on cells responding to growth factor stimulation or during viral infection [Ambros et al., 1975, Chinkers et al., 1979]. In contrast to the ruffling described by Abercrombie et al., the ruffles in stimulated and infected cells did not exclusively form at the cell rim. They were therefore termed "surface ruffles". The identification of CDRs as distinct structures goes back to 1983 and the work by Mellström et al., who investigated the reaction of human glial cells to stimulation with Platelet-Derived Growth Factor (PDGF) [Mellström et al., 1983]. Mellström et al. reported the morphology of these cells in detail based on scanning electron microscopy. In fact, Figure 1.1*C* is one of the micrographs of this publication. The study by Mellström et al. also revealed that CDRs are actin-based structures.

The formation of CDRs was subsequently discovered in several different cell lines as a response to different forms of stimulation, mainly by various types of growth factors [Chinkers et al., 1979, Dowrick et al., 1993, Edgar and Bennett, 1997]. With advances in biotechnological tools and in the understanding of the machinery of actin polymerization it turned out that the proteins located into CDRs are largely identical with the typical compounds of protruding lamellipodia [Legg et al., 2007, Payne et al., 2014]. The protein composition of CDRs will be dealt with in detail in the sections 2.1.1-2.1.5.

Within the last decade there has been an ongoing interest in CDRs, reflected by the publication of four review papers on this subject. In the earliest of these, Buccione et al. juxtapose CDRs to other cellular structures that also form rings of polymerized actin, namely podosomes and invadopodia [Buccione et al., 2004]. Orth et al. focus on the endocytotic properties of CDRs, especially with respect to receptor internalization [Orth and McNiven, 2006]. The two most recent reviews, by Hoon et al. and Itoh et al. respectively, emphasize the current advances in the research on the molecular composition of CDRs and propose possible pathways for their formation [Hoon et al., 2012, Itoh and Hasegawa, 2012].

To date, it is the standard method in the research on CDRs to stimulate their formation with growth factors such as PDGF (Section 8.2). The emergence of CDRs can usually be observed 5-10 min after their addition to the cell medium. Shortly after the stimulation, small dots of actin appear, which later form the typical rings that are the characteristic mark of CDRs. During their further life course, the rings constrict towards points, often followed by internalization of endocytotic vesicles. CDRs that form in response to stimulation have lifetimes ranging from 5 to 20 min and are singular events, i.e., no succeeding CDR formation is observed [Hoon et al., 2012, Itoh and Hasegawa, 2012].

While this coarse description constitutes the accepted picture of the dynamics of CDRs, there is less consensus regarding their morphology. Their eponymous ruffle-like protrusions are one of their clear features, as shown in several examples of micrographs of scanning electron microscopy [Mellström et al., 1983, Dowrick et al., 1993, Edgar

and Bennett, 1997]. In contrast, in other publications CDRs are depicted as smooth membrane ridges, which are marked by tiny bumps, devoid of sheet- and ruffle-like protrusions [Buccione et al., 2004, Orth et al., 2006]. The width of CDRs is commonly described to be uniform, whereas there is a disagreement between authors that report fixed maximal ring diameters [Itoh and Hasegawa, 2012] and others who highlight that there is no fixed ring size [Hoon et al., 2012].

The biological role of CDRs is not completely understood. However, there are several lines of thoughts regarding their potential functions. Shortly after stimulation of cells with growth factors, and corresponding CDR formation, the onset of motility can usually be observed, i.e., cells form lamellipodia and start to migrate. It was therefore hypothesized that CDRs facilitate the transitions from static to motile cell states. One potential mechanism explaining this is based on the observation that within the cell area surrounded by CDR wavefronts typically a clearly diminished number of actin stress fibres can be found in comparison to the remaining cell body. Stress fibres largely contribute to the stiffness of cells [Blanchoin et al., 2014]. It was therefore speculated that the local depletion of f-actin within CDRs could lead to an effective cell softening, facilitating cell migration [Hoon et al., 2012, Itoh and Hasegawa, 2012].

Another hypothesis of the function of CDRs is based on the observation that formation of CDRs often goes along with the formation of endocytotic vesicles [Swanson and Watts, 1995]. This process most frequently, but not exclusively, occurs upon CDR closure. CDR closure corresponds to macropinocytosis, the unspecific uptake of large amounts of extracellular liquid by cells [Dowrick et al., 1993, Doherty and McMahon, 2009]. Upon formation of endcytotic vesicles, cell membrane and also occupied membrane-bound growth-factor receptors are internalized, which clears the cell surface from occupied receptors [Orth et al., 2006, Orth and McNiven, 2006]. Moreover, this mechanism has been shown to be a major mechanism in integrin turnover [Gu et al., 2011].

The internalization of receptors through CDRs constitutes a self-inhibitory feedback of signalling events. Since cancerous cell lines generally form CDRs less frequently, this discovery led to the formulation of the hypothesis that the uncontrolled growth of these cells could be facilitated by their inability to form CDRs [Orth and McNiven, 2006]. On the other hand, the localization of metalloproteases (MMP2) to CDRs has led to the idea that CDRs might also contribute to the invasiveness of cells, enabling them to enter their surrounding tissue [Orth and McNiven, 2006]. Further, the endocytotic properties of CDRs make cells vulnerable for pathogen entry. Indeed, several viruses and bacteria are known to hijack CDRs as a method of gate opening for the entry of cells [Patel and Galán, 2005, Mercer and Helenius, 2009]. Therefore, the endocytotic properties of CDRs recently arose the attention from the medical research community [Mercer and Helenius, 2009].

To date, CDRs are comprehensively characterized with regard to their protein composition, as we will see in Section 2.1.1. However, it is not an established perspective in the biological community to view CDRs as waves of polymerizing actin. In the

recent literature CDRs are usually described as dynamic structures that are enriched in f-actin [Cortesio et al., 2010, Gu et al., 2011, Hasegawa et al., 2011, Hasegawa et al., 2012]. The term "wave", however, is not used in the articles cited above[b]. Although other publications do name CDRs as waves [Abella et al., 2010, Azimifar et al., 2012, Cortesio et al., 2010], a reference to their nature as waves of actin polymerization and depolymerization is entirely missing. The review articles by Buccione, Hoon, Itoh and co-workers stress the character of CDRs as that of actin waves [Buccione et al., 2004, Hoon et al., 2012, Itoh and Hasegawa, 2012]. However, in these articles the propagation of CDRs is mainly considered to consist of ring contraction.

Consequently, the actual mechanism that leads to the propagation of CDRs is not understood. It has been proposed that myosin contractility might cause CDR closing [Dowrick et al., 1993, Mercer and Helenius, 2009]. Indeed, myosin I, II and V have been found to localize to CDRs [Edgar and Bennett, 1997]. However, inhibition of at least myosin II has no effect on the dynamics of CDRs [Zeng et al., 2011]. Therefore, it seems unlikely that myosin-mediated contractility plays a role in CDR dynamics [Hoon et al., 2012].

The question on this mechanism has, however, also attracted the interest of the physics community. In 2011 two articles were published in which the propagation mechanism of CDRs was addressed. The model by Zeng et al. considers CDRs as waves in a classical reaction-diffusion scheme between two Rho GTPases [Zeng et al., 2011]. In contrast, Peleg et al. consider a mechano-chemical feedback mediated by the curvature of membrane-bound proteins, which are at the same time effectors of actin polymerization [Peleg et al., 2011].

The question of the wave mechanism underlying the propagation of CDRs is the main objective of this thesis. Especially the experimental testing of the models by Zeng and Peleg constituted in large parts the initial motivation for this work. A further motivation was provided by the observation that the dynamics of CDRs during their early life stages differs between cells that form CDRs spontaneously and cells that form CDRs in response to growth factor stimulation. The latter, i.e., the stimulation of cells via growth factors, is the established standard method for the research on CDRs. However, with this approach fundamental aspects of CDR dynamics are missed, as will be shown throughout this thesis and interpreted in an active media framework.

Even though it has long been known that CDRs are composed of actin, its structural organization inside of CDRs remains unclear [Hoon et al., 2012]. However, for a full understanding of the wave mechanism of CDRs this knowledge is mandatory. Moreover, as will be introduced in detail in Chapter 3, there is a lack of consensus regarding the overall morphology of CDRs. Therefore there is a clear need for structural investigations on CDRs, which constituted additional motivation for this work.

[b]The naming of the protein WAVE is not considered.

1.3 Waves in Biological Systems

The history of the research on waves in biological systems is closely linked to the problem of pattern formation in organisms. Patterns are found virtually everywhere in nature, ranging from growing bacteria cultures over the positioning of leaves on plants to the fur patterns of animals. The quantitative approaches to the understanding of pattern formation in biological systems dates back to the seminal paper "The Chemical Basis of Morphogenesis" by Alan Turing [Turing, 1952]. In his work, Turing described how two fictional "morphogens" can create patterns due to the processes of diffusion and reaction, i.e., the evolution of what we call a "reaction-diffusion system" today. Henceforth reaction-diffusion systems have been applied to a wide range of problems, among them some of the classes of patterns mentioned above, i.e., bacteria colonies and leaf positions [Murray, 2004b, Meinhardt et al., 1998].

The work of Turing focused on the unstable albeit steady states of reaction-diffusion systems. One decade after publication of Turing's fundamental work Hodkins and Huxley addressed the inherently dynamic problem of the spiking of nerve impulses on the giant axons of a squid with a set of differential equations [Hodgkin and Huxley, 1952]. FitzHugh and Nagumo found a simplified system that reproduces the dynamics of the system of Hodgkin and Huxley, using only two (effective) variables [FitzHugh, 1961, Nagumo et al., 1962, FitzHugh, 1968]. The inclusion of diffusion into the FitzHugh-Nagumo (FHN) model leads to the formation of propagating wave pulses, which will be comprehensively described in the theory chapter of this thesis (Section 2.3).

In fact, waves are common in biological and chemical systems. It is also due to this plenitude that the research on non-linear wave and pattern formation constitute a whole sub-branch in the theory of non-linear dynamics. A prominent example of a wave-forming chemical system is the Belousov–Zhabotinsky reaction in a shallow reactor that forms various patterns of travelling waves, among them spiral waves and concentric wave trains [Zaikin and Zhabotinsky, 1970]. Phenomenological similar wave patterns can be observed in cultures of *Dictyostelium discoideum* under starvation conditions, in which the individual cells of this unicellular slime mould assemble into a multi-cellular migrating slug [Tomchik and Devreotes, 1981, Pálsson and Cox, 1996]. During the aggregation process of the latter, waves of cyclic AMP can be observed that function as an external messenger for cell-cell communication in the aggregation process. The dynamics of both, the Belousov–Zhabotinsky reaction and aggregating *D. discoideum* amoeba have successfully be described by reaction-diffusion systems [Troy, 1985, Tyson and Murray, 1989, Kessler and Levine, 1993].

D. discoideum therefore has a tradition as a model system for the studies of waves in biological systems. Further, this slime mould was and is a popular model for the research on cell motility. It was probably also the earliest organism in which waves of polymerizing actin were described [Killich et al., 1994, Vicker, 2000]. However, it required the discovery of similar waves in a larger number of cell types to reveal the fundamental role that waves of polymerizing actin apparently play in cellular morphodynamics [Allard

and Mogilner, 2013].

1.4 Outline of the Thesis

It is the central hypothesis of this work that the actin machinery of cells constitutes an active medium for the propagation of CDRs. The leading question is that of the nature of the feedback system underlying the wave mechanism. The active media hypothesis will find large support throughout this work. Accordingly the following chapter, which deals with the theory of actin waves (Chapter 2), is dedicated in approximately equal parts to the biological background, introducing the molecular key players and mechanisms in CDRs, as well as to the theory of active media and theoretical models of actin waves.

The experimental results are presented in three chapters following on the theory chapter. The first of these deals with the structure and morphology of CDRs (Chapter 3). In this, questions regarding the localization of individual processes in CDRs are addressed using various methods of microscopy. The chapter closes with a summary and discussion of the results in form of an integrated picture of the morphology and the fundamental processes of the actin dynamics in CDRs. The results resolve a discrepancy in the literature and provide the basis for a formulation of a model description of CDRs.

The second results chapter is dedicated to the analysis of the dynamics of CDR wavefronts. A special emphasis lies on the identification of phenomena that are known to occur for waves in active media (Chapter 4). For this, a cell line forming CDRs spontaneously was employed allowing experiments under constant biochemical conditions. The results reveal a range of novel dynamics of CDRs, comprising spiral waves, breathing modes and collision annihilation.

To reduce the impact of the cell morphology on the dynamics of CDRs, a system for the study of CDRs that is based on microcontact printing was developed, which allows to force cells into the fixed and simple geometry of discs. Thus, in the following, we distinguish between cells of normal fibroblast morphologies, which we term "random-shaped cells" henceforth, and disc-shaped cells. Experiments on disc-shaped cells are combined with a microfluidic flow chamber, which enables to switch the biochemical state of cells in a controlled way. The results of experiments performed with this system are reported in the third results chapter (Chapter 5). The dynamics of cells in this new system yielded completely novel data of CDRs forming with remarkable periodicity and propagating with constant velocities. Varying the state of actin inside cells via drugs, applied using microfluidics, demonstrates the central role that actin plays in the wave mechanism underlying CDRs.

Due to the simple geometrical properties of disc-shaped cells, they permit a direct comparison between experimental data and the results of simulations. The experimental data are interpreted based on analogy to the dynamics of a prototype model of an active medium, i.e., the FitzHugh-Nagumo system (Chapter 6). It is shown that this system, in the presence of noise, is able to explain pivotal dynamic features of CDRs on disc-shaped cells.

The individual results are, where possible, discussed directly after their presentation in the text flow. The last section of each results chapter further summarizes and discusses the findings of the corresponding chapters in a holistic sense.

The significance of the findings for the fields of biology and biological physics are presented in the Conclusion (Chapter 7). This chapter further includes possible future directions for the research on CDRs and protein waves in general.

The methods and materials are presented after the results chapters (Chapter 8). The idea behind this is to attain maximal readability of the thesis. Therefore, the methods are shortly introduced in the text flow of the results chapters where necessary, whereas the chapter on materials and methods serves as a reference for details. In fact the establishment of methods for the analysis of CDRs required extensive developmental work, which is partially reflected by the extend in which individual methods are presented in Chapter 8. Especially the methods for image analysis and the design of the system for investigation of CDRs on disc-shaped protein patches in flow chambers demanded innovative developmental work.

This thesis has an appendix in which figures of minor importance and additional details are presented (Chapter 9).

Chapter 2

The Theory of Actin Waves

CDRs have been a research subject of the biology community for several decades. Therefore, their molecular composition is relatively well characterized. On the other hand, from the perspective of the theory of non-linear dynamics, the typical feedback schemes of wave-supporting systems are known. These systems normally comprise characteristic types of feedback loops between their functional elements. It is thus a reasonable approach to systematically dissect the cellular elements for the existence of the aforementioned feedback loops when aiming for an understanding of CDRs.

Accordingly, this chapter starts with an introduction to the biology of CDRs, i.e., their protein composition and the functional classification of these proteins. Further, the mathematical framework for the quantitative description of protein interactions is briefly introduced. From the physics perspective the process of diffusion is of outstanding importance to protein waves. It is therefore also briefly summarized as well as the role of the cell membrane as a two-dimensional subspace of the cell and a mechanic element. With this, the necessary biological and biophysical basis is laid for the introduction of actin waves. Basic properties and examples of the dynamic phenomena of such models are illustrated based on the example of a prototype system of active media - the FitzHugh-Nagumo model. The chapter closes with a brief summary of two theoretical models that were proposed for CDRs. These models will be further examined and juxtaposed to my results in the discussion (Chapter 7).

Despite the long history of research on CDRs there is currently only a modest understanding of this phenomenon. We will see later that this resulted in large parts from a lack of flexibility in perception from sides of the biological and the physical community alike. This thesis aims to promote an integrated perspective. Therefore, the following theoretical background was kept basic albeit comprehensive to equally foster approaches from readers with a background in physics or biology.

2.1 Biological and Physical Background

2.1.1 Protein Composition of CDRs

Corresponding to the progress of technology, first investigations on CDRs focused on their structure while later, with advances of biochemical techniques, also the molecular compositions could be characterized. Today, a large number of proteins is known to localize into CDRs. Further, the possibility of genetic knock-down experiments shed light on the functions and significance of single molecules. The review papers by Buccione, Orth, Mercer, Hoon, Itoh and co-workers summarize the status quo of the knowledge on the biology of CDRs [Buccione et al., 2004, Orth and McNiven, 2006, Mercer and Helenius, 2009, Hoon et al., 2012, Itoh and Hasegawa, 2012]. Table 2.1 lists the proteins and other molecules known to localize into CDRs. The proteins are assigned into different groups, corresponding to their typical functional roles. None of the proteins is uniquely found in CDRs; quite the opposite, most of them are relatively well known players in the organization of actin dynamics. It is therefore possible to sketch out the potential roles that individual proteins might have in CDRs, even though the molecular mechanism that orchestrates their interplay is not known at present. In the following, a coarse overview of the general framework of actin dynamics is given with focus on the processes that are likely essential for CDRs. In particular, this overview motivates the grouping scheme introduced in Table 2.1.

The undulations of cell shape going along with CDR formation are caused by actin polymerization. For this reason, actin is found largely accumulated in CDRs. Structural investigations revealed the sheet-like nature of upward directed membrane protrusions at the top of CDRs that resemble lamellipodia at the cell front [Chinkers et al., 1979, Mellström et al., 1983, Dowrick et al., 1993, Edgar and Bennett, 1997]. It is therefore not surprising to find actin factors such as the Arp2/3 complex enriched in CDRs, which is associated with a meshwork architecture of actin as found in lamellipodia. Further, proteins localize to CDRs that serve the processes of actin polymerization, stabilization and severing to name but a few. All these actin-organizing proteins directly bind actin and might thus be grouped in a class of "actin-associated factors" (see Table 2.1).

Actin-associated factors are controlled by signalling proteins, which form a group that comprises kinases, small GTPases, and adaptor proteins. These proteins are situated at different hierarchical layers. Prominent examples of proteins that directly control an actin-associated factor, the Arp2/3 complex to be more specific, are the members of the WASP-family [Pollitt and Insall, 2009]. Central regulators further upstream, i.e., proteins that do not directly bind actin-associated factors, include in particular molecular switches such as Rho GTPases and their corresponding GTPase-Activating Proteins (GAPs) and Guanine nucleotide-Exchange Factors (GEFs). Rho GTPases act on actin-associated proteins via signalling cascades through kinases and other signalling proteins.

Actin-Associated Factors	
α-actinin	[1]
Actinin-4	[2,3]
Arp2/3	[2,3,4]
Coronin	[1]
Cortactin	[2,3,5]
Dynamin-2	[2,3,5]
ERMs	[1]
Fascin	[1]
Filamin	[1]
Fimbrin	[1]
Gelsolin	[2,5]
Hsp27	[1]
Myosin-I	[2]
Profilin	[1]
Palladin	[5]
Small GTPases	
Rab5	[2,3,5]
Rac1	[3,4,5]
Ras	[2,3]
Rho	[4]
GAPs / GEFs	
ACAP1 / ACAP2	[2]
Arap1	[6]
ASAP1	[2]
RN-tre	[2,3]
Sos	[3]
SWAP70	[2]
Proteins of Unknown Function	
Microtubules	[4]
MMP2	[2,3,5]

Kinases	
Abl	[2,3,5]
PAK1	[2,3,5]
PI3K	[2,3,4,5]
PKA-RII	[2]
Pyk2 (PTK2B)	[3]
Src	[3,5]
Adaptor and Scaffolding Proteins	
Cbl	[2,3]
Crk	[3]
EPS8	[2,3,5]
GAB1	[3]
Nck	[3]
Paxilin	[2,3,5]
Vinculin	[2,5]
Signalling Proteins (Misc)	
Arf1	[4]
mAbp1	[3]
N-WASP / WASP	[2,3,4,5]
SH3YL	[3]
SHIP2	[3,4]
TAPP1	[4]
Vav	[3]
WAVE1 / WAVE2	[2,3,4]
WIP	[2,3]
Membrane Proteins/Molecules	
β-1-integrine	[3]
IRSp53	[3]
PIP_2	[3]
PIP_3	[3]
Receptor tyrosin kinases	[5]
Tuba	[3,5]

[1]: [Mercer and Helenius, 2009] [2]: [Buccione et al., 2004] [3]: [Hoon et al., 2012] [4]: [Itoh and Hasegawa, 2012] [5]: [Orth and McNiven, 2006] [6]: [Hasegawa et al., 2012]

Table 2.1: *Proteins and other molecules localizing to CDRs.* Note that the grouping scheme is not mutually exclusive, i.e., proteins might fall under more than one category simultaneously. The assignment of proteins to groups was based on the presumed principal roles they play in CDRs.

Proteins and other molecules that are permanently membrane bound have their own group in Table 2.1. The membrane plays a critical role for CDRs right from their initiation as a response to signalling from receptors for growth factors, which are introduced in detail in Section 2.1.5. These are trans-membrane proteins with extra- and intracellular domains. There are, however, also membrane-bound proteins localized into CDRs that are only integral or peripheral to the membrane, i.e., they do not extend throughout the membrane. Especially IRSp53 and Tuba are to name here, as they play a fundamental role in one biophysical model of CDRs that is introduced in Section 2.5. PIP_2 and PIP_3 are lipids whose function was proposed to indicate the presence of the cell membrane in actin dynamics [Pollitt and Insall, 2009]. Even though their precise role in CDRs is currently not elucidated the two most recent CDR reviews by Hoon et al. and Itoh et al. both propose central functions for PIP_2/PIP_3 [Hoon et al., 2012,Itoh and Hasegawa, 2012]. The results presented in Section 5.5 of this work will be interpreted in the light of PIP_2/PIP_3 as potential mediators of the inside/outside polarity of CDRs. This hypothesis is, besides of the work by Hoon, Itoh and co-workers, based on the fact that PIP_2/PIP_3 functions in the polarization of actin waves in *D. discoideum* [Gerisch et al., 2012].

Note that several of the proteins in Table 2.1 have both, cytosolic and membrane-bound states. These cover, e.g., the small GTPases and the members of the WAVE/Scar family. The diffusivity of membrane-bound species is typically drastically reduced compared to cytosolic diffusion (Section 2.1.7), which has important implications for formulations of reaction-diffusion systems, as will be discussed in Section 2.2.

The adaptor and scaffolding proteins listed in Table 2.1 will not be addressed further in the following and are only included for the sake of completeness here as they are not assumed to play key-roles. Furthermore, there are proteins such as microtubules and the metalloproteinase MMP2 located into CDRs. Whether they have a function in CDR dynamics is largely unknown at present.

In general a word of precaution might be necessary when thinking of the large number of proteins that have been reported to locate into CDRs. One must not forget that CDRs can form protrusions of several micrometers in height and that even a protein that has standard cytosolic concentrations in CDRs might appear as enriched in micrographs when labelled fluorescently, due to the integrated fluorescence in z-direction. Therefore, it is likely that some of the proteins included in table 2.1 are not essential for the wave mechanism of CDRs.

The following sections (2.1.2-2.1.5 and 2.1.7) introduce the potential key-elements of CDRs in more detail. The models of actin waves, which are introduced later, are based on the functional interplay of these proteins.

2.1.2 Actin

Actin is a 42 kDa protein of nearly globular shape with a slightly peanut-shaped undulation [Bray, 2001]. It is the most abundant protein in most eukaryotes, which, depending

on cell type, accounts for 5-20% of the total number of proteins in cells [Goodsell, 2001, Pollitt and Insall, 2009]. Actin can occur in two different states. One of these is monomeric (also "globular actin" or, short, "g-actin"), the other filamentous ("f-actin"). In the latter, several actin monomers are polymerized into elongated filaments. Out of these filaments, cells form different kinds of superstructures, ranging from rather static cytoskeleton compartments to highly dynamic structures that form cell protrusions. Cross-linking of parallel actin filament forms, e.g., long and rigid bundles that make up structures such as filopodia and actin stress fibers [Burnette et al., 2007]. Branching of actin filaments, on the other hand, leads to actin meshwork formation that is associated with thin and flat cell protrusions such as lamellipodia [Burnette et al., 2011]. As the formation of these protrusions are the basis for cell motility, actin is the most fundamental protein for cell locomotion with only one known exception - the sperm cells of nematodes. However, actin also plays a fundamental role in cell division and various other cellular processes [Bray, 2001].

Even though some of the f-actin-based structures like, e.g., stress fibres might appear as static objects, f-actin is indeed inherently dynamic, as it is constantly remodelled. This enables cells, e.g., to rapidly change their morphologies - an essential property for cell locomotion. For an understanding of actin dynamics, its interactions with the cellular fuel ATP has to be taken into account. In its monomeric form, each actin monomer can bind one ATP molecule. This causes slight conformational changes that allow for strong bonds between ATP-attached monomers that polymerize into f-actin. Since g-actin is not completely symmetric, f-actin is polarized. The equilibrium constants that result from the association and dissociation rates at the so called "plus-end" and the so called "minus-end" differ, leading to a faster growth at the plus-end. When organized as filaments, the individual actin monomers that make up filaments undergo ageing, which means that the attached molecule of ATP is hydrolysed to ADP. This causes a weakening of actin-actin bonds, i.e., the probability of unbinding events is enhanced. Since the plus-ends of filaments have higher binding affinities than the minus-ends, filaments are more stable at their plus-ends and increasingly unstable towards their minus-ends. Together with the association and dissociation events at both ends, the property of filament ageing leads to the so-called "treadmilling" or "tank-treading" of actin filaments. This means, that, in the frame of reference of filaments, the individual actin monomers flow from the plus- towards the minus-end. In the frame of reference of the laboratory, however, it is the filaments that change position, not the actin monomers, which favours the term tank- treading [Pollard and Borisy, 2003].

2.1.3 Actin-Associated Factors

Inside of cells, f-actin is organized into different kinds of super-structures. The last decades have seen an enormous increase in the understanding of the protein pathways that lead to the organization of actin into these structures that then result in different cell morphologies. Due to the large number of functions that actin fulfils in cells, there is an equivalently large number of proteins that can bind to actin: today there are more

than 160 proteins known to bind actin directly [Dos Remedios et al., 2003]. Due to this large number, only a limited overview can be given here. Thus, in the following the actin factors that are important in the organization of actin into branched networks are introduced, as this is the actin structure underlying CDRs.

A major player responsible for this architecture of actin is the Arp2/3 complex, due to the fact that it functions as a growth promoter and as a branching agent for actin filaments [Pollard and Borisy, 2003]. Insertion of Arp2/3 into filaments causes Y-shaped branches in which filaments have an opening angle of 70° with each other. Accordingly, a coupled meshwork of f-actin results that is underlying cellular structures such as lamellipodia and also membrane ruffles [Pollard et al., 2000]. The activity of Arp2/3 is in turn controlled by proteins of the WAVE/WASP family [Pollitt and Insall, 2009]. For CDRs, the WASP family member N-WASP has been reported to be the major mediator for Arp2/3 activity, whereas WAVE2 only plays a minor role and the role of WAVE1 is negligible [Legg et al., 2007]. However, the drug that was used to inhibit N-WASP in the latter mentioned study, namely wiskostatin, has been reported to be non-selectively and also influence the cellular ATP household [Guerriero and Weisz, 2007]. Therefore, it is currently not clear if N-WASP is indeed the major regulator of actin branching in CDRs.

A study by Weiner et al. has revealed that Hem-1, which is a compartment of WAVE proteins, posses autocatalytic properties. In its active, i.e., membrane-bound, state Hem-1 recruits more Hem-1 to the membrane. In contrast, f-actin deactivates Hem-1 [Weiner et al., 2007]. We will see later that this feedback system is sufficient to explain the formation of waves of polymerizing actin.

Approximately half of the amount of actin in cells is in form of monomeric g-actin [Pollitt and Insall, 2009]. Cells regulate the ratio of monomeric and filamentous actin by various proteins that have the task to sequester and buffer actin (profilin), depolymerize f-actin and therefore recycling g-actin (cofilin), and proteins that prevent further growth of f-actin by capping of the free ends (f-actin capping protein) [Bamburg et al., 1999, Pollard and Borisy, 2003]. Other important members of actin binding proteins are α-actinin, aiding the attachment of f-actin to the cell membrane and f-actin crosslinking, and the motorproteins of the myosin family [Borisy and Svitkina, 2000].

There are several groups of proteins on top of the level of actin-binding proteins, that regulate the activity of these actin-associated factors. In the language of biology, these different levels form signalling cascades that connect the functional and hierarchical layers. Situated upstream and at the heart of these pathways are the Rho GTPases as "central processing units". The activity state of these proteins decides on the structure into which actin gets organized upon polymerization.

2.1.4 Rho GTPases

The Rho GTPases are key-players in the regulation of cellular behaviour and they are crucial to the organization of actin dynamics. The discovery of their interaction schemes in the early 1990s dramatically changed the way protein pathways were pictured.

While most signalling cascades were portrayed strictly linear before, the discovery of the interaction schemes of Rho GTPases revealed that in fact crosstalk and feedback loops exist in protein pathways [Ridley et al., 1992, Ridley and Hall, 1992, Burridge and Wennerberg, 2004].

The Rho family of GTPases comprises about 20 members that can be divided further into the subfamilies of Rho-like, Rac-like, Cdc42-like, Rnd, and RhoBTB subfamilies [Burridge and Wennerberg, 2004, Guilluy et al., 2011]. The first three of these are central to the regulation of actin dynamics, as the activity of each of them is linked to the formation of characteristic structures from actin. Rho activity is linked to the formation of stress fibres, Rac activity to the formation of lamellipodia and ruffles while the activity of Cdc42 leads to the formation of filopodia [Ridley et al., 1992, Van Aelst and D'Souza-Schorey, 1997]. In the signalling cascades downstream of Rho GTPases, kinases and other signalling proteins play central roles [Bray, 2001, 92 p].

Rho GTPases are considered "molecular switches" as they can change between active and inactive states [Etienne-Manneville and Hall, 2002]. The active state corresponds a GTP-bound state, whereas the inactive state corresponds to a GDP-bound state [Guilluy et al., 2011] [Alberts et al., 2005, 579 pp]. The activity of Rho GTPases is mediated by three classes of proteins called GEFs, GAPs, and Nucleotide-Dissociation Inhibitors (GDIs). In many cases, the activity state of GEFs, GAPs and GDIs is in turn set by proteins of the Rho GTPase family. There are several known interaction schemes between pairs of Rho GTPases in which one can control the activity state of the other and vice versa [Guilluy et al., 2011]. When seen in the picture of protein signalling pathways, these interaction schemes correspond to feedback loops. The formation of waves requires elements that have properties of positive or negative feedback. The Rho GTPases are therefore of special interest in the research on protein waves.

2.1.5 Growth Factors and their Receptors

Similar to hormones, growth factors are molecules that serve the cell-cell communication in multicellular organisms. The first growth factors were discovered at the end of the 1950s in the scope of the establishment of the in vitro cell culture. Since it was observed that cell media required a range of substances apart from carriers of nutrition to make them grow, these were termed "growth factors". Today, growth factors are a standard constituent of cell media and are usually added in form of fetal bovine serum. In the research on cells of the immune system and on hematopoietic cells, molecules of similar functions were discovered and termed "cytokines". Later, however, the different terminology turned out to suggest an artificial differentiation between growth factors and cytokines as the latter were identified to contribute to cell-cell communication in cells that neither belong to the immune system nor to the blood-building system. Today, more than 200 molecules are known to belong to the class of growth factors, cytokines, and related proteins. These play substantial roles in cellular processes such as cell differentiation, transformation, synthesis, cell death and cell motility. The terminology of growth factors is often confusing, because names such as, e.g., "fibroblast growth

factor" or "epidermal growth factor" suggest cell type specific roles. Indeed, these names were historically often chosen according to the organism to which these growth factors were applied for the first time. Only later, it was discovered that, e.g., epidermal growth factor can also stimulate fibroblasts [Wordinger and Clark, 2008]. Growth factors that are known to stimulate the formation of CDRs comprise epidermal growth factor, macrophage colony-stimulating factor, and hepatocyte growth Factor [Mercer and Helenius, 2009].

In the research on CDRs, Platelet-Derived Growth Factors (PDGFs) find wide application. Applied to cells, and especially to fibroblasts, PDGF-BB potently stimulates the formation of CDRs within typically 5 min after application [Mellström et al., 1983, Buccione et al., 2004, Orth and McNiven, 2006, Hoon et al., 2012, Itoh and Hasegawa, 2012]. PDGF has been discovered in the 1970s in the search for a serum factor for cultivation of arterial smooth muscle cells [Ross et al., 1974, Hoch and Soriano, 2003]. Today it is known that PDGFs play critical roles in wound healing and migration as well as in the deposition of extracellular matrix factors. Hence, PDGFs are central in embryogenesis but also in adult animals [Hoch and Soriano, 2003, Jin et al., 2008]. Cells are equipped with receptors for the sensing of PDGFs. The function of these transmembrane receptors is not yet completely understood. It is, however, known that the intracellular domain of PDGF receptors contains a tyrosine kinase that plays a crucial role in the triggering of PDGF-related signalling events [Tallquist and Kazlauskas, 2004]. From PDGF receptors there are direct signalling paths leading to centrally situated Rho GTPases, mediated by kinases and other signalling proteins [Hasegawa et al., 2011, Hoon et al., 2012].

2.1.6 Protein-Protein Interactions

Most cellular processes are either a direct or an indirect consequence of the actions and interactions of proteins. Cells utilize several different strategies for their spatio-temporal organization. Proteins are created by the processes of DNA transcription, translation, and folding [Alberts et al., 2014, 299 p]. Taken together, however, these are too slow to account for the fast processes that occur in cells. To achieve a fast albeit economic household of proteins, cells widely utilize mechanisms that allow them to switch proteins between different states. One example of state discrimination, which is a major mechanism in cells, is the process of phosphorylation. In human cells, between 30-50% of the proteome is phosphorylated. In phosphorylation one or more phosphate groups are added to specific amino acids, mediated by protein kinases. The reverse process, dephosphorylation, is mediated by protein phosphatases [Alberts et al., 2014, 819 pp]. Phosphorylation and dephosphorylation are enzymatic reactions, in which the kinases or phosphatases function as enzymes. The protein undergoing a change of state is therefore termed the substrate.

An enzymatic reaction in which a substrate S undergoes a transformation into a product P, mediated by the enzyme E and formation of an intermediate enzyme-substrate

complex C, can be formulated with a mass action expression of

$$\mathrm{E} + \mathrm{S} \underset{k_\mathrm{r}}{\overset{k_\mathrm{f}}{\rightleftharpoons}} \mathrm{C} \xrightarrow{k_\mathrm{cat}} \mathrm{E} + \mathrm{P}, \tag{2.1}$$

in which the ks are the respective rate constants [Schreiber et al., 2009]. Since catalytic steps in enzymatic reactions are usually irreversible, the rate constant of the reversible reaction in the last step was neglected [Murray, 2004b, 175 pp] [Chen et al., 2010]. From the reaction scheme (2.1) a system of differential equations can be read-off, in which the stoichiometric formulation is replaced by the time-dependent concentrations $E(t)$, $S(t)$, $C(t)$, and $P(t)$ for enzyme, substrate, enzyme-substrate complex, and product respectively. For the formulation, the rates of the respective reactions are balanced, yielding one differential equation for each species:

$$\begin{aligned}
\frac{\mathrm{d}E(t)}{\mathrm{d}t} &= -k_\mathrm{f} \cdot E(t) \cdot S(t) + k_\mathrm{r} \cdot C(t) + k_\mathrm{cat} \cdot C(t) \\
\frac{\mathrm{d}S(t)}{\mathrm{d}t} &= -k_\mathrm{f} \cdot E(t) \cdot S(t) + k_\mathrm{r} \cdot C(t) \\
\frac{\mathrm{d}C(t)}{\mathrm{d}t} &= k_\mathrm{f} \cdot E(t) \cdot S(t) - k_\mathrm{r} \cdot C(t) - k_\mathrm{cat} \cdot C(t) \\
\frac{\mathrm{d}P(t)}{\mathrm{d}t} &= k_\mathrm{cat} \cdot C(t).
\end{aligned} \tag{2.2}$$

Since, if the number of molecules is a conserved property, two conservation equations for E and S hold, the full dynamics of reaction (2.1) can be grasped by only two differential equations

$$\begin{aligned}
\frac{\mathrm{d}C(t)}{\mathrm{d}t} &= k_\mathrm{f} \left(E_0 - C(t)\right) \cdot S(t) - (k_\mathrm{r} + k_\mathrm{kat}) \cdot C(t) \\
\frac{\mathrm{d}S(t)}{\mathrm{d}t} &= -k_\mathrm{f} \left(E_0 - C(t)\right) \cdot S(t) + k_\mathrm{r} \cdot C(t)
\end{aligned} \tag{2.3}$$

where the conservation equations for the initial concentrations of enzyme and substrate read

$$\begin{aligned}
E_0 &= E(t) + C(t) \\
S_0 &= S(t) + C(t) + P(t).
\end{aligned} \tag{2.4}$$

Enzymatic reaction kinetics often consists of a fast first reaction step, i.e., towards the substrate-enzyme complex. In this case, it can be sufficient to consider only the rate determining slow part of the reaction. Presence of a fast and slow time scale means that the problem can be separated into an fast "inner" solution and a slow "outer solution" under assumption of a quasi steady state. The outer solution is known as "Michaelis-Menten kinetics". The velocity of the reaction is then given by

$$V(t) = -\frac{\mathrm{d}S(t)}{\mathrm{d}t} = \frac{k_\mathrm{cat} E_0 S(t)}{S(t) - K_\mathrm{M}} \tag{2.5}$$

where

$$K_{\mathrm{M}} = \frac{k_{\mathrm{r}} - k_{\mathrm{cat}}}{k_{\mathrm{f}}} \tag{2.6}$$

is known as the "Michaelis constant". Even though enzymatic reactions are often approximated using Michaelis-Menten kinetics, its validity for processes in living cells is limited [Chen et al., 2010]. The Michaelis-Menten kinetics were derived in the early 19th century, when systems of differential equations could not be solved numerically with reasonable effort [Michaelis and Menten, 1913]. However, since the theories of actin waves are usually formulated as systems of partial differential equations that cannot be solved analytically, application of the Michaelis-Menten approximation is of limited use.

It is a common phenomenon for reactions between substrates and enzymes that an enzyme has more than one binding site, which leads to more complex reaction schemes than (2.1). Moreover, for enzymes with more than one binding site allosteric effects are often found, which means that the binding affinity of a given binding site depends on the occupation state of the other binding sites. The mathematical description of such systems results in a kinetics governed by so-called "Hill equations" in which the substrate concentration enter non-linearly [Murray, 2004a].

From a mathematical point of view, the equations describing protein-protein interaction, such as the example (2.3), fall in the class of non-linear ordinary differential equations. However, this formulation relies on the system being well-mixed so that no spatial variations occur. Obviously, in models of actin waves right the opposite is true: in the mechanisms responsible for formation of waves, spatial inhomogeneity is an essential property. With this, diffusion plays a key role.

2.1.7 Diffusion and the Role of the Plasma Membrane

A system of interacting molecular species that is not well mixed is usually described by means of fields of proteins $c(\vec{r}, t)$ that are functions of space and time. Due to the omnipresent Brownian motion on the microscopic scales of proteins, diffusion is a major contributor to the dynamics of concentration fields of proteins. Mathematically, the evolution of a concentration field due to diffusion is caused by non-balanced fluxes and is described by the diffusion equation

$$\frac{\partial c(\vec{r}, t)}{\partial t} = D \Delta c(\vec{r}, t), \tag{2.7}$$

in which $D\Delta c(\vec{r}, t)$ is the gradient of fluxes $-D\nabla c$ [Nelson, 2004, 108 pp]. The diffusion constant D sets the time scale of the diffusion process and depends, among others, on the size of the particle and the temperature of the system. Here we assumed that it does not vary spatially. Its value is, however, a function of the dimensionality of the space in which a species resides. Cytosolic proteins that are free to diffuse in all three dimensions of space can diffuse much faster than proteins that are membrane-bound and, therefore, are only free to diffuse in two dimensions. Indeed, the membrane is an essential compartment for the understanding of protein dynamics as it is estimated that

30% of the proteome is membrane-bound and that the function of 50% of the proteins relies on membrane interactions [Mäntele, 2012, 67 p]. For proteins that have different states of which one corresponds to a membrane-bound state and the other to a cytosolic state this results in a separation of time scales. In such cases, the diffusivity of the membrane-bound state can often be neglected in the formulation of minimal models.

The cell membrane naturally takes a central place in the understanding of the morphodynamics as it marks the boundary of a cell. Apart from the role of membranes in the formation of a two-dimensional compartment, also the mechanical properties of cell membranes are crucial for cell movement. Due to tension, membranes can act as global mechanical regulators that transmit signals with the speed of sound. Therefore, tension serves the mediation of different processes in the whole cell in a quasi-instantaneous fashion [Keren, 2011]. Further, the local shapes of membranes can determine the local concentration of proteins provided these are curvature-sensitive. As this mechanism is central to the model for CDR propagation formulated by Peleg et al. (Section 2.5), the theory of the mechanics of bending deformations of lipid bilayers is introduced in this section, following the theory of Helfrich and the textbook of Sackmann [Helfrich, 1973] [Sackmann and Merkel, 2000, 335 pp].

Cell membranes are thin bilayers formed by spontaneously self-assembly of a heterogeneous mixture of different types of phospholipids and have a typical thickness of about 4 nm [Schünemann, 2005, 4 pp] [Mäntele, 2012, 57 pp]. Depending on the relative number of lipids on the inner side of a closed lipid bilayer and the outer side, different states of curvature K can correspond to the minimal energy state[a]. The curvature that corresponds to the minimal energy is called the "spontaneous curvature" K_0. Deformations from this state cost the system energy [Nelson, 2004]. A bending deformation of a membrane is characterized by its two local principal curvatures K_1 and K_2 . The total energy upon bending deformation of a membrane of area S is therefore in quadratic order given by

$$\mathcal{H} = \frac{\kappa}{2} \int_S (K_1 + K_2 - K_0)^2 \mathrm{d}r^2. \tag{2.8}$$

Here, κ is the bending rigidity. For small membrane undulations, the Monge representation can be used, in which the membrane height is a function of the planar coordinates x and y: $h = h(x, y)$. The bending energy is then given by the Helfrich Hamiltonian [Helfrich, 1973]

$$\mathcal{H} = \frac{\kappa}{2} \int_S (\Delta h - K_0)^2 \, \mathrm{d}r^2. \tag{2.9}$$

There are cases where the curvature of membrane-bound proteins crucially influences their function. The probably best-known example of such a protein is clathrin, which

[a]It has a certain tradition to name the curvature c, whereas in this work the variable K is used. This is to avoid confusion with the variable denoting concentrations and contours (see list of variables on page xiii)

is responsible for the formation of small vesicles in the process of clathrin-mediated endocytosis [Alberts et al., 2014, 697 pp]. However, clathrin is not the only example of a protein that, by its structure, alters the membrane shape. Rather recently, it became clear that there is a whole class of proteins, the BAR domain superfamily, that is indispensable for several cellular functions, whose members are inducers of membrane curvature [Qualmann et al., 2011]. BAR proteins insert into membranes by either a scaffolding mechanism, in which the protein binds to negatively charged lipid head groups, or by hydrophobic interaction, in which hydrophobic parts of the protein extend into the inner parts of the cell lipid bilayer. The geometries of the members of the BAR family, comprising classical BAR, N-BAR, BAR-PH, PX-BAR, F-BAR and I-BAR, differ considerably and can induce both positive and negative curvature into membranes [Qualmann et al., 2011]. BAR proteins that have a SH3 domain can bind to WASP family members and formins, which in turn regulate actin dynamics [Heath and Insall, 2008]. From a biophysical perspective this class of proteins is very interesting, because it suggests that there can be feedback loops between actin polymerization, leading to changes in membrane shape, and concentration of BAR proteins, which in turn affect actin dynamics.

In many models of actin waves the field description of proteins only comprises the number of molecules per spatial unit, i.e., it does not consider their spatial extension. However, for molecules that bind to membranes such as, e.g., the BAR proteins their shape influences the local distributions, as mismatches between the shape of the proteins and the local membrane curvature costs the system energy. Therefore, an area coverage of membrane-bound proteins of ϕ induces a term into the Helfrich energy that equals a spontaneous curvature, given by $h_0 = H_0\phi$, where H_0 is the spontaneous curvature of the protein species [Leibler and Andelman, 1987, Seifert, 1993, Cox and Lowengrub, 2015]. With this, the Helfrich energy takes the following form

$$\mathcal{H} = \frac{\kappa}{2} \int_S (\Delta h - H_0\phi)^2 \, \mathrm{d}r^2. \tag{2.10}$$

Here, all other possible reasons for a spontaneous curvature such as, e.g., an asymmetric lipid composition were neglected. With the presence of membrane-bound proteins, the morphology of the cell, or more precisely the membrane shape, couples to the concentration fields of these proteins.

2.2 Models of Actin Waves

Based on the biophysical background presented in the last sections, the question arises how the individual elements interact to form CDRs, which are waves of polymerizing actin, as we will see later. Given the large number of model organisms and situations in which actin waves have been observed, there exists a correspondingly large number of models that aim to explain the mechanisms responsible for the propagation of actin waves. To identify the key-elements necessary for a working wave machinery it is useful

to start from an abstract point of view and the treatment of minimal systems. Even for systems with a large number of involved molecular species and functional modules it is usually possible to formulate reduced effective systems that show very similar behaviours to the original systems and thus capture the whole system's dynamics. In terms of reaction-diffusion systems, the reason for this lies in the different kinetics of the involved reactions. In case of several competing parallel reactions it is the fastest one that governs the dynamics, while for linear reaction schemes it is the slowest one that dominates the overall dynamics [Chen et al., 2010]. Often, a system can be reduced to a minimal set of two coupled partial differential equations. The FitzHugh-Nagumo model, that will be introduced in the following section, is probably the best known-example of such a reduced system. However, as a cost of simplification, the constituents of minimal systems, such as the FitzHugh-Nagumo model, do not necessarily have direct physiological representations.

Key to models that produce propagating waves are elements that interact with fast positive feedback and delayed negative feedback. Figure 2.1 shows the feedback schemes of the two most basic effective wave models describing two interacting species a and b [Allard and Mogilner, 2013]. Both schemes exhibit fast autocatalysis and delayed inhibition. In a current review on actin waves, Allard et al. classify models of actin waves into three different groups, depending on the nature of the positive feedback, which are introduced in the following [Allard and Mogilner, 2013].

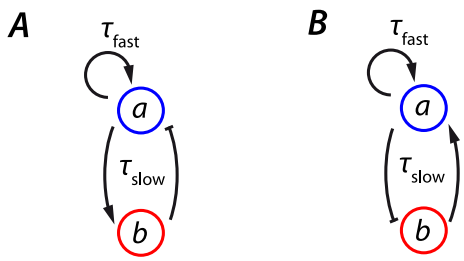

Figure 2.1: *Possible feedback schemes supporting wave propagation.* Sharp arrows denote activating interactions, blocked arrows indicate inhibitory interactions. Both systems have an autocatalytic feedback on a fast time scale τ_{fast} and an inhibitory feedback (direct in A, effective in B) on a slower time scale τ_{slow}. Reproduced from [Allard and Mogilner, 2013].

The first group covers models in which actin itself is the autocatalytic element. As described in the sections 2.1.2 and 2.1.3, actin polymerization is inherently autocatalytic, because the polymerization of actin creates binding sites for more polymerization of actin. This is especially apparent if one considers the filament-branching Arp2/3 complex, of which each incorporated unit creates two new actin binding sites. The wave propagation velocity of autocatalytic actin waves corresponds to the growth velocity of the actin meshwork, i.e., is in the range of $0.1\,\mu\mathrm{m\,s^{-1}}$ [Dubin-Thaler et al., 2008]. As an

example of autocatalytic actin waves, Bretschneider and co-workers have shown that actin waves in *D. discoideum* form even in the absence of regulatory proteins such as Scar/WAVE [Bretschneider et al., 2009].

In the second group of models, the positive feedback is mediated by proteins that are involved in the regulatory pathways of actin. These models are of classical reaction-diffusion type as the feedback propagates with the diffusion of the regulators [Mori et al., 2008, Holmes et al., 2012, Mata et al., 2013, Wasnik and Mukhopadhyay, 2014]. The resulting wave velocity scales with the square root of the regulator's diffusion coefficient and is also dependent on the regulator's turnover rate [Allard and Mogilner, 2013]. Examples of protein species with fast autocatalytic feedbacks, which have been devised to be central in actin waves, comprise the Hem1 complex, which is a constituent of the Scar/WAVE complex, and the Rho GTPase Rac [Weiner et al., 2007, Zeng et al., 2011]. In general, for pairs of Rho GTPases there is a large number of possible feedback loops that can form interaction schemes as shown in Figure 2.1. The reason for this is that Rho GTPases can mutually control their states of activity via GAPs and GEFs [Burridge and Wennerberg, 2004, Guilluy et al., 2011]. This makes them a very interesting group of molecules in terms of models of actin waves. It is important to note that actin does not necessarily form an active component in the propagation mechanism of theses waves. In models such as, e.g., that proposed by Zeng et al., the wave of actin only forms as a response of "hidden protein fields" (WGAP and Rac, in this case) that form the actual wave propagator [Zeng et al., 2011]. The visualization of such waves of regulatory proteins requires specific fluorescent labelling, whereas waves of f-actin, such as CDRs, can be observed without molecular staining. The model by Zeng et al. explicitly describes CDRs and is therefore introduced explicitly in Section 2.4.

The third group mentioned by Allard et al. shares a positive feedback in form of mechanical coupling. The mechanical compartments in this respect are mainly the cell membrane and the viscoelastic bulk material of the cell interior, of which the latter constitutes an acto-myosin gel. The cell membrane is mainly associated with its passive tension [Keren, 2011]. Acto-myosin gels, however, are active materials, as they can transfer chemical energy into pushing or pulling forces [Joanny et al., 2007].

In such systems, there are several possibilities for feedback mechanisms. One is through stresses in the actin gel that might be caused by pushing forces of growing actin filaments or the pulling forces of myosin motors and the interplay of both mechanisms with the cell membrane [Shlomovitz and Gov, 2007, Enculescu et al., 2010, Gholami et al., 2012]. However, in several cases, models that incorporate mechanical elements are inherently more complex than reduced feedback schemes as depicted in Figure 2.1. Therefore, for models that consider, e.g., steric interactions of actin filaments and their alignment or mobile boundaries (representing the cell membrane) the identification of a single positive feedback mechanism might not be feasible [Whitelam et al., 2009, Doubrovinski and Kruse, 2011, Dreher et al., 2014]. Therefore, an effective two-component description as shown in Figure 2.1 might not be applicable to such systems.

The last decade has seen large progress in the development of generic theories

for active polar gels. These theories are formulated systematically, similar to the theories of hydrodynamics or elasticity, based on conservation equations of mass and momentum [Landau and Lifshitz, 1989, Landau and Lifshitz, 1991]. The constitutive equations for active polar gels are then derived from the formulation of the free energy of the system and expressed via generalized fluxes as functions of generalized forces in the sense of an Onsager theory [Joanny et al., 2007, Marchetti et al., 2013].

In the context of CDRs, i.e., actin waves that deform and thus curve the cell membrane, the particular class of models that incorporate curvature-sensitive membrane-bound actin factors are of especial interest [Shlomovitz and Gov, 2007, Peleg et al., 2011]. Hence, and also because one of these models is explicitly dedicated to CDRs, they will be introduced in more detail in Section 2.5.

During this work it became clear that CDRs indeed show several typical characteristics of excitable media, as described by, e.g., minimal reaction-diffusion systems. The following section therefore introduces the FitzHugh-Nagumo model in detail, which is a prototype model of such an active medium.

2.3 The FitzHugh-Nagumo Model

The theory of reaction-diffusion systems is the basis for the interpretation of the data of this thesis. In the following, this theory is thus shortly introduced with a focus on the FitzHugh-Nagumo (FHN) system, which is a prototype model of an active medium that forms propagating waves. The FHN system has a certain tradition in biological research and has served, besides the description of travelling action potentials on neurons, as a basis for a minimal description of the cardiac tissue [Kogan et al., 1991, Aliev and Panfilov, 1996, Berenfeld and Abboud, 1996] and for waves of cortical depression in the brain cortex [Murray, 2004b, p 42].

In its original formulation, the variables of the system are the membrane potential V and the so called "recovery variable" R, where the latter has no direct physical correspondence [Edelstein-Keshet, 1988, p. 337]. The FitzHugh-Nagumo model with Diffusivity D reads:

$$\begin{aligned} \frac{\partial V}{\partial t} &= D\Delta V + V - V^3/3 - R + S \\ \frac{\partial R}{\partial t} &= \phi(V + a - bR). \end{aligned} \tag{2.11}$$

Much like the inhibitory variable R, the parameters ϕ, a and b have no direct physical meaning. The variable S describes an external stimulus and Δ is the Laplace operator. The temporal evolution of R lacks a diffusive term; accordingly, the FHN sytem can formally be seen as a two-component Turing system with vanishing diffusion of one of the species. The physical motivation behind the negligence of the diffusion of the recovery variable is that in two-component reaction-diffusion systems one species often has a much smaller diffusion coefficient than the other. This could be due to, e.g., the

slow species being membrane-bound, which much reduces its diffusion compared to a fast-diffusing cytosolic species. Another reason could be that the recovery variable corresponds to a species that forms large and therefore slowly diffusing complexes. In the scope of models of actin waves, the R-field could thus especially describe f-actin.

The feedback scheme of the FHN model corresponds to the type shown in Figure 2.1A. The reaction terms of the FHN model include non-linearities, which make the system excitable, under appropriate choice of parameters. Physically, such a non-equilibrium medium is called active, because it requires constant energy supply to maintain its excitability. In the following sections different characteristics of the FHN model are introduced in detail. Furthermore, a range of phenomena is presented, motivated by the fact that they were also found to occur in the analysis of dynamical data of CDRs.

Details regarding the numerical solutions of the FHN system can be found in Section 2.11.

2.3.1 Excitability and the Phase Space Picture

The FHN model can have up to three fixed points, because it contains a cubic term. However, we will focus on the simple case with only one fixed point, because this is sufficient to account for the phenomena observed for CDRs. In the aforementioned case, the V- and the R-nullcline only have one intersection point, i.e., the fixed point termed P in the following.

Figure 2.2A shows the phase space picture of the FHN model (2.11) for a choice of parameters of $a = 0.8$, $b = 0.7$, $\phi = 0.08$, and $S = 0$ [FitzHugh, 1968]. The fixed point is situated at $P = (V_0, R_0) \approx (-1.2, -0.6)$. A linear stability analysis reveals that P is of type stable spiral (see also Figure 2.4B) [FitzHugh, 1969, pp. 18] [Strogatz, 2007, pp. 123, pp. 150]. The vector field in Figure 2.2A indicates that a perturbation of the system slightly away from its fixed point leads an excursion following a cycle trajectory returning the system to its fixed point. This behaviour makes the system a relaxation oscillator and is basis for its ability to support travelling waves [FitzHugh, 1961].

2.3.2 Travelling Waves

Due to the fact that in the FHN system adjacent positions in space are coupled via diffusion (equation (2.11)), a local excitation spreads into its surrounding. There, this stimulus can be sufficient to reach a limit cycle trajectory, supported by the excitability property. Figure 2.2A includes an example trajectory of the system undergoing wave propagation. The trajectory was obtained via numerical integration of the system with a diffusion constant of $D = 1$. Initially, the system was placed close to its fixed point, equilibrated for a few iterations, and then locally perturbed with a stimulus S of constant amplitude for a short temporal duration. Two outwards travelling wave pulses originate from the point of stimulation in both the V- and the R-field (Figure 2.2B and C respectively). The pulses have a constant velocity and characteristic profiles, as shown in Figure 2.2D. Following the dynamics given by (2.11), V responds first to

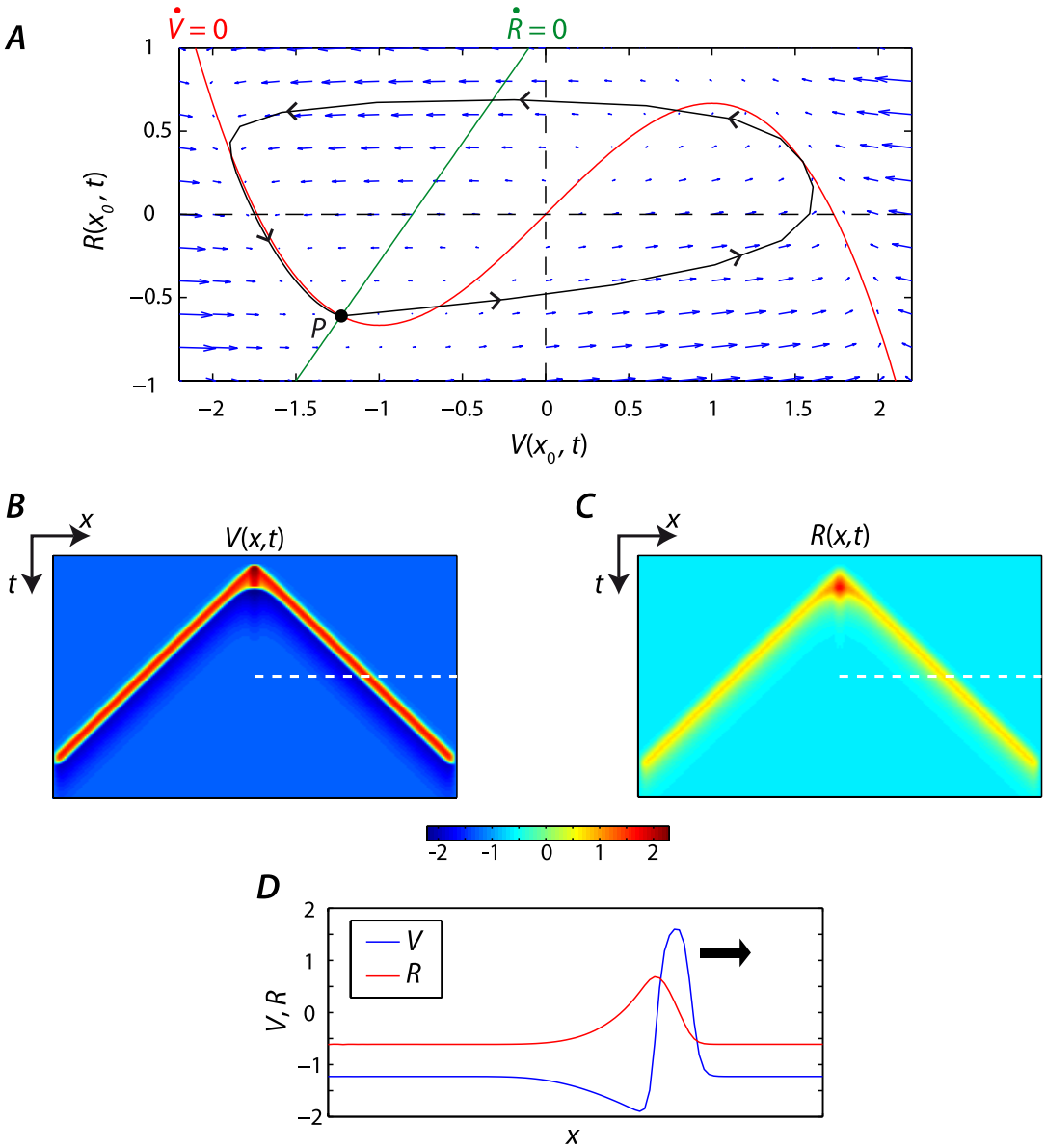

Figure 2.2: *Characteristic dynamics of the FHN system. A*: Phase space with vector field $(\dot{V}, \dot{R})$, the nullclines of the system (2.11) (red: V, green: R), and its fix point P (black dot). The black trajectory shows a characteristic phase space excursion supporting travelling waves (arrows: direction of time). *B* and *C*: Space-time plots of the V- and R-field respectively, visualizing two travelling waves of $\wedge$-shaped signature. The waves formed in response to a stimulus at the tip of the $\wedge$-shaped structure. The color bar applies for both *B* and *C*. *D:* Profiles $V(x, t_0)$ and $R(x, t_0)$, taken at the positions in *B* and *C* that were marked with dashed white lines. The direction of propagation is marked with a black arrow.

a stimulation and, given the choice of parameters and corresponding to the feedback scheme in Figure 2.1A, faster than the R-field. This behaviour can also be read-off from the trajectory in phase space (Figure 2.2A). Situated behind the maximum of the V-pulse lies the so called "refractive region" that supports no immediate formation or propagation of a second wave due to high values of R and small values of V.

The wave pulses resemble solitons in several of their characteristics, e.g., the coherent propagation of a single wave pulse of constant velocity. However, solitons are known to cross each other without perturbation [Bronstein et al., 2008, p. 567]. In contrast, this property is typically not found for wave pulses of the FHN system (with exceptions, as reported in [Argentina et al., 2000]).

2.3.3 Colliding Wavefronts

The behaviour of a system upon collision of wavefronts bears information on the wave mechanism. While waves obeying linear differential equations like, e.g., waves described by the linear equations of electromagnetism, can cross each other without perturbation, waves in non-linear systems behave differently. For excitation waves the mutual annihilation upon collision is a typical behaviour [FitzHugh, 1968, Allard and Mogilner, 2013].

The following description of the typical dynamics upon wave collision is supported by the time sequence in Figure 2.3. The plots show a two-dimensional solution of the FHN model in which the medium was stimulated in the time interval $5 < t < 15$ and at two points, forming two ring waves. The process of wave collision is shown in Figure 2.3.

Upon collision of two wave pulses, the V-field of both pulses superimposes causing a slight overshoot over the maximal value of the two pulses prior to collision ($54 \leq t \leq 64$ in Figure 2.3). The negative cubic term in equation (2.11) and the rise in R following a growing V, however, quickly pull this overshoot down again ($64 \leq t \leq 69$ in Figure 2.3). Since, after collision, the unified pulse is surrounded by the refractive zone of the former two pulses, it cannot propagate and gets finally destroyed by the R-field ($t = 74$ in Figure 2.3). This is the classical behaviour of an active medium.

Nevertheless, numerical research on the FHN system and also on its physical archetype, the axon, have shown that the mutual annihilation of wave pulses in active media is no dogma, because exceptions were found [Argentina et al., 2000, Gonzalez-Perez et al., 2014].

2.3.4 Periodic Wave Formation

The characteristic excursion in phase space of the FHN system upon formation and propagation of single wave pulses, as described in the previous sections, ends with the return of the system to its fixed point P (Figure 2.2A). This behaviour results from the nature of the fixed point of the system (with $a = 0.8$, $b = 0.7$ and $\phi = 0.08$) of a stable

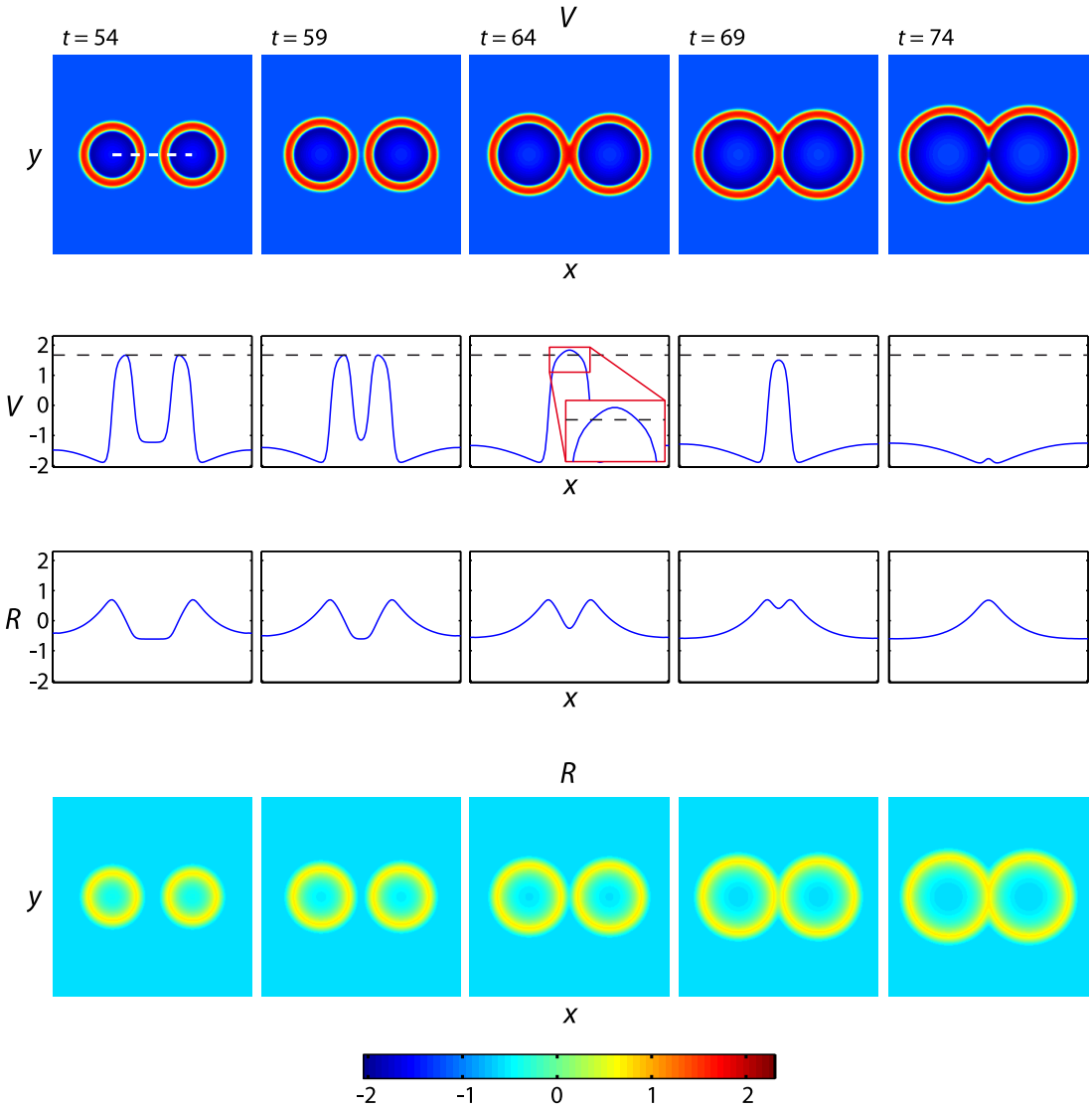

Figure 2.3: *Wave collision in the FHN model.* Upper row: fields $V(x, y)$, second row: profiles $V(x)$, third row: profiles $R(x)$, bottom row: fields $R(x, y)$. Data in one column belong to identical time points. The time stamps at the very top refer to the start of the simulation at $t = 0$. The profiles were sampled at the position highlighted in $V(x, y)$ at $t = 54$ with a white dashed line. The color bar applies for both V and R. The black dashed line in cuts of the V-field highlight the maximal value of single wave pulses. Upon collision, this value is slightly exceeded due to an overshoot (close-up view: red box).

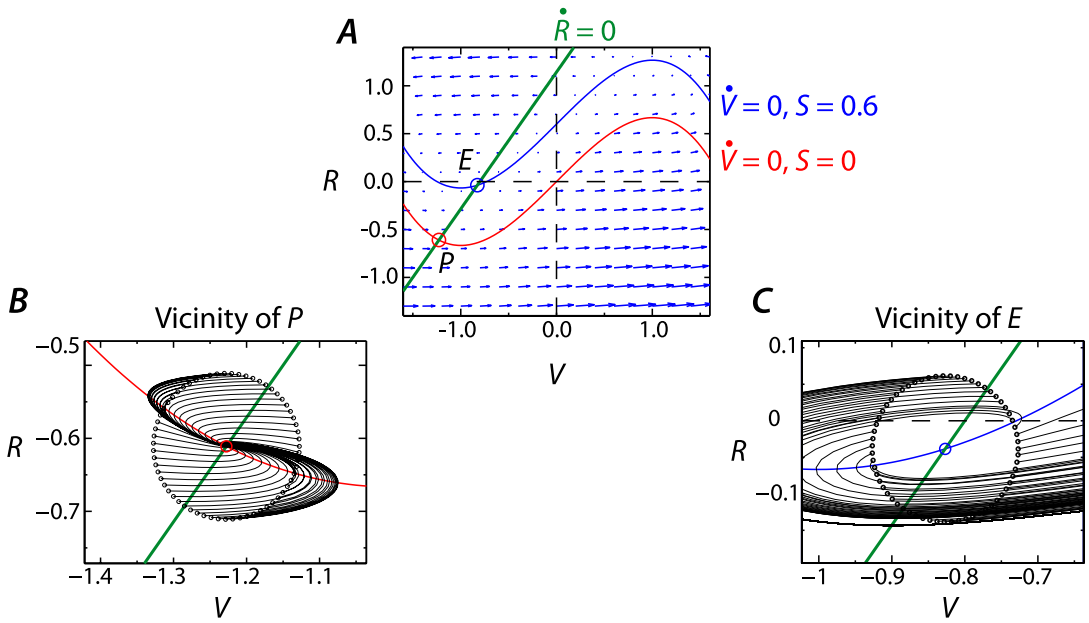

Figure 2.4: *Phase space of the FHN system forming repeated pulses. A*: Comparison of the $S = 0.6$ and the $S = 0$ phase space picture. The field of vectors $(\dot{V}, \dot{R})$ belongs to the non-zero S. *B*: For $S = 0$, the fixed point P is attractive. For illustration, trajectories originating from the black dots on a circle of small radius around P were plotted. *C*: For $S = 0.6$, the same procedure for E leads to trajectories undergoing large phase space excursions not approaching E.

spiral. This means that P has an attractive basin and trajectories in its vicinity end in the fixed point when undergoing evolution in positive time direction (Figure 2.4B).

However, when the system is altered by introduction of, e.g., a constant non-zero S of suitable magnitude, the phase space changes and so does the character of the fixed point. In the following, the case $S = 0.6$ is studied. Introduction of a positive S corresponds to a horizontal shift of the V-nullcline (Figure 2.4A). As a result, the intersection point, marking the fixed point, is no longer situated on the left branch of the cubic V-nullcline, but shifted towards the center branch. The fixed point of the excited system is called $E = (V_{\mathrm{E}}, R_{\mathrm{E}})$ in the following. A linear stability analysis reveals that E is an unstable spiral, i.e., all trajectories in its vicinity lead the system away from it and approach a stable limit cycle (Figure 2.4C) [FitzHugh, 1969, pp. 18]. Under these circumstances, repeated pulses are formed.

The behaviour of a one-dimensional system repeatedly forming wave pulses is shown in Figure 2.5. A two-dimensional analogue forms concentric wave trains ("target patterns") in this situation.

2.3.5 Spiral Waves

Spiral waves are an often-encountered phenomenon in two-dimensional reaction-diffusion systems [Strogatz, 2007]. Examples comprise the Belousov-Zhabotinsky reaction [Smolka et al., 2005], the segregation process of amoeba of *D. discoideum* [Pálsson and Cox, 1996] and abnormal activity patterns in cardiac tissue [Comtois et al., 2005]. In the following a mechanisms that leads to spiral wave patterns is illustrated, which is based on spatial inhomogeneities of the system. Since the FHN model is central to several studies of spiral patterns in cardiac tissue, the following content has its origin in the research of the beating heart [Panfilov and Keener, 1995].

In the functional heart, coherent wave trains coordinate the rhythmic contraction of the heart muscle. In the presence of, e.g., degraded or dead tissue, that might result from a heart attack, this pattern can be disturbed, giving rise to re-entry wave patterns. In this phenomenon, wave trains no longer propagate in sequence over the cardiac tissue, but one single wave pulse repeatedly enters the same region of the heart leading to cardiac arrhythmias and cardiac fibrillation. The emergence of spiral waves is one possible type of wave pattern in this malfunction of the heart [Qu et al., 2014].

A simple study of the FHN model reveals the origin of this phenomenon. The damaged heart tissue is assumed to exhibit dead and partially degraded tissue. The former is not excitable and the latter has a reduced time constant $\bar{\phi}$ of the inhibitory field R. One possible setup and its resulting dynamics is shown in Figure 2.6.

The medium was set up with a disc-shaped zone of dead tissue ($\dot{V} \equiv 0$, $\dot{R} \equiv 0$). The time constant of the inhibitory field of the medium was set to the reduced value $\bar{\phi}$ in a rectangular region beside this disc-shaped zone (see first frame in Figure 2.6). The parameters used for the two-dimensional simulation were: $D = 1 \times 10^{-4}$, $a = 0.8$, $b = 0.7$, $\phi = 0.22$, and $\bar{\phi} = 0.055$.

To account for the physiological situation in the heart, the simulation was started with the formation of two straight wavefronts with a short temporal delay ($t = 60$ in Figure 2.6). The first wavefront passes the obstacle, leaving a long-lasting refractory

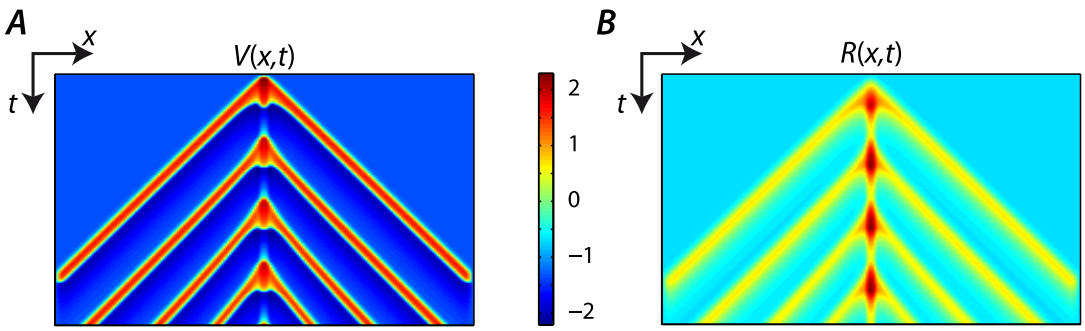

Figure 2.5: *Periodic wave formation in the FHN model.* The medium was subject to constant stimulation ($S = 0.6$) at the center of the x-axis. The color bar applies for both plots.

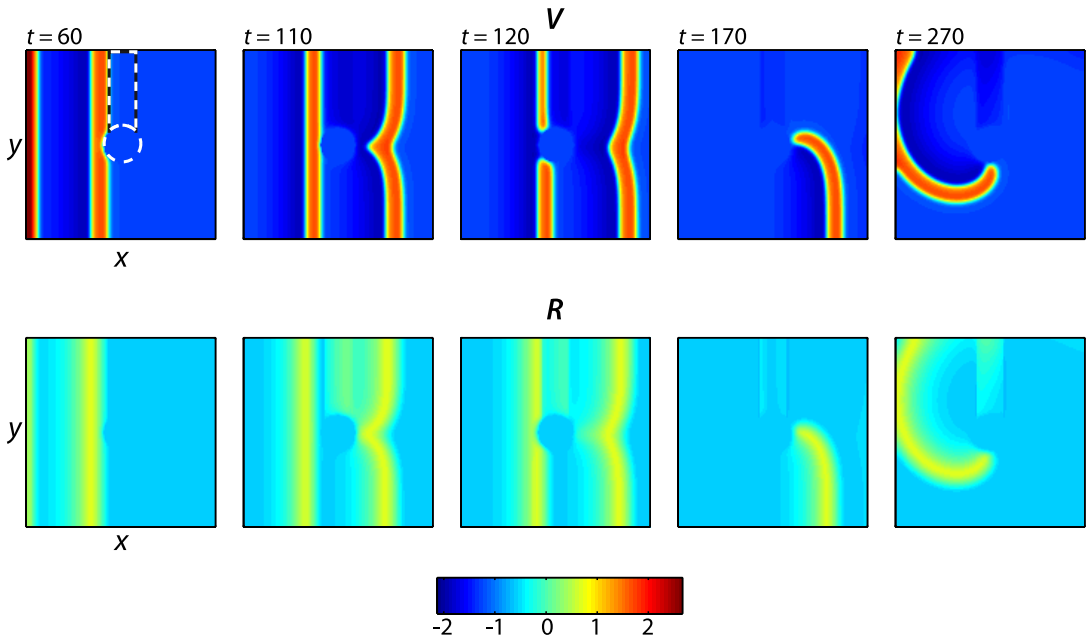

Figure 2.6: *Spiral waves in the FHN system.* Time sequence of the initiation of a rotating spiral pattern. Both the V- (top row) and the R-field (bottom row) were plotted for different time points (measured with respect to initiation of the first wavefront). The color bar applies both for V and R. The white circle encloses a non-excitable region and the black/white rectangle a region of reduced ϕ-values (constant setup for the whole simulation).

region in the area of slow inhibitor dynamics ($t = 110$ in Figure 2.6). Since the second wave arrives when this refractory region has not completely recovered, the wave extinguishes in this area ($t = 120$ in Figure 2.6). The remaining branch of the incoming wavefront then winds around the obstacle establishing a stable spiral wave pattern ($170 \leq t \leq 270$).

The example given above might be artificial, nonetheless there exist various scenarios that can give rise to spiral patterns. In general, situations where wavefronts have open ends are liable to evolve into spiral patterns. A second requirement for emergence of spiral patterns is a relatively slow inhibitory time scale, otherwise open ends lead to vanishing wavefronts.

The propagation velocities of different parts of the spiral-forming wavefront are typically not uniform, i.e., they vary as a function of the radial distance of the wavefront measured with reference to the spiral center. A closer examination reveals that the actual governing parameter is not the radial distance itself but the curvature of the wave front that decreases with increasing radius. Comtois et al. provide a simple explanation for the variation of wave propagation velocity with wave front curvature [Comtois et al., 2005]. In a reaction-diffusion system, such as the FHN model, the wave signal propagates with the diffusion of the activator. The coupling between adjacent elements of space is

mediated by the diffusive flux; the more positive influx an element has, the faster it can reach a super-threshold level and become exited in turn. For a plane wave, there is a one-to-one correspondence between the number of space elements in the wave front and the number of elements of the future wavefront that might be situated one space element ahead in propagation direction (Figure 2.7). For concave or convex wavefronts, however, a smaller or larger number of space elements must be exited respectively (Figure 2.7*B* and *C*). In the case of concave wavefronts the inward fluxes are higher, as a consequence of the unequal occupation number of space elements of current and future position and vice versa. As a consequence, concave wavefronts propagate quicker than convex wavefronts.

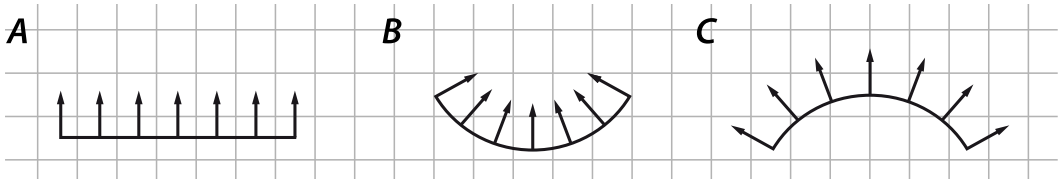

Figure 2.7: *The principal underlying the eikonal equation.* Space is discretized into a grid for illustration. *A*: In a plane wavefront, every grid element excites one grid element in propagation direction. *B*: For concave wavefronts a smaller number of grid elements needs to be excited. *C*: For convex wavefronts, a larger number of grid elements must be exited. Reproduced from [Comtois et al., 2005].

The relation between wavefront curvature and propagation velocity resembles the quantitative concept of the eikonal equation in electrodynamics, which links wave optics to ray optics [Fließbach, 2005]. Consequently, eikonal theories have been developed for waves in active media that describe the propagation velocity as a function of the wavefront curvature [Keener, 1991, Mulholland and Gomatam, 1996]. It will turn out that no eikonal relation can be measured for CDRs. For this reason the theory is not further introduced here.

2.4 Modelling CDRs via an Antagonistic Rho/Rac Reaction Scheme

In this section, a model by Zeng et al. is introduced that describes the formation and propagation of CDRs [Zeng et al., 2011]. Their work was inspired by observations on the effect of substrate stiffness on the formation of CDRs. Harder substrates led to enhanced stress fibre formation and also increased the lifetimes of CDRs.

A central idea of the model is that actin can be organised in different structures, such as stress fibres and lamellipodia. As introduced in Section 2.1.4, the former is associated with the activity of the Rho GTPase Rho, while the latter form in response to activity of the Rho GTPase Rac. Rho and Rac therefore compete in the organization of actin into their respectively associated structures. The full model is complex, comprising

more than 40 reactions and almost 30 parameters. The species included are, besides the aforementioned Rho and Rac, several GAPs and GEFs as well as signalling proteins for instance WAVE, PI3K and actin associated factors such as the Arp2/3 complex. The simulation captures the effects of hard substrates via high values of the focal adhesion kinase - a protein that is linked to the formation of focal adhesions, structures that are typically enhanced on hard substrates [Geiger et al., 2001]. The outcomes of the simulation show that hard substrates, represented by high values of focal adhesion kinase, indeed lead to longer CDR lifetimes.

Zeng et al. additionally present a minimal variant of their model that focusses on the mechanism of wave propagation. Key to this is the interplay of a (hypothetical) WAVE1-binding Rac GAP protein called "WGAP" and Rac. Being a member of the Rho family of GTPases, Rac has an inactive and an active state [Burridge and Wennerberg, 2004]. WGAP and Rac interact according to the scheme shown in Figure 2.8.

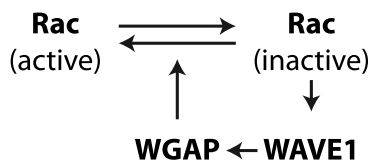

Figure 2.8: *Reduced reaction scheme as proposed by Zeng et al.* Adapted from [Zeng et al., 2011].

The reactions between WGAP and Rac are described by enzymatic reactions, described by Hill's equation and Michaelis-Menten kinetics. Further, polar coordinates are used to account for the symmetry of the problem. The reduced model for the radial coordinate R then reads

$$\begin{aligned} \frac{\partial X}{\partial t} &= D\frac{1}{R}\frac{\partial}{\partial R}\left(R\frac{\partial X}{\partial R}\right) + \frac{V_1\left(X_t - X\right)}{K_{m1} + X_t - X} - \frac{V_2 X^2 Y}{k_{\mathrm{m2}}^2 + X^2} \\ \frac{\partial Y}{\partial t} &= D\frac{1}{R}\frac{\partial}{\partial R}\left(R\frac{\partial Y}{\partial R}\right) + \frac{V_3 X\left(Y_t - Y\right)}{K_{m3} + Y_t - Y}. \end{aligned} \tag{2.12}$$

Here, X and Y represent active Rac and WGAP respectively, with X_t and Y_t being their total concentrations. Diffusivity is given by D, and all other variables are kinetic parameters and enzymatic activities. In the work by Zeng et al. teh evolution of none of the protein fields is plotted. Instead, the radial coordinate of the field representing Rac is plotted, which reveals that the perturbed system (2.12) forms rings that expand and shrink after some time of growth, finally collapsing back to one point.

2.5 Modelling CDRs via Curved Membrane Proteins

Since actin waves, such as CDRs, can create membrane undulations it is an attractive idea to think of the membrane shape as a feedback mediator of the wave mechanism.

Consequently, models have been formulated that incorporate functional modules in form of membrane-embedded species of asymmetric shapes as introduced in Section 2.1.7. Their geometry makes them prefer regions of the membrane that are curved (Figure 2.9*A*). Further, these species are "active proteins", such as proton pumps, or signalling proteins that trigger actin polymerization pathways [Ramaswamy et al., 2000,Shlomovitz and Gov, 2007]. A positive feedback can be in form of a convex species that promotes convex undulation by, e.g., triggering of actin polymerization. Negative feedback can be caused by concave proteins that promote protrusion or in form of convex proteins that trigger retraction, e.g., by activation of myosins [Shlomovitz and Gov, 2007].

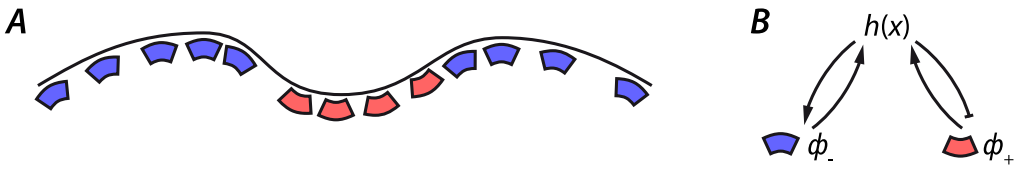

Figure 2.9: *Curved membrane proteins.* *A*: Schematic of convex (blue) and concave (red) activators bound to a membrane. Both types of activators can freely diffuse in the membrane, but prefer regions that match their own curvature. *B*: Feedback scheme between the local membrane height and the local concentration of convex (ϕ_-) and concave (ϕ_+) proteins. Reproduced in modified form from [Peleg et al., 2011].

In 2011, Peleg et al. proposed a model for CDRs based on the interaction of two types of curved membrane proteins that are effectors of actin polymerization [Peleg et al., 2011]. The remaining part of this section is dedicated explicitly to this model. There are two variants of the model that differ in the mobility of these proteins. The first considers permanently membrane-bound, diffusive species, while in the second variant the proteins do not diffuse but adsorb to the membrane from an infinite cytosolic reservoir. Both models lead to similar results, thus the focus is set on the first in the following. The key-mechanisms of the diffusion-variant of the model are summarized in Figure 2.9. There are convex and concave activators of actin, which are denoted by minus and plus signs respectively in mathematical formulations. As known examples of such proteins, and therefore possible candidates for the two components of their model, Peleg et al. name a complex composed of Tuba and N-WASP for a concave species and IRSp53 and WAVE as a convex complex.

The model by Peleg et al. differs from a classical reaction-diffusion scheme as proposed by Zeng et al. (Section 2.4), because it is built on a mechanical formulation via the identification of the free energy $\mathcal{F}$ of the system. The physical description is valid in the limit of small membrane undulations and expressed in the Monge gauge:

$$\begin{aligned}\mathcal{F} = \int_S \Big[&\frac{\kappa}{2}(\Delta h - H_-\phi_- - H_+\phi_+)^2 + \frac{\sigma_{\text{eff}}}{2}(\nabla h)^2 \\ &+ T \sum_{i=+,-} n_i^s \bar{\phi}_i (\log \bar{\phi}_i - 1)\Big] \mathrm{d}r^2.\end{aligned} \tag{2.13}$$

The first term under the integral corresponds to the Helfrich Hamiltonian under consideration of the induction of spontaneous curvature by curved activators of actin as introduced in equation (2.10). The fractional area coverage of these proteins is given by the fields ϕ_- and ϕ_+, while H_- and H_+ are their spontaneous curvatures. The second term considers the tension of the system, including the effective tension σ_{eff}. The last term describes the entropy due to the concentration fields ϕ_- and ϕ_+. The variable n_i^s describes the saturation concentration and T the temperature.

As a reaction to the presence of the activator fields, actin polymerizes at the membrane, creating a pushing force. The force is proportional to the difference between the local concentration and the average concentrations $\bar{\phi}_-$ and $\bar{\phi}_+$:

$$f_{\text{actin}} = A_+(\phi_+(\vec{r}) - \bar{\phi}_+) + A_-(\phi_-(\vec{r}) - \bar{\phi}_-). \tag{2.14}$$

The proportionality constants A_- and A_+ couple protein concentrations to force values.

The mobility of the activators is derived from equation (2.13) and takes the form of a diffusion equation

$$\frac{\partial \phi_i}{\partial t} = \frac{D_i}{n_i^s T} \nabla \left[\phi_i \nabla \left(\frac{\delta \mathcal{F}}{\delta \phi_i} \right) \right] \tag{2.15}$$

with i being either $+$ or $-$ and D_i the diffusion coefficient of the respective species. Both, curved proteins and pushing actin, build up forces that deform the membrane. The local hydrodynamic interaction within range d are mediated by the Oseen tensor η to the vertical velocity of the membrane:

$$\frac{\partial h}{\partial t} = \frac{d}{4\eta} \left(-\frac{\delta \mathcal{F}}{\delta h} + f_{\text{actin}} \right). \tag{2.16}$$

The model by Peleg et al. exhibits wave instability within certain ranges of the activity constants A_- and A_+. The feedback scheme of the model (Figure 2.9B) corresponds to the abstract one shown in Figure 2.1A, which requires a faster time scale for the positive feedback than for the inhibitory feedback. Consequently, Peleg et al. find that the dynamics of the convex activator (responsible for the instability) needs to have a faster time scale than the concave activator for wave formation. In a numerical simulation, Peleg et al. find their system to produced wave trains that propagate with velocities ranging from $11\,\text{nm}\,\text{s}^{-1}$ to $25\,\text{nm}\,\text{s}^{-1}$.

Chapter 3

Structure and Morphology of CDRs

When aiming for the understanding of the mechanisms that lead to formation of CDRs, the comprehension of their morphology is essential. The reasons for this are twofold. Firstly, the morphology results from the mechanism of wave formation. Therefore a judgement on the validity of model concepts has to be based on the ability of the models to reproduce the structure and morphology. Secondly, the structure itself might be essential for the wave machinery. Possible mechanisms for this include, e.g., a curvature-dependence of the distribution of actin factors as proposed by the model by Peleg et al. (Section 2.5) [Peleg et al., 2011]. Another potential interaction could be via phenomena of emergence, i.e., a hierarchy of structure formation in which large-scale structures result from the interplay of properties of small-scale structures. A motivation for the consideration of the latter is given by the observation that indeed within CDRs actin is organized into small, motile clusters, which will be introduced in detail later in this chapter (Section 3.1.2).

This thesis is not the first work aiming to elucidate the structure and morphology of CDRs. In fact, studies along these lines have a long history and date back to the 1970s and 1980s, the time period when CDRs and related structures were first discovered and described [Ambros et al., 1975, Chinkers et al., 1979, Mellström et al., 1983]. In these early works, phase contrast microscopy, fluorescence microscopy with stained actin, and scanning electron microscopy were utilized, revealing the eponymous ruffle-like protrusions of CDRs and their actin basis. With the advances in genetic techniques, video microscopy, and live cell imaging in the following decades also dynamic properties of CDRs were investigated revealing, e.g., their closing dynamics and the dynamic localization of regulatory proteins [Krueger et al., 2003, Orth et al., 2006].

However, the descriptions in the literature are partly contradictory, as we will see later, and lack fundamental information that I consider crucial for the understanding of CDRs. Especially, there is no work that explicitly deals with the question on how actin is organized within CDRs from a structural and a dynamic perspective. Nevertheless,

this question is certainly central for an understanding of the wave machinery underlying CDRs. In particular, and with respect to a potential description via reaction-diffusion systems, it is of outstanding interest whether actin is only recruited at the dorsal cell membrane or within the entire cytosol. The reason for this is that the characteristic diffusion times in two-dimensional spaces (such as the membrane) and three-dimensional spaces (such as the cytosol) usually differ by orders of magnitude, which has important consequences for the formulation of feedback schemes in modelling approaches.

In the following a comprehensive description of the structure and morphology of CDRs is presented, which also introduces basic aspects of their dynamical features. The dynamics will then be studied in depth in the next two chapters. The experiments in this chapter rely on various methods of imaging. Technical details regarding experimental procedures, materials and instruments are provided in Section 8.7.1 and others in the chapter on materials and methods (Chapter 8).

Investigations of dynamical features required live cell imaging, whereas for other experiments fixed cells could be used. Standard cell medium always contains growth factors in small concentrations (Section 2.1.5). It is the standard standard method for studies on CDRs to punctually stimulate their formation via addition of additional doses of growth factors such as PDGF to the cell medium [Mellström et al., 1983, Legg et al., 2007, Gu et al., 2011]. However, it is a fundamental finding of this work that this approach largely disturbs CDR wave dynamics and partially hides the wave character of CDRs. The reasons for this will be introduced in the next section.

To prevent such a disturbance of the wave dynamics I used a genetically modified fibroblast cell line (NIH 3T3 X2 [Singh et al., 2011], see Section 8.1 for details), which forms CDRs at high rates spontaneously under standard cell culture conditions without the need for additional growth factor stimulation. Therefore, NIH 3T3 X2 cells were used for all experiments on dynamical aspects in this chapter. Its genetically non-modified counterpart is the cell line NIH 3T3 WT, which is a standard cell line for studies on CDRs [Krueger et al., 2003, Zeng et al., 2011, Hasegawa et al., 2012]. The latter served for most experiments involving cell fixation in this chapter for its convenient ability to form high numbers of CDRs simultaneously in entire samples when stimulated by growth factors (see 8.1, 8.2, and 8.7 in the Materials and Methods for details). Moreover, this permitted a direct comparability to results from the literature. It was confirmed that both cell lines exhibited CDRs of identical dynamical features when stimulated with growth factors (Section 9.1 in the Appendix), justifying the use of NIH 3T3 X2 cells as a model organism that is equivalent to NIH 3T3 WT cells.

The results of individual experiments are reported in individual parts of the following sections. Throughout these the discussion of single findings is intentionally kept short, as the interpretation of several results requires the perspective of multiple imaging strategies. This chapter closes with a summary of the results in form of an integrated picture. In this final section, the results are discussed comprehensively and brought in the context of the existing literature.

3.1 Two-Dimensional Structure and Morphology

Cells grown on planar substrates take flat and spread morphologies. CDRs therefore propagate on a quasi two-dimensional medium. Thus, several of their properties can be well-studied with two-dimensional imaging. This section introduces the morphological features of CDRs and gives an overview about their dynamics, which will be quantitatively described in more detail in the next Chapter (Section 4.1).

This section is divided into two subsections. The first of them is dedicated to the morphodynamics of CDRs, i.e., it covers aspects of the shape dynamics of wavefronts. The second subsection deals with the internal structure, i.e., it addresses the question of the composition of CDR wavefronts and their internal actin organization.

3.1.1 Morphology and Overview about CDR Dynamics

In this section the typical life courses of CDRs are introduced with an emphasis on the differences between spontaneously formed and induced CDRs. The time-lapse sequences in Figure 3.1 show three examples of characteristic CDR life courses from which the CDRs in Figure 3.1*A* & *B* formed spontaneously (NIH 3T3 X2). In contrast, the CDR in Figure 3.1*C* was induced via growth factor stimulation (NIH 3T3 WT).

We first take a closer look at the dynamics of spontaneously formed CDRs. These originate from single points and form growing soliton-like waves of ring-shaped morphology. This part of a CDR life course will be called its "growth phase" in the following. The image contrast of wavefronts in their growth phase can vary considerably between individual CDRs as can be seen based on comparison of Figure 3.1*A* & *B*. Example *A* is only faintly visible initially (0.9 - 1.8 min), whereas *B* has high contrast throughout its whole life course. However, both rings clearly show pronounced growth phases.

In contrast, the growth phase of induced CDRs is typically far less pronounced. Instead, they appear as initially faint but extended objects that grow only marginally, eventually forming the characteristic ring-shaped wavefront that is also distinctive for spontaneously formed CDRs (Figure 3.1*C*, 0 - 1.5 min). The phases following on the CDR growth phase do not differ between spontaneously formed and induced CDRs.

The apparent contradiction between the initial dynamics of spontaneously formed and induced CDRs can be understood in the framework of an active media description of CDRs, as we will see in Section 4.6 of the next chapter. Therefore, we will leave the interpretation of this finding to the next chapter.

The normal velocity of outward growing wavefronts of spontaneously formed CDRs ranges from $0.08\,\mu\mathrm{m\,s^{-1}}$ to $0.38\,\mu\mathrm{m\,s^{-1}}$ and can vary considerably not only between the different locations on one single CDR, but also at the different time points of its life course and between different CDRs. The velocity distributions of CDRs are investigated in detail in Section 4.1.

When coming close to the cell edge or the nucleus, CDRs reverse and close back to points, which we call "CDR closing" or the "contractile phase" from now on [Hoon

et al., 2012]. The propagation velocities of opening and closing CDRs wavefronts are of similar magnitude, which will be further analysed in Section 4.1.

The CDR in Figure 3.1*A* undergoes isotropic growth (0.9 - 2.7 min) before deviating from circular geometry after collision with nucleus and cell edge, whereas the one in Figure 3.1*B* is of anisotropic form right from its origination. Being an induced CDR, the one in Figure 3.1*C* lacks a pronounced growth phase and takes a morphology that reflects the cell shape soon after its appearance.

As further discussed in the next chapter (Section 4.1), a pattern of isotropic growth that is disturbed upon reversal of propagation direction, i.e., with entering of the closing phase, is a typical behaviour of spontaneously formed CDRs.

The width of the wavefronts of CDRs is typically between 3-5 µm[a]. However, in later stages, usually upon entering into the contractile phase, CDRs might appear wider. This increased width goes along with the formation of halos in phase contrast. The reason for this is presumably the growth of CDRs in vertical direction, which will be investigated in detail in the following section.

Generally, CDRs avoid the region of the cell nucleus and cross this part of the cell only in rare cases. Upon approach of the nucleus CDRs therefore often deform. A typical example is given in Figure 3.1*A* at 3.6 min in which the initially circular CDR develops an indentation in proximity to the nucleus. We will see in the further course of this chapter that the avoidance of the cell nucleus might be a consequence of limited actin availability at this position of the cell.

A similar phenomenon can be observed when CDRs approach the cell edge. Trivially, CDRs cannot propagate beyond the cell body. The region of the cell in which a CDR was formed (bounded by the nucleus and the cell edge) constitutes the area for CDR growth and propagation. CDRs at maximal extension therefore tend to take shapes that reflect the local cell morphology. Figure 3.2*C*-*D* illustrates the resulting geometries CDRs take at cells of different sizes and morphologies. Since fibroblast are of random shapes, the form of CDRs at maximal extension varies considerably between different cells and typically largely differs from circular geometry. The live imaging data analysed in Chapter 4 will show that also the dynamics of CDRs is crucially influenced by the cell morphology, which will be exploited in Chapter 5 to restrict CDRs to one-dimensional propagation.

Fibroblast cells are motile. They move via formation of actin-based protrusions at the

[a] "Width" refers to the broadness of the wavefront. This is not be confused with the CDR diameter.

Figure 3.1 (facing page): *Examples of three CDR life courses. A & B*: spontaneous formation, *C*: induced formation (addition of PDGF at $t = 0\,\mathrm{min}$). Growth phase: 0 - 3.6 min in *A*, 0 - 5.1 min in *B*. *C* has no pronounced growth phase. Afterwards follows the phase of contraction. The respective last frames were overlaid with the contour of the cell in the respective first frame to visualize potential overall changes in cell shape. Red arrows mark regions in which pronounced phase halos indicate large vertical extensions. Time-lapse sequences were acquired in low-resolution phase contrast. Scale bars: 25 µm.

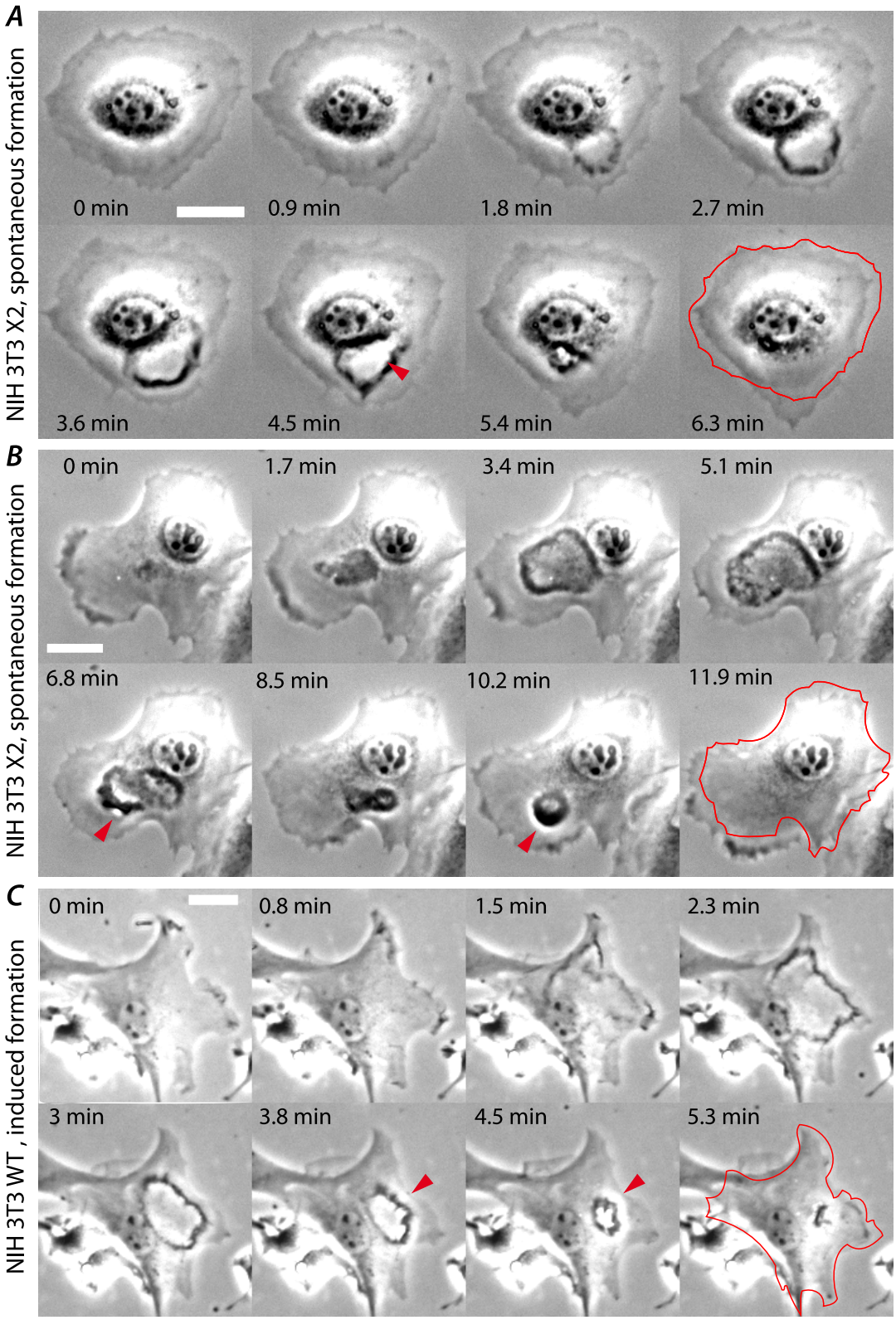
A
NIH 3T3 X2, spontaneous formation
0 min
0.9 min
1.8 min
2.7 min
3.6 min
4.5 min
5.4 min
6.3 min
B
NIH 3T3 X2, spontaneous formation
0 min
1.7 min
3.4 min
5.1 min
6.8 min
8.5 min
10.2 min
11.9 min
C
NIH 3T3 WT , induced formation
0 min
0.8 min
1.5 min
2.3 min
3 min
3.8 min
4.5 min
5.3 min

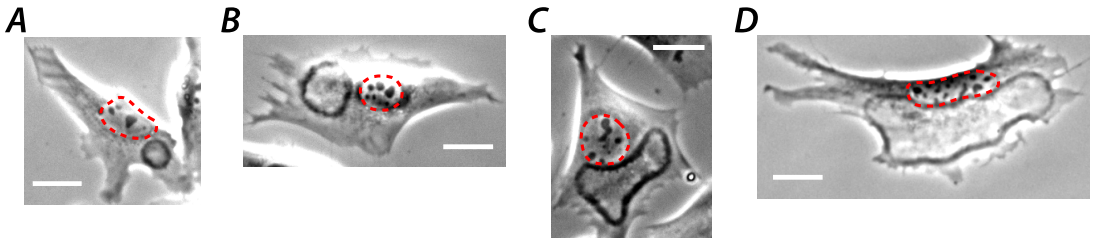

Figure 3.2: *CDR sizes adapt to the free area for propagation.* The dashed red line highlights the boundary of the cell nucleus. Cells: NIH 3T3 X2, no stimulation, live cell imaging, scale bars: 25 µm.

leading edge and contractile activity at the rear [Abercrombie et al., 1970a, Abercrombie, 1978]. CDRs are assumed to facilitate cell migration [Itoh and Hasegawa, 2012, Hoon et al., 2012]. Two of the cells shown in Figure 3.1 (A & B) show the onset of motility by formation of protrusions in form of extending lamellipodia directly following the extinction of CDRs. This can be well observed by comparing the cell shape before CDR formation with the shape directly after CDR extinction. The cell shown in Figure 3.1C changes its shape only slightly. The modest degree of lamellipodia protrusion is, however, not a typical mark of PDGF-stimulated cells, but a coincidence in this particular example.

The lifetimes of CDRs can differ considerably, which will be investigated in detail in the next chapter. In general, those of small CDRs tend to be short, whereas large CDRs live longer (Section 4.4). The shortest lifetimes are in the range of 1 min (Section 4.4). The longest lifetimes that I observed in my experiments were in the range of 90 min (sections 4.2-4.3). Long-living CDRs do, however, often exhibit phenomena like coherent translocation, formation of spiral patterns, or CDR stalling. Spiral waves and CDR stalling usually goes along with an opening of wavefronts in which CDRs, despite their name, deviate not only from the shape, but also from the topology of circles. In particular, open CDRs often take arc-shaped morphologies. Figure 3.3 shows an example of a CDR whose wavefront fragmented into three arc-shaped parts. This observation is an interesting feature as open wavefronts propagating in active media tend to take arc-shapes, which was demonstrated in Chapter 2 based on precursors of spiral waves (Figure 2.6).

3.1.2 Internal Structure and Dynamics

The description of the CDR morphology in the previous subsection was based on low-resolution phase contrast imaging. This approach has the benefit of yielding high-contrast images that reliably represent the presence of CDRs as dark rings even if there are slight differences in the z-position between individual CDR parts or cell compartments. However, low-resolution imaging cannot capture the substructure of CDRs. Thus, in the following high-resolution imaging is applied. There are several techniques of contrast formation in microscopy suitable for that, each having benefits

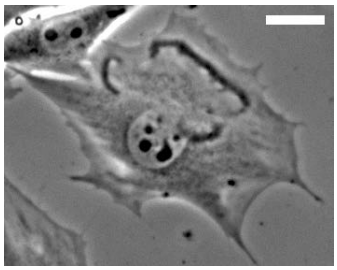

Figure 3.3: *Arc-shaped CDRs.* The three arc-shaped wavefronts result from the fragmentation of one large CDR. NIH 3T3 X2 cell, no stimulation, live cell imaging, scale bar: 25 µm.

and drawbacks. Therefore, in this thesis various imaging methods were used, which means that CDRs appear differently in different images. Figure 3.4 illustrates the distinctive appearances of the same object in three methods of imaging, namely phase contrast, fluorescence microscopy and Differential Interference Contrast (DIC). Each image shows a CDR and the nucleus of the cell. A comparison of Figure 3.4*A* with the Figures 3.1 - 3.3 reveals the differences of power of resolution of image details and contrast.

Notably, there are several vesicles around the cell nucleus (highlighted with green arrows in Figure 3.4*A*). Since CDRs facilitate endocytosis, vesicles are often present in cells that undergo or underwent formation of CDRs [Dowrick et al., 1993]. The fluorescence of stained f-actin is notably reduced in the area of the cell that is surrounded by the CDR (Figure 3.4*B*).

The images in Figure 3.4 show that CDRs are of a granular substructure. Since CDRs are composed of polymerized actin the granular structure is visualized by phase contrast, fluorescence of f-actin, and DIC alike. Note, however, that the different characteristics of contrast formation of the individual techniques prohibit a direct comparison of contrast between the images [Murphy and Davidson, 2013].

The micron-sized actin particles, or clusters, that are the basis for the granular substructure of CDRs are highly dynamic and of hand fan-shapes. For brevity, we name these structures HAPs (Hand fan-shaped Actin Particles) in the following. Figure 3.5*A*-*C* shows stills from a time-lapse sequence of a CDR in which individual HAPs can be well observed due to their relatively low density. The band where HAPs are of highest density corresponds to the wavefront, which would appear as a dark contour in phase contrast. The CDR in the given example moves only slightly. Nevertheless, the HAPs of which the CDR is composed perform rapid movements in apparent random directions. Figure 3.5*D* illustrates the separation between the time scales of movement of the HAPs and of the wavefront based on an overlay of an average image of the time-lapse sequence, from which stills are shown in Figure 3.5*A* - *C*, and the standard deviation of a temporarily high-pass filtered version of the sequence. Due to the static nature of the actin cytoskeleton, the average image shows no blurring of its signature. Also the CDR resides within a limited band in the averaged image, which highlights the stationary

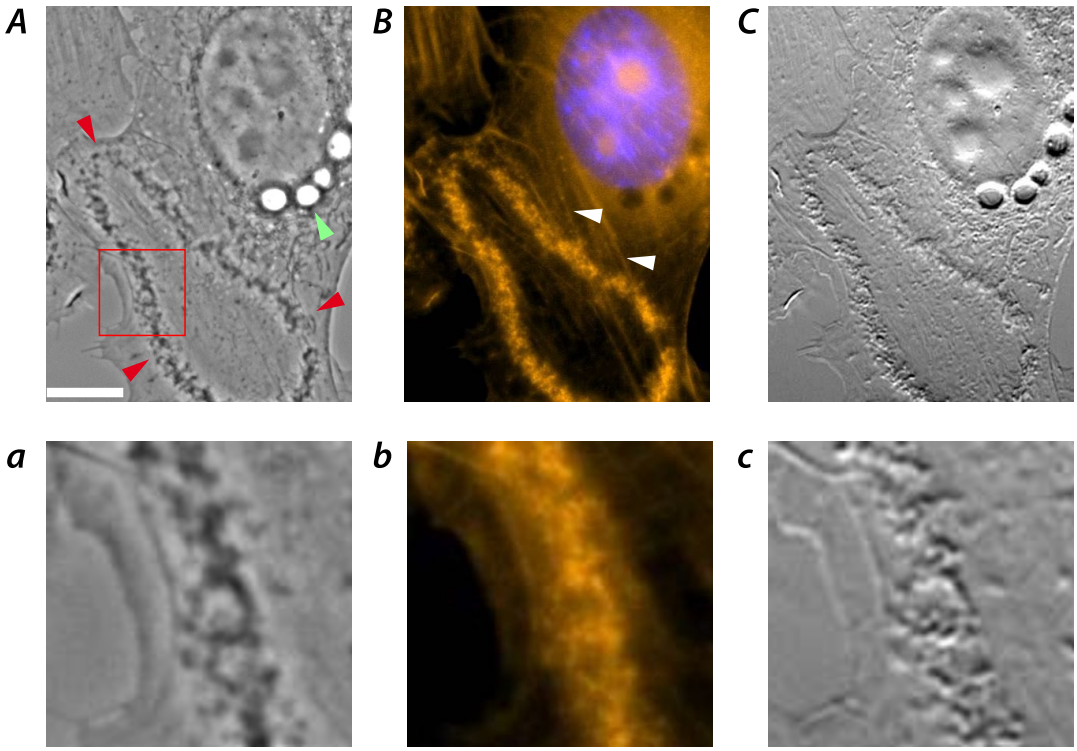

Figure 3.4: *CDR imaged with different methods of contrast formation.* *A*: Phase contrast, *B*: Fluorescence microscopy (orange: f-actin, blue: DNA), *C*: DIC. The CDR was highlighted with red arrows. The green arrow highlights vesicles. White arrows highlight actin stress fibres. The position of the cell nucleus corresponds to the blue region in *B*. Images *a*-*c* are enlarged version of the images *A*-*C* and the ROI highlighted with a red square in *A* respectively. They reveal that CDRs are composed of numerous small actin particles (HAPs). The NIH 3T3 X2 cell was fixed and f-actin was stained using rhodamin/phalloidin, DNA was stained using DAPI. No stimulation. Scale bar: $10\,\mu\mathrm{m}$.

nature of the average wavefront position in this example. The standard deviation of the high-pass filtered image has high contributions only within the CDR, highlighting fast variations within the CDR, which has its origin in the dynamics of HAPs. To measure the velocity of individual HAPs a kymograph analysis was performed (Figure 3.5*E* - *F*). For this, kymographs were sampled along the growth direction of HAPs from which the velocities were then read off. In Figure 3.5*G* the resulting distribution is plotted as a histogram. The mean value of the data set is $0.128 \pm 0.006\,\mu\mathrm{m\,s^{-1}}$ ($\pm$ SE). However, since the movement of HAPs is not restricted to the xy-plane, in which the velocities were measured, the data suffer from projection artefacts. An estimation of the impact of geometrical effects yields a true velocity of $0.175 \pm 0.009\,\mu\mathrm{m\,s^{-1}}$ (($\pm$ SE), see Section 9.2 in the Appedix for details).

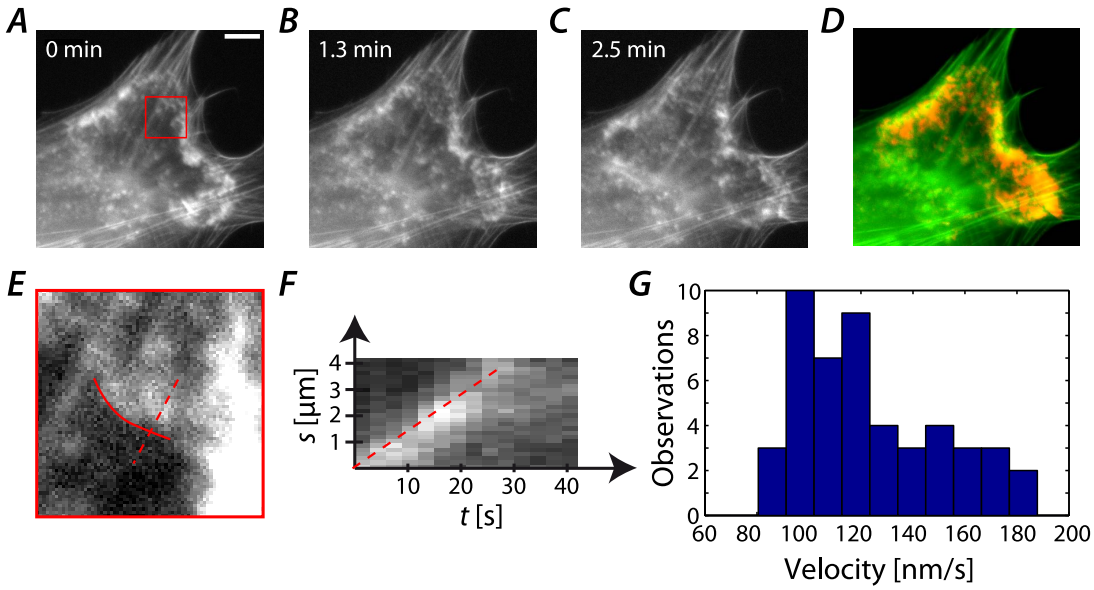

Figure 3.5: *Dynamics of actin clusters within CDRs.* *A* - *C*: Time-lapse sequence of actin dynamics within CDRs. NIH 3T3 X2 cell, no stimulation, f-actin was stained with pLifeActGFP-TagGFP2. *D*: Overlay of the average intensity of the $2.5\,\mathrm{min}$-interval (green) and the standard deviation of the high-pass filtered sequence (red, cutoff period: $1\,\mathrm{min}$). The static cytoskeleton appears green, while red colors highlight dynamic structures within CDRs. Note that the wavefront is stationary. *E*: Close-up view of the red ROI in *A* (enhanced contrast), highlighting the growth front of an actin cluster (red solid line). *F*: kymograph sampled along the red dashed line in *E* with highlighted slope (dashed red line). *G*: Velocity distribution of actin clusters. Scale bar in *A*: $10\,\mu\mathrm{m}$.

Kymographs of individual HAPs also permit to read off their typical lifetimes, which are typically below $30\,\mathrm{s}$ (Figure 3.5*F*). At fixed positions, the turnover from local high to low concentrations is on the order of $10\,\mathrm{s}$, indicating high rates of polymerization and depolymerization.

Formation of contrast in all three techniques of microscopy that were applied so far can result both from differences in local protein densities and from differences in local cell thickness. For a more detailed investigation of the structure of CDRs and, especially, the actin distribution within them, three-dimensional imaging must be applied.

3.2 Three-Dimensional Structure and Morphology

While several aspects of CDR morphology and dynamics can be understood via a simplified picture, in which they constitute protein waves in a two-dimensional medium, for a deeper comprehension their three-dimensional nature must be taken into account. We will see throughout this section that CDRs can form protrusions of considerable

extension into vertical direction. A central question, which follows from this observation, is how these structures can translocate upon CDR propagation. Therefore, in this section the results of different approaches for a characterization of CDR in three dimensions are presented.

SEM micrographs from the literature on CDRs clearly show that they can considerably deform the cell membrane in vertical direction (Figure 1.1*C*) [Mellström et al., 1983, Dowrick et al., 1993, Edgar and Bennett, 1997]. This raises the question whether the vertical protrusions result from an up-piling of actin and the mere fact that the vertical direction is the only one that permits the formation of a protrusion. Alternatively, there could be a mechanism at work that restricts the polymerization of actin in CDRs to the dorsal membrane via an actin-recruiting protein that is membrane-bound, such as the proteins of the WASP family (Section 2.1.3).

To answer this question, cells exhibiting CDRs were simultaneously imaged in TIRF- and epifluorescence microscopy and the resulting micrographs were then juxtaposed (Figure 3.6). In TIRF microscopy, only the first 100-200 nm-thick layer above the substratum is illuminated while fluorophores situated further upwards remain dark [Murphy and Davidson, 2013, 252 pp].

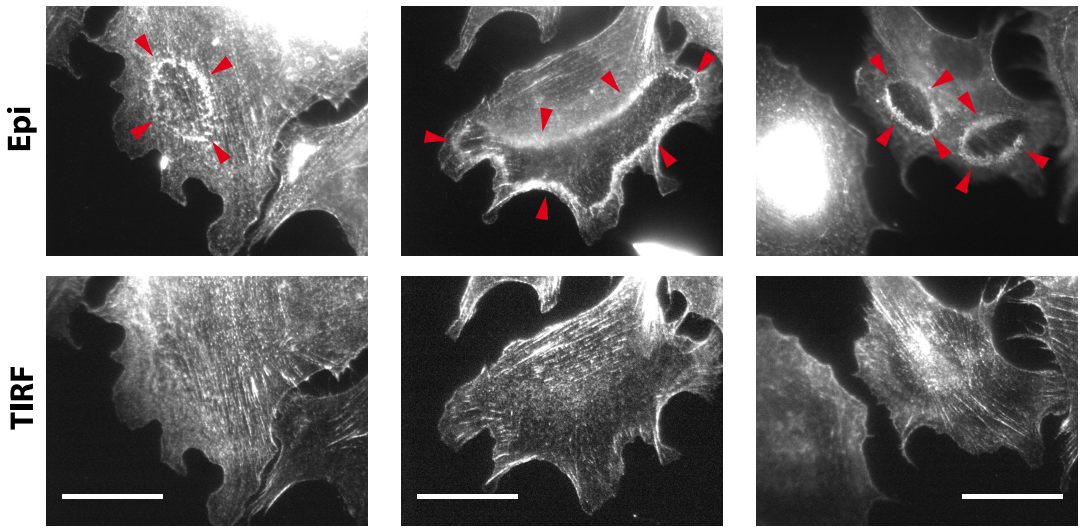

Figure 3.6: *Location of CDRs in vertical dimension.* Upper row: epifluorescence, lower row: TIRF. The cells in each column are identical. NIH 3T3 WT cells were stimulated with PDGF, fixed and stained with Rhodamin/Phalloidin. CDRs (marked with red arrows) are only visible in epifluorescence. Scale bars: 25 µm

A comparison of images obtained via TIRF and epifluorescence reveals that CDRs are virtually invisible in TIRF micrographs. CDRs do, nevertheless, leave a footprint in the part of the cell that is close to the substratum in form of the aforementioned actin depletion within the area that is surrounded by their wavefronts. The CDR-forming

f-actin, however, is apparently completely situated at the dorsal side of the cell. This means that the reason for the formation of vertical protrusions of CDRs is not due to an up-piling of f-actin. Indeed, the results are a very strong hint towards the alternative hypothesis, i.e., an involvement of a membrane-bound protein in the recruitment of f-actin into CDRs. This membrane-bound protein would thereby only be found in the dorsal cell membrane. The identity of the latter will be further discussed in the final section of this chapter (Section 3.3).

To study the three-dimensional distribution of actin within cells forming CDRs further, Laser Scanning confocal Microscopy (LSM) was utilized. While TIRF is of outstanding resolution in z-direction it is limited to a single imaging plane, which is the layer directly above the substratum [Murphy and Davidson, 2013, 252 pp]. For LSMs the opposite is true [Murphy and Davidson, 2013, 265 pp]. While the resolution in z-direction of an LSM cannot compete with that of TIRF, the former can capture the entire vertical extension of a cell.

Figure 3.7 shows a cell exhibiting a CDR that was imaged via LSM. The corresponding image slices, in which image intensity is plotted as a function of height z and a local spatial direction (s-direction), reveal the actin distribution within CDRs and the height of these structures. In comparison to images of epifluorescence and TIRF (Figure 3.6), where the presence or absence of CDRs is clearly visible to the human eye due to its capabilities of feature detection, the interpretation of xz-cuts of LSM images requires more dedication and a constant consultation of both, the slice images themselves (Figure 3.7*b1-b4*) and the maximum-intensity projection version of the whole stack (Figure 3.7*B*). A comparison of the cuts and the maximum intensity projection reveals that CDRs take ridge-morphologies, i.e., they consist of a ring-shaped bulge. The magnitude of this protrusion, i.e., the CDR height, lies between 1 - 3 µm in the example shown in Figure 3.7. An inspection of the actin distribution inside of the ridge reveals the consistency of the results from TIRF and LSM. The concentration of actin in CDRs is maximal within the part of the cell that forms the actual protrusion, while below these, i.e., towards the ventral cell side, we generally find lower concentrations of f-actin. Indeed, there are cases in which actin also appears in high concentrations below CDRs. However, a careful comparison of the slice cuts with the maximum-intensity projection (Figure 3.7*B*) and the focal plane of stress fibres (Figure 3.7*A*) reveals that this actin can be accounted to actin stress fibres that run below the CDR. Figure 3.7*C* & *D* illustrate this based on an example of enlarged versions of the respective image parts. In general the amount of f-actin, and correspondingly the number of stress fibres, within CDRs is low compared to the remaining part of the cell, as can clearly be seen in Figures 3.7*B* and 3.7*b1-b4*.

Cells utilize f-actin for the formation of various different structures, some of them of relatively static nature such as, e.g., the actin cytoskeleton or the actin cortex. While it is apparent from Figure 3.7 that actin cortex and stress fibres contribute a level of "background f-actin", e.g. f-actin that is not involved in dynamic structures such as lamellipodia or CDRs, the same figure also reveals that above the cell nucleus only very

little f-actin is found. This observation offers an explanation to the avoidance of the nucleus exhibited by CDRs. Together, the observation of f-actin depletion inside of CDRs and the avoidance of the cell nucleus as a potential consequence of low f-actin concentrations above the nucleus, suggest that CDRs are built from actin that is, at least partially, recruited from the dissolution of actin stress fibres.

Despite its ability to image three-dimensional distributions of actin, LSM imaging goes along with some disadvantages. Besides the limits in resolution mentioned above, LSM imaging of CDRs requires the fixation of cells. The reason for this is that the time for acquisition of images such as, e.g., Figure 3.7 typically lasts several ten minutes, which is long enough to exceed the lifetime of a large proportion of CDRs. Fixation, in turn, involves the risk of creation of artefacts in cell morphology. Therefore, I validated my results with DIC microscopy, which is a label-free technique that can acquire images rapidly and thus enables live cell imaging.

The point spread function of a microscope operated in DIC mode quickly decays in z-direction, which makes it very suitable for optical sectioning [Allen et al., 1969, Kam, 1998]. While DIC cannot visualize protein distributions specifically, the principle of image formation of DIC makes it especially well-suited for the visualization of edges of objects. CDRs were therefore imaged on living cells with DIC optical sectioning to address the question of their three-dimensional morphology. I was especially interested in the clarification of a controversy in the literature, i.e., that in some articles CDRs are described as "ridge[s] of extended dorsal plasma membrane", i.e., flat membrane structures, containing "numerous similarly-sized bumps," [Buccione et al., 2004]. In contrast, other publications emphasize their sheet-like morphology [Mellström et al., 1983, Dowrick et al., 1993], or differentiate between flat and sheet-like ruffles in assigning them to different types [Edgar and Bennett, 1997].

The microscope was set up to acquire image stacks of living cells at equally spaced z-positions. The time between individual images was on the order of tenth of seconds, i.e., CDRs could not alter their shape or position significantly within acquisition of a complete z-stack.

The subset of images of a z-stack shown in Figure 3.8 presents a CDR that exhibits both, a ridge-shaped region resembling a flat and smooth bump, while in other parts

Figure 3.7 (facing page): *CDR imaged with LSM.* F-actin: yellow (Rhodamin/Phalloidin), DNA: blue (DAPI). *A*: Ortho-slice visualization of a 3-d image stack (blue: xy-, green: xz-, red: yz-plane). The position of the CDR is highlighted with white arrowheads in the xz-view. The lower cell part is in focus in the xy-view and the CDR thus only appears very weakly. *B*: Maximum-intensity projection of the same image stack. White lines indicate the positions where the slice cuts *b1*-*b4* where taken. The dashed white lines in *b1*-*b4* highlight the z-position of the substratum. The origin of the local direction s lies outside of the cell. *C*: enlarged ROI from *A* around slice cut *b1* with numbered stress fibres. *D*: slice cut *b1* in which the same stress fibres are highlighted with white circles. NIH 3T3 WT cell, PDGF stimulation, fixation, scale bar: $25\,\mu\mathrm{m}$

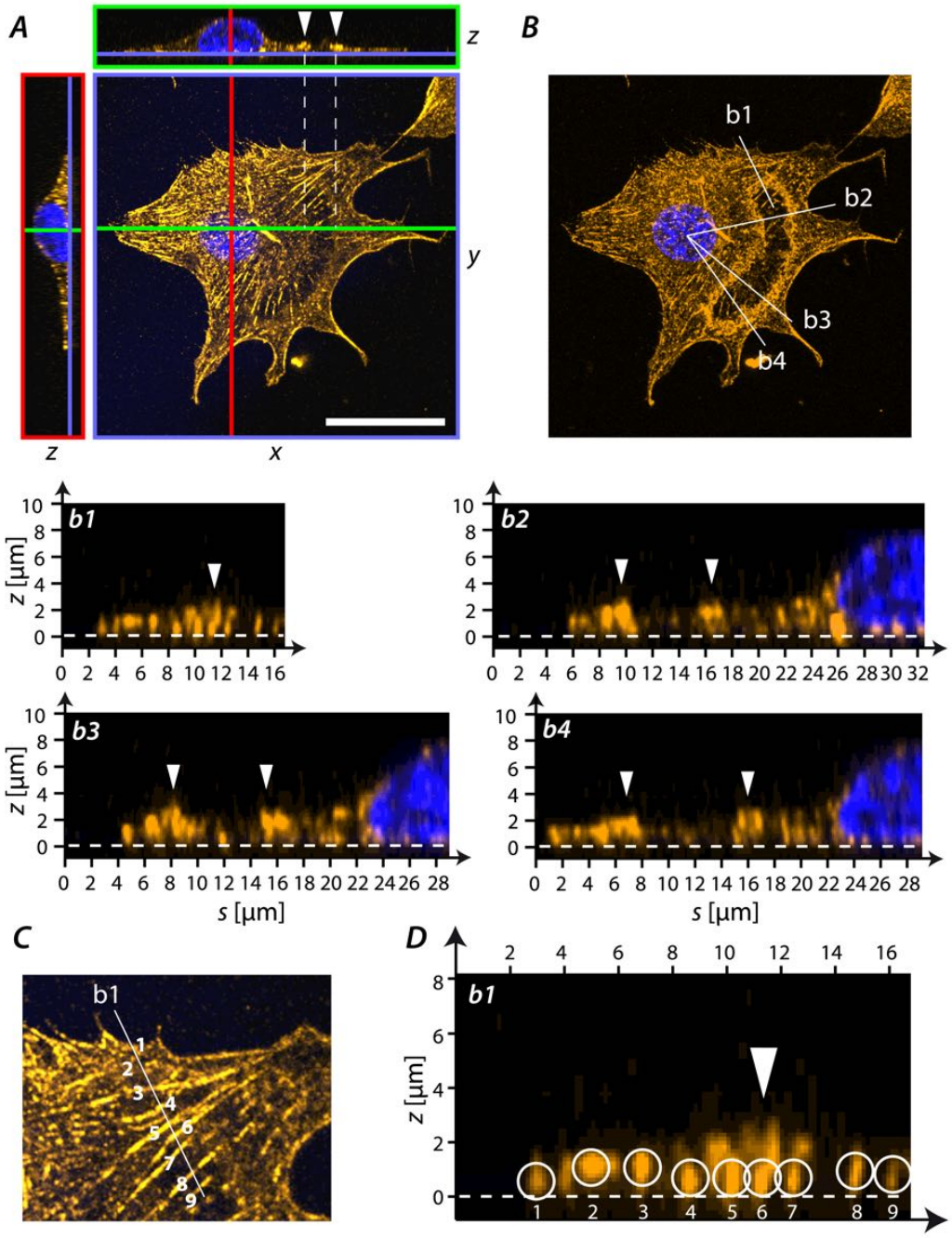
A
z
y
z
x
B
b1
b2
b3
b4
b1
b2
b3
b4
z [µm]
s [µm]
C
b1
D
b1
z [µm]

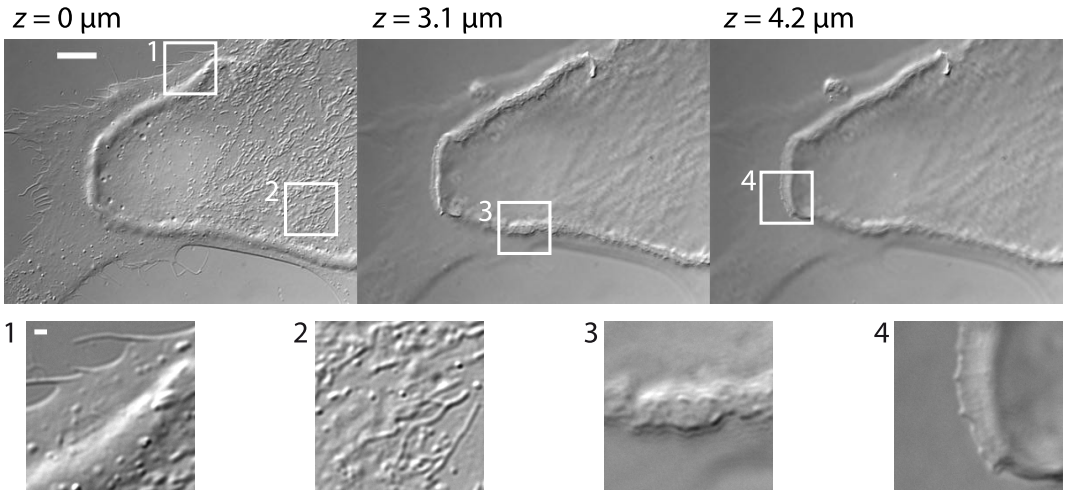

Figure 3.8: *DIC optical sectioning.* DIC micrographs of the same CDR at nearly identical time points at different vertical positions. White rectangles mark the positions of the ROIs 1-4. The close-up views of the ROIs highlight details of the cell, verifying that the respective part of the cell is in focus. NIH 3T3 X2 cell, no stimulation, live cell imaging, scale bar top row: $10\,\mu\mathrm{m}$, scale bar ROIs: $1\,\mu\mathrm{m}$ (valid for all ROIs).

of the same CDR vertically extending lamellipodia-like membrane sheets are visible. This is demonstrated on the in-focus situation of different cellular features in the ROIs of the stack. Three z-positions were selected to show the cell at substratum level ($z = 0\,\mu\mathrm{m}$, ROI 1 & 2), the top of the flat region of the apparent smooth part of the CDR ($z = 3.1\,\mu\mathrm{m}$, ROI 3) and the edge of the vertical membrane sheet ($z = 4.2\,\mu\mathrm{m}$, ROI 4). The implication of this is that CDRs that form flat membrane ridges and CDRs that form sheet-like protrusions are indeed no different structures per se, as the same CDR can contain both morphological features.

We further learn that the small approximately micron-sized HAPs inside of CDRs, which were introduced with Figures 3.4 and 3.5, correspond to small protrusions of the cell membrane. Collectively and in a large number, HAPs lead to the apparent smooth structure of CDRs of low vertical extension. Ridge-like and sheet-like parts of a CDR differ in their mere vertical extension. The height of the flat structures is smaller (up to approximately $3\,\mu\mathrm{m}$) than that of individual membrane sheets that can easily exceed $4\,\mu\mathrm{m}$.

While the results presented in this section provided very valuable insights into the functional elements of the wave mechanism of CDRs, the question on the actin dynamics within extended CDR ridges remains unclear. The reasons for this are that the only imaging technique that in principle permits the corresponding experiments, namely LSM, has a too low resolution in z-direction and is also too slow for live imaging. Imaging of the f-actin ultrastructure within CDRs via transmission electron microscopy

might be a suitable approach to solve at least the first issue.

3.3 Discussion - An Integrated Picture

The results presented in the previous sections provide a comprehensive characterization of the dynamical morphology and structure of CDRs. In this section the individual findings will be discussed in an integrated sense. We start with a short summary of the morphological features that are typical for each individual stage of CDR life courses. This summary closes with a discussion of the emerging picture in the light of the literature. In the remaining part of this section the relevance of individual aspects of the structure and morphology of CDRs for the wave mechanism are discussed. This section closes with the presentation of a sketch that summarizes the localization of functional elements in CDRs.

Since each of the different imaging techniques that were employed in this chapter only allowed to capture individual aspects of the CDR morphology, a 3-dimensional model sketch was drawn that summarizes the characteristic features of CDR morphology in one single image (Figure 3.9).

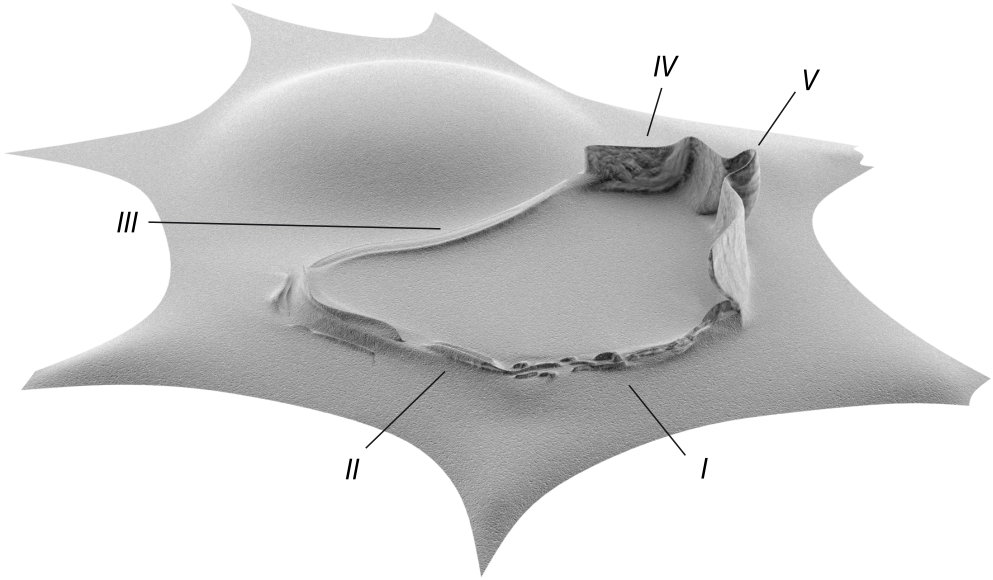

Figure 3.9: *Three-dimensional model sketch of a cell exhibiting a CDR.* Roman numerals highlight specific features. *I*: ridge-shaped region, consisting of small membrane bumps, *II*: bumps forming precursors of sheet-like protrusions, *III* characteristic dent of CDR close to the nucleus, *IV*: high sheet-like protrusion, *V*: instability of a sheet-like protrusion that is folding on itself, forming an inclusion.

The nature of the first phase of CDR life courses depends on whether the respective

CDRs formed spontaneously or in response to growth factor stimulation. Spontaneously formed CDRs originate from points and grow as, initially faint, circular wavefronts. In contrast, stimulated CDRs form extended rings shortly after stimulation, without a noticeable growth phase (Section 3.1.1). The differences between these two behaviours will be interpreted in Section 4.6 of the next section.

The ring width of CDRs typically ranges from 3 µm to 5 µm. Both, DIC and LSM microscopy revealed that in vertical direction the rings correspond to ridges that elevate up to 3 µm in z-direction with respect to the substrate level. The ridges are composed of small HAPS of typical sizes of 1 - 3 µm (Figure 3.9*I*) as shown by different methods of high-resolution microscopy (sections 3.1.2-3.2). A closer look revealed that HAPs are composed of actin, are of hand fan-shapes, and move rapidly in an apparent random fashion within the width of the CDR wavefront. As a general feature, CDRs avoid the cell nucleus and therefore wavefronts approaching the nucleus typically dent (Figure 3.9*III*, Section 3.1.1).

With increasing lifetime of CDRs, individual HAPs can grow into sheet-like protrusions (Figure 3.9*II* - *IV*). Their growth is indicated by increasing halo formation in low-resolution phase contrast and was also visualized by DIC optical sectioning. Sheet-like protrusion on CDR ridges can easily reach several micrometer in height (Figure 3.9*IV*, sections 3.1.1 & 3.2).

We might speculate that the height of a CDR is proportional to the probability of a buckling or collapse event, which can lead to inclusion of membrane area and therefore to vesicle formation (Figure 3.9 *V*). Therefore, endocytosis does not necessarily require CDR closure. Indeed, the formation of vesicles could often be observed to occur independently of closing events. We will see in the next chapter that especially high CDRs tend to move rapidly. The reason for this might be the buckling and succeeding fold back of the protrusions to the surrounding cell membrane.

The characterization given above complements the picture of CDR morphology that is provided in the literature. Especially, the results resolve the discrepancy of the depiction of CDRs as either flat ridges, according to Buccione et al. [Buccione et al., 2004], or sheet-like protrusions into vertical direction, as described by various other groups that performed SEM imaging [Dowrick et al., 1993, Edgar and Bennett, 1997, Mercer and Helenius, 2009]. Figure 3.8 clearly shows that indeed both morphological features, i.e., a flat and smooth appearance and sheet-like protrusions, can co-exist on the same CDR simultaneously. Sheet-like protrusions are a typical mark of CDRs in their late life stages, which was suggested by the SEM data by Dowrick et al. before [Dowrick et al., 1993]. Due to the fixation that is mandatory for SEM, the results by Dowrick et al. were, however, not based on dynamic data.

The inclusion of endocytotic vesicles by CDRs requires the collapse of extended sheet-like protrusions, which likely involves buckling instability. A detailed analysis of this process was beyond the research question of this work, as the actin machinery driving the propagation of CDR wavefronts is likely only of minor importance in this process. However, the topic is highly interesting from the perspective of membrane

physics as it, according to SEM images from the literature [Dowrick et al., 1993, Edgar and Bennett, 1997], implies a series of non-trivial topological transition and lysis events of lipid bilayers.

Interestingly, the initial growth of CDRs from points is not described in the literature, with the exception of the work by Zeng et al. [Zeng et al., 2011]. Apart from the latter article, there appears to be a consensus that CDRs become visible as an established ring minutes after stimulation of cells via growth factors [Buccione et al., 2004, Itoh and Hasegawa, 2012, Hoon et al., 2012]. Indeed, I also found this behaviour when stimulating cells with growth factors. With this method, however, the absence of a pronounced growth phase largely hides the wave character of CDRs. In contrast, spontaneously forming CDRs clearly initiate from points and grow outwards as ring-shaped waves. It will be shown in the next chapter that this apparent contradiction can be well understood within the framework of an active medium description (Section 4.6). It is an interesting observation that the established method for CDR studies, which is - out of historical reasons - the use of growth factors, largely prevented the full grasping of the wave nature of CDRs.

The individual HAPs, which are the basis for the granular substructure of CDR wavefronts, are restricted to the dorsal cell membrane (Section 3.2) and exhibit rapid movement as well as short lifetimes (Section 3.1.2). The sketches in Figure 3.10*A* & *B* summarize the findings of this chapter regarding the structure of HAPs and the hypothetical distribution of regulatory proteins of actin, which are responsible for the fast dynamics of HAPs. Moreover, this figure illustrates the hypothetical overall distributions of regulatory proteins in CDRs, which will serve the discussion in the further course of this section.

The fast turnover in form of growth and decay of HAPs points to simultaneous high rates of actin polymerisation and depolymerisation. Since the entire cytosol is subject to dissolution of actin structures the depolymerizer of actin is likely cytosolic, whereas the promoting species of actin polymerization was found to be probably membrane-bound (Section 3.2). This implies that HAPs can only grow at their membrane-touching front region, which causes the membrane to be pushed outwards [Borisy and Svitkina, 2000]. Due to filament ageing [Pollard and Borisy, 2003] and the activity of the cytosolic depolymerizer, the part of HAPs that is not in contact with the membrane constantly decays and thereby forms the rear of these structures (Figure 3.10*B*). Similar to the situation in protruding lamellipodia [Pollard and Borisy, 2003] or the rocketing bacteria *Listeria monocytogenes* [Carlier et al., 1999], the machinery of polymerization at the front and dissolution of f-actin at the back leads to a net displacement of HAPs. A comparison to SEM micrographs implies flat and thin morphologies of HAPs (Figure 1.1*C*), which is reminiscent to ruffles at the cell periphery and points to a meshwork architecture of actin inside of HAPs [Borm et al., 2005, Shutova et al., 2012]. Figure 3.10*A* summarizes the dynamical processes underlying HAPs. Since the actin distribution in vertical direction could not be resolved in sufficient detail it is currently not clear what constitutes the

mechanical counterforce that is needed to balance the force resulting from membrane deformation by HAPs.

Before we discuss the distribution and identity of regulatory proteins inside of CDRs in more detail, we first discuss the granular structure of CDRs in the light of the literature.

In the literature on CDRs the existence of particles (HAPs) was described previously [Mellström et al., 1983, Buccione et al., 2004]. These "phase dense particles were formed near the leading edge and coalesced into circular waves along the cell cortex" [Krueger et al., 2003]. The early work by Mellström et al. was the first to link these actin particles to tiny membrane folds on the dorsal cell side via SEM imaging [Mellström et al., 1983]. However, so far no mechanistic explanation for this dynamics was offered. We will see shortly that in fact an interpretation of this finding is well founded within the understanding of f-actin as an autocatalytic element.

In general it is not surprising that the granular substructure of wavefronts in form of HAPs is most obvious in the early CDR life stages. We have seen that with increasing CDR lifetime and, therefore, CDR height their substructure simply cannot be resolved by the microscope - not even by LSM (Section 3.2). The motility patterns of HAPs reminds of the swarming behaviour of active particles such as birds, fish, or bacteria on a first glance [Couzin and Krause, 2003]. Such systems are known to be able to self-assemble into states of ordered collective motion [Vicsek et al., 1995], including band structures resembling propagating wavefronts [Ginelli et al., 2010]. However, in the aforementioned examples the emergence of order and collective velocity patterns are typical features [Cavagna et al., 2010], which is not a striking characteristic of the motion of HAPs (Section 3.1.2). Furthermore do birds, fish, and bacteria usually live much longer than it takes them to travel their own characteristic size, which is not the case for the highly transient HAPs.

Motile spots of actin, resembling HAPs, have been observed in cells of *D. discoideum* that recover from global depolymerization of f-actin [Gerisch et al., 2004]. In these experiments, Gerisch et al. found a characteristic particle velocity of $0.17\,\mu\mathrm{m\,s^{-1}}$, which is very well inside the range of velocities around $0.175 \pm 0.009\,\mu\mathrm{m\,s^{-1}}$ ($\pm$ SE) that was found for HAPs in CDRs. The propagation velocities of CDR wavefronts were found to range from $0.08 - 0.38\,\mu\mathrm{m\,s^{-1}}$ and are therefore comparable to the velocity of HAPs. Also lateral actin waves at the lamellipodia of wing disc cells of flies and intracellular actin waves in neutrophils were found to have similar velocities [Döbereiner et al., 2006, Weiner et al., 2007].

Considering the autocatalytic properties of polymerizing actin, induced by the branching agent Arp2/3, it is not surprising to find actin organized into motile clusters. Consequently, the dynamics of actin particles in *D. discoideum* has been modelled via a FHN-based system in which actin is associated with the species of positive feedback [Whitelam et al., 2009]. The model further includes steric interactions between actin filaments, which likely also play a role for actin clusters close to the membrane in CDRs. In the model by Whitelam et al. individual actin particles can fuse to wave-like

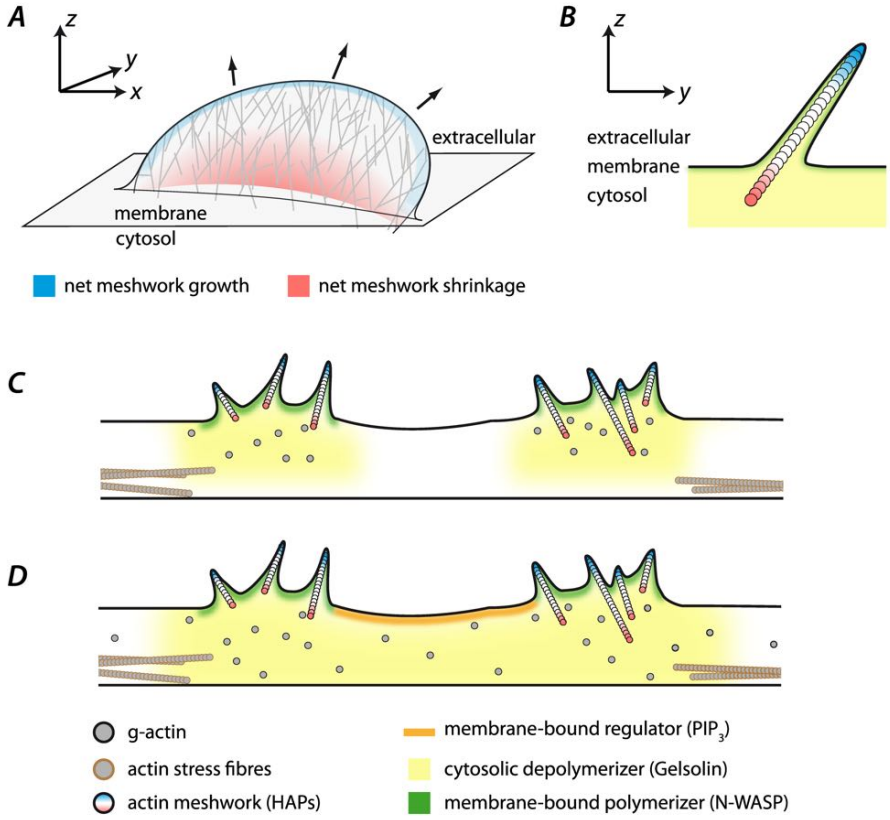

Figure 3.10: *Sketch of functional elements of actin regulation in CDRs. A*: Three-dimensional sketch of a HAP embedded in the dorsal cell membrane. The actin meshwork of the HAP grows at the membrane-attached side due to a membrane-bound polymerizer of actin, causing protrusions along the direction highlighted by arrows. The HAP is exposed to the cytosol bulk at its rear, which leads to net dissolution at this side due to a cytosolic depolymerizer of actin. *B*: Side-view of a HAP highlighting the compartmentalization of the regulatory proteins of actin. *C* & *D*: Models of the overall distributions of regulatory proteins within CDRs (vertical cross sections through two wavefronts). There are two variants, as the true distribution of g-actin remains unknown. In both versions actin polymerizes into vertical membrane protrusions in form of HAPs where the cytosolic depolymerizer and the membrane-bound polymerizer of actin co-localize. The dissolution of f-actin incorporated into stress fibres leads to local high availability of g-actin within CDRs. The polarity between CDR inside and outside might results from the mechanism of substrate depletion (*C*) or be be mediated by a membrane-bound regulatory protein (*D*) such as PIP_3 [Itoh and Hasegawa, 2012].

structures.

Whether the motion of HAPs in CDRs significantly contributes to the mechanism of wavefront propagation of CDRs remains an open question. The reason for this is that the vertical extension of CDRs poses a considerable challenge for high-resolution imaging of HAPs. However, these data would be required to correlate the motion of individual HAPs to that of the overall wavefront. This situation is less complicated for actin particles in *D. discoideum*, as these form at the ventral cell membrane, which permits imaging via high-resolution LSM and TIRF microscopy [Whitelam et al., 2009, Gerisch et al., 2004, Gerisch et al., 2012]. Given the current data situation it seems unlikely that the motion of HAPs is a major contributor to the wavefront dynamics of CDRs.

It is not clear whether actin reorganization on fast time scales, as observed for HAPs, also applies for actin structures within the sheet-like vertical protrusions that are a feature of late CDR life stages (Figure 3.9*IV*-*V*). Structural data based on TEM microscopy might have the potential to account for questions along these lines, even though with this strategy no direct dynamic picture can be obtained.

Besides actin waves in *D. discoideum* also actin waves in neutrophils [Weiner et al., 2007] and podosomes have been reported to localize to the ventral cell side [Buccione et al., 2004]. The latter are actin-rich ring-shaped structures in macrophages and kidney cells. In contrast, HAPs are restricted to the dorsal side of the cell and do not internally extend down to the ventral cell side, as it was shown in this chapter by TIRF and LSM imaging (Section 3.2). This identification of the site of actin polymerization has an important possible implication, as it suggests a membrane-bound activator of actin polymerization that is exclusively located at the dorsal side of cells. The panels *B*-*D* in Figure 3.10 illustrate this compartmentalization based on two-dimensional model sketches of cuts through CDRs.

It was one of the main motivations behind the experiments described in this chapter to identify the effective mechanisms of actin dynamics, which lead to wave propagation in their interplay. In contrast, it is not the aim of this thesis to identify the molecular key players of the wave machinery underlying CDRs. However, from the proteins known to localize into CDRs listed in Table 2.1 (Section 2.1.1) the WAVE family proteins WAVE2 and N-WASP are likely candidates for the membrane-bound activator of actin discussed above. Especially the role of N-WASP has been highlighted in the work by Legg et al. [Legg et al., 2007]. Proteins from the WAVE family are also known to play an essential role in ventral actin waves in neutrophils [Weiner et al., 2007]. Weiner et al. propose a model in which the WAVE component Hem-1 constitutes the active feedback loop of the wave machinery. In fact, Hem-1 is also contained in N-WASP [Park et al., 2010] and might therefore also have autocatalytic functions in CDRs.

With the oppositional different positions of the cell membrane where waves form in neutrophils and fibroblasts, one might, however, ask why the same activator of actin should be specific for the ventral cell side in one case and specific for the dorsal cell side in the other. One might further ask, on a more general basis, why the dorsal cell side is a distinguished compartment of fibroblasts at all. The physiological habitat of

these cells is the connective tissue, in which fibroblasts certainly lack a polarization into dorsal and ventral cell side. When grown on planar substrates, however, polarization is, amongst others, established via receptors of growth factors. As standard cell media always contain growth factors in small amounts (Section 2.1.5), the dorsal cell side is the only part of the cell that is subject to binding events between growth factors and their receptors. At this stage we might hypothesize that occupied receptors of growth factors might play a role not only for wave initiation, but also for the propagation mechanism of CDRs. This hypothesis will be further discussed in the following chapters.

The model by Peleg et al. offers another explanation for the exclusive formation of CDRs at the dorsal cell side. In their model the polarization of cells is established via the fact that the dorsal cell side is the only one that permits the formation of protrusions. The curvature of these protrusions is then the actual mediator of wave propagation, via curved membrane proteins that recruit WAVE family proteins [Peleg et al., 2011]. However, also for systems that do not include curved membrane proteins the local membrane shape could play a critical role. The reason for this is that local membrane deformations go along with changing surface to volume ratios, which might affect, e.g., the diffusion time scales of cytosolic species. This might have implications for CDRs as we have seen large evidence for a cytosolic depolymerizer and a membrane-bound activator of actin dynamics in this chapter (Figure 3.10*B*-*D*).

The finding of depleted f-actin in the areas of cells that are enclosed by CDR wavefronts has been reported by several groups previously [Krueger et al., 2003, Buccione et al., 2004, Itoh and Hasegawa, 2012, Hoon et al., 2012]. Again, it was the pioneering work by Mellström et al. that described this phenomenon first [Mellström et al., 1983]. From a dynamical perspective, it is not surprising to find an element of high f-actin depolymerization within CDRs, as the propagation of wavefronts requires a rapid turnover of f-actin structures [Hoon et al., 2012]. The observation of very short turnover times of actin on the order of ten seconds for HAPs within CDR wavefronts gave clear hints that these regions are marked by simultaneous high rates of both, polymerization and depolymerization (Section 3.1.2). However, it could be shown for the first time in this thesis that the f-actin depletion within the region surrounded by CDRs is found to extend down to the ventral cell side (Section 3.2). In contrast to the hypothetically membrane-bound activator of actin in CDRs, the depolymerizer of actin in CDRs is therefore probably cytosolic. From the actin-associated factors that are known to localize to CDRs (listed in Table 2.1), gelsolin is associated with disassembly of f-actin and might thus be enriched in CDR interiors (Figure 3.10*C* & *D*). Gelsolin has been proposed previously to be a major regulator of actin dynamics of CDRs [Krueger et al., 2003].

Actin depletion in the rear of actin waves has not been reported for *D. discoideum*. Human trabecular meshwork cells overexpressing caldesmon, however, form concentric circular or arc-shaped actin waves that, much like CDRs, leave a zone of f-actin depletion behind travelling waves [Grosheva et al., 2006]. Nevertheless, also in the latter system the identity of the responsible molecule for this phenomenon is not known.

Based on the observation of f-actin depletion in CDR interiors it is an obvious idea to assume that a mechanism is at work that consumes cytoskeletal f-actin and remodels it into CDR-incorporated f-actin [Krueger et al., 2003]. This observation is the basis for one of the hypothetical functions of CDRs, i.e., the overall weakening of the cytoskeleton that fosters cell migration [Buccione et al., 2004, Itoh and Hasegawa, 2012]. From the perspective of the theory of non-linear waves this observation is reminiscent of models of the substrate depletion kind. In these, waves live on the support of a substrate, which is consumed as a result of wave events [Bak et al., 1990, Meinhardt, 2012]. Therefore, propagating waves leave a depletion zone behind. Indeed, the model for CDRs proposed by Zeng et al. includes elements of a substrate depletion mechanism, as it builds on the idea of a competition between the organization of actin into either stress fibres or CDRs [Zeng et al., 2011]. In this framework the CDR interior cannot recover from depletion, because actin is a conserved species that is entirely drawn into CDRs, due to the high affinity for actin to incorporate into these structures. Figure 3.10C illustrates the protein distribution in a hypothetical qualitative model for CDRs that is based on substrate depletion. In this, the wavefronts are regions of simultaneous high activity of polymerization and depolymerization of actin. Since the depolymerizer is cytosolic, it not only facilitates actin turnover in CDR wavefronts, but also degrades the cytoskeleton. Behind wavefronts actin is entirely depleted, due to high actin affinity of the nucleation promoting factor in CDR, as outlined above.

We have seen in this chapter that CDRs include considerable amounts of actin due to their vertical extension. The perspective of a mechanism of cytoskeletal actin consumption offers an explanation for the origin of the actin required for CDR growth. Moreover, this idea would be in agreement with the hypothesis that the void of f-actin at the nucleus is the cause for the fact that CDRs tend to avoid this region of the cell, which was formulated in Section 3.2.

However, the idea of substrate depletion as a major mechanism of CDR propagation rises several questions. The first of these is based on the observation that CDRs that result from growth factor stimulation do not originate from points. Nevertheless, they exhibit f-actin depletion in their interiors, regions that did not support waves. Furthermore, we will see in the next chapter that pronounced f-actin depletion also exists behind open wavefronts and persists for long times (tens of minutes). However, this time should actually be sufficient for recovery of the cytoskeleton as we will see in later experiments with Latrunculin A (Section 5.6). Additionally, we cannot be sure whether actin depletion really exists, as only f-actin was visualized, whereas the distribution of g-actin remains unknown.

Thus, we will discuss an alternative perspective in the following. The asymmetry between the interior and exterior regions of CDRs, induced by f-actin depletion, generally reminds of waves in two-state systems. A prominent example of a corresponding minimal reaction-diffusion equation is given by the Fisher-Kolmogoroff model [Murray, 2004a, 439 pp]. The behaviour of CDRs to close back to their point of origin might naturally occur

in such a framework[b], although it does not provide a mechanism for the actual reversal of wavefronts. Further, those systems cannot support concentric wave trains, which also applies for CDRs, as will be discussed in the next chapter.

For CDRs, the two phosphorylation states of a phospholipid, i.e., PIP_2 and PIP_3, might constitute a two-state element, which could be responsible for the polarisation of CDRs into an interior and an exterior (Table 2.1). This idea has been proposed by Itoh et al. in form of a qualitative mechanism that is based on the conversion from PIP_3 to PIP_2 in which the former is localised in patches at the plasma membrane as a response to cell stimulation with growth factors [Itoh and Hasegawa, 2012]. PIP_3 is then converted to PIP_2 via SHIP2 and SH3YL1, which in turn promotes the polymerization of g-actin into f-actin, forming the characteristic vertical protrusions of CDRs. A similar mechanism is discussed by Hoon et al. [Hoon et al., 2012]. The wave-forming dynamics of the PIP_2/PIP_3 system has also been studied in the regulation of the actin dynamics in *D. discoideum* [Gerisch et al., 2012]. Indeed, Khamviwath et al. propose a quantitative model for actin waves in *D. discoideum* that is closely reminiscent of the qualitative model proposed for CDRs by Itoh, Hoon et al.s [Khamviwath et al., 2013].

Figure 3.10*D* illustrates a hypothetical scenario in which PIP_3, or a related membrane-bound regulator, constitutes the polarity between CDR inside and outside. In this variant actin is assumed only to be present in its monomeric form in CDR interiors. This is to highlight that within a framework in which PIP_3 either functions to facilitate f-actin depolymerization, or to stop actin polymerization, g-actin is not necessarily entirely depleted in CDR interiors. Interestingly, Hasegawa et al. have shown recently that indeed the PIP_3-recognizing Arap1 is organized in a secondary ring within CDRs. Remarkably, Hasegawa et al. do not talk about wavefronts in this respect nor is the term "wave" mentioned in the entire article. Arap1 functions as a GAP for deactivation of the small GTPase Arf1, which is in turn associated with promotion of actin polymerization [Hasegawa et al., 2012]. Therefore, the secondary ring of Arap1 within CDR wavefronts could be a mark of the negative feedback loop in CDRs, which is responsible for suppression of actin polymerization. We will come back to the discussion of the mechanism of actin depletion in the CDR interior in Section 5.5.

The results presented in this chapter constitute a basic understanding of some of the most important processes involved in the wave machinery of CDRs. In the following chapters, the focus lies on the analysis of the dynamics of CDRs, which will further contribute to this picture. The results from the next chapters will add support to the hypothesis that actin availability is a crucial component in CDR dynamics. However, we will also find evidence confirming the idea of an inherent polarization of CDRs. Indeed the final picture will be in favour of a scheme as shown in Figure 3.10*D* in which additionally a limiting factor is constituted by a finite actin reservoir.

[b]This idea was proposed by Prof. Nir Gov (Weizmann Insitute of Science, Rehovot, Israel) in a personal communication.

Chapter 4

Wave Dynamics on Random-Shaped Cells

It is the main thesis of this work that cells form an active medium for the propagation of CDRs. In this section I will present evidence for this stance based on the identification of features of the dynamics of CDR wavefronts that are well known to occur also for waves in two-dimensional active media. In particular, live imaging data sets were systematically scanned for the following events:

- periodic reappearances of CDRs
- annihilation of wavefronts during collisions
- the occurrence of spiral waves.

The wavefront dynamics will be further investigated with respect to the evolution of the velocity as a function of time and local wavefront curvature. Moreover, the behaviour of waves close to the boundaries of cells will be examined.

The data were acquired in long-term experiments, in which cells were imaged under biochemically constant, physiological conditions for several hours. This experimental approach differs from the traditional experimental strategy for investigations on CDRs, which relies on the stimulation of CDR formation by growth factors such as, e.g., PDGF directly before or during imaging [Mellström et al., 1983, Krueger et al., 2003, Itoh and Hasegawa, 2012, Hoon et al., 2012]. The reason why I chose to refrain from the temporarily punctual addition of growth factors to the cell medium is that this approach involves two issues, which complicate the understanding of the dynamic events resulting from cell stimulation. Let us use the analogy of the stimulation of waves in the FHN system for illustration. The FHN system responds with wave formation to spatiotemporal punctual stimulation of the medium (Section 2.3). However, in experiments on cells this is, due to technical reasons, not easily achievable. In contrast, the stimulation of cells with growth factors means that the whole cell body is exposed to a stimulus. Accordingly, with growth factor stimulation, no singular point of CDR origin can be

determined, which is the first issue. This case will be investigated in Section 4.6. The second issue is based on the fact that cells are known to adapt to sudden changes in their environment such as biochemical disturbance by growth factor stimulation [Itoh and Hasegawa, 2012, Hoon et al., 2012]. In the framework of an active medium description such a disturbance, and the corresponding adaptation of cells, corresponds to a change of the phase space of the system in time, which largely complicates an understanding of the resulting dynamics.

To gain acceptable data yield without the need for external stimuli, I used a cell line (NIH 3T3 X2) that forms CDRs spontaneously at high rates in standard cell medium without the need of punctual growth factor stimulation. Since this approach differs from the standard procedure in the literature, I confirmed that the resulting CDRs have equivalent dynamics as induced CDRs in test experiments (Appendix: 9.1). Differences between spontaneously formed and stimulated CDRs were only found in their initial growth phase, as introduced in the Section 3.1.1. The latter was less pronounced for stimulated CDRs. A possible explanation for this is given by the assumption that growth factor stimulation leads to simultaneous stimulation of the complete dorsal cell surface. This notion will be discussed in detail in Section 4.6. Spontaneous CDR formation, in contrast, is of stochastic nature and only locally leads to wave triggering.

Phase contrast microscopy was used to guarantee that no photo-induced biochemical disturbances occurred, which is - due to phototoxicity - a common issue in fluorescence microscopy. The positions of wavefronts of polymerized actin can equally well be localized based on phase contrast micrographs (Section 8.9.1). Details on the experimental procedures of this chapter are described in Section 8.7.2.

From 41 experimental runs, 600 cells that exhibited CDRs were visually categorized and assigned to subselections, according to the encountered phenomena. This filtering reduced the number of cells that were finally analysed considerably; the respective numbers for each category are explicitly stated in the following presentation of the findings of the phenomena encountered for CDR dynamics. Each of the subsequent sections is dedicated to one specific aspect of CDR dynamics. Whenever possible, we interpret and discuss the data directly in the respective section. The final section (Section 4.7) is a summary and discussion of the data in a holistic sense.

4.1 Characteristic Wavefront Dynamics

Spontaneously formed CDRs originated from points and grew outwards as closed, soliton-like structures. Shortly after formation CDRs typically had ring-like morphologies. Their growth rates were maximal directly after formation. Then they expanded with negative acceleration, leading to decreasing velocity and eventually to reversal of propagation direction and CDR closure. In this section we will investigate this dynamics in more detail, motivated by questions arising from the point of view of an active media description of CDRs. Especially, we will compare experimental data with the predictions of theoretical models of actin waves (Section 2.2). Potential correlations between velocity

and curvature of wavefronts, as suggested by the eikonal theory (Section 2.3.5), further motivated a contour analysis of CDR wavefronts.

We start with an investigation of the symmetry between the processes of CDR opening and closing. Figure 4.1*A* shows a typical example of a CDR life course following the pattern of formation, growth, reversal, and CDR closure without coherent translocation of the whole wavefront. Thus, the CDR in this example originates and extinguishes at the same point, which suggests a visualization of the dynamics via kymographs (Figure 4.1*B* & *C*).

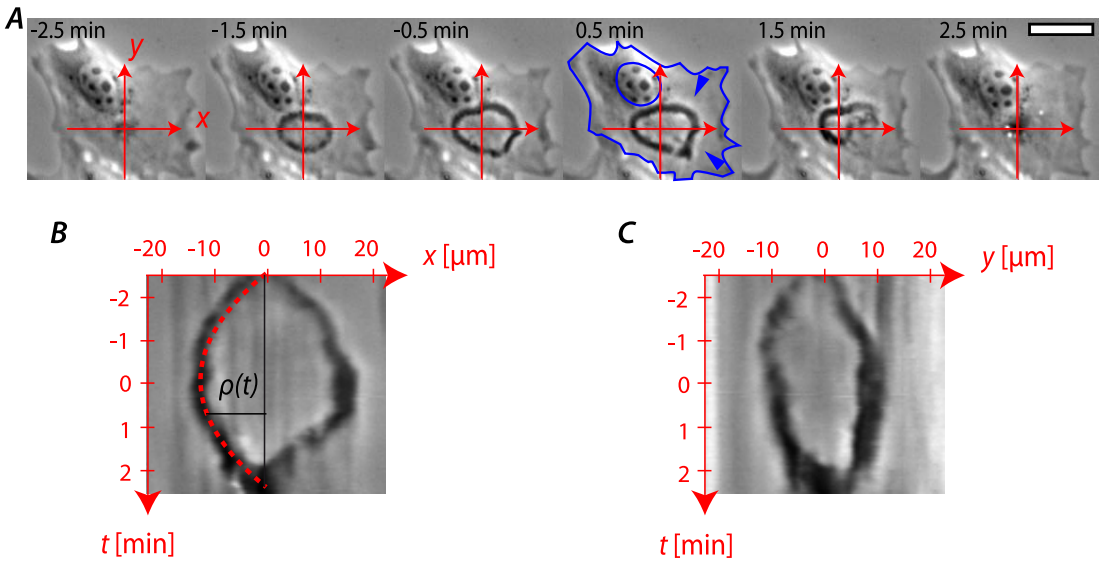

Figure 4.1: *Characteristic radial dynamics of CDRs. A*: Time-lapse sequence showing the life course of a CDR. The red coordinate system marks the positions in which kymographs were sampled. Blue lines highlight the cell and nucleus boundary, the blue arrow heads a phase halo. *B* & *C*: Kymographs sampled along the x- and y-axis in *A* respectively. The dashed red line in *B* is a fit with the empirical parabola 4.1. Scale bar: $25\,\mu\text{m}$.

The two kymographs (Figure 4.1*B* & *C*) were taken from the time-lapse sequence in Figure 4.1*A* along the axes of a local xy-coordinate system with origin in the point of CDR creation and extinction. We start our analysis with inspection of the negative part of the x-axis (Figure 4.1*B*). The evolution of the CDR radius $\rho(t)$ with time is apparently highly symmetric and can be approximated with a parabolic profile given by

$$\rho(t) = \rho_{\max} - at^2, \tag{4.1}$$

where $a = 6 \times 10^{-4}\,\mu\text{m/s}^2$ is the acceleration. We measure time with respect to the moment of maximal CDR radius $\rho_{\max} = 12.5\,\mu\text{m}$. The two extreme values of the CDR velocity at $\rho = 0$ are therefore $\pm 0.09\,\mu\text{m}\,\text{s}^{-1}$ in this example.

A comparison of the symmetric profile (negative x-direction in Figure 4.1B) with the profiles along the other three directions (positive x-direction in Figure 4.1B, negative and positive y-direction in Figure 4.1C) reveals that the latter three are far less symmetric in time. To understand this discrepancy, it is helpful to identify the corresponding parts of the wavefront in the time-lapse sequence (Figure 4.1). These parts are the intersections between x- or y-axis and the wavefront respectively. Along positive y-direction the CDR collides with the cell nucleus. As introduced in Section 3.1.1 and 3.2, this part of the cell is characterized by low concentrations of f-actin and, therefore, tends to disturb CDR dynamics. It was also shown in Section 3.1.1 that encounters between CDRs and the cell edge perturb their wavefront dynamics, which leads to the reversal of the propagation direction of CDRs. Consequently, the close encounter of the part of the CDR that propagates in negative y-direction and the cell edge, leaves a footprint in the corresponding kymograph (Figure 4.1C). Along positive x-direction, formation of a pronounced halo points to large CDR extension into vertical direction. In this example it coincides with partial decay of the CDR upon reversal of propagation direction (Figure 4.1A at $t = 1.5\,\mathrm{min}$).

We thus conclude that the evolution of CDR radius with time has a tendency to be symmetric. However, due to the interactions of CDRs with different cellular compartments and the irregular shapes of fibroblast cells in fact rather asymmetric profiles can be found.

We restrict our further analysis to a set of 13 CDRs that exhibited nearly circular geometries without any obvious disturbances of their dynamics by cell features like the cell edge or nucleus. These CDRs followed the scheme of origination, growth, reversal and closure. From each single frame of the time-lapse sequences contour data were extracted, as described comprehensively in the sections 8.9.1-8.9.4 and in Section 9.5. Figure 4.2 illustrates the contour representation of wavefronts. For a dynamic description I calculated the local normal velocity and the local curvature of the contours. The motivation for this stems from the question whether there is an eikonal equation governing the dynamics of CDRs, i.e., if there is a functional relation between wavefront curvature and velocity (Section 2.3.5). Furthermore, the morphodynamic theory for CDR propagation introduced in Section 2.5 implies a correlation between wavefront curvature and velocity.

For the correlation analysis the local contour curvature was plotted versus the local velocity of wavefronts. Since contours typically comprise some hundred points traditional scatter plots of the resulting data appear crowded. To avoid this velocity and curvature space were discretized and the data points in each of the resulting bins were counted. The corresponding matrix was then plotted with a logarithmic color bar (Figure 4.3). The plot reveals no correlation between local velocity and local curvature.

So far, our analysis was based on absolute scales of velocity and curvature. Since the size of CDRs does, however, vary with the cell size, i.e., large CDRs form on large cells and vice versa, one might ask if there is a mechanism of size adaptation. We therefore proceeded with an analysis of correlations on relative scales.

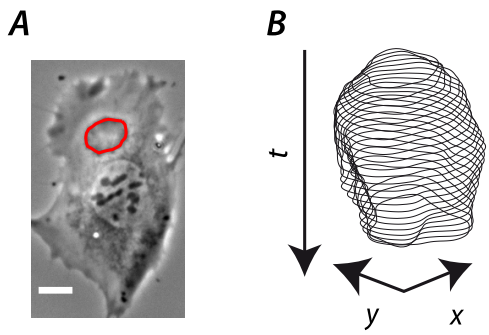

Figure 4.2: *Contour representation of wavefronts.* *A*: Representative CDR of the data set with overlaid contour representation (red curve). *B*: Contour set of the wavefront at different time points. Scale bar in *A*: $25\,\mu\mathrm{m}$

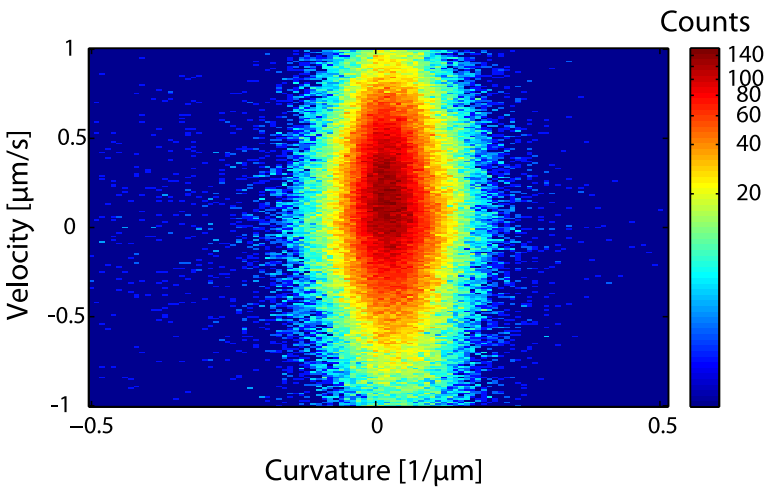

Figure 4.3: *Scatter plot of contour curvature and velocity.* Each pixel corresponds to one bin. The number of data points in each bin was counted and coloured according to a logarithmic scale.

I checked if an integral measure, such as the CDR size quantified by its area A, could be governing the dynamics of the wave velocity. A reasonable hypothesis could be that CDRs incorporate a significant portion of, e.g., the available actin of cells. Indeed, there are several possible CDR constituents that could play the role of a limiting resource. Along this line of thought, the limiting resource is used up with increasing CDR size, until a state of depletion sets in, which limits further growth.

Given that the available resource is proportional to the cell size the maximal size of a CDR would scale accordingly. Therefore, I normalized the area data with respect to their maximal values. Figure 4.4 shows this normalized area $\widetilde{A}$ plotted versus the

contour mean velocity.

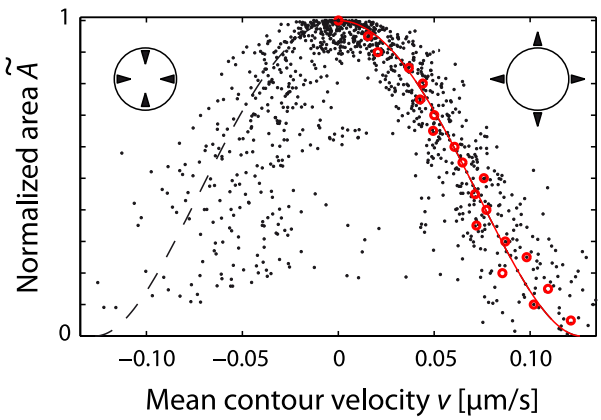

Figure 4.4: *Scaling of velocity with relative area.* Black dots are individual data points, red dots denote median values of velocity at constant normalized area. The lines are a semi-empirical fit function. The red part of the line highlights the part that was actually fitted, the dashed line is an extrapolation. The symbolic inlets denote the growth and closing regime of the plot.

The data points of all 13 CDRs roughly collapse on one trajectory. Positive velocities correspond to CDR opening and negative velocities to CDR closing. The data for CDR closure exhibit a more pronounced scattering. The reason for this is that shrinking CDRs tended to partially collapse, often going along with formation of vesicles. The presence of both, instability and vesicles, lead to jumps in the contour causing the aforementioned scattering.

As noted before, CDRs that propagate undisturbed, i.e., without hitting the cell boundary or nucleus tended to have parabolic radius evolutions in time, as described by equation (4.1). Since the mean velocity for circular CDRs corresponds to $v = \mathrm{d}\rho/\mathrm{d}t$, one can derive a function $\widetilde{A} = \widetilde{A}(v)$ from equation (4.1), which describes the evolution of the normalized area as a function of the mean velocity:

$$\widetilde{A}(v) - 1 = -2\alpha v^2 + \alpha^2 v^4. \tag{4.2}$$

The only free parameter of this equation is $\alpha = 1/(4a\rho_{\max})$. This function was fitted to the data in Figure 4.4. The fact that CDRs are slowest when they are large leads to an unequal number of data points for the different life phases of CDRs. To avoid the over-representation of large CDRs I calculated median values of velocity in bins of relative area with a width of 0.05. The fit of (4.2) to the data of positive velocity in Figure 4.4 shows the consistency of the whole data set with equation (4.1). The data of negative velocities have a much more pronounced scattering and the fit, therefore, matches only poorly for this part of the data set. I attribute the scattering to the aforementioned partial collapses of closing CDRs. However, the data for closing CDRs

still roughly follow equation (4.2). This means that CDRs tend to have velocity profiles that are symmetric with respect to opening and closing.

The propagation velocity of CDRs is a dynamic variable and, thus, a typical value cannot be stated. Nevertheless, since we find a universal scaling in CDR dynamics we can state one characteristic velocity, which is the maximum velocity, attained at vanishing CDR area. Using function (4.2) to extrapolate the velocity towards this point one finds $v(\widetilde{A} = 0) = 0.13\,\mu\mathrm{m\,s^{-1}}$.

The analysis presented in this section has several implications. First, we find symmetry between CDR opening and closing. This is a strong hint towards the existence of just one mechanism underlying these two processes. On the contrary, it has been proposed before that CDR closure is facilitated by contractile forces mediated by, e.g., the activity of myosin motors [Buccione et al., 2004]. In this framework CDR opening and closing would constitute fundamentally different mechanisms and a symmetry between the dynamics of these two would be a very unlikely finding. My results are therefore rather in line with the study of Peleg et al., which proofed that the activity of one particular type of molecular motor, namely myosin IIb, does not alter CDR dynamics [Peleg et al., 2011].

Secondly, the overall dynamics of CDRs is not governed by an eikonal equation, as we find the local curvature in the xy-plane and the local velocity of wavefronts uncorrelated. This result disagrees with the model by Peleg et al., as the latter implies a correlation between local membrane curvature and wavefront velocity[a], even though the explicitly considered curvature in the model is that in the xz- and yz-plane [Peleg et al., 2011]. One of the reasons why the curvature of wavefronts in the xy-plane also have an effect on the distribution of curved proteins that are actually sensitive for curvature in the xz- and yz-plane is due to the rotational degree of freedom of membrane proteins. The time scale of rotational movements is much faster than that of the wave dynamics [Chou et al., 2001]. Consequently, curved proteins effectively also sense the shape of membranes in the xy-plane.

In fact, the finding of no eikonal relation is a puzzling result. The implications of a dependency between local curvature and local velocity lead to an effective smoothing of small scale undulations of wavefronts (Sections 2.3.5), which is indeed observed for CDRs. Moreover, we will see in Section 4.2 that CDRs form spiral waves in some cases, which also indicates an eikonal relation. An explanation for this apparent paradox is that there indeed exists an eikonal relation, albeit not as the most dominant effector of CDR dynamics. Instead, the velocity is governed by a scaled measure for CDR size, i.e., the normalized CDR area. Therefore, the velocity does not depend on an absolute but on a relative quantity. A possible interpretation is that a limited resource, such as a protein species involved in CDR dynamics, sets the propagation velocity of CDRs. Furthermore, the membrane area is a candidate for the limiting species. Regardless of its identity the availability of the resource should scale with the cell size and, thus, allow CDRs to grow to correspondingly different sizes. This explains why all data in

[a]Personal communication with Nir Gov, Weizmann Institute of Science, Israel

Figure 4.4 collapse on one trajectory. We will see later that the idea of large impact of a limited species might also explain the reversal of CDR wavefronts.

Waves are a frequently encountered phenomenon in active media. One of the simplest models that captures basic traits of CDRs is the FHN system. It was illustrated in the sections 2.3.2 and 2.3.4 how the FHN system forms propagating waves of circular geometry. The full dynamics of CDRs, however, is more complex than that of waves in the FHN system. CDRs, e.g., extend with a non-uniform velocity profile and reverse at boundaries or cell nuclei without obvious reasons. Further, the FHN system was formulated from a very abstract point of view and does not, apart from the existence of certain feedback loops, consider any processes, which are specific to, e.g., characteristics of polymerizing actin.

For an explicit modelling of actin waves several systems have been formulated in which one of various possible feedback mechanisms constitutes the wave propagator (Section 2.2). Zeng et al. formulated a model, which is dedicated explicitly to CDRs. In the latter two antagonistic Rho-GTPases form a two-component reaction diffusion system, which exhibits propagating ring-shaped waves that reverse their propagation direction after some time of ring growth (Section 2.4) [Zeng et al., 2011]. The reason for the reversal of the waves in the model by Zeng et al. is the slow kinetics of the inhibitory species, which just eventually catches up with the expanding wavefront of the polymerizer of actin. However, the dynamics of CDR opening and closure differ considerably in the model; CDR closure is a much faster process than CDR opening. My experimental data show that this is not the case for actual CDRs, which, in contrast, exhibited rather symmetric velocity profiles.

The fact that we found a universal description of the CDR dynamics, which depends on the relative size of the wavefront, points to a limiting effect due to a finite resource. The pronounced depletion of f-actin in the CDR interiors suggests that the limited resource could indeed be actin. This is also in line with the observation that wavefronts avoid the cell nucleus, which is a region of low f-actin concentration (Section 3.2). However, this is just one of several possibilities.

A series of theoretical studies by Edelstein-Keshet and co-workers deal with reaction-diffusion systems in which one species is conserved [Mori et al., 2008, Holmes et al., 2012, Mata et al., 2013]. Interestingly, the outcomes of these models include several aspects that are central also for CDR dynamics, among them wavefront reversal. Since these models are relevant to more than one single aspect of CDRs, they will be discussed in the summary of this chapter (Section 4.7).

Despite the fact that there are models of actin waves that are able to explain, e.g., wave reversal we have to bear in mind that also the compartmentalization in cells could largely effect the wave dynamics. Also this point has further implications for the following sections and will be discussed in Section 4.7.

4.2 Spiral Wavefronts

CDR formed rotating spirals only in very few cases. Indeed only two of the 600 cells, which were analysed, exhibited clear spirals.

Spiralling wavefronts can be well visualized as projections of rendered volume representations in *xyt*-space [Killich et al., 1994]. For this, time-lapse sequences were binarized via gray value threshold segmentation (Figure 4.5*A1-A2*) and artefacts were removed manually from the resulting black and white image stacks. Spiralling CDRs then correspond to white pixels in stacks of images. Since the position of the wavefront only changed slightly between acquisition of succeeding frames the spiralling CDR forms a connected object in *xyt*-space. This object can be visualized via volume rendering in *xyt*-space using, e.g., the software FIJI (Figure 4.5*A3*) [Levoy, 1988, Schindelin et al., 2012].

In the panels *B1-C2* of Figure 4.5 two examples of spiralling CDRs are shown. Note that the first of these (Figure 4.5*B1-2*) allows to identify the spiral character of the wavefronts relatively easily based on the time-lapse sequence presented in Figure 4.5*B1* alone. In contrast, the time-lapse of the second example (Figure 4.5*C1*) requires a more careful look for the identification of the spiral movement. The *xyt*-volume visualizations of both examples, however, clearly show the rotational movement of CDRs around one center, resulting in a screw-like signature (Figure 4.5*B2* & *C2*). From these plots, the characteristic dimensions of spiral waves can be read off. The two CDRs shown in Figure 4.5 differ in diameter D (*B1*: $D \approx 38\,\mu\text{m}$, *C1*: $D \approx 68\,\mu\text{m}$), period for one rotation T_R (*B1*: $T_\text{R} \approx 10\,\text{min}$, *C1*: $T_\text{R} \approx 3 - 5\,\text{min}$), and the total number of full rotations (*B1*: 8, *C1*: 3). Note that spiral waves derive from established CDRs only after the phase on CDR opening and partial decay of the initially circular wavefront. In Figure 4.5 this sequence is marked by the funnel-shaped tip of the screw structure, corresponding to CDR opening, that then disappears at all but one position. From this position the actual spiral-shaped wavefront starts to rotate visualized by the screw structure originating from this point.

Spiral waves are a typical feature of waves in active media [Murray, 2004b, Strogatz, 2007]. We will see throughout this chapter that CDRs indeed exhibit several characteristics of waves in excitable systems. Spiral waves are also common for actin waves in *D. discoideum* [Killich et al., 1994, Vicker, 2000]. In fact, in this slime mould spiral waves can even be selectively induced [Gerisch et al., 2004, Schroth-Diez et al., 2009, Whitelam et al., 2009]. Further, we can safely assume that spatial inhomogeneities, that were shown in Section 2.3.5 to facilitate the birth of spiral patterns, are often encountered on cells. This arises the question: why do CDRs form spiral waves only in rare cases?

One obvious explanation for this apparent contradiction is that cells are usually simply too small to form spiralling CDRs. The width of their wavefronts is often of an extension that is comparable to the mean radius of the area of the cell from which the CDRs originate. The two spiral-forming cells shown in Figure 4.5*B1* & *C1* are therefore

special as they are of extraordinary large sizes. Besides the extension of the area for CDR origin, its geometry favours or opposes formation of spirals. Spiralling CDRs were only found in regions that were approximately disc-shaped. However, fibroblasts are random-shaped, which explains the uncommonness of spiral waves on these cells.

We have seen in the previous sections that CDR dynamics is largely governed not only by the interaction with the cell boundary, but also with the nucleus. In contrast, actin waves in *D. discoideum* do not interact with the nucleus based on a study of time-lapse sequences of spiral waves in corresponding publications [Gerisch et al., 2004, Whitelam et al., 2009]. This is likely because the latter propagate at the ventral cell side, which is not marked by limited actin availability at the nucleus.

Moreover, the finding of spiral waves is somewhat puzzling in the light of the results of Section 2.3.5, as it seems to contradict the finding of no correlation between local wavefront velocity and curvature. In general spiral waves are in fact known to obey eikonal relations [Keener, 1986]. However, we have also found evidence for large impact of a limited species on CDR dynamics (Section 4.1). Together with the sensitivity of CDRs with respect to cell compartments and the boundary this explains the apparent contradiction that we do not find a correlation between wavefront velocity and curvature in general, and correspondingly no spiral waves. Only in rare cases, when a cell exhibits a large area in which CDRs can propagate unperturbed, spiral waves can form. The implication is that the wave propagator of CDRs indeed obeys an eikonal relation. However, usually the effects of boundary interactions and limited resources predominate the dynamics of CDRs, as discussed in the previous section (Section 4.1).

4.3 Stalling Wavefronts

In the previous sections, the special role of the cell boundary was emphasized. It is generally not surprising to find the behaviour of a system to differ between its bulk and its boundaries. Accordingly, CDRs exhibit distinct dynamics close to cell edges. At this position CDRs typically reversed their propagation direction. The approach of CDRs to the cell edge was thereby marked by a decrease in velocity. The actual reversal of propagation direction took place typically 5-10 µm before the position of the cell edge.

However, in some cases the decrease in velocity was not followed by propagation reversal, but by stalling of the wavefronts close to the cell edge. Stalled CDRs fluctuated

Figure 4.5 (facing page): *CDRs forming spiral waves. A1-3*: Principle of visualization of spiral waves. Time-lapse sequences (*A1*) were binarized (*A2*, red overlay in *A1*) and stored as 3-dimensional arrays. Volume representations of rotating spiral waves in xyt-space (*A3, B2, C2*) resemble screws. *B1* and *C1*: Stills from time-lapse sequences of two different cells exhibiting spiral waves rotating counter clockwise and clockwise respectively. Red circles mark the center of the spiral rotation. *B2* and *C2*: Visualization of the respective spirals in volume representation in xyt-space. All spatial (vertical in *B2* & *C2*, horizontal in *B1* & *C1*) scale bars: 25 µm, all temporal (horizontal in *B2* & *C2*) scale bars: 10 min.

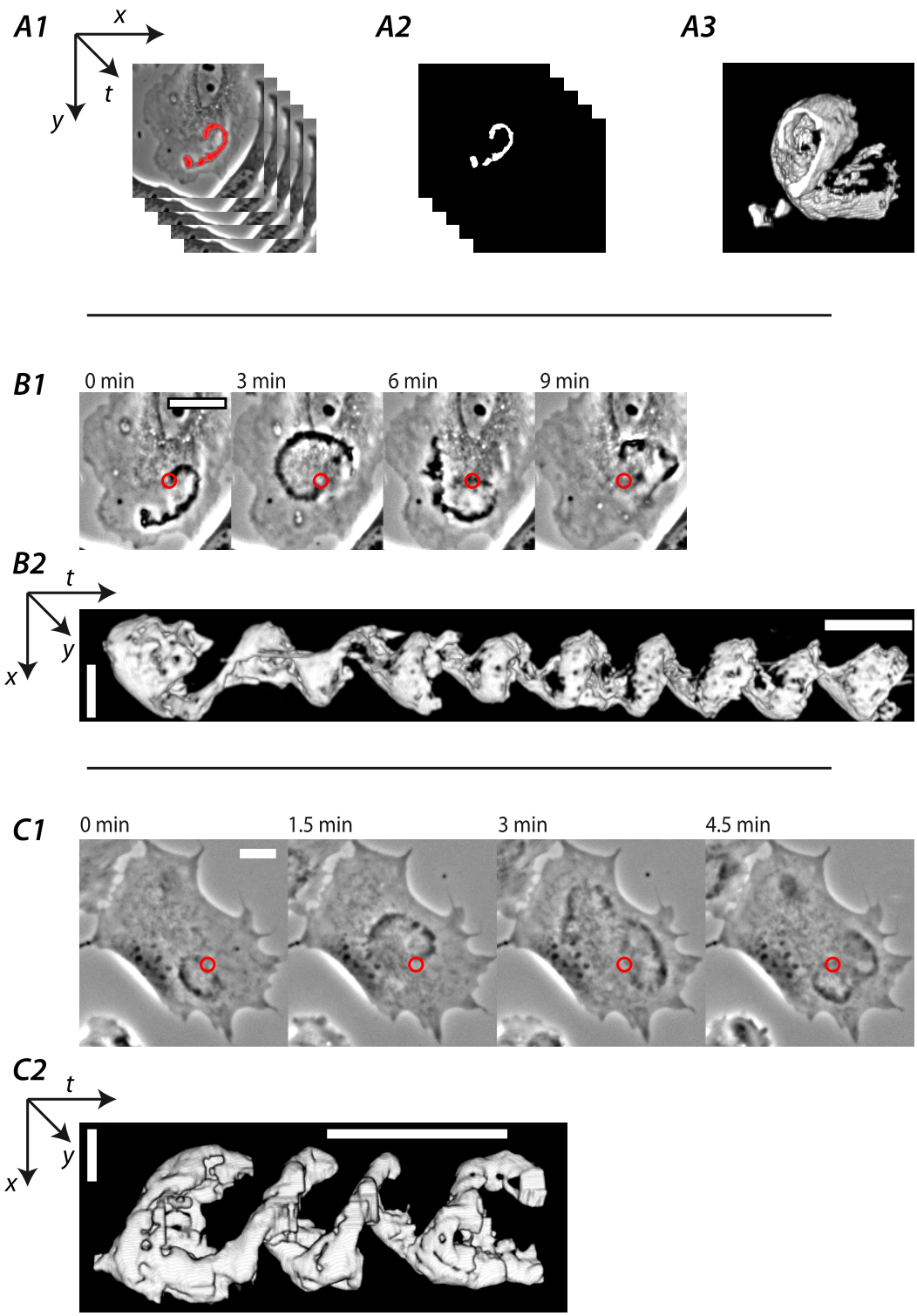
A1
x
t
y
A2
A3
B1
0 min
3 min
6 min
9 min
B2
t
y
x
C1
0 min
1.5 min
3 min
4.5 min
C2
t
y
x

oscillatory around an average position. Figure 4.6 shows that stalled CDRs could keep a fixed average position for very long times, in this case for more than one hour. CDR stalling was observed on 42 of the 600 cells that were analysed.

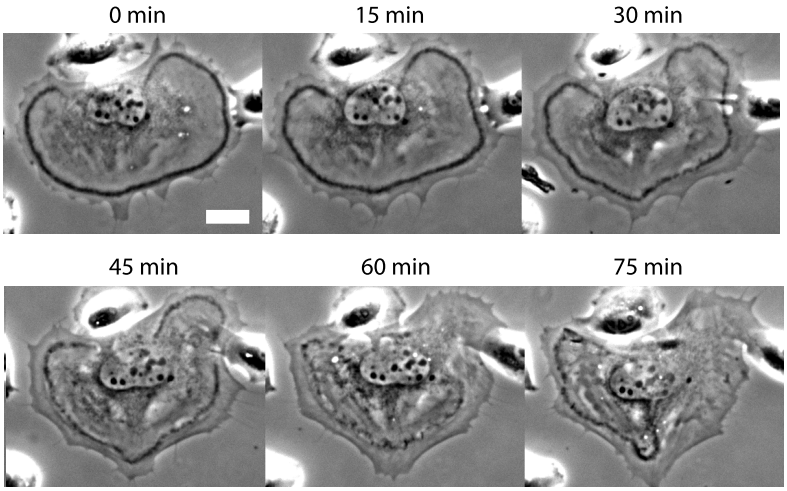

Figure 4.6: *CDR stalling at edges.* Time-lapse sequence of a cell exhibiting a CDR with a lifetime of more than one hour. The CDR finally partially collapses in a region marked by changes in cell morphology ($60\,\mathrm{min}$ - $75\,\mathrm{min}$). Scale bar: $25\,\mu\mathrm{m}$.

The investigation of the distribution of f-actin inside of cells in Section 3.2 revealed that there are only very low concentrations of background f-actin above the nucleus. Since this compartment of the cell is avoided by CDRs we hypothesized previously that CDRs are not able to propagate in regions that are devoid of f-actin (Section 3.2).

Imaging of the actin dynamics of stalled CDRs via fluorescence microscopy indeed showed a pronounced f-actin depletion also in the cytosol behind stalled CDRs (Figure 4.7*A*). Figure 4.7*B* is the corresponding kymograph of Figure 4.7*A*, showing the stationary nature of stalled CDRs together with the typical positional fluctuations.

The stalling of wavefronts has been theoretically described in the work by Edelstein-Keshet et al. [Mori et al., 2008, Holmes et al., 2012, Mata et al., 2013]. The initial motivation for this series of publications is the problem of cell polarization [Mori et al., 2008]. In the corresponding reaction-diffusion system polarization occurs by a mechanism termed "wave pinning". Pinned waves resemble stalled CDRs as they form stationary wavefronts that oscillate around one fixed position in space [Holmes et al., 2012, Mata et al., 2013]. The work will be further discussed in the final section of this chapter (Section 4.7) in the scope of a potential role of PIP_2/PIP_3 in the phenomenon of wave pinning.

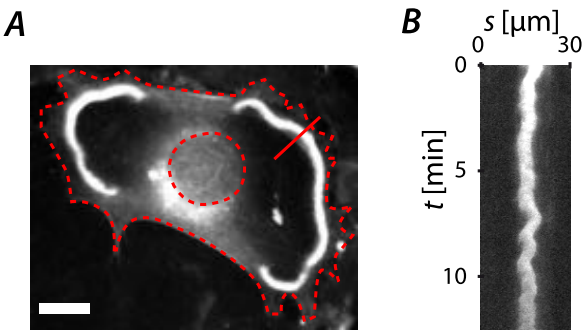

Figure 4.7: *Actin dynamics of stalled CDRs. A*: Fluorescence micrograph of a cell with two stalled CDRs. F-actin was stained via pLifeAct-TagGFP2. The red dashed line highlights the cell edge and the nucleus. *B*: Kymograph taken at the red solid line in *A*. Distance s has its origin in the cell interior. Note that the fading of intensity with time is due to photobleaching. Scale bar: $25\,\mu\mathrm{m}$

4.4 Oscillatory CDR Reappearance

In the literature CDRs are described as non-recurring structures [Buccione et al., 2004, Itoh and Hasegawa, 2012]. Indeed, I could confirm this in my experiments when following the traditional protocol from the literature, i.e., the stimulation of cells via growth factors (see, e.g., Figure 9.1*A* & *B* in the Appendix). In contrast, in experiments on NIH 3T3 X2 cells under constant biochemical conditions, as described in this chapter, CDRs often formed repeatedly at the same position; in terms of numbers on 153 of the 600 cells.

From the active media perspective travelling waves and local oscillations are closely related phenomena (sections 2.3.1-2.3.2, 2.3.4). The period between two successive excitation events in an active medium can yield information on its recovery time τ. Therefore, the dynamics of repeatedly forming CDRs is investigated in more detail in the following.

CDRs were most likely to reappear periodically when they emerged on a region of the cell that was bounded by the cell edge and the nucleus in a way that would not allow CDRs to grow much, limiting their sizes to diameters as low as $10\,\mu\mathrm{m}$. Since the characteristic wave width of CDRs is about 3 - $5\,\mu\mathrm{m}$, very small CDRs did not appear as pronounced rings but rather as phase-dark spots (Figure 4.8*A*). Oscillatory reappearing CDRs formed stationary pulsating or "breathing" structures (Figure 4.8*C*). In the following we briefly discuss two different methods for visualization of pulsating CDRs.

The first method is to define an ROI containing the reappearing CDRs and subsequent plotting of a global measure of image intensity within this ROI such as, e.g., its mean or minimal value as a function of time. Since CDRs appear as phase-dark objects, often surrounded by bright halos, they have a clear signature in such plots. They, e.g.,

usually constitute the darkest pixel in ROIs and therefore govern the minimal intensity value. Moreover, they tend to increase the mean intensity due to the halo formation. In Figure 4.8*B* the minimal intensity within an ROI containing reappearing CDRs was plotted as a function of time. Due to the fact that the succeeding CDR events appear as valleys in the minimal intensity, the recovery time can conveniently be read off from this plot as the length of plateaus between the CDR events.

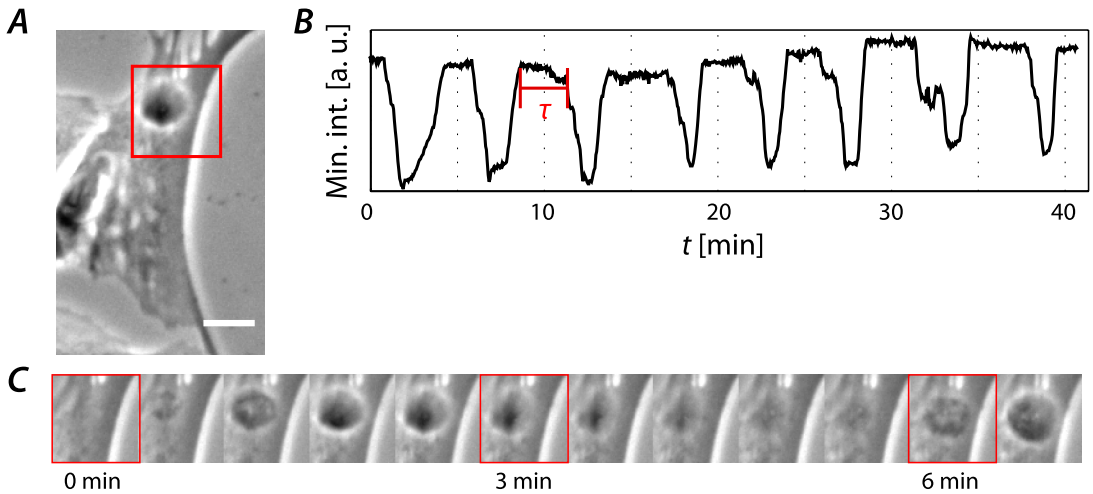

Figure 4.8: *Pulsating CDR reappearance.* *A*: Cell exhibiting pulsating CDR reappearance. *B*: The minimal intensity in the red ROI in *A* plotted as a function of time. Valleys in the graph correspond to CDR events. The temporal length of plateaus between valleys is the recovery time (around $\tau = 5\,\mathrm{min}$). *C*: Time-lapse of the ROI in *A*, showing CDR breathing. Scale bar in *A*: $25\,\mu\mathrm{m}$.

The other method is to display pulsating CDRs via kymographs (Figure 4.9). The advantage of this method is that it allows to read off CDR sizes directly. However, it also requires CDRs to reappear exactly at the same position, which is not always met in practice (see Figure 4.9*A*). In the following we analyse the recovery times of the active medium cell, i.e., the quiescent time between two successive CDR events.

Figure 4.9 (facing page): *CDR size and recovery time.* *A*: Periodically reappearing CDRs. Image intensities were sampled along the red line in *A*, yielding kymograph *B*. Note that the CDRs do not reappear at identical positions (e.g., $t = 13.3\,\mathrm{min}$), introducing artefacts into kymographs. CDRs appear with a peak-to-peak period of about $2.5\,\mathrm{min}$ in the first half of the time-lapse. Dashed red lines mark the frames that are shown in *A*. The average recovery time τ increases with maximal CDR radius ρ_{max}: *B*-*D*. Note that the recovery time was measured at fixed positions, even though some CDRs did not close back to their point of origin. (*D* $t = 25 - 30\,\mathrm{min}$). *E*: Box and whisker plot visualizing this trend. N values represent the number of observations within each group. Plot legend: page xiv. Scale bar: $25\,\mu\mathrm{m}$.

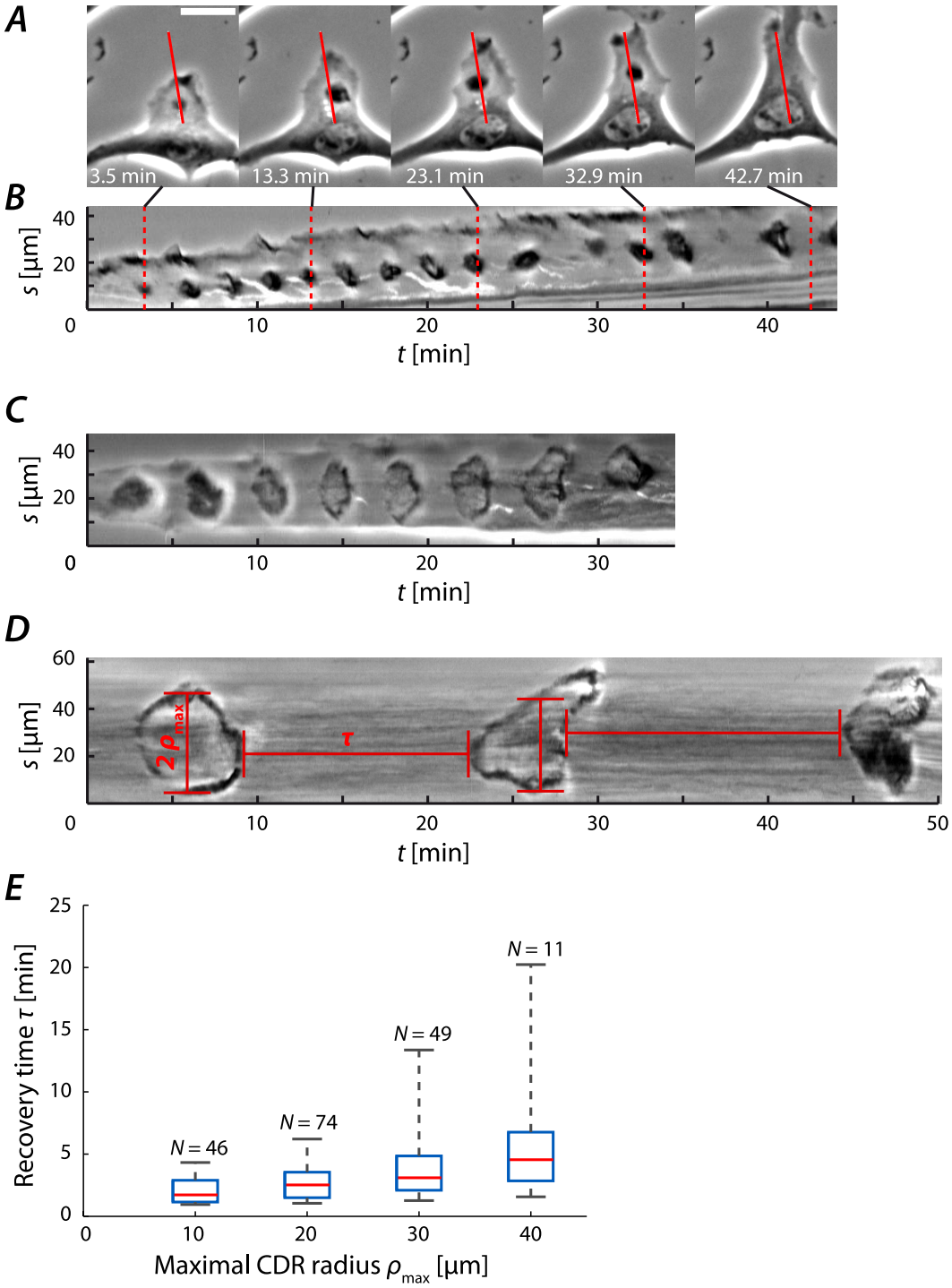
A
3.5 min
13.3 min
23.1 min
32.9 min
42.7 min
B
s [µm]
t [min]
C
s [µm]
t [min]
D
s [µm]
2 ρmax
τ
t [min]
E
Recovery time τ [min]
N = 46
N = 74
N = 49
N = 11
Maximal CDR radius ρmax [µm]

I correlated the maximal CDR size with the recovery time based on a kymograph analysis (Figure 4.9). For this CDRs were grouped based on their maximal radii into bins of 10, 20, 30, and 40 µm. From the data within each of these bins the median, the 25th-, and 75th percentile were calculated and displayed in form of a box and whisker plot (Figure 4.9E). Maximal CDR radii $\rho_{\max}$ and the median values of the recovery time are positively correlated. However, the minimal recovery time between successive CDR events varies only weekly, ranging between 1-2 min. The number of observations N for each size class of CDRs reflects the commonness of reappearing CDR events for the respective groups. For CDRs with $\rho_{\max} > 30$ µm pulsating dynamics was relatively rare.

The finding of periodically reappearing CDRs presented above contradicts the prevailing descriptions of CDR as singular events [Buccione et al., 2004, Itoh and Hasegawa, 2012]. The origin of this disagreement lies, without much doubt, in the experimental framework that was chosen in this work, i.e., the use of a cell line that forms CDRs spontaneously versus the traditional approach of using growth factors to stimulate CDR formation. This raises questions regarding the origin of CDR formation in both situations that we will discuss in the following.

From the biological perspective, the formation of CDRs is commonly described as a specific response to binding events between extracellular growth factors and growth factor receptors in the cell membrane [Buccione et al., 2004, Hoon et al., 2012, Itoh and Hasegawa, 2012]. Therefore, it is a standard procedure in studies of CDRs to add a growth factor, usually PDGF, to the cell medium. Closure of the resulting CDRs goes along with internalization of occupied receptors, as CDR closure is an endocytotic process [Dowrick et al., 1993, Orth et al., 2006, Gu et al., 2011]. The resulting void of growth factor receptors in the cell membrane offers an explanation why CDRs are only formed once in such experiments, even though growth factors are still present in the cell medium. The replenishment of the cell membrane with new receptors takes time, which is the reason why only one burst of CDRs is observed at the time point of growth factor addition. Moreover, cells might adapt their biochemical states towards the newly faced environmental conditions.

However, standard cell medium always contains small concentrations of growth factors as these are essential to guarantee survival and proliferation of the cell culture (Section 2.1.5). Several growth factors are known to cause CDR formation. The constituent containing these growth factors is Fetal Bovine Serum (FBS). The amounts of growth factors in cell medium are usually too small to trigger CDR formation in standard fibroblast cell lines such as NIH 3T3 WT. But why, in contrast, do NIH 3T3 X2 cells form CDRs frequently without extra stimulation?

To elucidate the role that growth factors play in the spontaneous formation of CDRs on NIH 3T3 X2 cells I conducted experiments in which these cells were kept under serum-free conditions. Surprisingly, NIH 3T3 X2 cells without serum in their medium still formed CDRs. I calculated the fraction of cells exhibiting CDRs in serum-free conditions and compared this to the fraction of cells with CDRs under normal culture

conditions. A total number of about 500 cells was analysed for each situation. The box and whisker plot in Figure 4.10 shows the results.

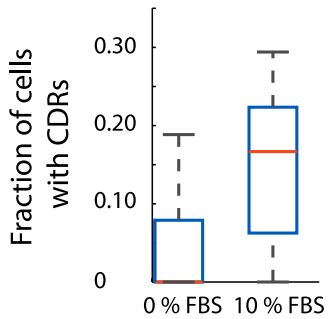

Figure 4.10: *Formation rates of CDRs under growth factor-free and growth factor-containing conditions.* The box and whisker plot shows that NIH 3T3 X2 cells form CDRs spontaneously under serum-free conditions, albeit at much reduced rates when compared to normal culture conditions. 10% FBS corresponds to the standard concentration of serum in the cell medium. Plot legend: page xiv.

Under serum-free conditions, the number of cells exhibiting CDRs is considerably reduced. The median value of the fraction of cells with CDRs is 0.17 in standard cell medium and 0 under serum-free conditions. This reduction of the median value is statistically significant at $\alpha = 5\%$ as could be confirmed via a two-sided Mann-Whitney U test. Even though the median value is zero, this does not mean that CDR formation was completely abolished, as indicated by the box and whisker in positive direction of cells in serum-free medium in Figure 4.10. This means that there must be another mechanism for the formation of CDRs that is independent of growth factor stimulation, which will be discussed in the following.

The active media picture offers an alternative explanation for the spontaneous formation of CDRs on NIH 3T3 X2 cells, which does not depend on growth factors. In the appropriate regime active media such as the FHN system respond to disturbances with the formation of waves. The external stimulation via growth factors is one possible kind of such a disturbance. Additionally, in living cells there are several possible intracellular mechanisms that might correspond to such a disturbance from an abstract point of view, due to, e.g., the omnipresent Brownian noise in biological systems [Tsimring, 2014]. Since the emergence of waves of polymerizing actin is common in living cells, it is a reasonable assumption that cells are situated close to a phase space regime of wave instability. In a similar fashion it could be shown that, e.g., *D. discoideum* indeed organizes its actin machinery in a state that is close to an oscillatory regime [Westendorf et al., 2013].

Apart from the spontaneous formation of CDRs, NIH 3T3 X2 cells exhibit features that point to disturbed actin dynamics, which might facilitate CDR formation as a consequence of growth factor independent dynamics. These are, e.g., their large size

and the often found existence of two or more nuclei in one cell, indicating defective division events. In the latter, actin dynamics plays a crucial role. We may therefore hypothesise that this cell line permanently operates in a state close to wave instability of actin dynamics. The formation of waves under serum-free condition indicates that intracellular noisy events are sufficient to trigger wave formation.

The periodic reappearance of CDRs on NIH 3T3 X2 cells under serum-containing conditions follows naturally from this picture. Situated close to an oscillatory regime, an active medium such as the FHN system, can be driven into a mode of constant firing by the presence of noise [Pikovsky and Kurths, 1997]. The reason for this lies in its integrating properties, which in turn follow from its excitability. When we assume that the binding events between growth factors and growth factor receptors is of stochastic nature, it constitutes an additional source of noise, which is in some cases sufficient to drive the system towards a mode of constant firing.

This framework of an internal and an external source of noise explains why serum is not required for CDR formation, although the rate of CDR formation increases with growth factor concentration and can even reach modes of periodic reappearance. A detailed analysis of the role of noise in active media will be demonstrated in Chapter 6. The biological implications of the recovery time of the system between succeeding wave pulses will be discussed in Chapter 5 in detail.

The pulsating nature of CDRs was most commonly observed on cells in which wave pulses formed in narrow and confined regions. We have seen in Section 2.3.4 that the FHN system is able to support continuous oscillatory wave formation, albeit with patterns of concentric wave trains, which are not observed for CDRs. However, when confined to a narrow region with Dirichelt boundary condition $V(\rho_0) = V_0$ the FHN system forms pulsating structures as shown in Figure 4.11, which resemble small periodically reappearing CDRs. This simulation was carried out on a domain of radial symmetry with radius $\rho_0 = 3$ and a constant stimulus of $S = 2.5$ in the central domain $0 \leq \rho \leq 2$ (all other parameters were chosen as in Section 2.3.4).

Nevertheless, CDRs on cells form sequences in which there is always just one wave at the same time originating from the same spot, regardless of the size of the region from which CDRs originated. It requires the collapse of one wave before the next wave can form, i.e., concentric wave trains do not occur.

We must bear in mind that the FHN model is a minimal system for the description of active media and we thus cannot expect that all phenomena are correctly described. Vasiev has shown in a study of pattern formation of a modified FHN system that it only requires addition of diffusivity to the inhibitor species to produce a rich scope of wave dynamics [Vasiev, 2004]. Especially, this system is able to produce opening and closing of wavefronts and pulsating spots termed "breathing modes" without the necessity of spatial confinement. Breathing modes closely resemble oscillatory reappearing CDRs. This finding might contribute to the development of a future biological model for CDRs.

The reasons underlying the tendency of increasing recovery times with increasing maximal radii of CDRs remain unclear. Small CDRs usually did not form endocytotic

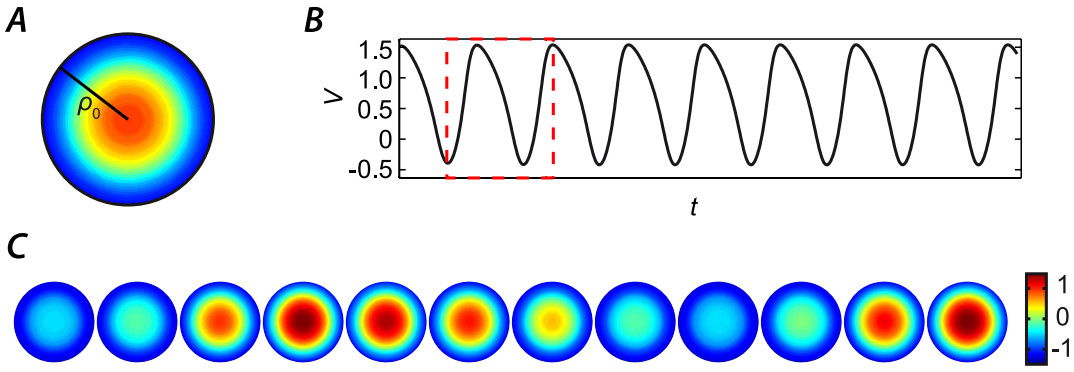

Figure 4.11: *Repeated pulse formation of the FHN system in a narrow domain. A*: geometry of the problem with radial symmetry and Dirichlet boundary condition. *B*: Dynamics of V in the domain center. *C*: Time-lapse (equidistant time points) of the V-field within the time frame marked with a red rectangle in *B*.

vesicles upon closure. It might therefore be hypothesized that cells with large CDRs, which could form vesicles and hence internalize receptors, tend to have longer recovery times, because a reduced number of receptors goes in hand with less stimulatory input to the CDR forming system. This would explain why the increase of recovery time with CDR size is no strict trend, as the minimal period of recovery was unaffected by CDR size. However, with no further investigations along these lines this hypothesis remains a speculation.

We will come back to the topic of periodically reappearing CDRs and the analysis of recovery times in Chapter 5, as on disc-shaped cells CDRs generally tend to form repeatedly.

4.5 Mutual Annihilation of Wavefronts

The observance of collision events between CDR wavefronts required the coincidental formation of two CDRs in close vicinity. Only two clear events of this kind could be observed among 600 cells. The head-on collisions of wavefronts led to their mutual annihilation as illustrated in Figure 4.12*A*. Consequently, CDRs did not form intersecting rings as characteristic for colliding waves obeying linear equations. Mutual annihilation upon collisions of waves pulses is a typical feature of waves in active media [Allard and Mogilner, 2013]. However, a detailed analysis of collision events via kymographs (Figure 4.12*B*) reveals that colliding CDRs exhibit a feature that is not captured by the prototype active medium described by the FHN system: the wavefronts start to faint and become extinct before they actually make contact. The critical distance d, from which on a fading is detectable by phase contrast microscopy, ranges from 10 to 12 µm.

In contrast, colliding waves in the FHN model superimpose forming a characteristic overshoot in amplitude and only then start to fade. Both fields in the FHN model, the activator V and the inhibitor R, show this feature (Section 2.3.3, Figure 2.3).

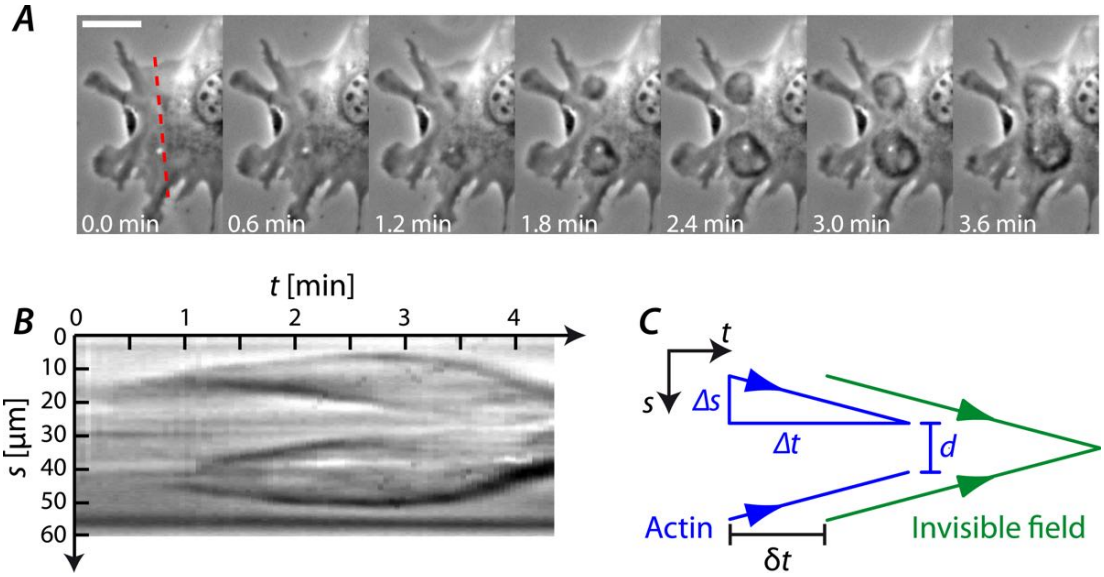

Figure 4.12: *Collision of CDRs. A*: Time-lapse sequence showing two colliding CDRs. The red dashed line marks the position where kymograph *B* was sampled. *C*: Space-time sketch of the collision of two wavefronts, showing the characteristic values of the slope ($\Delta s/\Delta t = 0.7\,\mu\mathrm{m\,s}^{-1}$) and distance at wave annihilation ($d = 11\,\mu\mathrm{m}$). Further, the idea of an invisible protein field preceding the visible actin waves by δt is outlined. Scale bar: $25\,\mu\mathrm{m}$.

In the previous sections we have seen that CDRs exhibit several phenomena that are in accord with an active media description. So far the identity of the corresponding protein fields was not discussed. Clearly the protein field of f-actin forms a wave, as it is f-actin that leads to formation of cell undulations, which makes CDRs visible under the microscope. Nevertheless, this does not necessarily mean that actin constitutes one of the feedback loops for the propagation mechanism of CDRs.

The collision behaviour of CDRs is crucial for the understanding of the protein fields of the wave propagator. It strongly favours the hypothesis that there is an invisible protein field, which precedes the visible actin wave at a temporal distance of δt (Figure 4.12C). This protein field is responsible for the promotion of actin polymerization. It was shown that for the activity of Rho family GTPases in protruding lamellipodia there are typical distances and delay times between the activity of individual members of this family and the actual protrusion events [Machacek et al., 2009]. Even though the collision dynamics of CDRs implies a similar pattern, the characteristic delay time δt between visible actin wave and invisible wave of actin promoter unfortunately cannot be deducted from the data, as the regulatory field remains unknown and invisible at this stage.

4.6 Waves in the FHN System Resulting from Noisy Initial Conditions

In Section 3.3 of the previous chapter we shortly discussed the apparent paradox that there is a difference between the initial dynamics of spontaneously formed and induced CDRs. For the latter typically a pronounced ring appeared only some minutes after stimulation, whereas spontaneously formed CDRs originated from points and then formed outward growing, ring-shaped wavefronts. We will see in the following that this apparent contradiction follows naturally from the active medium description of CDRs. For this, a basic model for growth factor stimulation is presented.

Let us assume that the dorsal cell surface is covered with receptors and that towards the cell edge the density of these receptors decreases. Let us further assume that upon addition of growth factors to the cell medium a field of randomly occupied receptors results. Active receptors then trigger wave formation. We model this by a disc-shaped field of Gaussian-distributed random variables in a rectangular domain. Choosing the noise amplitude relatively high an above threshold situation results, at various positions on the cell. Figure 4.13 shows the outcomes of a simulation in which the disc-shaped region in the center of the medium was subject to a Gaussian noise at $t = 0$.

Due to the initial noisy stimulus wave seeds form from which small wavefronts emerge at numerous positions (Figure 4.13, $t = 1$). The high density of these wavefronts and their collision-annihilation behaviour leads to mutual extinguishing after a short time (Figure 4.13, $4 \leq t \leq 17$). This results in formation of an area that is completely in the refractory state (Figure 4.13, $t = 21$). Wave seeds that are situated at the boundary of the stimulated region can propagate freely outwards, as they do not meet other wave seeds in this direction. This results in a ring-shaped wavefront travelling away from the area that was the subject of stimulation (Figure 4.13, $21 \leq t \leq 45$).

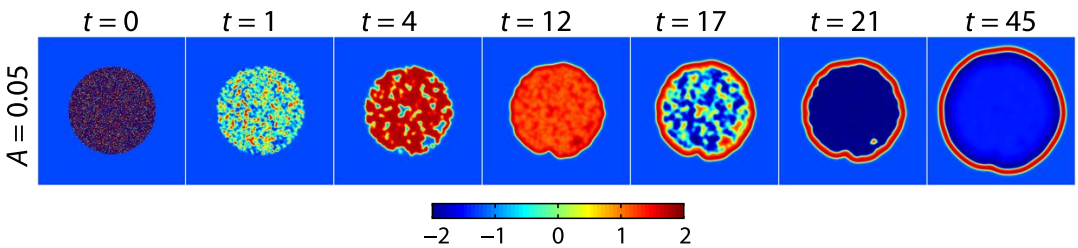

Figure 4.13: *Ring-shaped wavefronts originating from an area with noisy initial conditions.* Only the V-field is shown. Note that the noise pattern at $t = 0$ is too fine to be resolved by eye.

This result explains why there is no pronounced growth phase in which wavefronts originate from points after growth factor stimulation. In contrast to spontaneously formed CDRs, induced CDRs therefore appear directly as ring-shaped objects. The question remains why the initial dynamics of ring formation is not visible in experiments. An obvious explanation is that it requires a certain actin density and CDR height to be

detected by fluorescence and phase contrast respectively. In this case the initial wave seeds of stimulated CDRs would simply lack the time to grow into a visible wavefront before they mutually annihilate.

4.7 Discussion

The analysis of the wavefront dynamics in this chapter revealed that CDRs exhibit several phenomena known from waves in excitable systems. These phenomena were introduced based on the FHN system in the theory chapter of this thesis (Chapter 2). Features such as the emergence of spirals (Section 4.2) and the repeated formation of waves (Section 4.4) are novel for CDRs and have not been reported in the literature. This also holds true for the finding of mutual annihilation of colliding wavefronts (Section 4.5), which is a "signature of excitation waves" [Allard and Mogilner, 2013]. Together, these results provide evidence that CDRs indeed can be interpreted as waves in an active medium, as first proposed by Zeng et al [Zeng et al., 2011].

Given the fact that CDRs were known for a long time, it is surprising that this work is the first to show that CDRs clearly bear several hallmarks of waves in excitable systems. The reasons for this are twofold. Firstly, it was shown in this chapter that phenomena such as spiral waves and collision annihilation are relatively rare and where only exhibited by less than one percent of the cells. Their identification required an extensive search with the guided eye.

Secondly, and more importantly, all phenomena only occurred, because no growth factor stimulation was used in my experiments. It was already shown in the previous chapter that the use of growth factor stimulation largely hides the wave nature of CDRs, as stimulated CDRs appear as established rings without notable growth after PDGF treatment. This could be very well reproduced by the FHN system when a large area of space is excited simultaneously mimicking the effect growth factor stimulation (Section 4.6).

As a prototype system of an active medium, the FHN model is able to capture several basic traits of the phenomena observed for CDRs, among them concentrically growing wavefronts, oscillatory reappearing waves, annihilation events upon collisions, and the formation of spiral waves (sections 2.3.2-2.3.5). The details of these phenomena are, however, only partially correctly described by the FHN system. This is not surprising, as it is, by definition, a minimal model of an excitable system, which was chosen in this thesis for illustration of basic phenomena only for this exact reason of simplicity. The perpetual contrasting juxtaposition of features of CDRs that can and features of CDRs that cannot be captured by the FHN model gave us information on the nature of the processes that a realistic model for CDRs should include.

The collision behaviour of CDRs (Section 4.5) bears hints towards the nature of the protein fields involved in CDRs. The fact that wavefronts of colliding CDRs start to faint before they actually make contact strongly suggests that in the propagation

mechanism of CDRs actin is not the dominant autocatalytic element, but another protein field that precedes the visible wave of polymerized actin. The identity of this protein remains unclear at this stage. However, the identification of the dorsal cell membrane as the compartment of actin polymerization in Chapter 3 suggests that CDRs follow a mechanism that is similar to those which have been proposed for actin waves in neutrophils [Weiner et al., 2007, Doubrovinski and Kruse, 2008]. In these models the autocatalytic feedback is mediated by a nucleation-promoting factor of actin, which has been associated with Hem-1 of the WAVE complex [Weiner et al., 2007].

The results of this chapter indicate that interaction of waves with the cell boundaries and the nucleus have large impact on the wavefront dynamics. Fibroblasts are random-shaped which means that CDRs can, depending on the local cell geometry at the point of CDR creation, exhibit drastically different dynamics. The characteristic features comprise small pulsating structures in narrow regions and formation of pronounced wavefronts of a characteristic, size-dependent dynamics on large regions. "Narrow" and "large" are to be understood relative to the typical thickness of wavefronts. "Narrow" therefore means on the order of 10 µm which is twice the typical wavefront thickness (Section 4.4). "Large" regions, in contrast, have diameters that are considerably larger than the width of CDR wavefronts (sections 4.1-4.3). However, in most cases the diameter of the areas available for CDR propagation, bounded by cell edge and nucleus, exceeded the width of wavefronts by only one order of magnitude. We can therefore assume that typically the boundaries play a dominant role for the dynamics of CDRs. As a striking exception spiral waves were only found on relatively large areas where we can expect relatively mild impact of the boundary effects (Section 4.2). The central role of the cell boundary was further drastically illustrated by the propagation reversal of wavefronts and the stalling of wavefronts at this position.

Another contribution that presumably largely influences CDR dynamics is the non-homogeneous distribution of proteins in the cell. We have seen that, e.g., the distribution of f-actin inside of cells is non-uniform (Section 3.2), and that places of f-actin gradients correlate with distorted wave dynamics. The cell nucleus is the most prominent example for this. However, also the stalling of wavefronts at edges goes in hand with formation of strong actin gradients, which points to a potential cross-talk between boundary effects and protein distributions. This is not surprising as this constitutes a form of protein compartmentalization, which is fundamental in cell organization [Alberts et al., 2005, 527 pp]. In systems of pattern formation non-homogeneous media are known, not surprisingly, to give rise to more complex patterns than homogeneous systems [Page et al., 2005].

The dynamic data of CDRs gave hints towards large impact of limited availability of a central species of the wave machinery. The corresponding results were in particular the universal dynamics of propagation velocity as a function of the relative CDR size (Section 4.1) and the pronounced depletion of f-actin behind stalled CDRs (Section 4.3).

The dominance of limiting effects and boundary interactions on the dynamics of CDRs offers an explanation for the paradox that we do find local wavefront curvature and velocity uncorrelated in general, while we observe spiral wavefronts in rare cases - the latter being a clear indicator for the existence of an eikonal relation.

Limited availability of one of the protein species of a wave-supporting system is considered in several models for actin waves [Doubrovinski and Kruse, 2008, Khamviwath et al., 2013, Wasnik and Mukhopadhyay, 2014]. The modelling work by Edelstein-Keshet et al. explicitly illustrates the effects of limited protein availability on the wavefront dynamics. The limited resource is suggested to be a member of the Rho family of GTPases, which cycles between an active and an inactive state [Mori et al., 2008, Holmes et al., 2012, Mata et al., 2013]. Further, a model variant dedicated to actin waves considers a negative feedback that f-actin has on the state of the GTPase, which is responsible for its polymerization [Holmes et al., 2012, Mata et al., 2013]. The resulting wave dynamics exhibits phenomena such as temporally symmetric wavefront reversal at boundaries and wave pinning, which were also found to occur for CDRs in this chapter. The mechanism of wave pinning in the model depends on three conditions, which are: (*i*) conserved mass and no flux boundary conditions, (*ii*) a spatial uniformity of the GTPase in its inactive state, and (*iii*) a bistable reaction scheme. The second requirement is naturally met by the fact that the active state of Rho GTPases usually corresponds to a membrane bound state and the inactive one to a cytosolic state, which results in fast diffusion of the inactive form.

With the prerequisites for wave pinning in the model by Keshet et al., its actual mechanism results from the depletion of the pool of Rho GTPase of inactive state upon wave propagation. This affects the reaction rate towards the corresponding active state until an equilibrium point between forward and reverse reaction is reached, which stops the further propagation of the wave [Mori et al., 2008].

The third premise for wave pinning as suggested by Edelstein-Keshet et al. stands in contrast to the version of the FHN system that was considered in this thesis, as it was not parametrized for bistability. CDRs, however, involve a feature that reminds of bistability, i.e., the state of f-actin inside (depleted) and outside (organized cytoskeleton) of CDRs, which was shown in Chapter 3. In the same chapter it was hypothesized that the dynamics of PIP or Arap1 could constitute a two-state element in the protein dynamics of CDRs. It will be a future challenge to understand the reasons underlying this polarity in detail.

In summary, the work by Edelstein-Keshet et al. shows that the consequences of the limited availability of one species cover several of the phenomena one can observe in CDR data. These are namely: (*i*) the growth limitations of CDRs, (*ii*) the stalling of wavefronts, (*iii*) and depletion phenomena behind stalled wavefronts. Further, the model also explains the reversal of wavefronts at boundaries. Thus, a future model for CDRs should include conserved protein dynamics. Moreover, the role of bistability should be investigated in more detail.

Considering the large impact of the cellular morphology on wave dynamics it is

highly favourable to gain control over the cell geometry. Indeed, this approach has recently been applied to *D. discoideum* via electric-pulse-induced cell fusion resulting in giant cells [Gerhardt et al., 2014]. On these, actin waves had velocities that were undiminished from boundary effects. We will see in the next chapter that an alternative approach for reduction of boundary effects is given by cell shape control via microcontact printing. Especially this approach will permit us to discuss the collision behaviour of waves in more detail; we will see that the mutual annihilation upon CDR collision is not a strict rule. Further, an interpretation of the biological meaning of the recovery time between succeeding CDR events will come into reach.

Chapter 5

Wave Dynamics on Disc-Shaped Cells

The results of the preceding chapter suggest that CDRs follow a highly regulated mechanism and that they can be described as waves in an active medium. The range of phenomena found provided valuable insights into the nature of the constituting wave machinery. However, it also limited the analysis of CDR dynamics to a mainly qualitative level. The main reason for this is that the random cell shapes of fibroblasts lead to manifold appearances of CDRs due to the impact that the cell morphology has on CDR dynamics. This resulted in drastic variations between the dynamics of individual wave events and the consequence that a direct comparability between data of individual cells was not given. Even worse, as highlighted in Section 3.1.1, cells typically underwent changes of their morphology within the lifetime of CDRs. The time scale of the dynamics of cell morphology and of CDRs dynamics is thereby identical. Therefore, cells of uncontrolled, dynamically changing random morphologies constitute a poorly defined system for quantitative and reproducible data.

Inspired by observations of greatly reduced complexity of CDR dynamics on cells that coincidentally happened to have disc-like morphologies (Figure 5.1), I incorporated microcontact printing to overcome the difficulties described above (see Section 8.4 for details). To achieve the highest possible symmetry I decided to force cells into the shape of discs by seeding them on accordingly shaped patches of fibronectin. On theses substrates cells kept disc morphologies for several hours. Only the activity of the lamellipodium lead to slight morphological fluctuations around the cell periphery. The nucleus of disc-shaped cells located at the cell center and the actin cytoskeleton homogenized, reflecting the symmetry of the cell. Figure 5.2 shows these two features based on a comparison between a random-shaped and a disc-shaped cell. Even though we focus here on the actin cytoskeleton, the distribution of other cytoskeletal proteins in cells is known to symmetrize with the cell shape as well [Théry et al., 2006].

Also on disc-shaped cells CDRs avoided the cell nucleus. They formed and propagated in the ring-shaped zone between cell edge and cell nucleus. Compared to the situation

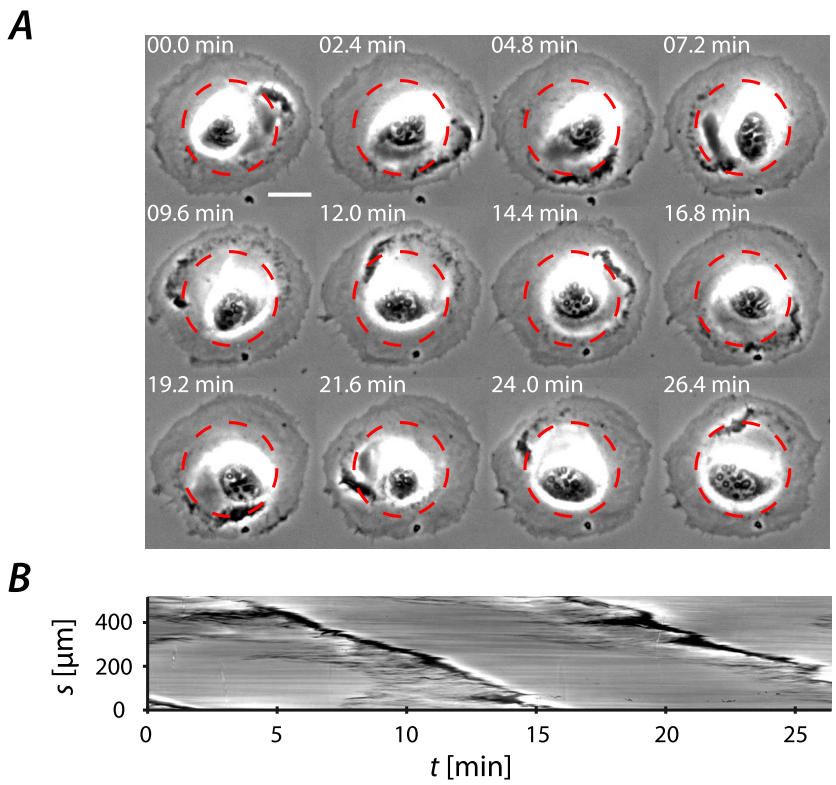

Figure 5.1: *Naturally disc-shaped cell exhibiting lateral CDR propagation.* *A*: Time-lapse sequence showing almost two full rotations of a CDR. Red circles denote the position where the circular kymograph (*B*) was sampled. *B*: Lateral CDR movement leaves stripe signatures in the kymograph, indicating roughly constant propagation velocity. NIH 3T3 X2 cell, no stimulation, scale bar: $25\,\mu\mathrm{m}$.

on random-shaped cells, where CDRs usually grew and then reversed upon approach of the cell edge, on disc-shaped cells CDRs could propagate undisturbed laterally due to the periodic boundary conditions in this dimension. Their velocities remained constant and they typically exhibited periodic cycles of repeated formations. Combined, the one-dimensional propagation of CDRs in lateral direction and the fact that cells on fibronectin patches are immobile, greatly simplify the visualization of CDR dynamics, which can be achieved via circular kymographs. These kymographs contain all information of the wave dynamics including: the propagation velocities, creation and extinction events, the periods between successive waves, and the number of CDRs present on a cell at the same time as well as their interaction events. Due to the uniform shape and size of cells in experiments with microcontact printing, the data of individual cells can be directly compared. Further, the one-dimensional propagation on a medium with periodic boundary conditions provides a very suitable basis for modelling approaches and fosters the direct comparability of simulations and experiments. This will be demonstrated in

Chapter 6.

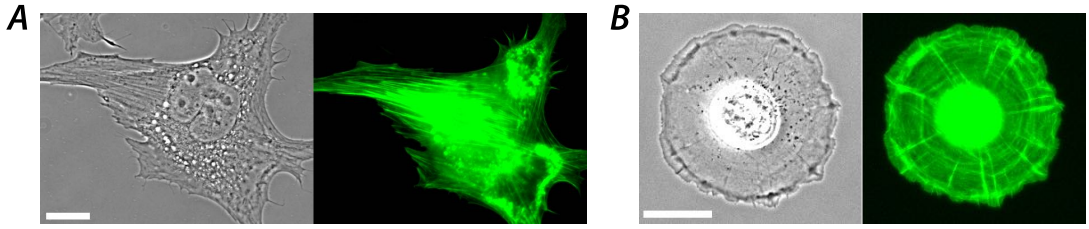

Figure 5.2: *Symmetry of disc-shaped cells.* The left side of each panel is a phase contrast micrograph, the right side a fluorescence image. *A*: random-shaped NIH 3T3 X2 cell exhibiting typical fibroblast morphology, *B*: disc-shaped NIH 3T3 WT cell. F-actin was stained with pLifeAct-TagGFP2. Scale bars: 25 µm.

In the following a method of analysis is introduced and then applied to a large data set to quantify the characteristic dynamics of CDRs on disc-shaped cells. Based on the dynamic data the spatiotemporal wave patterns in circular kymographs are discussed and the governing mechanisms underlying pattern formation are identified. The system for studies of CDRs introduced above is then used to analyse the role that actin plays in the wave mechanism underlying CDRs via experiments with the actin drug Latrunculin A. In the last section (Section 5.7) the results are summarized and referred to the current scientific context. Further, this final section motivates the last results chapter (Chapter 6), which is exclusively dedicated to the interpretation of the data of this chapter using the FHN system as a basic prototype model of an active medium.

5.1 Characteristic Dynamics on Disc-Shaped Cells

Disc-shaped protein patches with a radius of 31 µm were most suited for experiments, meaning that on these a large number of cells obtained disc-shapes with a ring-shaped area allowing lateral CDR propagation. In contrast, on larger substrates cells would often not occupy the entire patch of fibronectin, resulting in non-disc shapes, whereas on smaller substrates the nuclei often extended almost to the cell edge, leaving no space for CDRs to form. Therefore, all experiments described in the following were carried out with cells on fibronectin discs with a radius of 31 µm, unless explicitly stated otherwise. A detailed description of the experimental setup and procedures is given in Section 8.7.3 in the chapter dealing with materials and methods.

The geometry of disc-shaped cells was such that they entirely covered the underlying fibronectin patch, only slightly overlapping its area with their lamellipodia (Figure 5.3*A* & *B*). The cell nucleus typically extended from one third up to half of the cell radius so that a ring with a width of $15 - 20\,\mu\text{m}$ was available for CDR propagation. Therefore CDRs were restricted to relatively small diameters and, correspondingly, often appeared as phase-dark spots rather than fully developed rings (Figure 5.3*B*). The morphology of

CDRs on disc-shaped cells therefore resembled that of the breathing modes described in Section 4.4. Similar to the latter, in some cases CDRs did not propagate albeit exhibiting oscillatory reappearance. We will see later that in other cases CDRs had open morphologies that resembled half-moon shapes in which the open side was oriented in propagation direction (Figure 5.10).

Interestingly, CDRs on disc-shaped cells formed spontaneously on NIH 3T3 WT cells without external growth factor stimulation, whereas this cell line only rarely exhibited CDRs when grown on unstructured substrates, i.e., when having random-shaped, normal fibroblast morphology. All experiments in the following course of this chapter were performed on NIH 3T3 WT cells. When disc-shaped cells were treated with PDGF most of them developed lamellipodia protrusions, but no CDRs. In contrast, for normal-shaped fibroblasts CDR formation is the common response to PDGF stimulation. In the few cases when disc-shaped cells responded to PDGF the corresponding CDRs had the same morphology and dynamics as spontaneously formed CDRs (Appendix, Section 9.1). The reason for the moderate response of disc-like cells to PDGF in terms of CDR formation is not entirely clear. It might, however, be understood on the basis of the results in Section 4.6, in which the FHN model was used to demonstrate the effect of simultaneous stimulation of large parts of the cell surface as a consequence of PDGF exposure. Due to the periodic boundary conditions on disc-shaped cells the numerous CDR precursors emerging as a consequence of stimulation might completely annihilate each other and thus do not form pronounced CDRs.

The centres of the circular ROIs for sampling of kymographs were aligned with the cell nucleus and the cell edge. Their radii were chosen to intersect with the centres of propagating CDRs (Figure 5.3*B* & *C*). In the following the dynamics of CDRs on disc-shaped cells and the corresponding characteristic features in circular kymographs (hereafter termed "kymographs" for simplicity) are discussed based on the example in Figure 5.3.

CDR formation on disc-shaped cells was followed by their splitting, leading to bidirectional lateral propagation of two wave pulses. In other cases the propagation was unidirectional, i.e., a coherent propagation of one single CDR. In kymographs such as, e.g., Figure 5.3*D* bidirectional propagation of CDRs has a characteristic signature of "<"-shaped structures, whereas unidirectional propagation leads to "/"- or "\"-shaped signatures (green arrows in Figure 5.3*D*).

In most cases cells exhibited high rates of CDR formation leading to frequent collision events. Predominantly, collisions lead to mutual wave annihilations, which have ">"-shaped signatures in kymographs (solid red arrow in Figure 5.3*D*). However, also one-sided annihilations were observed, corresponding to "λ"- or "Y"-signatures (hollow red arrow in Figure 5.3*D*).

Due to the periodic boundary conditions bidirectionally propagating CDRs, which originated from the same spot, collided with their respective twin-pulses, provided that they were the only CDRs present on the cell. Due to the constant propagation velocity each of the pulses travelled half of the full arc length around the nucleus

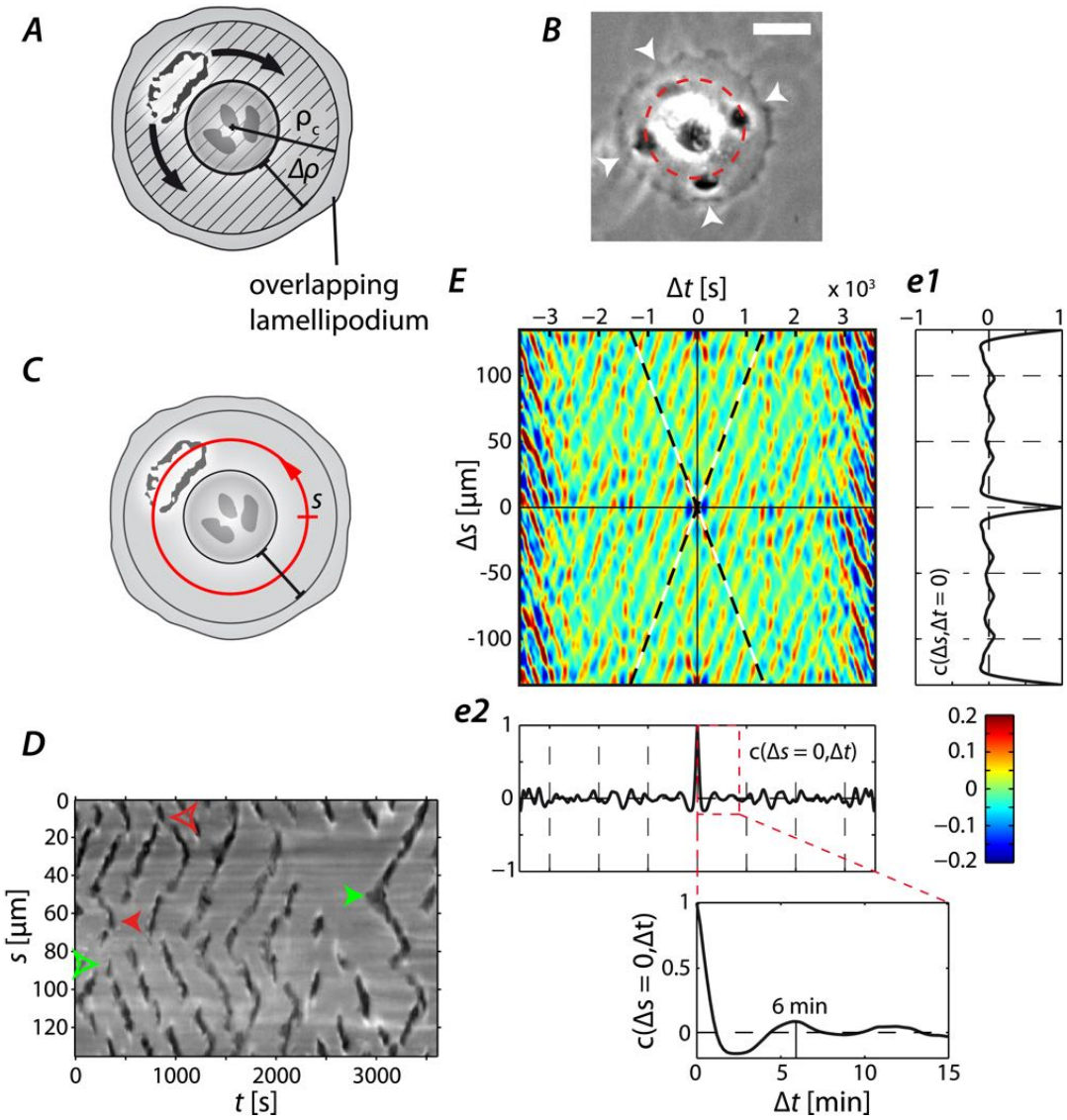

Figure 5.3: *CDR dynamics on disc-shaped cells.* *A*: CDRs propagate laterally around the nucleus within a ring of width $\Delta\rho$ between nucleus and the edge of the underlying fibronectin patch of radius ρ_c (patch: shaded region). *B*: A cell exhibiting four CDRs (highlighted by white arrows, scale bar: $25\,\mu\mathrm{m}$). *C*: Circular kymographs are assembled from intensity values along the arc length s of a circle situated in the middle of the lateral propagation zone (red solid line). *D*: Circular kymograph, sampled along the red dashed line in *B*. The green arrows highlight wave creation events, that are either followed by bilateral propagation (solid arrow, "<"-signatures), or unilateral propagation (hollow arrow, "/"- or "\"-signatures). Red arrows mark wave annihilation events (solid: mutual, ">"-signatures. Hollow: one-sided, "λ"- or "Y"-signatures). *E*: Autocorrelation function $c(\Delta s, \Delta t)$ of kymograph *D* with cuts at constant lag of arc length $\Delta t = 0$ (*e1*) and time $\Delta s = 0$ (*e2*). The slope of the black and white dashed lines in *E* corresponds to the propagation velocity. The close-up in *e2* shows the dominant period of $6\,\mathrm{min}$.

before the collision occurred polar opposite of their place of origin. The kymograph in Figure 5.3*D* does not show such an event, but we will investigate this case in more detail in Section 5.4.

The quantification of velocities and periods in kymographs was based on the calculation of two-dimensional autocorrelation functions $c(\Delta s, \Delta t)$. A detailed description of the data analysis is given in the sections 8.9.7 & 8.9.8. In short, kymographs were binarized such that the wave events corresponded to a value of one and the background to a value of zero. Visualized as two-dimensional black/white plots the wave signatures corresponded to white stripes on a black background. With the binarization, information about phase contrast intensity were discarded, which was necessary to prevent undefined input from the non-linear contrast formation underlying phase contrast microscopy into autocorrelation functions. The binarized kymographs were then used to calculate autocorrelation functions (Figure 5.3*E*). The regular wave patterns in kymographs lead to sequences of stripe signatures in autocorrelation functions. The slope of the stripe going through the origin $(\Delta s, \Delta t) = (0, 0)$ corresponds to the characteristic velocity of the kymograph. The slope was quantified via Radon transformation of autocorrelation functions (see Section 8.9.8 for details). In the example shown in Figure 5.3*E* this analysis revealed a propagation velocity of $0.10\,\mu\mathrm{m\,s^{-1}}$.

The cuts $c(\Delta s = 0, \Delta t)$ and $c(\Delta s, \Delta t = 0)$ reveal information about the spatiotemporal patterns in kymographs. The period between successive wave formations can be read off from the cut $c(\Delta s = 0, \Delta t)$ (Figure 5.3*e2*). In the example shown, the first side-peak flanking the central maximum of the autocorrelation function is situated at $\Delta t = 6\,\mathrm{min}$.

The cut $c(\Delta s, \Delta t = 0)$ bears information on the dominant spacing between CDRs that are present on the cell at the same time. In the example Figure 5.3*e1* a dominant number of four CDRs exists simultaneously, reflected by the four peaks in the autocorrelation function. However, since the spacing between "<" shaped structures is constantly changing and autocorrelation functions have averaging properties, the peaks in Figure 5.3*e1* are relatively weak.

In the following an overview about the characteristic dynamics of CDRs is given based on the application of the analyses introduced above on an ensembles of cells. Cells were monitored in microfluidic channels at zero flow, as outlined in detail in Section 8.7.3. Closed chambers were used to ensure constant physiological conditions as cells in open containers exhibited temporally varying wave dynamics (Appendix, Section 9.3). From the time-lapse sequences of individual cells subsequences of 30 min duration were cropped out and treated as independent samples. Below we discuss characteristics of wave velocities, periods between wave formations, and CDR interaction patterns. Each of these is treated in separate sections, starting with one on the velocity of CDRs.

5.2 Wave Velocities

On random-shaped cells the velocity of wavefronts roughly followed a parabolic evolution as a function of the CDR mean radius (Section 4.1). This dynamic nature of the wavefront velocity hindered a detailed analysis and the comparability of data from different cells. In contrast, CDRs on disc-shaped cells had constant propagation velocities whose distributions can be analysed systematically.

For a quantification of propagation velocities ROIs from kymographs of individual cells were cropped out, binarized and analysed via autocorrelation functions and Radon transformations as described above. The temporal length of all ROIs was 30 min and only those containing travelling CDRs were selected. The resulting ensemble of 189 ROIs yielded the distribution of velocities plotted as a histogram in Figure 5.4. The data follow a Gaussian distribution with a mean value of $0.14\,\mu\mathrm{m\,s^{-1}}$ and a standard deviation of $0.03\,\mu\mathrm{m\,s^{-1}}$.

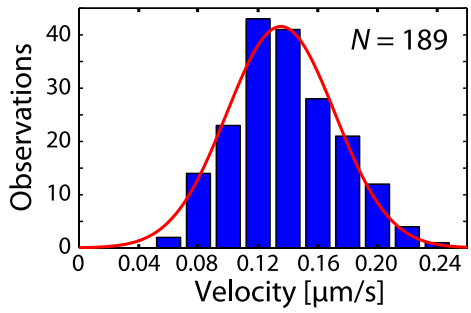

Figure 5.4: *Ensemble velocity histogram.* The red curve is a Gaussian fit to the distribution, yielding the mean value of $0.14\,\mu\mathrm{m\,s^{-1}}$ and the standard deviation $0.03\,\mu\mathrm{m\,s^{-1}}$.

The ensembles' mean value agrees very well with the velocity of CDRs on random-shaped cells directly after their formation, which was found to be $0.13\,\mu\mathrm{m\,s^{-1}}$ in Section 4.1. Indeed, also the sizes of CDRs on disc-shaped cells and on random-shaped cells directly after formation are comparable.

In Section 4.1 we discussed the potential role of a limiting resource as the cause for the typical dynamics of fast initial growth of CDRs that then decelerate and reverse on random-shaped cells. On disc-shaped cells the size of CDRs is constrained and, thus, the amount of proteins and membrane area needed to form and sustain a CDR is invariant under their propagation, because it is limited to mere translation. The same geometrical constraint also leads to constant curvature of CDRs on disc-shaped cells. Therefore, the constant propagation velocity on these cells is in line with the hypothesis of both, the existence of an eikonal relation and the impact of a limited species.

Interactions in form of wave annihilations were common on disc-shaped cells with high rates of CDR formation. This led to fragmented wave patterns, a feature that will be investigated in detail in Section 5.4. However, fragmentation also occurred

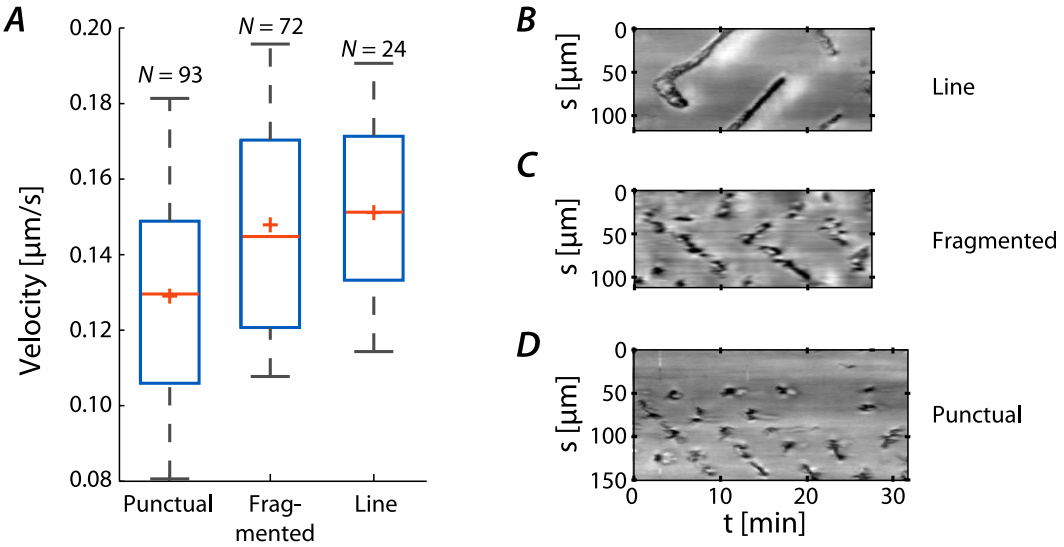

Figure 5.5: *Velocity distribution as a function of pattern type. A*: Box and whisker plot of the velocity distributions of different pattern types *B-D* (box and whisker plot legend: page xiv). The N-values denote the number of observations. *B-D*: Typical examples of each pattern type. The bright regions behind stripes (*B* & *C*) originate from the halo of the cell nucleus that slightly moved with CDRs.

without noticeable interaction. To check for a potential correlation between the degree of fragmentation and the wave velocities, the data underlying the distribution plotted in Figure 5.4 were grouped into three different classes. Kymographs in which wave pulses were visible as long and uninterrupted signatures ("line patterns") formed one group. Interrupted signatures that, however, clearly followed stripe patterns ("fragmented lines") constituted another class. The third group contained patterns in which mainly isolated signatures could be found that often had no extension that would allow to read off slopes reliably, but that had clear correlations of positions of appearance in kymographs. We term the latter "punctual patterns" thereafter. The velocity data for each group were then visualized in form of box and whisker plots. Figure 5.5 shows this plot (A) together with one typical example for each of the three groups of pattern types (B-D). All three histograms of the different patterns were nearly Gaussian-distributed and had comparable standard deviations (reflected by the symmetry and size of the boxes in Figure 5.5A). The characteristic values of the distributions are shown in Table 5.1.

The mean values of velocity of punctual and fragmented patterns are statistically significantly different (t-test, means not identical with a probability of >99.9%), whereas those of line and fragmented patterns are not significantly different (t-test, probability of a type one error of assumption of identical means: 65%).

The analysis presented above is only half-quantitative, as it relies on a visual classification of patterns. Especially, fragmented and line patterns might not in all

Pattern	$\bar{v}$ [µm s^{-1}]	std(v) [µm s^{-1}]	std(v)/$\sqrt{N}$ [µm s^{-1}]
punctual	0.129	0.033	0.003
fragmented	0.148	0.034	0.004
line	0.151	0.028	0.006
line $\bigcup$ fragmented	0.149	0.033	0.003

Table 5.1: *Characteristic velocities of CDRs forming different pattern types.* Since type line and type fragmented are statistically not significantly different, the set union of the data sets line $\bigcup$ fragmented is introduced.

cases be well discriminable, which explains the overlapping velocity distributions. Thus, and based on the statistically not significant difference between the distributions, we will assume equality of fragmented and line patterns in the following. The resulting distribution (line $\bigcup$ fragmented) has a mean of $0.149 \pm 0.003\,\mu\mathrm{m\,s}^{-1}$ (mean $\pm$ SE).

Punctual wave patterns have clearly reduced wave velocities, which raises the question of the responsible mechanism. A close inspection of punctual patterns reveals that the individual events are situated at the intersection points of spatiotemporal cross grids. For illustration the pattern in Figure 5.5 was plotted again in Figure 5.6, overlaid with a corresponding cross grid in red. The parallel lines defining the grid have identical slopes for clockwise motion and for anticlockwise motion respectively. In contrast, the temporal spacing between lines were chosen judged by eye to give the best fit of the pattern and are not of equal period, violating the periodicity enforced by the periodic boundary conditions. The reasons why the punctual patterns do not follow a strict periodicity remains unclear at this stage. It might, however, be due to the striking feature that no signatures appear between $0 \leq s \leq 50\,\mu\mathrm{m}$.

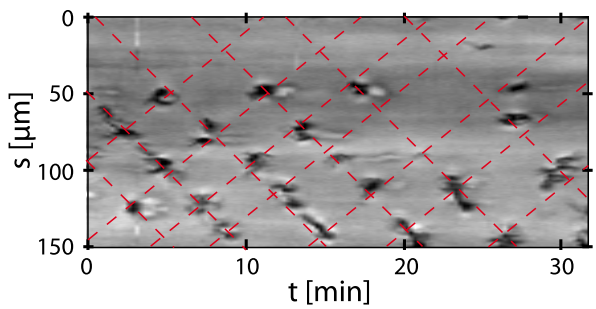

Figure 5.6: *Punctual patterns in kymograph defined by spatiotemporal grid points.* The grid has one slope for clockwise motion and one for anticlockwise motion. The temporal distance between individual lines was chosen to give the best fit as judged by eye.

It is an obvious idea that the correlation of individual events in punctual patterns results from the superposition of waves that run both in clockwise and anticlockwise direction around the cell. These hypothetical waves themselves are not visible in phase contrast, which means that they do not involve high amounts of f-actin. Only at the

intersections of two waves actin polymerisation is sufficient to form visible signatures. This result is pivoting as it suggests that wave annihilation, which is the dominant behaviour of colliding CDRs, does not occur in punctual wave patterns. Instead, waves seem to superimpose and then continue propagation undisturbed, as known from classical linear waves.

We will see in the following sections that wave patterns of CDRs in kymographs result from an interplay of the periodic boundary conditions, constant propagation velocities and characteristic time scales of CDRs on disc-shaped cells. These properties might lead to resonance-like phenomena causing fragmentation of wave patterns. A possible theoretical framework for the underlying mechanism is further given by the behaviour of active media in the presence of noise, which will be dealt with in detail in Section 6.

On random-shaped cells the wavefront velocity of CDRs was a highly dynamic variable and, thus, no single characteristic wave velocity could be stated. In contrast, on disc-shaped cells measurements of velocity were reproducible. With this, the propagation velocities of CDRs can be compared to the velocities of actin waves reported in other studies. We will first discuss the published studies on CDR velocities.

Interestingly, the issue of non-constant wave velocities of CDRs is not discussed in the literature. Instead, the work by Peleg et al. states characteristic values and also the work by Zeng et al. allows to deduce characteristic velocities from plots of CDR radius evolution. Peleg et al. measured the area of shrinking CDRs on living cells and calculated the average velocity from the temporal change of the mean radius with time. They report a mean value of $2.3 \pm 0.6\,\mu\mathrm{m\,s^{-1}}$ [Peleg et al., 2011]. Also Zeng et al. measured the CDR area as a function of time. However, their analysis was based on cells that were fixed subsequent to PDGF stimulation at different time intervals in different experiments. The plots in their work allow to read off velocities on the order of $0.1\,\mu\mathrm{m\,s^{-1}}$ for opening CDRs, whereas closing CDRs exhibit values of $0.03\,\mu\mathrm{m\,s^{-1}}$ [Zeng et al., 2011]. The values of the study by Zeng et al. and Peleg et al. clearly disagree. The reasons for this are not entirely clear. Based on the results of drastic variations of the wave velocities of CDRs on random-shaped cells, as presented in the sections 3.1.1 & 4.1, it is not surprising to find these variations also reflected by the values that are reported in the literature.

Further we have seen in Section 4.1 that the process of CDR closing often goes in hand with an instability and buckling. This process can indeed lead to apparent high velocities of CDR motion, which might have contributed to the high values measured by Peleg et al. In contrast, in the work by Zeng et al. averaged area data from non-living cells were plotted. Thus the velocity for closing CDRs might be affected by the non-uniform lifetimes of CDRs. In summary, the discrepancy shows that a measurement of the characteristic velocity of CDRs is hard to obtain on random-shaped cells. This underlines the advantages that an investigation of CDRs on disc-shaped cells bears.

CDRs are very likely formed by an excitable system of the reaction-diffusion kind, as we have seen in Chapter 4. For different types of actin waves, which are also assumed to

be formed by the same class of mechanisms, wave velocities on the order of $0.1\,\mu\mathrm{m\,s^{-1}}$ are common. Examples comprise the actin waves in *D. discoideum*, travelling with a velocity of $0.12\,\mu\mathrm{m\,s^{-1}}$ [Bretschneider et al., 2009], and in neutrophils, propagating with $0.06 - 0.08\,\mu\mathrm{m\,s^{-1}}$ [Weiner et al., 2007]. Also cells over expressing the actin factor caldesmon form actin waves of velocities of $0.17\,\mu\mathrm{m\,s^{-1}}$ [Grosheva et al., 2006].

Actin-driven waves that presumably involve contractile elements apparently tend to exhibit higher velocities than reaction-diffusion driven systems. For example, lateral membrane waves in different cell lines have values ranging from $0.1{-}0.4\,\mu\mathrm{m\,s^{-1}}$ [Döbereiner et al., 2006, Asano et al., 2009]. Furthermore curvature waves in migrating *D. discoideum* have velocities of $0.6\,\mu\mathrm{m\,s^{-1}}$ [Driscoll et al., 2012].

While the elastic properties of acto-myosin gels might contribute to the propagation velocities of systems with contractility, in reaction-diffusion systems the wave velocities are governed by the diffusion constants of the involved protein species and the reaction rates [Allard and Mogilner, 2013]. This explains the differences of wave velocities between reaction-diffusion dominated systems and systems involving contracitility and the similar values within the class of reaction-diffusion governed systems.

The similarity of wave velocities of reaction-diffusion type actin waves suggests that the same mechanisms are governing in these systems, e.g., the membrane-bound state of actin regulators, mediating their relatively low diffusion constants. It is important to note that also the net polymerization velocity of actin meshworks, as measured in protruding lamellipodia [Döbereiner et al., 2006] and on individual HAPs in this thesis (Section 3.1.2), is on the order of $0.1\,\mu\mathrm{m\,s^{-1}}$. The characteristic wave velocity of $0.1\,\mu\mathrm{m\,s^{-1}}$ is therefore also consistent with the idea that propagation by growing actin filaments critically contributes to the wave dynamics [Doubrovinski and Kruse, 2008, Whitelam et al., 2009, Carlsson, 2010]. We have, however, also seen in Section 3.1.2 and discussed in Section 3.3 that the motion of individual fan-shaped actin particles within CDR wavefronts exhibited no obvious correlations with the movement of the wavefront. Instead, the particles performed apparent random swarming motility patterns. Therefore it remains unclear at this stage whether advection-driven transport contributes to the propagation mechanism of CDRs.

5.3 Periodicity

For an analysis of the periods between successive wave formations the same experimental data set described in the previous section was analysed. ROIs of kymographs of a duration of 30 min that contained three or more CDR events were selected. This filtering scheme yielded a total number of 228 suitable ROIs. The data processing was based on autocorrelation functions as described above. Cuts of the autocorrelation functions at zero space lag $c(\Delta s = 0, \Delta t)$ were analysed with respect to the position of the first side maximum flanking the central peak at zero time lag. Figure 5.7 illustrates this based on a typical example.

Figure 5.8 shows the distribution of the periods of the complete data set. The

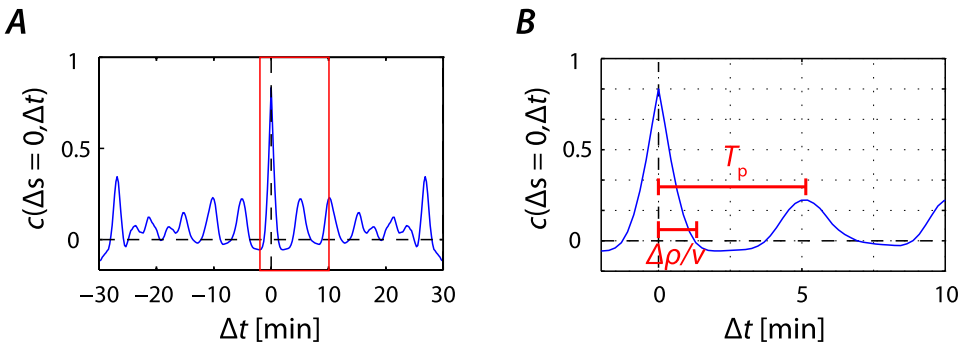

Figure 5.7: *Periods of CDR reappearance in autocorrelation functions.* *A*: Example of an autocorrelation function at zero space lag. *B*: Enlarged version of the ROI highlighted with a red rectangle in *A*. The characteristic period is $T_\mathrm{p} = 5.2\,\mathrm{min}$ in this example. The characteristic time that a CDR needs to travel its own diameter is $\Delta\rho/v$.

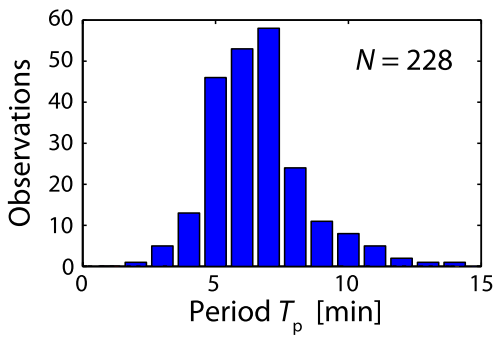

Figure 5.8: *Ensemble period histogram.*

plot reveals a striking peak for periods in the range from $5-7\,\mathrm{min}$. Values outside of this interval follow a relatively broad distribution. To interpret this finding we must consider that there are three potential causes for periodicity in the system, namely: events of wave re-entry, the recovery-time of the system, and the rate of spontaneous CDR formation.

The first of these, i.e., wave re-entry, is based on the periodic boundary condition of the system, which enables CDRs to re-enter a previously occupied position after one full rotation around the nucleus. The time a CDR takes to completely encircle the nucleus is

$$T_\mathrm{R} = \frac{S}{\bar{v}}, \tag{5.1}$$

where $\bar{v}$ is the characteristic CDR propagation velocity and S the circumference of the cell at position of the CDR (i.e., the circumference of the red circle in Figure 5.3*C*). With the typical dimensions of cells, as introduced in Section 5.1, and the mean velocity

from Figure 5.4 we find

$$T_{\mathrm{R}} = \frac{2\pi * 20\,\mu\mathrm{m}}{0.14\,\mu\mathrm{m\,s}^{-1}} = 15.0\,\mathrm{min}.$$

However, the distribution in Figure 5.8 has almost decayed to zero at $T_{\mathrm{P}} = 15\,\mathrm{min}$, which indicates that the direct contribution of the time scale of CDR re-entry is of minor importance and, thus, other process dominate the period distribution. Nevertheless, it is a striking feature that T_{R} closely matches the most frequent value of T_{P} in Figure 5.8 multiplied by two, which might cause one to think along the lines of resonance phenomena in the system.

The recovery time of the medium is the second contributor to the distribution of periods, as it sets a minimal temporal spacing between succeeding wave events. For its estimation we assume that the medium tends to form waves spontaneously at the maximal rate permitted by the recovery time. Then the recovery time is the duration of quiescence between succeeding wave events. Since CDRs have a spatial extension the period between successive wave formations and the recovery time of cells are related by

$$\tau = T_{\mathrm{p}} - \frac{\Delta\rho}{v}. \tag{5.2}$$

Here $\Delta\rho/v$ is the time it takes a CDR to cross its own diameter. In cuts of autocorrelation functions at constant space lag $c(\Delta s = 0, \Delta t)$, $\Delta\rho/v$ is the characteristic decay time of the central peak (Figure 5.7B). To read this time from autocorrelation functions requires a strict definition of its position. This is not possible without ambiguity, as the decay of the central peak depends on the gray value threshold that was used to binarize kymographs. In contrast, the position of the first side peak, which we chose here for definition of the period between wave events, is free from any influence of the segmentation threshold. Therefore, we use this quantity together with characteristic values for the other variables to estimate τ. From Figure 5.4 we choose the mean velocity of $\bar{v} = 0.14\,\mu\mathrm{m\,s}^{-1}$ and from Figure 5.8 the most frequent period of $T_{\mathrm{p}} = 7\,\mathrm{min}$. Since on microcontact printed substrates CDRs typically could obtain a diameter of $\Delta\rho = 18\,\mu\mathrm{m}$, equation (5.2) gives us an estimate of $\tau = 5\,\mathrm{min}$.

In Section 4.4 the recovery times of cells of random shapes were analysed. For CDRs of sizes ranging between $10 - 20\,\mu\mathrm{m}$, i.e., having comparable spatial extension as CDRs on disc-shaped cells, we found characteristic values between $2 - 3\,\mathrm{min}$. The recovery times of disc-shaped cells therefore exceed those of random-shaped cells, while being still of a similar magnitude. In the following we discuss this finding from two different perspectives.

At this stage we have to remember that the model system that served for experiments with random-shaped cells was the fibroblast line NIH 3T3 X2, whereas NIH 3T3 WT fibroblasts have been used for the experiments described in this chapter. NIH 3T3 X2s formed CDRs spontaneously under normal culture conditions, whereas this was only rarely observed for NIH 3T3 WTs (Section 3.1.1). We discussed in Section 4.4 that this might be due to a biochemical state of NIH 3T3 X2 cells that is inherently close to a

wave instability. The finding of different recovery times between NIH 3T3 WT and NIH 3T3 X2 cells might thus be explained by different positions that these two cell lines have in the phase space of the dynamic system.

There is also another possible explanation for the different recovery times found for random- and disc-shaped cells. The CDRs on random-shaped cells forming breathing modes, presented in Section 4.4, collapsed at the point of their origin, in contrast to CDRs on disc-shaped cells that only repeatedly propagated over the same position. CDRs store considerable amounts of actin, which is set free locally when they collapse. This local increase in actin concentration might facilitate a succeeding re-formation of a CDR, reflected by short recovery times. This event is absent for CDRs that propagate over the same region repeatedly on disc-shaped cells, which explains the relatively long recovery times. We will further discuss the nature of the recovery time in summary in the discussion section of this chapter (Section 5.7), as additional evidence of a critical role of actin availability will follow from experiments with Latruculin A (Section 5.6).

So far we have assumed that CDR formation occurred at the maximum possible rate allowed by the recovery time. Nevertheless, this cannot be always the case. Otherwise the distribution in Figure 5.8 would be much narrower and singular wave creation events, as shown in Figure 5.5*B*, would not be possible. A hypothetical explanation for the variations in rates of CDR formation is founded on the assumption of a stochastic process being involved in spontaneous CDR creation, an idea that was introduced in Section 4.4.

The rate at which this stochastic process exceeds a threshold leading to CDR formation is the third contributor to the distribution of the measured periods between CDR events. Unfortunately the stochastic process is beyond a direct experimental quantification. We will therefore investigate its role based on computer simulations in Chapter 6. It will turn out that the observed period distribution in Figure 5.8 can be well understood based on the assumption that the periodicity of CDR formations in cells of the sample is partially dominated by noise and partially by the recovery time of the system. The nature of the stochastic process will be examined in the discussion section of this chapter (Section 5.7).

5.4 Wave Interactions and Patterns in Kymographs

We have seen in the previous sections that both, the velocity of CDRs and the periods between their formations, follow certain distributions. In this section we will investigate the resulting spatiotemporal patterns in kymographs.

The periodic boundary conditions on disc-shaped cells have a special significance for the formation of wave patterns. Further, the number of CDRs that are present on one cell at the same time is a determinant of pattern formation. Indeed, this number can vary as illustrated in Figure 5.9. The frames of the different time-lapse sequences in this figure were chosen such that the CDRs are equally-spaced. Note that the number of

CDRs increases with cell size; the cells *A*-*C* were plated on disc patches of a radius of 31 µm and cells *D*-*E* on disc patches of a radius of 40 µm. As mentioned in Section 5.1, cells could extend over the adhesive protein patch by formation of lamellipodia, leading to slight variations in cell size even on substrates of identical sizes.

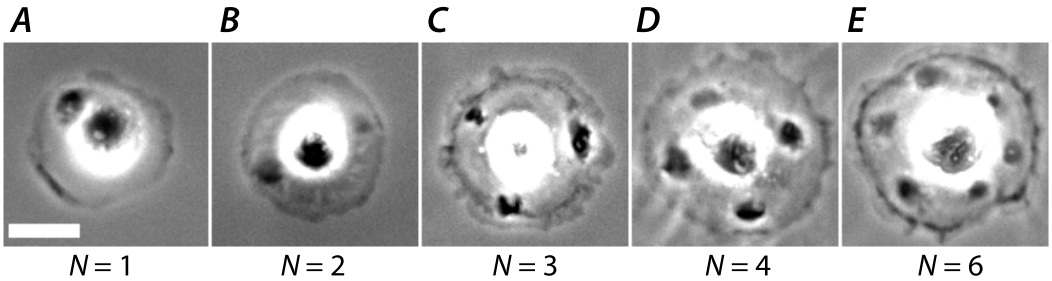

Figure 5.9: *Modes of CDR occupation.* Note that *A*-*E* are all non-identical cells. The radii of the underlying protein patches are *A*-*C*: 31 µm, *D*-*E*: 40 µm. Scale bar: 25 µm (valid for all micrographs).

To understand how the patterns in kymographs depend on the number of CDRs that are simultaneously present on one cell we proceed with some considerations regarding their states of movement. For this we consider CDRs as physical objects, rather than maxima in a concentration field, that annihilate upon collision.

Each CDR can travel in one of two possible directions, which is either clockwise (cw) or counter-clockwise (cc). We introduce the configuration $q = (n_{\mathrm{cw}}, n_{\mathrm{cc}})$ that indicates the number n of CDRs that travel in the two possible directions respectively. Since there are events of CDR formation and destruction these numbers are time-dependent. The total number of CDRs we denote with $N = n_{\mathrm{cw}} + n_{\mathrm{cc}}$.

The lifetime of a given configuration depends on the proportion between n_{cw} and n_{cc}. For each configuration there are two states of unidirectional propagation, i.e., $q = (N, 0)$ and $q = (0, N)$. Within the dynamics of these configurations no collisions between CDRs occur, which implies that these states could basically have infinite lifetimes. All other configurations include bidirectional CDR movements as their configurations are $q = (n_{\mathrm{cw}}, n_{\mathrm{cc}})$ with $n_{\mathrm{cw}}, n_{\mathrm{cc}} \neq 0$. For these configurations collisions and therefore annihilations occur, which restrict their lifetimes. Figure 5.10 illustrates the most basic cases of unidirectional and bidirectional configurations, i.e., cells with $q = (1, 0)$ (A), $q = (1, 1)$ (B), and $q = (2, 0)$ (C). The life course of a bidirectional state $q = (1, 1)$ is marked by formation of twin-CDRs that each encircle the nucleus in different directions and finally collide. Due to the symmetry in propagation velocity of both wave pulses CDR creation and destruction events take place at polar opposite positions of the cell (Figure 5.10B).

In fact, the lifetimes of unidirectional configurations are also limited, even though not by collision-annihilation. Empirically one finds that they rarely perform more than one full rotation around the nucleus before they decay spontaneously. The CDR life course

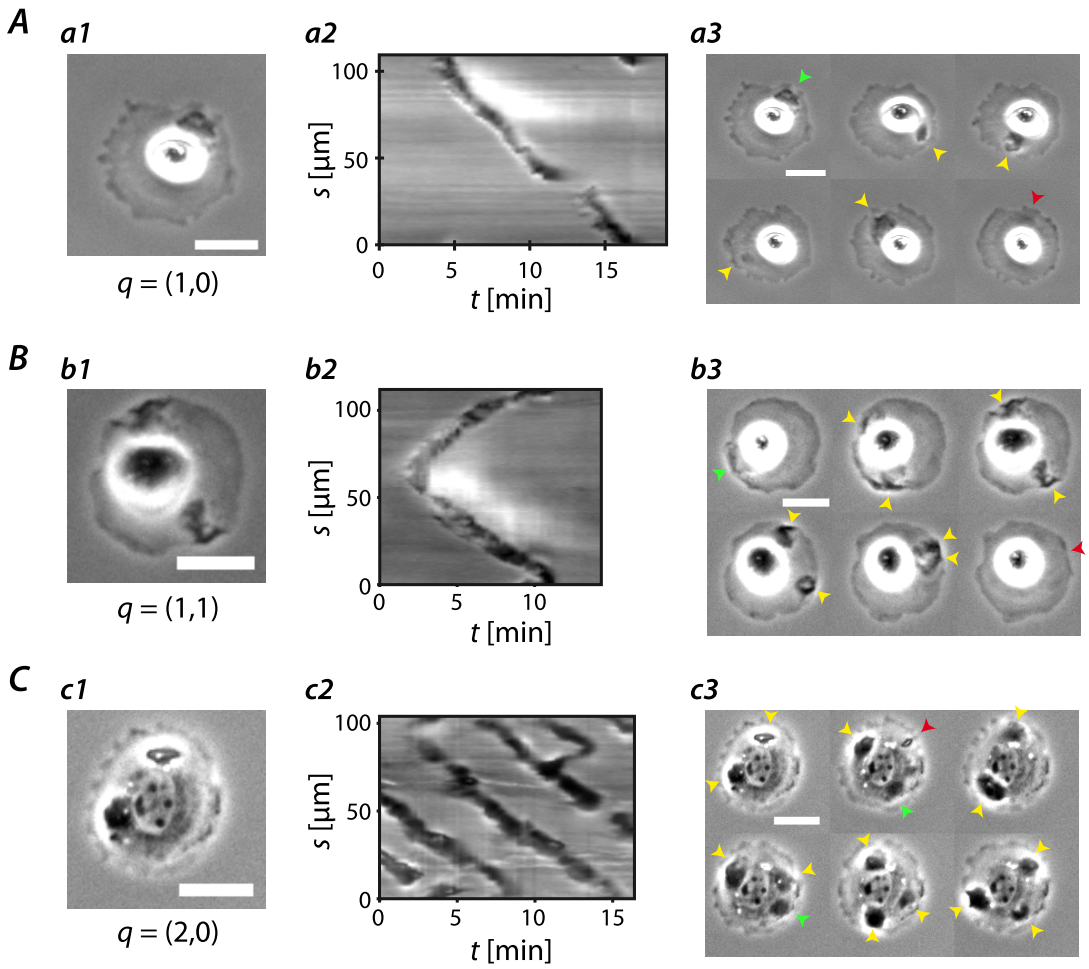

Figure 5.10: *Basic configurations of single and twofold CDR occupations.* Row *A*: A single CDR propagating clockwise. Row *B*: Bidirectional propagation of two CDRs leading to collision annihilation. Row *C*: Unidirectional propagation of predominantly two (at times three) CDRs in clockwise direction. Column *1* shows one still of the respective underlying image sequences, column *2* the kymographs and column *3* montages of frames. The time points in the latter are equidistant within each montage. Arrows indicate CDR positions. Green: creation events, yellow: propagation, red: extinction events. Scale bars: $25\,\mu\mathrm{m}$.

shown in Figure 5.10*A* is therefore a typical example. Thus the characteristic maximal CDR lifetime of unidirectional configurations is T_{R}, as introduced in equation (5.1). In contrast, bidirectional configurations have shorter lifetimes, because they only exist up to collision events that lead to transitions towards new configurations $q' = (n'_{\mathrm{cw}}, n'_{\mathrm{cc}})$ with $n'_{\mathrm{cw}} < n_{\mathrm{cw}}$ and $n'_{\mathrm{cc}} < n_{\mathrm{cc}}$. The average lifetimes of configurations with bidirectional propagation can be calculated based on the assumption of equally spaced initial CDR

positions. Their lifetime is then given by

$$\lambda(n_{\mathrm{cw}}, n_{\mathrm{cc}}) = \frac{T_{\mathrm{R}}}{2N} \qquad \text{where } n_{\mathrm{cw}}, n_{\mathrm{cc}} > 0, \tag{5.3}$$

i.e., the time that CDRs moving towards each other travel before they collide. Figure 5.11 illustrates different configurations for N ranging up to four. The positions of collisions annihilation are marked with red lines. The average lifetime $< \lambda >$ of all configurations for a given number of CDRs is then

$$\begin{aligned} < \lambda > (N) &= \frac{1}{Z} \sum_{i}^{Z} \lambda_i \\ &= \frac{1}{2^N} \left(2T_{\mathrm{R}} + (2^{N-1} - 1) \frac{T_{\mathrm{R}}}{N} \right). \end{aligned} \tag{5.4}$$

Here $Z = 2^N$ is the number of possible configurations. The first term in the second line of this equation accounts for the two unidirectional configurations that exist for each number of CDRs, whose lifetime we presume, like that of $q = (1, 0)$ and $q = (0, 1)$ configurations, to be T_{R}.

We further assume that the formation probability of each configuration is identical and that the impact of the rate of CDR formation on the distribution of lifetimes is small compared to that of the longest possible lifetime T_{R}. Then the distribution of the mean lifetimes is directly proportional to the probability distribution of the number of states $p(N)$.

The experimentally found probability distribution of the number of CDRs was calculated based on CDR counting in binarized kymographs (radii of fibronectin patches underlying cells: 31 µm). The distribution is plotted in Figure 5.12 together with its theoretical equivalent as given by equation (5.4). Both functions were normalized according to $\int_0^{10} < \lambda > (N) \mathrm{d}N = 1$.

The theoretical curve of equation (5.4) captures the basic trend of the data well. However, it only converges slowly towards zero with increasing CDR number, whereas the experimental data indicate that the distribution reaches zero at around $N = 7$. There are several effects that have not been covered so far explaining this discrepancy. Firstly, we neglected that some of the decay events of one configuration give rise to a new configuration with a smaller number of CDRs via transitions $q \to q'$ that should be included into the statistics. Further, there are finite size effects to be considered, as the spatial extension of CDRs typically only allows six CDRs to reside on one cell at once for the size of the substrates used in the experiments. For this we assumed that the typical diameter of CDRs is identical with their typical distance to the cell center. Further, the minimal recovery time of the active medium, $\tau = 2.7$ min, sets a minimal spacing between CDRs for stable propagation of the configuration. Assuming again equal spacing between CDRs, a maximum of $N = S/(\bar{v}\tau) = 6$ can simultaneously propagate on one cell.

We also did not consider the processes of de novo CDR formation or spontaneous CDR decay, which in fact also have large impact on the lifetime of CDR configuration. This is because each of these events creates a new configuration, which corresponds to the destruction of the previously existing one. The probability distribution found based on the multiplicity of states is therefore only valid for low rates of CDR formations and spontaneous decay rates, in which existing configurations are not too frequently destroyed.

Another reason for the deviation between the theoretical and the empirical distribution is that the computer routines for counting of CDRs in kymographs of experimental data are not able to correctly resolve the differences between propagating CDRs and CDR creation events. As CDRs have a finite extension two CDRs originating from the same spot would be counted as one CDR until a markable separation occurs. Figure 5.13 illustrates this problem based on two examples. The distribution of the data therefore has a slight bias towards smaller numbers.

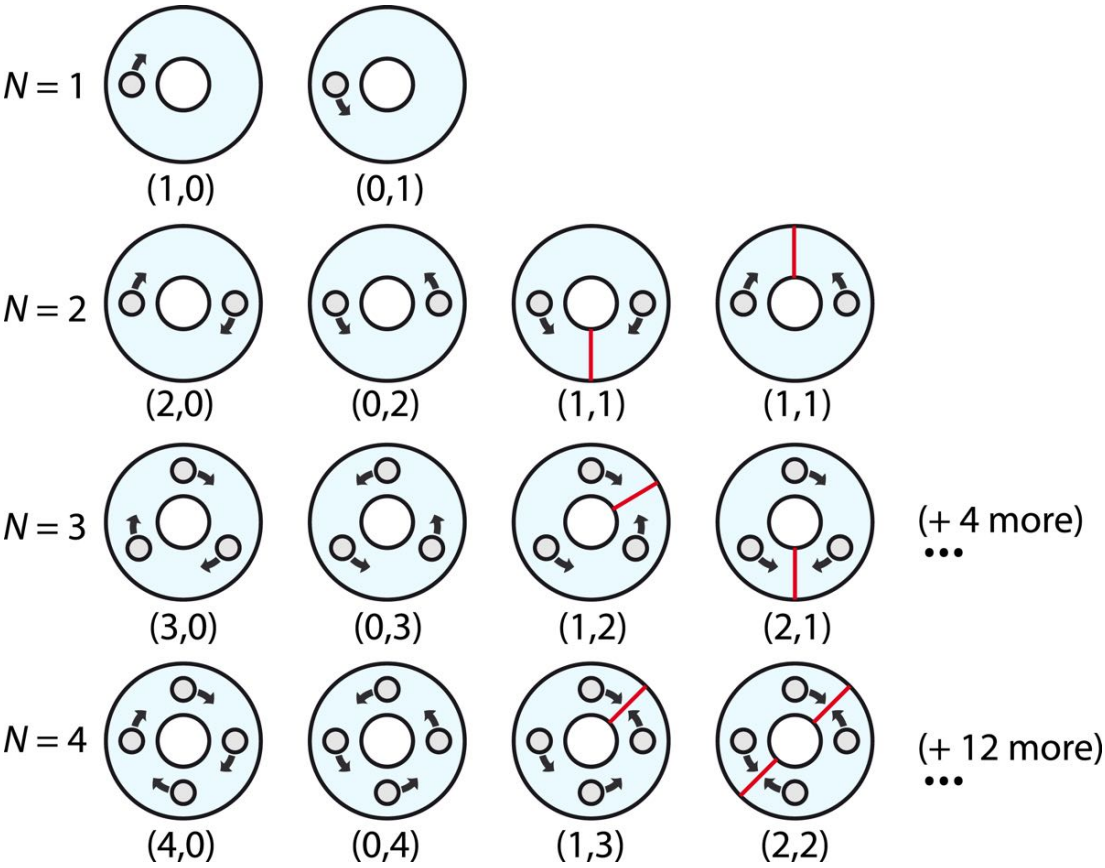

Figure 5.11: *Examples of configurations of CDR states of movement.* The terms in brackets denote the configuration $q = (n_{\mathsf{cw}}, n_{\mathsf{cc}})$. Red lines indicate the positions at which CDRs annihilate.

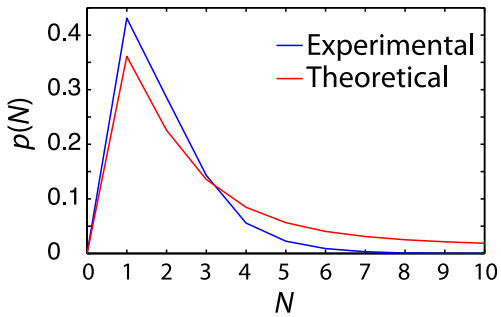

Figure 5.12: *Comparison of the theoretical and experimental probability densities of CDR occupation numbers.*

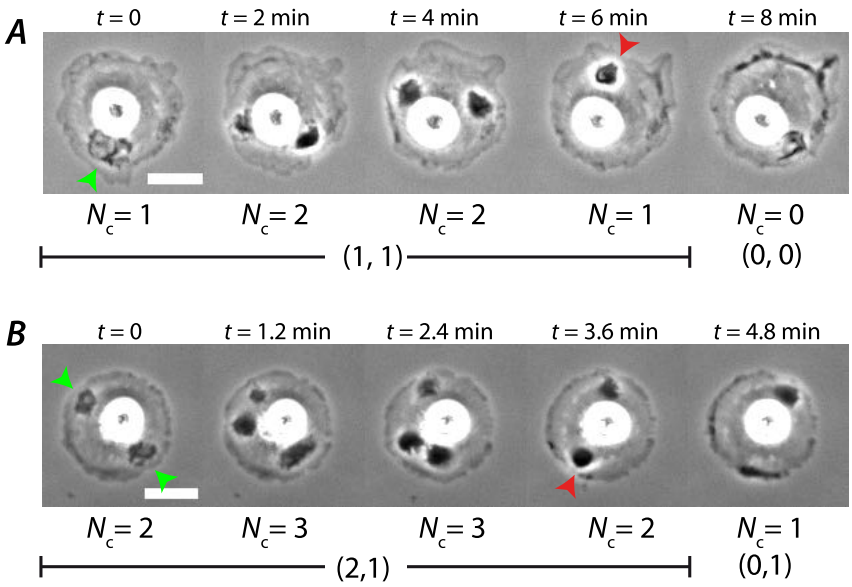

Figure 5.13: *Algorithm-induced bias in CDR counting.* Terms in brackets denote CDR configurations $q = (n_{\mathsf{cw}}, n_{\mathsf{cc}})$, N_{c} is the number of CDRs as counted by the algorithm, whereas the actual number is $N = n_{\mathsf{cw}} + n_{\mathsf{cc}}$. *A*: Bidirectional propagation of two CDRs. In the initial and the final state of CDR life courses only one CDR is counted by the algorithm, even though the events are a two-pulse CDR creation event (green arrow) and a collision annihilation event (red arrow), respectively. *B*: A similar example for a more complex pattern of a configuration of three CDRs. Scale bars: $25\,\mu\mathrm{m}$

So far we have focused on basic events of pattern formation in kymographs, i.e., CDR formation, propagation, and collision with mutual annihilation. We will see shortly that in fact also more complex processes can occur. We have, e.g., already seen in the introductory example in Figure 5.3*D*, in the beginning of this chapter, that wave

collision does not necessarily lead to mutual wave annihilation, as one-sided annihilation events could be found in this kymograph. This feature is unique to waves on disc-shaped cells, as colliding ring-shaped wavefronts on random-shaped cells were found to mutually annihilate (Section 4.5). For the discussion of more complex patterns we will study kymographs that include numerous repeated CDR formations in the following.

Figure 5.14 shows seven examples of kymographs obtained from cells on disc-shaped protein patches of different radii with a temporal length of typically more than 50 min. Indeed these kymographs include pronounced examples of basic configurations. For example, the kymographs C and D in Figure 5.14 exhibit phases of predominately unidirectional configurations ($q = (2, 0)$ in C between $t = 10 - 50\,\text{min}$, $q = (0, 5)$ in D between $t = 0 - 20\,\text{min}$). Also the kymographs A and B in Figure 5.14 include examples of the basic configuration $q = (1, 1)$, in which CDRs originate from one point, forming twin-pulses that each encircle the nucleus half before they collide with each other and annihilate polar opposite of their point of origin. This type of pattern element is therefore similar to those in Figure 5.10B and 5.13A. Single creation and destruction events are marked with green and red arrows in Figure 5.14 respectively.

However, as the first mark of a more complex element of pattern formation the point of CDR origin in Figure 5.14B stays the same for multiple CDR formations (”<<<-shaped signature”). This behaviour can be attributed to the existence of a refractive footprint that waves leave in excitable systems. This will be demonstrated and discussed in Chapter 6 based on numerical solutions of a noisy FHN system.

Regarding the collision behaviour of CDRs we find three different types of signatures in the kymographs in Figure 5.14. These are: mutual annihilation (solid red arrows, ”>”-signatures), one-sided annihilation (hollow red arrows, ”λ”- or ”$\curlyvee$”-signatures), and wave crossing (yellow arrows, ”X”-signatures). A classification and counting of wave collision events revealed that in 80% of the cases they led to mutual annihilations, while in the remaining 20% at least one of the two pulses survived the collision.

Wave crossing events only occur for CDRs of weak phase contrast. In fact, several of the kymographs in Figure 5.14 show long-range correlation of visible wave signatures that persist or reappear even after apparent collision annihilation events (especially well-visible in Figure 5.14D). In contrast, the signatures in Figure 5.14E lack visible collision events, but still seem to interact and re-appear spatiotemporally correlated, which leads to highly fragmented patterns. We have seen in Figure 5.6 that also the opposite was found: waves that only form visible phase contrast at their intersection points.

At this stage we have to keep in mind that our previous assumption of the mechanisms of CDR interactions as those of physical objects is not realistic, and was only introduced for a basic understanding of the mechanisms of pattern formation. In fact, CDRs are maxima in concentration fields that, most likely, follow a dynamics governed by non-linear reaction terms. Their interactions can therefore be caused by very slight variations in concentrations that cannot be visualized by phase contrast microscopy. Therefore we cannot assume that kymographs reliably reveal the true concentration in

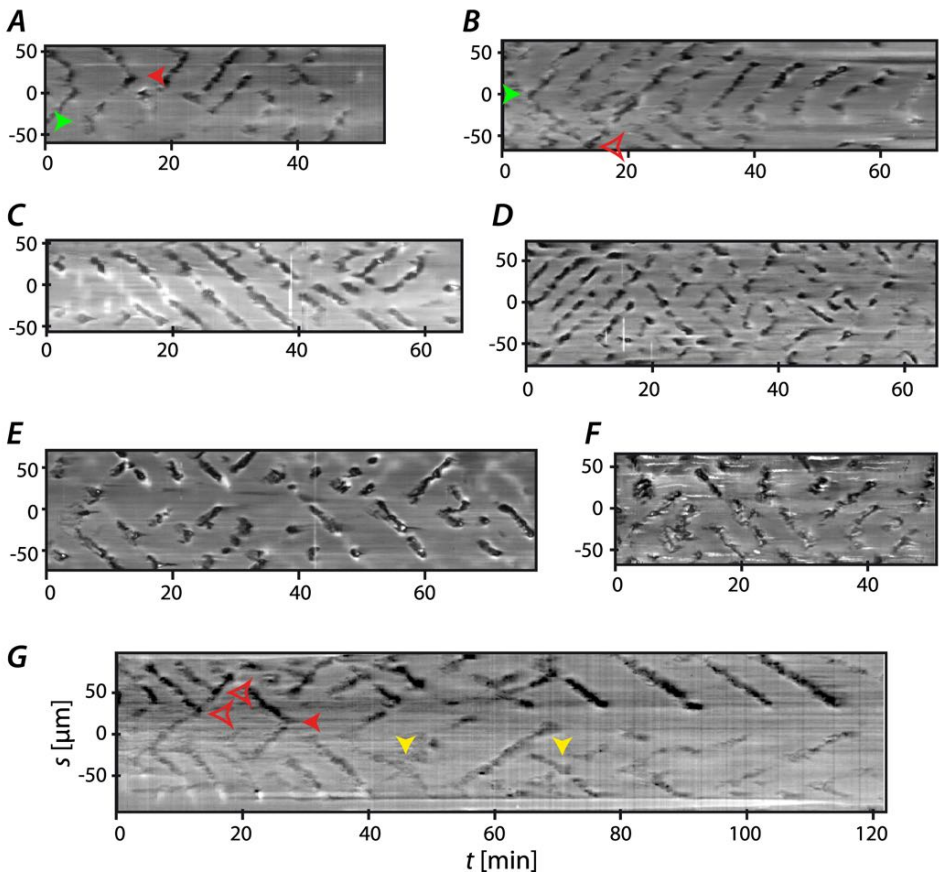

Figure 5.14: *Examples of CDR dynamics on disc-shaped cells.* All kymographs *A*-*G* have the same scaling, i.e., periods and wave velocities (i.e., slopes) can directly be compared. Green arrows: examples of CDR creation events, red arrows: examples of CDR collision events. Hollow red arrows mark unilateral annihilation, solid red arrows mutual annihilation. Yellow arrows mark CDR crossing events. Only those events are marked by arrows that are discussed in-depth in the main text. The radii of the fibronectin discs are *A*-*F*: 31 µm, *G*: 44 µm.

f-actin.

Interestingly the degree of fragmentation of patterns does not correlate with the number of CDRs a cell supports simultaneously. In Figure 5.15 the distribution of CDR numbers found in experiments for cells on disc-shaped protein patches of radii of 31 µm is plotted. In contrast to their visualization in Figure 5.12, Figure 5.15 discriminates between the appearance of patterns in kymographs according to the scheme introduced in Figure 5.5, i.e., into line patterns, fragmented line patterns, and punctual patterns. Additionally the class "punctual stationary" is introduced in Figure 5.15 that corresponds to spot-like patterns without correlation in space-time,

i.e., randomly occurring stationary CDRs.

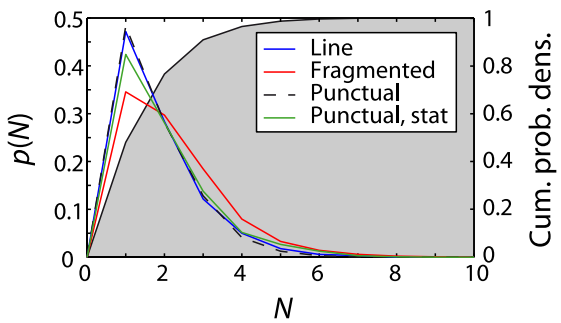

Figure 5.15: *Pattern type-resolved probability density of CDR occupation numbers.* The shaded gray region is the cumulative probability, calculated from the cumulative density function of the average of all four probability functions (black solid line).

The plot reveals that the probability distribution of the CDR number is independent on the type of pattern formed. Only the type "fragmented" shows a slight bias towards higher CDR number that can, however, be explained by the fact that these patterns are marked by frayed signatures in kymographs (see, e.g., Figure 5.5*C* and Figure 5.14*F*) that can induce counting errors in the form of a shift towards higher CDR numbers. Only in less than 4% cells on fibronectin patches of a radius of 31 µm exhibit four or more CDRs simultaneously. This can be seen based on the cumulative density function of the averaged data in Figure 5.15.

The basic idea to describe the patterns in kymographs via randomly formed states, whose lifetimes are limited by their collisions, allows no clear interpretation of the result of Figure 5.15. However, it will be shown in the next chapter (Chapter 6) that the observed distribution can indeed be understood as a result of the interplay of collision events, stochastic formation rates, and the recovery time of an excitable system. Numerical solutions of a noisy FHN system will show that within the same set of parameters for noise intensity and recovery time different types of patterns can transiently exist. These can drastically vary in their fragmentation, much like CDR patterns, e.g., in the kymograph in Figure 5.14*D*.

5.5 Actin Depletion within Propagating CDRs

Within CDRs one usually finds a pronounced depletion of cytoskeletal f-actin structures. This raises the question whether this phenomenon is either a side effect of the wave machinery underlying CDRs, or if it is an integral constituent of the wave mechanism. It could be hypothesized that, e.g., CDR growth requires the consumption of a substrate (here: possibly cytoskeletal f-actin). These ideas were discussed in depth in Chapter 3.

In the framework of a simple substrate consumption mechanism (Figure3.10*C* in Section 3.3) coherently propagating CDRs would leave a footprint of depleted cytoskeletal f-actin in form of a tail in the regions they occupied last. The depletion state of the substrate would then prohibit an immediate successive wave formation until the substrate is rebuilt. In this framework the recovery time between successive CDR events could be the recovery time of the f-actin substrate. This would explain the absence of target patterns of wavefronts. This assumes that the recovery time of the substrate is longer than the typical lifetime of a CDR.

In contrast, an inherent polarisation between the regions situated inside and outside of CDR wavefronts mediated by a two-state regulatory protein implies a fundamentally different picture (Figure3.10*D* in Section 3.3). For such a system the depletion of the substrate might occur as a side effect, however, a wave would not require the consumption of a substrate. Thus wavefronts of systems with a two-state regulatory protein would be able to propagate over previously occupied regions, because the substrate does not need to be in a recovered state to support a wave. The time between two succeeding wave events would then be set by another feature of the system than the recovery of the substrate. The absence of target wave patterns follows naturally from this framework, as two-state systems cannot support wave trains. Especially the zone of f-actin depletion would remain inside coherently propagating CDRs.

The constraints on the CDR propagation direction on disc-shaped cells allow us to address the question of the role of f-actin depletion within coherently propagating CDRs systematically. For this, NIH 3T3 WT cells were transiently transfected with pLifeAct-TagGFP2 and plated on disc-shaped fibronectin patches. Cells were then stimulated with 30 nM PDGF and imaged in fluorescence contrast. Figure 5.16 shows the dynamics of f-actin in a coherently propagating CDR. The kymograph in Figure 5.16*B* shows that the polarity between inner and outer region of the CDR, regarding the depletion of f-actin, is maintained during its propagation. The Kymograph permits to read off a velocity of $0.1\,\mu\mathrm{m\,s^{-1}}$ and a typical diameter of the inner region of the CDR of $7\,\mu\mathrm{m}$. It therefore takes the CDR approximately 1 min to cross its own diameter, which is the maximal time it takes the cytoskeletal f-actin to return to background levels. In fact, the fluorescence intensity even recovers to higher intensities, as can be seen from Figure 5.16*B* and verified by an intensity plot (not shown).

This result contradicts the hypothesis that CDR propagate simply by the consumption of cytoskeletal f-actin as a substrate, especially when interpreted in the light of the results of the previous chapters of this thesis. We have seen above that the depletion zone of cytoskeletal f-actin entirely stays inside of the CDR wavefront and that there is no tail of depleted f-actin behind the part of the wavefront that marks the rear of a propagating CDR. The cell can therefore support two successive wavefronts within a time period of approximately 1 min. If this recovery time was sufficient for a succeeding wave formation large CDRs, as shown in the figures 3.4, 3.6, and 3.7, should at least in some cases contain secondary wavefronts, i.e., form target patterns. However, this was never observed.

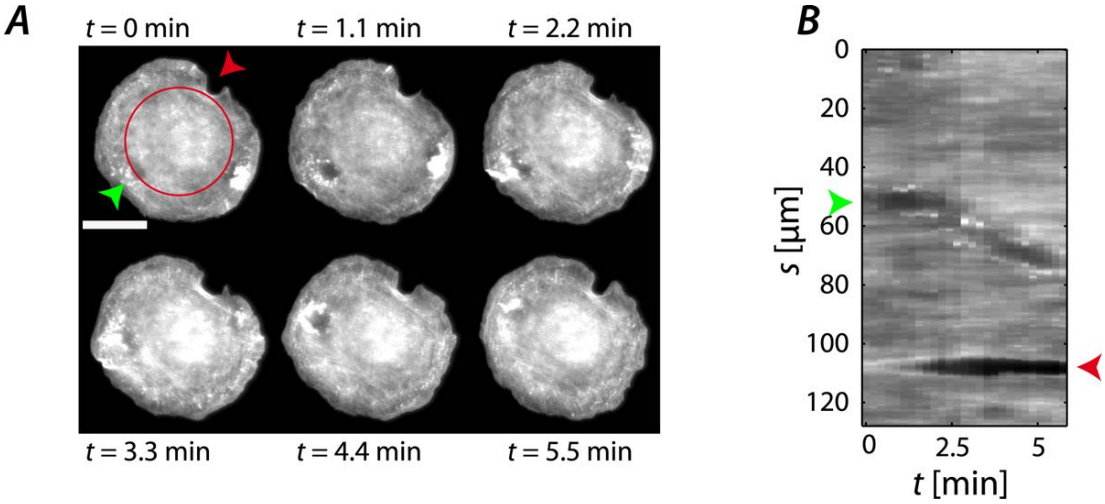

Figure 5.16: *Depletion of f-actin in a coherently propagating CDR. A*: Time-lapse sequence. F-actin was stained with pLifeAct-TagGFP2. *B*: Kymograph, sampled along the red circle in *A*. The green arrows highlight the formation of a CDR, which encloses a zone of f-actin depletion. Upon propagation, this zone constantly stays within the CDR wavefront, as shown by the dark band in *B*. The red arrows denotes a dent in the cell that must not be confused with a zone of f-actin depletion. Scale bar: $25\,\mu\mathrm{m}$.

The above finding is therefore in favour of the idea of a two-state character of the system, i.e., that a polarity between CDR in- and outside exists at the level of regulatory proteins of actin. The interconversion scheme between the phospholipids PIP_2 and PIP_3, as proposed by Itoh et al., constitute a framework for the interpretation of this result [Itoh and Hasegawa, 2012], which was discussed in Section 3.3 and visualized in Figure 3.10*D*.

However, we have also seen much evidence for the hypothesis that CDR dynamics is crucially influenced by the limited availability of a protein species involved in the wave mechanism throughout this work, especially in Chapter 4. These result suggested a mechanism of substrate consumption in the wave machinery. In case that the species that is most limiting is actin the consumption of cytoskeletal f-actin could indeed facilitate the increasing demand on actin of growing CDRs, as CDRs incorporate considerable amounts of actin. In contrast, for CDR translocation CDR-incorporated actin could simply be recycled. This picture implies a competition for the organization of actin into either CDRs or cytoskeletal structures, which is a central aspect of the model by Zeng et al. [Zeng et al., 2011].

5.6 The Effect of Enhanced Actin Depolymerization

Disc shaped cells clear the way for systematic and comparative investigations of the wave machinery underlying CDRs. In particular the constant propagation velocities of

waves and their regular spatiotemporal patterns facilitate a standardized analysis. With this a testing of the model proposed by Zeng et al. comes into reach, which proposes that CDRs form through a mechanism of interaction between GTPases, i.e., exclusively at the level of regulatory proteins [Zeng et al., 2011]. In this framework the visible wave of polymerizing actin is governed by a wave of a protein upstream of actin. To answer the question of the validity of this concept I performed experiments in which I interfered with the dynamics of actin via the drug Latrunculin A.

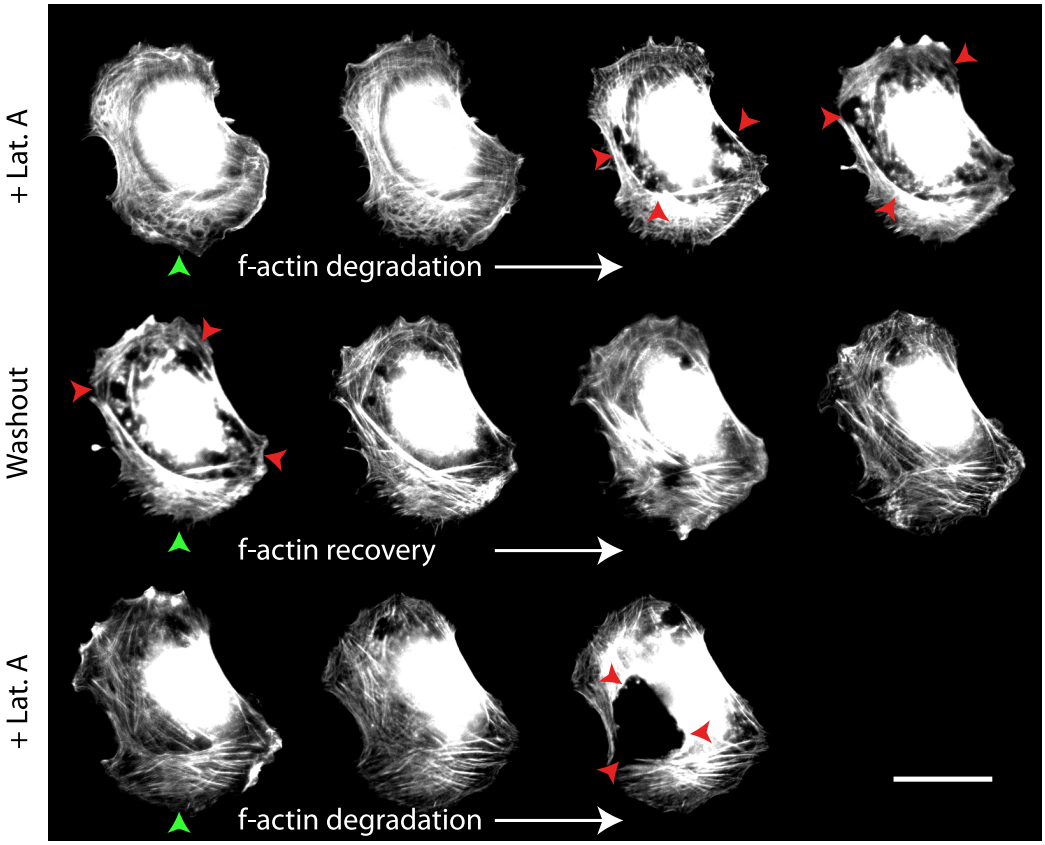

Figure 5.17: *The effect of Latrunculin A and its reversibility.* A NIH 3T3 WT cell was stained for actin (lifeAct TagGFP2) and imaged every 5 min with a fluorescence microscope (time direction: reading direction). The green arrows mark the time points when the state of the cell medium was altered. Red arrows highlight positions of especially pronounced cytoskeletal disruption. Scale bar: 50 µm.

Latrunculins tightly bind actin monomers by direct formation of 1:1 complexes [Bray, 2001]. In vivo this sequestering leads to a rapid disruption of the actin cytoskeleton when added to the medium of cultured cells [Yarmola et al., 2000]. At Latrunculin A concentrations exceeding 1 µM cells take round and arborized shapes due to the collapse of actin filaments. Its ability to disrupt actin filaments and to sequester actin from the

pool of polymerizable monomers makes latrunculins highly interesting for the research on actin dynamics. Hence this drug is widely used in cell biology [Spector et al., 1989].

The effect of Latrunculin A on the cytoskeleton is reversible, i.e., after a washout cells re-gain normal cytoskeletal structures and morphologies. Figure 5.17 demonstrates this based on a cell that was treated with Latrunculin A in a cycle of application, washout, and a succeeding second application. The concentration of Latrunculin A was 1 µM in this experiment. Ten minutes after the treatment obvious changes in the cytoskeletal structure can be seen. A large fraction of the actin filaments were disrupted and lumps of actin were formed instead. After washout, the cell recovered and built up an intact cytoskeleton again. A second application of Latrunculin A once more led to disruption of filaments and formation of a hole in the cell's cytoskeleton ten minutes after exposure to Latrunculin A.

To test the impact of Latrunculin A on CDR propagation experimentally a series of experiments at different concentrations of this drug was performed. As in the previous sections I used disc-shaped patches of fibronectin of a radius of 31 µm that were printed on the bottom slide of flow chambers. The flow chambers were attached to a computer-controlled flow system that permitted changing buffer conditions as a function of time as described in Section 8.3. Since I did not aim to completely disturb the actin cytoskeleton of cells, but only to alter its dynamics, I chose low to moderate concentrations of Latrunculin A (5 nM, 50 nM, 500 nM). The buffer conditions were changed every 30 min in an alternating fashion between Latrunculin-containing and Latrunculin-free states. After the medium exchange, cells were imaged under zero-flow conditions. The wave dynamics was visualized via kymographs. The time frame of 30 min allowed observation of several wave events and, therefore, to read off wave velocities and frequencies from kymographs.

We have seen in the previous sections that cells, despite their identical buffer conditions and identical morphologies, exhibited remarkably different wave patterns in kymographs. It is therefore highly desirable to visualize the effect of Latrunculin A based on single-cell experiments and not based on ensemble averages, where effects might hide in the variation between different cells. The use of microfluidics permits this and, in combination with a programmable xy-stage of the microscope, further enables acquisition of many of those experiments in parallel (see Section 8.3 for details).

Figure 5.18A-C shows a selection of kymographs that illustrate the effect that Latrunculin A in concentrations from 5-500 nM had on the patterns of CDRs on disc-shaped cells. To emphasize the patterns and the transitions between them the kymographs are repeated once in both, positive and negative spatial direction. This makes it easier for the eye to account for the periodic boundary conditions of the systems. At a concentration of 5 nM (Figure 5.18A) the wave patterns show no noticeable change upon insertion of Latrunculin A.

With increasing concentrations, however, the insertion of Latrunculin A is marked by drastic differences in the wave patterns of kymographs. At a concentration of 50 nM (Figure 5.18B) wave events become less frequent when compared to the zero-Latrunculin

A counterparts within the kympgraphs of each individual cell. At 50 nM waves do still form periodically, whereas at 500 nM wave formation is almost completely abolished. In both cases, however, cells return to states of periodic wave formation upon washout of Latrunculin A. Cells that cycle between zero and 50 nM Latrunculin A conditions show an extended period between repeated CDR formations at 50 nM. In the example shown in Figure 5.18 *b1* the period under influence of Latrunculin is approximately twice as long as the period at zero Latrunculin A (0 nM: typically 4 min, 50 nM: typically 9 min).

Since at 500 nM CDR formation is suppressed in most cases, there is no period of reappearance. However, the few CDRs formed at 500 nM Latrunculin A have much reduced characteristic wave velocities when compared to those of CDRs under zero-Latrunculin A concentration. As shown in Figure 5.18*c1* the wave events at 500 nM create only faint signals and are therefore highlighted by red arrows. The wave velocity of both wave events, that can be observed in Figure 5.18*c1*, is comparable, although they take place almost one hour apart and are separated by a phase of zero-Latrunculin concentration. Reading off the slope of the wave signatures reveals a typical velocity of $0.14\,\mu\mathrm{m\,s^{-1}}$ at zero Latrunculin A and $0.06\,\mu\mathrm{m\,s^{-1}}$ at 500 nM Latrunculin A.

From a dynamic perspective the binding between Latrunculin A and actin has two implications. First, existing filaments are more quickly disassembled in the presence of Latrunculin A when compared to physiological rates of f-actin depolymerization. Second, the actin monomers that are sequestered by Latrunculin A are no more available for polymerization into f-actin, which means that the concentration of free g-actin monomers is anti-proportional to the concentrations of Latrunculin A. Since the polymerization rate of actin is proportional to the concentration of available monomeric actin there is, hence, also a negative correlation between Latrunculin concentration and the polymerization rates of actin. The dynamic properties of actin are therefore heavily impacted by Latrunculin and one, thus, expects a correspondingly drastic effect of Latrunculin A on the wave dynamics of CDRs. However, this is only valid provided that actin plays an active role in the wave mechanism and does not simply follow the dictated dynamics of a wave-generating regulatory field. In the latter case, one would rather expect faint waves with albeit unaltered dynamics upon treatment with Latrunculin A.

The results presented in this section indicate that actin indeed plays a key role for the wave machinery underlying CDRs. This excludes a wave mechanism in which the essential feedback schemes are exclusively upstream of actin as proposed by Zeng et al. [Zeng et al., 2011].

Actin waves rather tended to form static patches than travelling waves with increasing

Figure 5.18 (facing page): *The effect of Latrunculin A on CDR patterns on disc-shaped cells.* Two examples are shown for each concentration of 5 nM (*A*), 50 nM (*B*), and 500 nM (*C*). Red lines mark the time points when the medium conditions were changed. Note that kymographs were replicated in spatial dimension to emphasize the patterns.

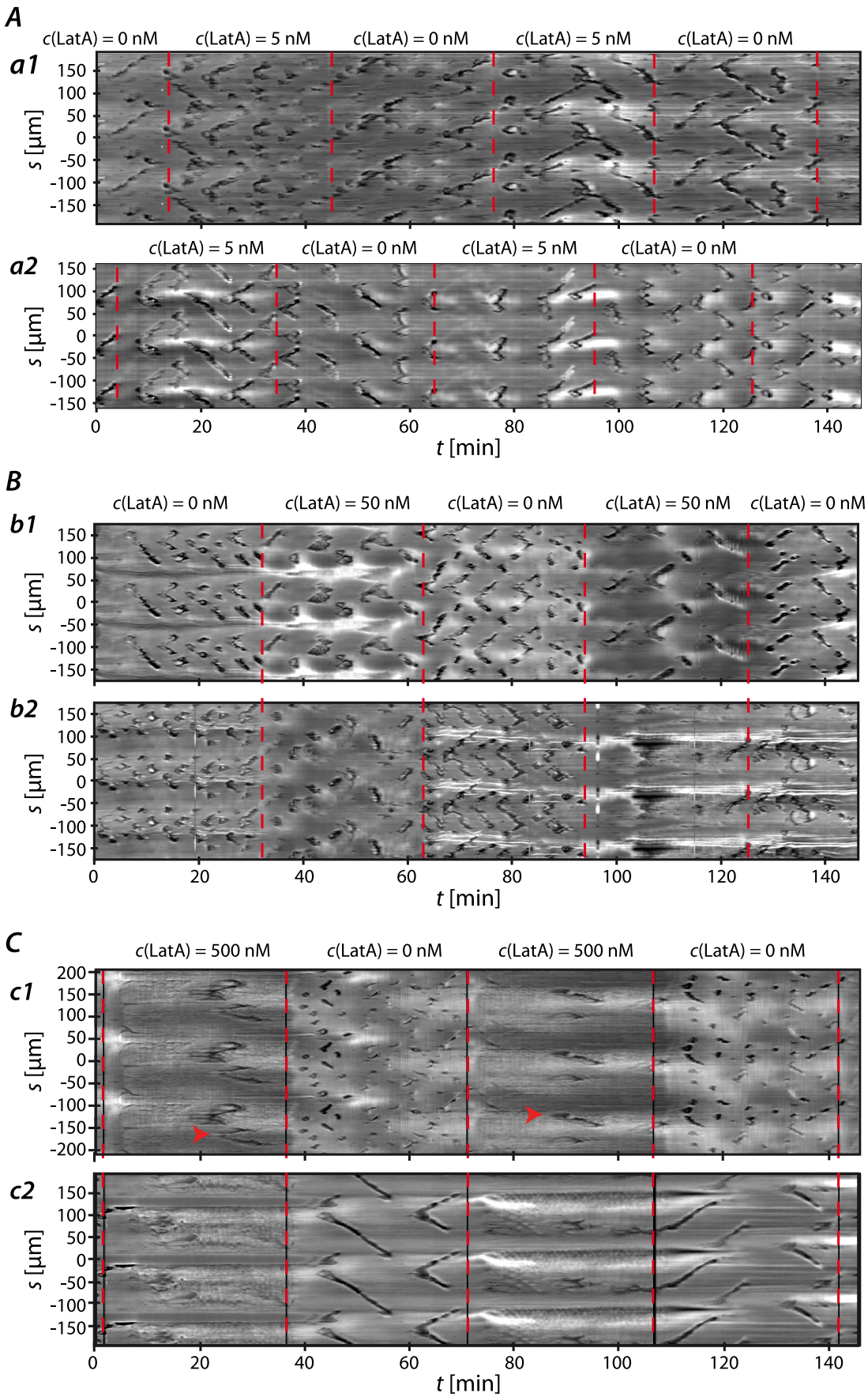
A
a1
c(LatA) = 0 nM
c(LatA) = 5 nM
c(LatA) = 0 nM
c(LatA) = 5 nM
c(LatA) = 0 nM
s [µm]
a2
c(LatA) = 5 nM
c(LatA) = 0 nM
c(LatA) = 5 nM
c(LatA) = 0 nM
t [min]
B
b1
c(LatA) = 0 nM
c(LatA) = 50 nM
c(LatA) = 0 nM
c(LatA) = 50 nM
c(LatA) = 0 nM
b2
C
c1
c(LatA) = 500 nM
c(LatA) = 0 nM
c(LatA) = 500 nM
c(LatA) = 0 nM
c2

concentrations of Latrunculin A and, therefore, lower concentrations of free monomeric actin. This result suggests wave mechanisms in which actin functions as a central element. Indeed, this observation closely resembles results of experiments on *D. discoideum* which, upon recovery from actin depolymerization with Latrunculin A, first form static patches of f-actin that then transform into travelling actin waves [Gerisch et al., 2004, Bretschneider et al., 2009]. These results have successfully been reproduced by models in which autocatalysis of f-actin growth is mediated by branching of existing actin filaments [Whitelam et al., 2009, Carlsson, 2010]. The latter of these two studies by Carlsson explicitly models the impact of low concentrations of monomeric actin which omits wave formation in favour of patch formation. The model predictions by Carlsson are therefore in agreement with the results presented here.

However, there may also be other central positions of f-actin in the wave machinery than in form of the direct autocatalytic element. Also the morphodynamic wave mechanism proposed for CDRs by Peleg et al. crucially relies on actin activity [Peleg et al., 2011]. This model indeed predicts decreased wave velocities as a consequence of limited actin polymerization rates. In other models, inspired by actin waves in neutrophils, the activatory role and also the autocatalytic element is not constituted by actin but by nucleation-promoting factors of actin such as Hem-1 of the WAVE complex [Weiner et al., 2007, Doubrovinski and Kruse, 2008]. In the latter, the growth of f-actin is promoted by Hem-1 but f-actin itself removes Hem-1 from the cell membrane, thus functions as the inhibitory element, which is also a central role for the formation of waves. Interestingly, Weiner et al. also conducted experiments on Hem-1 waves with latrunculin in which they found a reduction of wave velocity from $0.065 \pm 0.025\,\mu\mathrm{m\,s^{-1}}$ (zero latrunculin) to $0.0068 \pm 0.0003\,\mu\mathrm{m\,s^{-1}}$ (non-zero latrunculin, concentration not provided) [Weiner et al., 2007].

As discussed in Section 3.3 before the wave machinery of CDRs has been shown to crucially rely on the activity of N-WASP, which, being a member of the WAVE family of proteins, contains a Hem-1 domain [Legg et al., 2007, Park et al., 2010]. Therefore, the results of this section are in line with the hypothesis that Hem-1 indeed might also play a central role in CDRs.

5.7 Discussion

In this chapter a novel system for the study of actin waves in cells was introduced that is based on microcontact printing and microfluidics, which allowed simultaneous control over both, shape and biochemical state of cells. The design of this system was motivated by findings of the previous chapters, i.e., that the governing role of the cell morphology together with the randomness of fibroblast shapes lead to a manifold of wave dynamics of CDRs, which complicated their systematic analysis. In contrast, on cells of controlled morphologies CDRs exhibited largely simplified dynamics, enabling the study of their propagation behaviour untangled from boundary effects. Using array arrangements of disc-shaped patches of adhesion proteins in microfluidic channels, a large number of

data could be obtained in parallel under controlled constant or changing biochemical conditions on cells of identical morphologies.

The uses of microcontact printing and microfluidics have become standard tools of modern microbiological research [Weibel et al., 2007]. However, to the best of my knowledge this thesis is the first work combining these two techniques for the simultaneous control over the morphology and biochemical state of cells. Nevertheless, due to the rapid progress in the field of microfabrication for biological applications there might be work that I missed in my literature search.

The idea to consider the geometry of a wave-forming biological system as a parameter that can be adjusted has recently also been applied to other organisms. For experiments on *D. discoideum* electric-pulse-induced cell fusion was used to generate giant cells in order to reduce the impact of boundary effects in measurements of the inherent length scale of excited states of actin/PIP_3 waves [Gerhardt et al., 2014]. For *Escherichia coli* a symmetry breaking in the mechanism of division site control was induced, giving rise to bacteria with considerably changed morphological aspect ratios. For this, the growth-limiting system of these cells was manipulated biochemically [Bonny et al., 2013].

In this thesis the cellular geometry of fibroblasts was simplified to discs, which limited the degree of freedom of CDR propagation towards one, at the same time imposing periodic boundary conditions. On disc-shaped cells CDRs formed spontaneously and periodically, propagating with constant velocities. Due to the simple geometry of disc-shaped cells the complete CDR dynamics could conveniently be analysed via kymographs. In these, travelling CDRs, which re-appeared periodically, formed extremely regular patterns (sections 5.1-5.4).

The significance of the cell geometry for propagation of actin waves is implied by several previous studies. These comprise, e.g., work on actin waves in *D. discoideum*. These cells take round morphologies after treatment with Latrunculin A, which has become a standard method for induction of waves on these cells [Gerisch et al., 2004]. Other types of disc-shaped cells have been reported to form lateral waves of actin polymerization. These cells obtained their disc-morphologies from either isotropic cell spreading [Döbereiner et al., 2006] or genetic modification [Asano et al., 2009]. The lateral waves they formed exhibited constant propagation velocities, similar to the CDRs described in this thesis. Interestingly, the wave patterns in [Döbereiner et al., 2006] were of varying degree of fragmentation, which depended on the cell type. Mouse fibroblasts in the prespreading basal phase had spatiotemporally correlated lateral protrusion events leading to patterns that closely resemble spatiotemporal CDR patterns of type punctual in Figure 5.5*D*. Wave patterns that were reminiscent of type fragmented in Figure 5.5*C* have been reported for lateral membrane waves of freshly spread mouse T cells [Döbereiner et al., 2006].

However, the simple shapes of cells in the articles mentioned above either only lasted several minutes, or were accompanied by interference with the cell's biochemistry. In contrast, the system developed in this thesis allows the observation of cells for several hours without any biochemical disturbance. Together, the results from the literature

and from this thesis highlight the impact that the cell morphology has on actin waves, as they emerge especially pronounced on systems with simple boundary geometries.

This is also true for other types of waves in biological systems, such as action potentials travelling on one-dimensional neuronal axons [Hodgkin and Huxley, 1952] [Alberts et al., 2005, 436 pp] or waves of cyclic AMP in two-dimensional cultures of starving amoeba of *D. discoideum* [Tomchik and Devreotes, 1981, Pálsson and Cox, 1996]. Both systems have in common that they are isotropic and of a certain homogeneity on the spatial scale of their corresponding wavelengths. In contrast, waves of polymerizing actin typically inherently propagate on less homogeneous media. The reason for this is that their wavelengths are typically of the same order as the dimension of the system. Moreover, these waves have the outstanding capability to modulate the shape of the medium in which they are travelling. Even though the understanding of the interplay of wave dynamics and cell shape is certainly one of the most exciting challenges in the research on cell motility this interplay also largely complicates the understanding of the mechanisms of the wave propagation alone. Both of the aforementioned problems have seen considerable progress in the last years [Dreher et al., 2014, Holmes et al., 2012, Khamviwath et al., 2013, Wasnik and Mukhopadhyay, 2014, Weiner et al., 2007]. With respect to the general structure of models leading to actin waves there is a certain consensus on the characteristic types of feedback schemes, as introduced in Section 2.2 and discussed by Allard et al. [Allard and Mogilner, 2013]. However, regarding the molecular mechanisms constituting the feedbacks there is less agreement reflected by the numerous different models that have been proposed for actin waves [Carlsson, 2010, Dreher et al., 2014, Wasnik and Mukhopadhyay, 2014, Khamviwath et al., 2013]. Using cells of controlled shapes for experiments on actin waves permits the minimization of the impact that boundary effects have on wave propagation and therefore bears a large potential for a clearer understanding of these waves.

While wave data of random-shaped cells could not easily be compared among each other (Section 3.1.1) comparability was given for disc-shaped cells due to their identical morphologies. This permitted the recording of large data sets that could be analysed systematically, which was shown throughout this whole chapter. The data sets obtained on disc-shaped cells reveal fundamental insights into the wave mechanism underlying CDRs. Especially the wave velocity could be quantified based on reliable and reproducible data, yielding a typical propagation velocity of $0.149 \pm 0.003\,\mu\mathrm{m\,s^{-1}}$ (mean $\pm$ SE, values for patterns of clear stripe signatures). This value is in the range of other systems forming actin waves that are assumed to be based on reaction-diffusion mechanisms [Grosheva et al., 2006, Weiner et al., 2007, Bretschneider et al., 2009] and are further consistent with modelling approaches that include the growth of actin filaments as a central element [Doubrovinski and Kruse, 2008, Whitelam et al., 2009, Carlsson, 2010].

On disc-shaped cells also the periods between successive wave events became easily accessible. The corresponding distributions had clearly enhanced probabilities for periods

between $5-7$ min. The distribution of periods can be understood as a consequence from mainly two inherent time scales of the system. The first of these is the recovery time of the active medium. The second is the rate at which stochastic processes involved in the actin machinery push the system above the threshold of its excitability, leading to spontaneous wave formation. Indeed, the spatial extension of the system, together with the characteristic wave velocity, defines a third time scale. If this has an impact on the system's dynamics, e.g., via resonance effects, remains a subject for future experiments. In the following a biological interpretation of both, the recovery time and the nature of the noise is given.

When we assume that a reaction-diffusion scheme is underlying the wave mechanism of CDRs the recovery time, which we estimated to be of 5 min, is strongly dependent on the net reaction rates that lead to the dissociation of existing f-actin structures incorporated into CDRs. The molecular identities of the corresponding actors are currently not clear. However, there are strong hints that further local actin availability might largely contribute to the recovery time of the system. This became obvious in two cases. The first of these was the observation that the recovery time of the medium differed depending on whether CDRs formed breathing modes, i.e., structures that formed and disappeared at the same spot on random-shaped cells (Section 4.4), or repeatedly propagated over the same region of disc-shaped cells (Section 5.3). Only breathing modes involve CDR collapse and therefore the local release of actin, resulting in short recovery times.

The second case was the doubling of the periods between successive CDR formations in experiments where 50 nM Latrunculin A was added to the cell medium. Latrunculin sequesters free actin monomers and therefore effectively reduces the amount of actin available for CDR formation, leading to increased recovery times.

The spontaneous de novo formation of CDRs on disc-shaped cells points to a stochastic element involved in the wave mechanism of CDRs. Biological systems on small spatial scales are inherently subject to noise due to the omnipresent Brownian motion of suspended particles [Tsimring, 2014]. Moreover, for active gels the local input of energy gives rise to non-thermal fluctuations, which can give rise to pronounced jumps in dynamic variables [Stukalin and Kolomeisky, 2006, Weber et al., 2015]. However, it has also recently been shown that for a two-dimensional model of actin waves spatiotemporal chaos can occur, which leads to an only seeming stochastic behaviour of the system [Dreher et al., 2014].

Since there are numerous possible sources of noise that likely all have impact on the wave mechanism of CDRs the identification of one particular stochastic element is not reasonable. However, we discussed in Section 4.4 that an additional, external source of noise might result from stochastic binding events between growth factors contained in the cell medium and their respective receptors. The fact that this external source of noise is restricted to the dorsal cell side makes it a very interesting candidate for a functional element of CDR dynamics. The reason for this is that noise is known to support the propagation of waves in sub-excitable active media, a phenomenon called "stochastic

resonance" [Jung and Mayer-Kress, 1995, Kádár et al., 1998][a]. As receptor-mediated noise would foster wave formation exclusively at the dorsal cell side it would inherently hold the answer to the question why CDRs only form at this side of the cell.

In the next chapter the role of noise as the trigger of wave formation will be investigated based on numerical studies of the FHN system. It will be shown that indeed the amplitude of the noise, together with the recovery time of the active medium, regulates the rate of wave formation. These two contributions therefore cannot be strictly separated.

The assumption that the amount of available actin is determining the rate of CDR formation might facilitate the understanding of the limited number of CDRs that cells can support at the same time. It was shown in this chapter that this number only rarely exceeds four. Limited actin availability might also hold the answer to one of the most fundamental questions arising for the dynamics of CDRs on disc-shaped cells, namely: why do CDRs form spontaneously at high rates on disc-shaped cells, whereas the same cell line formed these waves only rarely when having their normal random-morphology? We must not forget that the disc-shaped patches of fibronectin, on which cells were plated, not only enforce disc-morphology to cells. They also limit their adhesion area, in some cases below the areas to which they would spread without external limitations. For cells adhering to non-structured substrates the available membrane area is a critical determinant of spreading area [Gauthier et al., 2011, Gauthier et al., 2009, Figard and Sokac, 2014]. When we assume that structures of f-actin, such as the cell cortex and stress fibres, form with the same area densities, regardless whether cells are externally or internally limited in their spreading areas, implies that cells with external growth limitations have excess availability of g-actin. This in turn might foster the spontaneous formation of CDRs. As cells are known to precisely regulate their protein household and, e.g., use buffer proteins to control the pool of available actin [Pollard and Borisy, 2003], this hypothesis needs experimental support.

Filamentous actin appears depleted in the areas surrounded by CDR wavefronts (sections 3.1.2 & 3.2). This observation reminds of systems of the substrate depletion kind, in which a propagating wave consumes the substrate on which it is travelling. However, in this chapter it was shown that the region of f-actin depletion travels with coherently propagating CDRs, thereby staying in the CDR interior (Section 5.5). Since this coherent propagation means that CDRs can travel over regions of depleted f-actin a mechanism of substrate depletion can be excluded as a necessary element of the CDR wave machinery. However, substrate depletion might promote the growth of CDRs.

The results show that CDRs have an inherent polarity between their interior and exterior. Whether both, f-actin and g-actin, or only f-actin is depleted in CDR interiors remains an open question. The latter case would indicate high activity of a depolymerizer of actin in CDR interiors, which would lead to high availability of g-actin inside of CDRs.

[a]The idea that stochastic resonance might have significance for CDRs goes back to a discussion with Prof. Marc Hütt, Jacobs University, Germany

Experiments in which the dynamics of both, f- and g-actin is imaged simultaneously are clearly needed to clarify this point.

Experiments involving Latrunculin A revealed that at large concentrations of this actin drug a decrease of CDR propagation velocity could be observed (Section 5.6). This finding is in accord with experimental results obtained for actin waves in neutrophils [Weiner et al., 2007]. It adds large support to the hypothesis that actin has a central part in the wave machinery of CDRs and does not simply follow the dynamics of a regulatory field.

Experiments without Latrunculin, however, partially contradict this hypothesis. Among the different spatiotemporal patterns that CDRs formed in kymographs were also spatiotemporally correlated punctual patterns of actin that seemingly lacked a connection in form of a wave of poylmerized actin. This suggests that an invisible field of regulatory proteins forms counter propagating waves, without pronounced f-actin signature, which only leads to notable actin polymerization at intersection points of two waves. Nevertheless, since the experiments in this chapter mainly relied on phase contrast microscopy, which resolves actin-driven undulations, but not actin itself, there might be actin dynamics involved in the formation of punctual patterns in kymographs that could not be resolved by this mode of imaging.

One could also speculate that punctual patterns in kymographs are a result of limited actin availability. From this perspective the lack of actin would not allow the system to build fully established waves, i.e., continuous wave signatures. This could explain the reduction of wave velocities observed for punctual patterns, which is then in line with the results of experiments with Latrunculin A. In terms of numbers the wave velocity from line patterns in kymographs, formed by CDRs propagating with $0.149 \pm 0.003\,\mu\mathrm{m\,s^{-1}}$, was reduced to $0.129 \pm 0.003\,\mu\mathrm{m\,s^{-1}}$ for punctual patterns (mean $\pm$ SE).

The formation of spatiotemporal patterns in kymographs is a complex process that involves several processes. In this chapter the impact of collision annihilation events on pattern formation was investigated in detail. It was shown that simple considerations along the lines of the multiplicity of configurations of possible CDR propagation states can explain the basic trend in the probability distribution of actual experimental data of CDR occupation numbers. However, it was also shown that this framework is of limited validity as collision annihilation is not always visible in kympgraphs. Regardless of the occurrence of collision-annihilations the probability distributions of CDR occupations had identical forms for all kinds of pattern types.

In the next chapter the pattern-forming processes will be investigated in detail based on a noise-driven FHN model as the simplest possible description for CDRs on disc-shaped cells. With this also the benefits of the simplified geometry and boundary conditions of disc-shaped cells are demonstrated.

Chapter 6

Studying Wave Patterns via a Noise-Driven Active Medium

The main thesis underlying this work is that CDRs constitute waves in an active medium. We have seen much evidence for this idea in the previous sections, especially in Chapter 4, which was in large parts dedicated to this hypothesis. However, the wave dynamics of CDRs on random-shaped cells was usually complex and indicated undefined crosstalk from, e.g., wave interactions with cell boundaries. This did not allow for a direct comparison of CDR dynamics to simulations of active media systems.

In Chapter 5 a system was introduced that drastically simplifies CDR dynamics. This was attained by forcing cells in disc-morphology. These cells constituted a homogenized medium with periodic boundary conditions and the reduction towards one-dimensional CDR propagation direction. We have seen in the preceding sections that, compared to random-shaped cells, on disc-shaped cells CDRs indeed exhibited largely simplified propagation dynamics. This led to formation of pronounced spatiotemporal patterns of outstanding regularity in kymographs. The potential role of noise underlying the stochastic and repeated formation of waves was discussed as a possibly crucial mechanism for the understanding of those patterns.

The simplified geometry of disc-shaped cells constitutes ideal prerequisites for a comparison between experimental data and numerical simulations. This permits the testing of the idea of the description of CDRs as waves in an active medium, which is the topic of this chapter.

In the following, the results of numerical solutions of a noise-imposed active medium are studied regarding the mechanisms of formation of spatiotemporal patterns. The motivation behind this is the interpretation of the results of the preceding chapter on an abstract level, especially with respect to the potential role of noise. Initially it was a central question for the motivation of the simulations whether the degree of fragmentation of patterns found in the preceding chapter can be explained as a consequence of varying noise amplitude. We will see in the following that increased pattern fragmentation indeed occurs, albeit together with other features that contradict

the idea of noise as the cause for fragmentation of CDR patterns.

I chose the FHN model as a prototype system of an active medium, which was introduced in Section 2.3 in detail. This choice is motivated by its basic structure and its popularity, which fosters the transparency of the results. In particular the refractive state of the FHN system has a distinct signature, which facilitates the interpretation of the significance of this feature regarding pattern formation.

In the following we will see that, correspondingly, the dynamics of CDRs on disc-shaped cells can be well described by a noise-imposed version of the one-dimensional FHN model with periodic boundary conditions, which supports the idea of an active medium description of CDRs.

Here the noise is chosen to act on the time evolution of the activating variable V, which gives it formally the place of the stimulus S in the equations of the system (2.11). The time-dependent noise $\eta(t)$ is weighted with the amplitude A:

$$\begin{aligned} \frac{\partial V}{\partial t} &= D\frac{\partial^2 V}{\partial s^2} + V - V^3/3 - R + A\eta(t) \\ \frac{\partial R}{\partial t} &= \phi(V + a - bR). \end{aligned} \tag{6.1}$$

The distribution of η was chosen to be Gaussian so that the stochastic nature of the integrated system corresponded to a Wiener process. The equations were solved numerically using XMDS2 [Dennis et al., 2013].

The values of the parameters a, b, D and ϕ were as in Section 2.3.1. The size of the spatial domain was chosen such that its ratio with the wave width corresponded to the characteristic ratio that was found experimentally for CDRs on disc-shaped cells (domain length / wave width ≈ 10).

Figure 6.1 shows a typical outcome of a simulation. The noise amplitude was set to $A = 0.15$ resulting in frequent spontaneous wave formations. The spatiotemporal pattern closely resembles those that CDRs leave in kymographs, as indicated by visual inspection (compare, e.g., Figure 6.1 and 5.14).

Since the noise only directly acts on the time evolution of V the corresponding field shows a direct footprint of the noise, whereas the refractive variable R appears rather smooth, because it is an integrated variable of V. The wave patterns, however, are equally well visible in both fields (Figure 6.1).

In the following sections of this chapter the mechanisms that lead to pattern formation in the noisy FHN system will be examined. Especially the role of the noise will be investigated in detail. The analogy between the numerical results of the FHN system and actual data of CDR dynamics will then be discussed regarding the structure of a theoretical model for CDRs in the final section of this chapter.

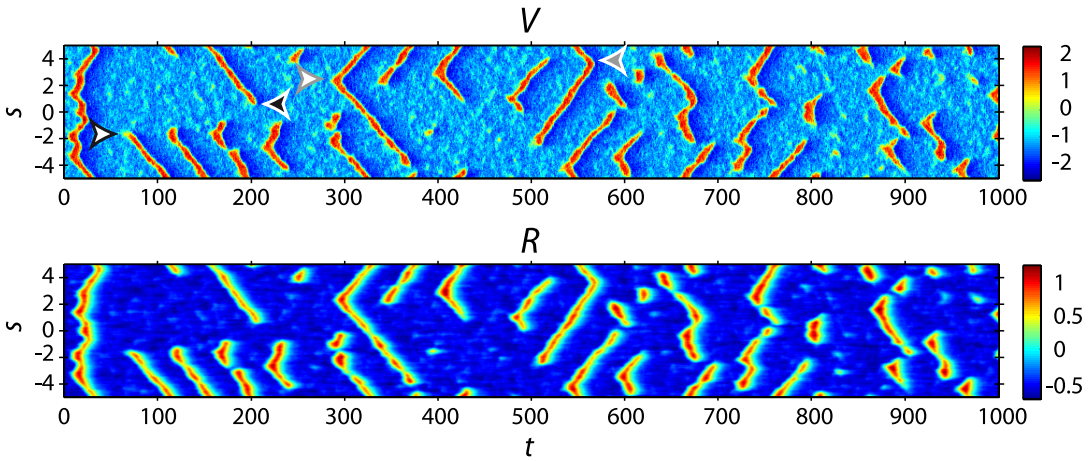

Figure 6.1: *One-dimensional, noisy FHN system with periodic boundary conditions.* The choice of parameters corresponds to that of Section 2.3.1. Values of V smaller than -1.2 correspond to refractory regions (deep blue in the upper plot). Wave creation events are highlighted by white arrows with either black (unidirectionally propagating wave, "\"-signature) or gray (bidirectionally propagating wave, "<"-signature) contours. Arrows of white contours highlight annihilation events ("\"-signature and black filling: spontaneous, ">"-signature and gray filling: collision).

6.1 The Mechanisms underlying Pattern Formation

In Section 5.4 we discussed three major features underlying pattern formation in kymographs. These were (i) wave collision events, (ii) the system's recovery time, and (iii) the rate of stochastic de novo formation of waves. The collision behaviour of waves was discussed in depth in Chapter 5. However, the recovery time and the resulting refractive region left behind by propagating waves were not accessible and could only be estimated for experimental data. Further, the role of the noise remained unclear. Its existence could only be deduced from the dynamic data. In contrast, in numerical simulation we have access to all variables of the system and can therefore study their meaning in detail even though they are only abstract and effective variables with, presumable, no direct physiological representation. Nevertheless, simulations allow especially to study, e.g., the effective role of the noise.

In the following we will discuss the mechanisms of pattern formation in the noisy FHN system based on the kymograph in Figure 6.1. The respective simulation was started from the steady state of the system. Therefore, the noise leads to a strong initial wave burst ($0 \leq t \leq 50$) forming five bidirectionally propagating wave pairs. This high occupation number leads to short lifetimes of wave pulses, as discussed in Section 5.4. The individual wavefronts collide and mutually annihilate, which is the general behaviour found for collision events in the FHN system studied here. A typical example is highlighted in Figure 6.1 by a gray arrow with a white contour. Therefore,

collision annihilation is a major mechanism of pattern formation in the noisy FHN system. This is consistent with experimental data, whereas in the latter also wave crossings and one-sided wave annihilation was observed.

The initial wave burst leaves behind a refractory zone ($t < 30$, dark blue regions in V-field following the first positive peak), which, as introduced in Section 2.3.2, inhibits the direct formation of succeeding waves. The second generation of wave pulses starts where the refractory region recovers first, which marks the onset of the actual pattern.

The refractive region and its corresponding time scale, i.e., the recovery time τ, introduce a periodicity into the pattern. Only after passing of this characteristic time, the noise can trigger wave formation again. This feature can be well observed in the V-field in Figure 6.1 based on the dark blue regions behind wave pulses. The wave signatures in patterns formed by CDRs also exhibited a characteristic spacing, which were interpreted to result from a recovery time of the system (Section 5.3). However, for experimental data this remained a hypothesis, whereas simulations allow to actually visualize the refractive region.

Since bidirectional wave pulses have <-shaped or "wedge signatures" the medium recovers first at the spatial positions corresponding to the tips of the wedges. This property alone is a sufficient prerequisite for the emergence of repeated sequences of waves originating from the same point, i.e., <<-shaped signatures. Similar structures were also observed in kymographs of actual CDR dynamics, e.g., in Figure 5.14*B*.

However, a close inspection of Figure 6.1 reveals that at times not only bidirectional waves, but also unidirectionally propagating pulses form. This means that one of the wave pulses decays without noticeable collision interaction-events with other wave pulses. The only possible way in which this can happen is via the noise. We therefore see that the noise does not exclusively lead to wave formation. Indeed, it can also destroy existing waves, which is especially true for developing ones. The noise therefore, similar to collision events, prevents the existence of long-living ordered structures in kymographs.

Another mechanism of pattern formation is the entrance of a wave into the refractive region of another previously existing wave. Also this leads to annihilation albeit no direct collision is observed. Consequently isolated wave fragments result that are reminiscent of the fragmented wave patterns formed by CDRs, which occasionally also lacked visible wave interaction events (compare, e.g., the wave pattern in Figure 5.14*E* with that in Figure 6.1 at $t > 700$).

In conclusion, the three features of (i) wave collision, (ii) recovery, and (iii) stochastic de novo formation indeed explain the spatiotemporal patterns to a large extent. The results of simulations revealed that these features have implications that are not accessible for experimental data. We have seen that, e.g., there are three causes for the destructions of existing wave pulses. The first is collision annihilation that was comprehensively discussed before, using the concept of CDR propagation states (Section 5.4). However, also the noise can destroy existing wave pulses, contributing largely to the stochastic nature of patterns. Within the same simulation we therefore find relatively regular sequences of succeeding wave formations, as well as highly fragmented patterns. The

same was observed in experimental data in the previous chapter. Thirdly, wave entry in the refractive zone of a previously existing wave leads to wave annihilation. Accordingly fragmented wave patterns without noticeable wave interaction result, which were also observed for CDR signatures in kymographs in Chapter 5.

We have further seen that the existence of a recovery time in an active medium not only introduced periodicity into patterns, but in addition underlies the repeated formation of waves from one identical spatial position.

The results presented above crucially relied on the existence of noise. However, so far no motivation was given for the particular choice of the amplitude of $A = 0.15$. In the next section the effect of a variation of noise amplitude will be studied.

6.2 Tuning of the Pattern Formation by Variation of the Noise Amplitude

The effect of noise on the formation of patterns is twofold: it leads to de novo creation but also to the destruction of existing waves, as we have seen in the previous section. Therefore, one expects increasing fragmentation of patterns with increasing noise amplitude.

In experimental data the spatiotemporal correlations of wave signatures of highly fragmented patterns corresponded to significantly lower velocities than that of non-fragmented patterns (Section 5.2, Figure 5.5). The number of CDRs that cells supported simultaneously was thereby not correlated with the pattern type (Section 5.4, Figure 5.15). One might therefore ask if the fragmentation of patterns of an active medium has implications for the characteristic spatiotemporal correlation of wave signatures.

To approach this question the impact of the noise amplitude on wave patterns is studied in the following based on a series of numerical solutions of the FHN system (6.1) under systematic variation of A (Figure 6.2*A1*-*A4*). For each of the values of A of 0.1, 0.15, 0.2, and 0.25, ten runs of the simulations were carried out with different seeds for the random number generator. Since the wave patterns are equivalently well-visible in V and R in the following only the V-field is plotted as it shows, in contrast to the R-field, the refractive zone following wave pulses.

Our qualitative discussion of the outcomes of the simulations in the following is supported by quantifications of the patterns using the same methods and routines that found application for the data of actual experiments. This means kymographs were analysed via binarization and calculation of autocorrelation functions (Section 5.1), which allowed to read off periods (Figure 6.2*C*) and, via application of the Radon transformation, the calculation of characteristic velocities. The variations in the Radon transformation were plotted color-coded in Figure 6.2*D*, which reveals the characteristic velocities as the position of the maxima of the plot (Section 8.9.8).

A visual inspection of the kymographs in Figure 6.2*A1*-*A4* clearly shows that increasing noise amplitudes lead to increasing fragmentation of patterns. At low noise ($A = 0.1$, Figure 6.2*A1*) waves only form rarely. However, this also means that

established waves have long lifetimes. This is due to the fact that both, wave collisions and disturbances due to shots in the noise, are rare at low noise amplitudes, as discussed in the previous section. Consequently wave re-entry occurs at low noise (Figure 6.2*A1*, $250 < t < 450$). The dominant number of waves pulses simultaneously supported by the medium is one at $A = 0.1$ (Figure 6.2*B*).

At low noise amplitudes, the rate of above threshold shots of the noise governs the periodicity of patterns. The reason for this is that, trivially, it requires an above-threshold shot of the noise to form waves, whereas recovery of the medium alone does not lead to wave formation.

With increasing noise amplitude, waves form more frequently. Indeed, presumably up from $A = 0.15$ the recovery time of the FHN system governs the periodicity of wave formation, because the noise alone would provide above threshold situations permanently. Consequently the period between wave formations drastically drops between $A = 0.1$ and $A = 0.15$, which is quantitatively shown in Figure 6.2*C*. The error bars in this plot mark the standard deviation of the period. As the noise-governed time-scale is of a highly stochastic nature and only few wave events occur in each run of the simulations the error bars are very high for low noise amplitudes.

However, with further increasing noise amplitudes also the probability to push the system above threshold out of the refractory state rises; indeed for high noise rates the characteristic period between succeeding wave formations slightly decreases with increasing noise amplitudes (Figure 6.2*C*).

Frequent wave formation goes along with frequent wave interaction events that can be either by direct wave collisions, or interactions via the refractive regions left behind by wave pulses, as discussed in the previous section. Further, at high noise the probability that noise shots destroy existing waves is high. Together these features lead to increasing fragmentation of wave patterns with increasing noise amplitudes. Indeed this trend goes along with an increasing number of simultaneous wave events, as can be seen in Figure 6.2*B*. The number distribution of wave pulses at $A = 0.15$ gives a close match to the distribution for actual CDRs in experiments. The pattern in the corresponding kymograph (Figure 6.2*A2*) qualitatively agrees very well with those in kymographs of experimental data (e.g., in Figure 5.14).

Figure 6.2 (facing page): *The effect of the noise amplitude on the FHN system. A1-A4*: Numerical solutions of the V-field. All kymographs are overlaid with black/white lines of the slope of wave pulses in example *A1* ($v = 0.1$), for comparison of velocities. *B-D*: Averaged quantified characteristics of the patterns from ten repeated runs of simulations for each noise amplitude. *B*: Probability distribution $p(N)$ of pulse numbers. The dashed black line represents the average distribution from experiments (see Figure 5.12). *C*: Period T_p as a function of noise amplitude A (error bars: one standard deviation, line for guidance of the eye). *D*: Velocity (v) distribution as a function of noise amplitude, visualized via the variance of the Radon transformation. The variance is highest for the dominant velocity. Note that the inherent propagation velocity of wave pulses ($v = 0.1$) is not the dominant signal for $A > 0.15$.

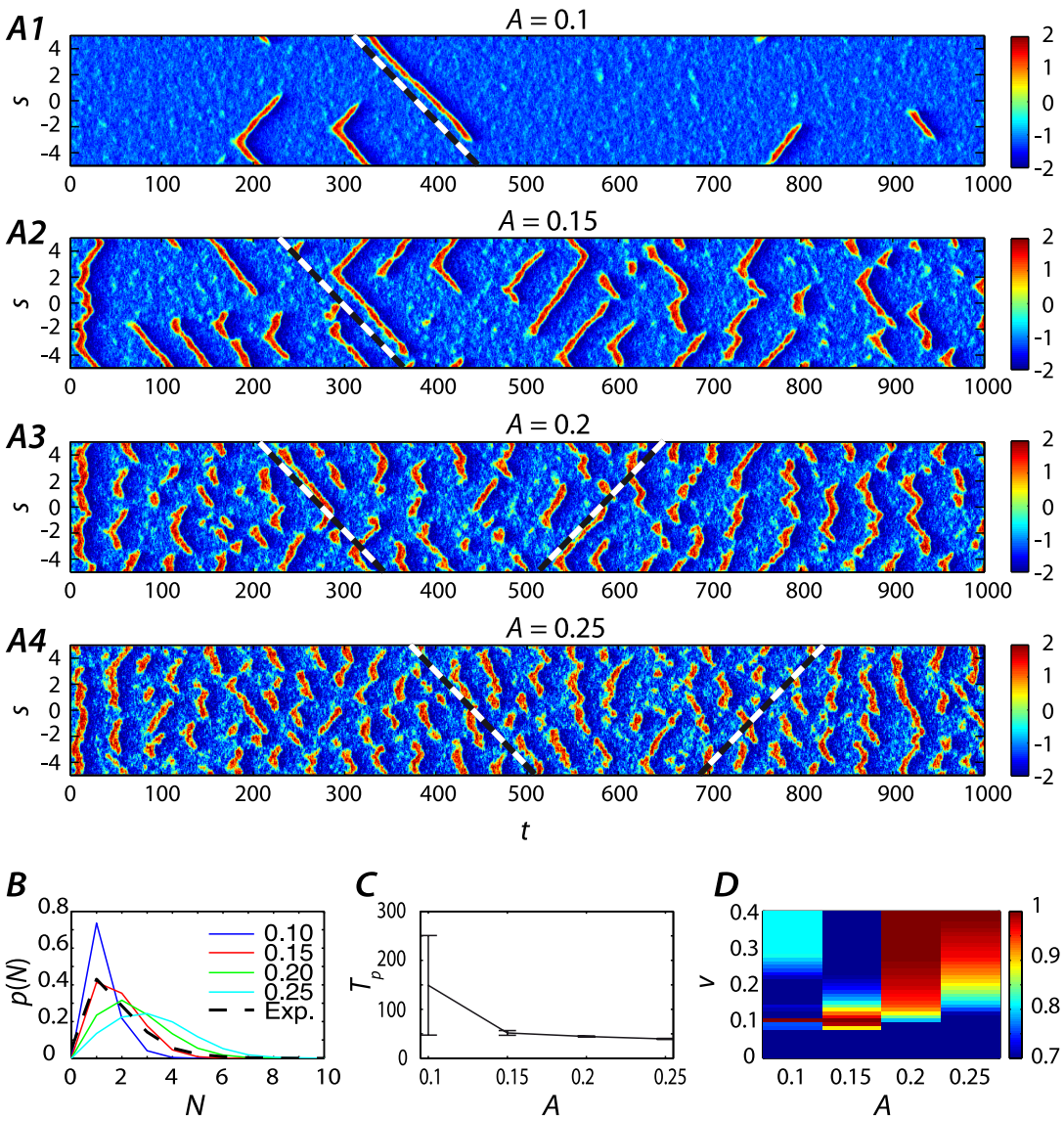
A1
A = 0.1
A2
A = 0.15
A3
A = 0.2
A4
A = 0.25
s
t
B
p(N)
N
0.10
0.15
0.20
0.25
Exp.
C
T_p
A
D
v
A

With increasing noise amplitudes the typical lifetimes of waves decrease. Therefore, their characteristic signature in kymographs, i.e., that of stripe patterns, shifts towards wave fragments, which on first glance reminds of the type of punctual patterns introduced in the previous chapter (see Figure 5.5). Such patterns were marked by spatiotemporal correlations corresponding to slower velocities compared to that of pronounced wave signature ("stripes"). A visual inspection of the spatiotemporal correlations in kymographs as a function of noise amplitude shows that for the numerical data presented here the opposite is true: with increasing noise the wave fragments loose a unique correlation along one single spatiotemporal direction. Moreover they exhibit correlations corresponding to much higher velocities. To simplify the comparison of the characteristic slopes, the kymographs in Figure 5.14*A1-A4* were overlaid with the characteristic slope of Figure 5.14*A1*. The quantification of the characteristic velocities via the Radon transformation of correlation functions supports this observation, as Figure 5.14*D* shows increased broadness of the distributions and enhanced values towards higher velocities.

However, we have to bear in mind that the spatiotemporal correlation of fragments is not identical with that of actual waves. For the latter this correlation is indeed the propagation velocity. In contrast, that of wave fragments results from a complex interplay of noise-induced super threshold regions, diffusion, excitation, and recovery.

In summary, we see that noise indeed can act as a key element of spatiotemporal pattern formation. Increasing noise amplitudes correlate with the fragmentation of patters, the decrease of periods between successive wave events, and an increase of the typical number of wave pulses present simultaneously in the noisy FHN system studied here. Moreover, the spatiotemporal correlations shift towards higher velocities with increasing noise.

6.3 Discussion

CDRs share features of waves in active media. Evidence for this hypothesis was presented throughout this whole work. However, so far only limited comparability was possible between experimental and theoretical data such as those presented in the theory chapter of this thesis (sections 2.3.1-2.3.5). In contrast, with the introduction of disc-shaped cells as a model system for systematic investigation of actin waves a direct comparison between experiment and theory came into reach. This was demonstrated in this chapter based on the juxtaposition of experimental data and numerical results from a noisy FHN system. It could be shown that the theoretical framework of a one-dimensional noisy FHN system captures almost all dynamic features exhibited by CDRs on disc-shaped cells. Indeed, there are only slight details in which the patterns obtained from simulations differ from their experimental counterparts that we will discuss shortly.

This result underlines that CDRs not only share features of active media, but can in fact be very comprehensively described within this framework. It further adds large support to the hypothesis from Chapter 4, i.e., that the complicated dynamics CDRs exhibited on random-shaped cells is due to their interaction with irregular boundaries

and, possibly, also limited availability of a species involved in the wave machinery. The governing processes underlying CDR propagation, however, can effectively be reduced to a simple feedback scheme such as that of the FHN system, as demonstrated here.

The results of this chapter further clearly outline the significance that stochastic processes have in the formation of the spatiotemporal patterns. The consideration of a driving noise allowed to tune the FHN system towards a very close match between experimental and numerical results. Depending on the noise amplitude the periods between successive wave formations were either dominated by the system's recovery time or the probability of the noise to exceed the threshold for wave formation. This observation offers an explanation for the distribution of periods of experimental data shown in Figure 5.8 of the previous chapter. From this perspective the apparent bimodal character of the distribution has one sharp peak ($5\,\mathrm{min} \leq T_\mathrm{P} \leq 7\,\mathrm{min}$), which results from the recovery time, and one broad peak, which is a signature of noise-dominated periods.

Besides the noise only the existence of the typical characteristics of an active medium, such as its recovery time and the collision behaviour of its waves, were needed for the understanding of the processes underlying spatiotemporal pattern formation. However, as the FHN model is an abstract model and was not designed for actin waves, there is no direct interpretation that could be deduced for the actin machinery in CDRs.

Nevertheless, we also encountered the limitations of the formulation of the FHN system that was studied here. For example the approach that was followed to tune the noise amplitude to mimic the fragmentation of patterns of experimental data led to results that were inconsistent with the experimental observations. We can therefore safely discard the idea of high noise being the major reason for pattern fragmentation. Also no examples of wave crossings or unilateral wave annihilation could be found in the numerical outputs but exclusively mutual wave annihilation. It is important to note, however, that collision annihilation is a typical albeit not dogmatic characteristic of active media. As shown by Argentina et al the FHN system does indeed support the crossing of wave pulses under certain conditions [Argentina et al., 2000].

Certainly also a formulation or extension of the FHN model could be found that is able to reproduce the observed patterns even more accurately including the simultaneous support of fragmented and line patterns with conserved numbers of waves. However, such an extension should be built on biologically and physically founded considerations.

In this chapter the role of the noise was mainly that of a trigger of wave formation. It has been shown that noise can in fact also be the reason for wave propagation in active media that are in a sub-excitable regime via stochastic resonance [Kádár et al., 1998]. If this phenomenon has significance for CDRs remains an open question at this stage.

Chapter 7

Conclusions

The phenomenon of ring-shaped actin structures on the dorsal side of adherent eukaryotic cells, termed CDRs, has been puzzling the biological community for several decades [Mellström et al., 1983, Dowrick et al., 1993, Krueger et al., 2003, Payne et al., 2014]. The research on this subject has lead to their sound proteomic characterization and revealed that CDRs are central to, e.g., cell motility and endocytosis, which highlights their biological as well as their medical significance [Buccione et al., 2004, Hoon et al., 2012, Itoh and Hasegawa, 2012, Mercer and Helenius, 2009]. However, the mechanism that orchestrates the protein interplay towards formation of these structures remained elusive.

The central hypothesis underlying this work is that CDRs can be understood as waves in an active medium, which is constituted by the cellular actin machinery. This idea was first proposed by Zeng et al. and is also implied by the work of Peleg et al. [Zeng et al., 2011, Peleg et al., 2011]. However, a detailed experimental survey of this hypothesis is missing. It was the motivation underlying this work to contribute the experimental data that are needed to link the biological knowledge on CDRs to theoretical concepts. This provides the basis for validation of existing models and shows directives for future modelling approaches.

My data gave much support for the idea that CDRs are waves in an excitable system and provided several novel and fundamental insights into the nature of the corresponding wave machinery. The implications for the fields of biology and biological physics will be outlined in the following. This includes results that are specific to CDRs. However, throughout this work also a new methodological framework for systematic studies on protein waves was introduced that has implications for virtually all areas in which protein waves are involved.

7.1 CDRs are Actin Waves in an Excitable Medium

The classification of CDRs as waves of polyermizing and depolymerizing actin is not an established perspective in the current literature from the biological community [Cortesio

et al., 2010, Gu et al., 2011, Hasegawa et al., 2011, Hasegawa et al., 2012]. In contrast, my work clearly shows that CDRs constitute waves in an excitable system. Central to this finding was a new experimental protocol, in which cells were imaged under constant biochemical conditions instead of being subject to growth factor stimulation. I could show that the latter method, which is the standard protocol in the literature [Hoon et al., 2012], does not fully reveal the wave character of CDRs. In contrast, the nature of CDRs as waves of polymerizing actin is obvious on cells that form CDRs spontaneously (Section 3.1.1). The wavefronts usually originated from points, grew outwards as expanding rings that then reversed propagation direction and closed back to points. It was demonstrated based on a range of phenomena that CDRs bear clear marks of waves in active media (sections 4.2-4.5). These comprised several completely novel dynamic features, among them spiral waves and annihilation of colliding wavefronts. Contrary to the accepted picture from the literature [Buccione et al., 2004, Itoh and Hasegawa, 2012] CDRs have a strong tendency to reappear periodically forming breathing modes (Section 4.4). However, also this feature required that no growth factors were used. It was shown based on computer simulations that the apparent contradictions mentioned above can easily be resolved via an interpretation of the process of growth factor stimulation in the active media framework.

The use of growth factors provides convenient means to stimulate synchronous formation of CDRs on a large number of cells. Therefore, growth factors were also used in this work for sample preparation for experiments with fixed cells (Section 3.2). For questions on the dynamics of CDRs, however, the use of growth factors should generally be avoided. In fact my work shows that the established protocol from the literature greatly interfered with the understanding of the dynamical processes underlying CDRs for several decades.

The character of CDRs as that of active waves in an excitable system became especially obvious when the impact of the cell morphology on the wave dynamics was reduced. This was achieved via the enforcement of cells into disc-shapes via microcontact printing (Chapter 5). On this system CDRs were constricted to quasi one-dimensional propagation on a domain with periodic boundary conditions. CDRs formed periodically and propagated with constant velocities exhibiting frequent collisions. The corresponding spatio-temporal patterns could be very closely reproduced with a noise-driven prototype model of an active medium, i.e., the FHN system (Chapter 6). Even though the latter is a simple and abstract model without biological representation it constituted a well-suited basis for the interpretation of the mechanisms of pattern formation on an abstract level as the consequence of spontaneous wave formation, a characteristic recovery time of the medium, constant propagation velocity, and wave collision annihilation. Especially, it highlighted the significance of stochastic processes in the formation of CDRs.

7.2 The Feedback System Underlying the Wave Machinery

The finding that CDRs can indeed be described as non-linear waves of polymerizing and depolymerizing actin raises the question of the nature of the underlying feedback system [Allard and Mogilner, 2013]. While CDRs are well-characterized in their proteomic compositions, the question of the dynamic interplay of the corresponding proteins is not clear. As a matter of fact, CDRs have seen only modest attention from the biophysical community if compared to other model systems for actin waves. Modelling approaches have been conducted by Peleg et al. and Zeng et al., contributing the essential feedback loops to morpho-sensitive species and interaction schemes of RhoGTPases, respectively [Peleg et al., 2011, Zeng et al., 2011]. However, these models are hard to verify experimentally, as RhoGTPases are central to several regulatory processes in cells and three-dimensional live imaging on the time scale of CDR dynamics is beyond the capabilities of microscopy (Section 3.3). Moreover, both models have been shown to partially conflict with experimental results (sections 4.1 & 5.6).

However, it was shown throughout this work that in fact CDRs seem closely related to actin waves in other organisms, which have seen considerably more attention from the biophysical community and have become well-characterized standard systems for studies on actin waves. Especially CDRs share features with actin waves in neutrophils [Weiner et al., 2007] and *D. discoideum* [Millius et al., 2009,Schroth-Diez et al., 2009]. Indeed, the propagation velocities of actin waves are comparable between these systems (Section 5.2). Moreover CDRs exhibit a similar organization of f-actin in form of small motile particles within wavefronts as found in *D. discoideum* [Gerisch et al., 2004] (Section 3.1.2). On the other hand, the response of CDRs to treatment with the actin drug latrunculin A (Section 5.6) was closely reminiscent to that of neutrophils [Weiner et al., 2007].

Most current modelling approaches of actin waves are inspired by neutrophils and *D. discoideum* [Doubrovinski and Kruse, 2008, Carlsson, 2010, Wasnik and Mukhopadhyay, 2014]. Based on the aforementioned similarities to CDRs, the structure of these models is potentially highly relevant for CDRs. For actin waves in neutrophils, the positive feedback loop is assumed to be constituted by autocatalytic properties of Hem-1 [Weiner et al., 2007]. Being a member of the WAVE-family complexes, this protein promotes actin polymerization at the membrane and is presumably inhibited in the presence of f-actin. Since Hem-1 is a component of N-WASP, which has been shown to be a critical element in CDRs [Legg et al., 2007], it might indeed also constitute the positive feedback system in CDRs. It has been shown that the effects of a downregulation of actin polymerization via latrunculin A (Section 5.6) are consistent with equivalent experiments in neutrophils [Weiner et al., 2007]. The fact that CDRs form, in contrast to actin waves in neutrophils, at the dorsal cell side can be explained by a pathway that is mediated by PI3K and PIP_3 in transmission from growth factor signalling events at the dorsal cell side leading to the activation of WAVE1 and N-WASP, as proposed by Hoon et al. [Hoon et al., 2012].

In contrast to the actin waves in neutrophils, those in *D. discoideum* are not

dependent on SCAR proteins, which are *D. discoideum*'s homologue to WAVE proteins in humans, indicating that Hem-1 is not required for actin waves in these slime moulds [Bretschneider et al., 2009]. Instead, the dominant positive feedback mechanism is assumed to be constituted by the autocatalytic properties of f-actin, mediated by filament branching via the Arp2/3 complex. The emergence of micron-sized motile clusters of f-actin in *D. discoideum* could indeed be accounted to autocatalytic properties of actin in a theoretical study [Whitelam et al., 2009], however, it has also been described in a system that additionally includes nucleation promoting factors of actin [Carlsson, 2010]. Furthermore CDRs exhibit a granular substructure of wavefronts in form of small hand fan-shaped actin particles (termed HAPs in this thesis, Section 3.1.2), suggesting a potential relevance of actin autocatalysis also for CDRs. However, it was shown by Legg et al. that inhibition of N-WASP abolishes the formation of CDRs [Legg et al., 2007], which indicates that actin autocatalysis alone is not sufficient to form CDRs. It might, nevertheless, be the cause for the emergence of HAPs. Since it has been shown that the drug used in the experiments on the role of N-WASP, namely wiskostatin, might non-selectively perturb the ATP dynamics of cells, experimental confirmation of the findings by Legg et al. are highly needed [Guerriero and Weisz, 2007].

A unique feature of CDRs is the pronounced degradation of f-actin in wavefront interiors (Section 3.2). The origin of this phenomenon has been proposed to result from the role of CDR wavefronts as consumers of cytoskeletal f-actin [Mellström et al., 1983, Krueger et al., 2003]. This suggests that the wave machinery of CDRs involves elements of models of the substrate depletion kind. In this work it was shown that this framework indeed accounts for aspects of CDR dynamics, e.g., their avoidance of the cell nucleus (Section 3.1.1). However, it cannot be the only reason for actin depletion in CDR interiors. In fact, evidence was shown that a polarity between CDR interior and exterior must exist at the level of regulatory proteins (Section 5.5). A corresponding theory has been proposed by Itoh et al., which is based on an interconversion scheme between PIP_2 and PIP_3 [Itoh and Hasegawa, 2012]. A current study by Hasegawa et al. can be linked to this model and offers an explanation for the suppression of actin polymerization in CDR interiors based on high local concentrations of Arap1. Indeed, waves of PIP have also been shown to be the central mediator of polarity for actin waves in *D.discoideum* [Gerisch, 2010, Khamviwath et al., 2013, Gerhardt et al., 2014].

In the light of the actin basis of CDRs and their considerable heights (Section 3.2) it is an obvious thought that actin availability might influence their dynamics. Indeed, various results throughout this thesis indicate that availability of g-actin plays a central role in the wave mechanism underlying CDRs (e.g., sections 4.1 & 4.3). On disc-shaped cells, CDRs formed repeatedly at high rates, presumably due to high actin availability caused by morphological constrictions (Section 5.3). Also the formation of breathing modes (Section 4.4) can be interpreted from this perspective, as the collapse of CDRs sets free high amounts of actin locally, that then might trigger succeeding wave formation. The most striking evidence, however, was given by the results of experiments involving Latruncunlin A (Section 5.6). This actin drug reduces the amount of available g-actin,

resulting in strong impact on wave patterns and a reduction of the periods of successive wave formations. Actin limitation might indeed also be the cause for the reversal of CDR wavefronts (Section 4.1), as discussed in the framework of the work by Keshet et al. (Section 4.7) [Holmes et al., 2012].

The interpretation of my results built on previous work on actin waves in CDRs, neutrophils, *D. discoideum*, and other organisms from the community of biological physics and the work on the protein composition of CDRs from the biological community. The synthesis of the findings in the aforementioned provide clear directives for future experiments, which are explicitly designed to question the exact nature of the feedback system in CDRs more closely. These comprise, e.g., simultaneous imaging of the dynamics of both, f- and g-actin in CDRs. Moreover, live imaging of PIP_3 and Arap1 will largely contribute to our understanding of the feedback systems in CDRs. Further, in the tradition of my experiments with Latrunculin A, biochemical interference with actin and its polymerization agents would be enlightening. On the level of actin, a promising drug is jasplaklinolide, which promotes actin polymerization. Also the role of Arp2/3 could be addressed via its inhibitor CK-548. Future experiments with wiskostatin are desirable, provided its selectivity for N-WASP could be guaranteed.

7.3 The Impact of the Cell Morphology

The formation and propagation of waves in active media is mediated by the feedback loops of the system. However, we have seen strong evidence at various parts of this work that the morphology of cells was another crucial effector of CDRs dynamics (chapters 4 & 5). In particular, CDRs exhibited pronounced interactions with cell boundaries and the nucleus. This was the basis for the discovery of diverse phenomena of wave dynamics (Chapter 4). However, it also led to poor comparability of data obtained on different cells. This issue was solved by development of a new experimental system (Chapter 5), which constituted a breakthrough for the analysis of CDRs and bears implications that extend to studies of other cellular protein waves. For its design, the interactions of CDRs with cell boundaries and the nucleus were systematically exploited via the enforcement of disc-shaped to cells via microcontact printing.

Cells of disc-morphology constituted a homogenized medium with periodic boundary conditions, on which CDR dynamics was reduced to one-dimensional propagation. Under these conditions, CDRs formed with extremely regular periods and travelled with constant propagation velocities around the nucleus. The uniformity of the resulting patterns is outstanding and has no counterpart in any other experimental system for actin waves. The data allowed the systematic characterization of the propagation velocities and periods of formation based on large sample sizes. Especially, this regularity was the basis for the comprehensive quantitative characterisation of CDRs regarding their propagation velocity and periodicity (sections 5.2 & 5.3).

Given this framework, experiments could reach a new level of precision and com-

parability. It could, e.g., be shown that the propagation velocity of CDRs is correlated with the degree of fragmentation that spatio-temporal CDR signatures exhibited in kymographs (Section 5.2). A further directive for future work was demonstrated with regard to biochemical interference with the wave machinery underlying actin waves using drugs applied via mircrofluidics (Section 5.6). With this, one gains simultaneous control over both, shape and biochemical state of cells.

The simplified geometry of disc-shaped cells further provided optimal prerequisites for the comparison between experiment and theory, which was demonstrated based on numerical data from the FHN system (Chapter 6). The results of experiment and simulations could be analysed and interpreted within the same framework and the use of the same computer algorithms. Fundamental aspects of the spatio-temporal patterns formed on disc-shaped cells could be understood by elementary considerations regarding the collision annihilation of waves in active media and the spatial dimension of the system as well as the recovery time of the active medium.

In summary, these results show the fundamental impact that boundary conditions have on cellular protein waves. This is especially complicating the understanding of actin waves, as these deform the medium in which they are propagating. I expect that the enforcing of stationary cell shapes will serve as a fundamental tool for our future understanding of actin waves in orthogonal direction to the current progress in the modelling concepts of moving cell boundaries [Dreher et al., 2014, Camley et al., 2014]. In a project on the dynamics of lamellipodia-embedded filopodia precursors this system could be applied very successfully [Strübig et al., 2015].

Studies in which features of CDRs such as their ring sizes [Hasegawa et al., 2012] or their lifetimes [Zeng et al., 2011] serve as observables raise questions when viewed in the light of the large impact of the cell morphology on CDR dynamics. Therefore, I propose the use of cells of controlled morphologies for the future research on CDRs and protein waves in general. Even though the dynamic interactions between cellular morphology and protein waves constitute an exciting future challenge for a deeper understanding of cellular morphodynamics, fixed morphologies clearly provide a very suitable starting point for a basic understanding of the protein dynamics decoupled from complicated boundary effects. An elegant albeit fundamentally different experimental approach for the reduction of boundary effects on actin waves has recently been described by Gerhardt et al. [Gerhardt et al., 2014]. The strategy in the latter work is to create giant cells of *D. discoideum* by electric-pulse-induced cell fusion. For the research on CDRs this strategy will likely not be reasonable, because it lets the impact of the cell nucleus unaffected. Rather, the removal of cell nuclei might constitute a promising idea for experiments on CDRs of large sizes.

From the perspective of an active medium description it would be very interesting to advance the studies on the impact of cellular shapes and sizes. In experiments on Min waves in *E. coli* this approach led to broken symmetry of the wave-forming system in short and thick cells. For CDRs experiments with a systematic variation of the diameter of disc-shaped fibronectin patches might reveal potential resonance effects in patterns.

Chapter 8

Materials and Methods

This chapter includes detailed information on the cell culture, sample preparation, and design of the experiments underlying this thesis (Chapters 3-5). Further, information on materials, the data processing, and -analysis are presented here. The depth in which individual aspects are described reflects to some degree the level of innovation and intensiveness of the work that was invested for their implementation. Following this principle sections containing mere technical details are kept short albeit complete, whereas sections that document developmental work are more comprehensive.

8.1 Cell Culture

In this thesis two fibroblast cell lines were studied. One was the standard fibroblast type NIH 3T3 (ATCC®CRL1658^{TM}, "NIH 3T3 WT" in this thesis) and the other a genetically modified variant termed NIH 3T3 X2 [Singh et al., 2011]. NIH 3T3 X2 cells over express the serine/threonine phosphatase POPX2, which is associated with down-regulation of PAK [Koh et al., 2002,Susila et al., 2010]. Compared to NIH 3T3 WT cells, an enlarged fraction of NIH 3T3 X2 cells exhibited CDR formation spontaneously, i.e., without the stimulation of growth factors others than those present in cell media at small background concentrations.

Cells were grown under standard conditions in Dulbecco's MEM containing $3.7\,\mathrm{g\,L^{-1}}$ $NaHCO_3$, $4.5\,\mathrm{g\,L^{-1}}$ D-Glucose (Biochrom, Germany), $100\,\mu\mathrm{g\,mL^{-1}}$ Penicillin/Streptomycin (PAA Cell Culture Company, Great Britain), and 10% Fetal Bovine Serum (Biochrom, Germany). Cells were split at 80% confluency using Trypsin/EDTA (Biochrom, Germany). The cell culture was a gift from Louis Lim (Institute of Molecular and Cell Biology, ASTAR Singapore, Singapore). Cells were mycoplasma free.

8.2 Stimulating CDR Formation with the Growth Factor PDGF

It is the standard procedure in the research on CDRs to stimulate cells with the growth factor PDGF-BB (Section 2.1.5). Most studies use concentrations on the order of 10 ng/(mL). Table 8.1 gives an overview about experiments in which CDR formation was stimulated on different cell lines.

Conc. [ng/(mL)]	Cell line	Study
10	Primary MEF	[Legg et al., 2007]
10	MEF	[Peleg et al., 2011]
20	Primary MSF	[Gu et al., 2011]
20	MEF (NIH 3T3)	[Hasegawa et al., 2012]
30	MEF (NIH 3T3)	[Krueger et al., 2003]
30	Primary HFF	[Krueger et al., 2003]
30	Pancreas epithelial	[Krueger et al., 2003]
30	Prostate cancer	[Krueger et al., 2003]
30	MEF (NIH 3T3)	[Zeng et al., 2011]
40	Human diploid glial	[Mellström et al., 1983]
50	Embryonic kidney	[Azimifar et al., 2012]
50	Fibroblast	[Azimifar et al., 2012]

Table 8.1: *Overview about PDGF concentrations for stimulation of cells in different studies.* MEF: Mouse Embryonic Fibroblasts, MSF: Mouse Synovial Fibroblasts, HFF: Human Foreskin Fibroblasts

In contrast, in this thesis most experiments relied on spontaneous formation of CDRs on the cell line NIH 3T3 X2, which enabled studies of CDR dynamics under constant biochemical conditions. Therefore, no growth factors others than those contained in standard cell medium were used for experiments on the dynamics of CDRs.

However, experiments on the structure of CDRs required fixed cells with preferably high numbers of CDRs in each culture dish. Therefore in the experiments on the structure of CDRs, cells were treated with $30\,\mathrm{ng\,ml^{-1}}$ PDGF-BB 5-10 min prior to fixation to enhance CDR formation, in accord with other studies on NIH 3T3 WT cells [Krueger et al., 2003, Zeng et al., 2011, Hasegawa et al., 2012].

8.3 Microfluidic Perfusion System

Experiments with varying buffer conditions were realized with the help of a computer-controlled perfusion system that was developed throughout this work together with the master student Malte Ohmstede. Figure 8.1*A* shows a sketch of the setup. In the following, the single components of the system are introduced.

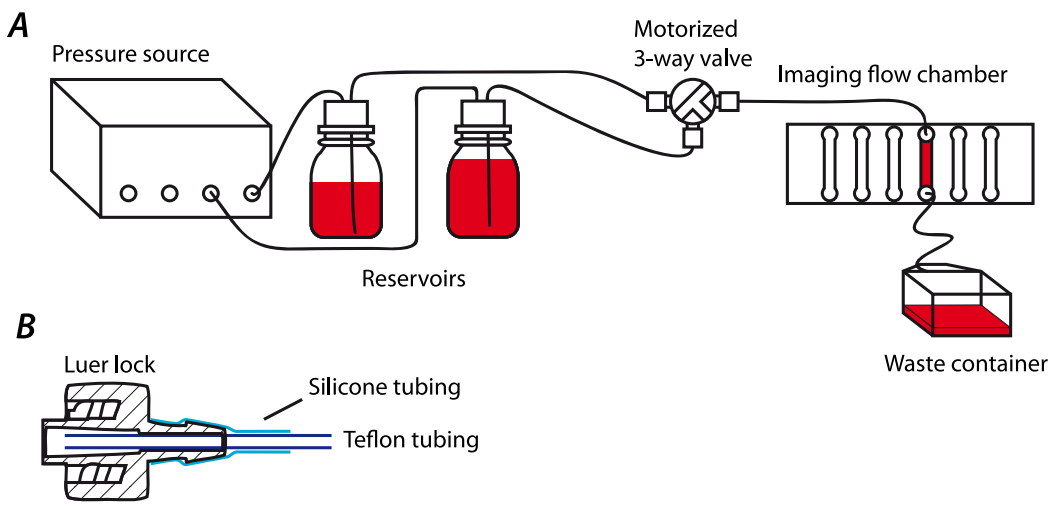

Figure 8.1: *Microfluidic flow system. A*: Overview about functional parts of the setup. *B*: Scheme to establish gas-tight connections between Luer locks and Teflon tubing.

I used commercially available imaging flow chambers (Ibidi sticky-Slide VI$^{0.4}$, Ibidi, Germany) that consisted of a bottomless plastic slide into which the channels and adapters for the tubing were integrated. Glass slides could be mounted to the lower part of plastic dishes via a biocompatible adhesive tape, sealing the channels. Ibidi sticky-Slides were equipped with Luer locks for the connection between flow chamber and tubing. I used Teflon tubing (Techlab GmbH, Germany) for its properties of being biocompatible and impermeable to gasses, which prevented the formation of air bubbles in the flow system. Teflon is of very low elasticity and therefore could not be mounted to Luer locks (IDEX Health and Science, USA) directly. I used short pieces of silicone tubing as adaptors for the mounting of Teflon tubes to Luer locks. Silicone is permeable to air and tended to introduce bubbles into the tubing. For that reason, the Teflon tubing (outer diameter: 0.75 mm) was introduced into the Luer locks (outer diameter: 2.4 mm) (Figure 8.1*B*). With this setup it was the Teflon and not the silicone that was in contact with the fluid. Therefore, no air bubbles could enter the system during experiments. To prevent de novo air bubble formation in experiments by de-gassing of the medium upon warm up, the completely mounted and filled setup was placed in an incubator at 37 °C for 4 h prior to experiments. All air bubbles formed during this equilibration were then flushed out with high pressure. The system then remained bubble-free in the actual experiments.

The flow chamber was tubed to a motorized 3-way valve (Discofix 3SC, Braun, Germany) that was connected with two reservoirs of cell medium of which one usually contained cell medium with Latrunculin A while the other contained standard cell medium. The reservoirs were made from 50 ml-Duran flasks (Duran Group, Germany).

The lids of the flasks were tightened to air with O-rings and equipped with self-made threads that allowed to mount Luer-locks to it. Each flask was connected to the flow system with a Teflon tube that was immersed into the fluid and to a multi-channel precision pressure controller system (P^2CS, Biophysical Tools). Further, the flow chamber was connected to a container for collection of waste fluid.

The 3-way valve was controlled by a servo motor (RS-22YMB, Modelcraft, USA) via a micro controller board (Arduino Uno, Arduino, Italy), which was in turn controlled by a computer (Raspberry Pi, Raspberry Pi Foundation, Great Britain) via an interactive GUI developed in the Master's thesis of Malte Ohmstede. The GUI also controlled the pressure source and therefore allowed to run fully automated experiments with varying buffer conditions via a newly developed script language. A complete description of the perfusion system is the subject of the Master's thesis of Malte Ohmstede [Ohmstede, 2015].

8.4 Microcontact Printing

Microcontact printing is a technology that allows to print proteins in patterns of well-defined geometries on substrates such as glass. Using proteins facilitating cell adhesion this technology can be used to force cells into specific morphologies. In the scope of this thesis, microcontact printing served to form cells into disc-shapes for systematic investigations of CDR dynamics.

In the last few years, microcontact printing has gained enormous popularity with the consequence that there are well-established techniques available for its implementation [Folch and Toner, 2000, Théry et al., 2006, Azioune et al., 2010, Berre et al., 2014]. In this thesis a protocol by Théry and Piel was followed [Théry and Piel, 2009].

In the following the steps for production of protein stamps and the actual stamping of proteins are illustrated in brief. This brevity is justified by the comprehensiveness of the protocol by Théry and Piel. Only the parts of this thesis that deviate from the protocol by Théry and Piel are described in more detail.

8.4.1 Fabrication of Protein Stamps

Figure 8.2 summarizes the steps involved in the printing of adhesive protein patches for controlled cell adhesion. The first step is the production of a silicon mould that serves the later casting of PDMS-made protein stamps (Figure 8.2*A*-*B*). Deviating from the protocol by Théry and Piel the silicon mould was etched directly into a silicon wafer, resulting in a silicon master that was resistant to organic solvents, which facilitates a long lifetime. The wafer layout consisted of discs, and other shapes, of different sizes, whose areas were chosen based on contact area measurement of a large number of adherent cells (Appendix: Section 9.4). The layout was drawn using AutoCAD 2013 (Version G.55.M.208, Autodesk) and then printed on transparent foil (Zitzmann GmbH, Germany). The foil served as a template of the structures in the micro fabrication

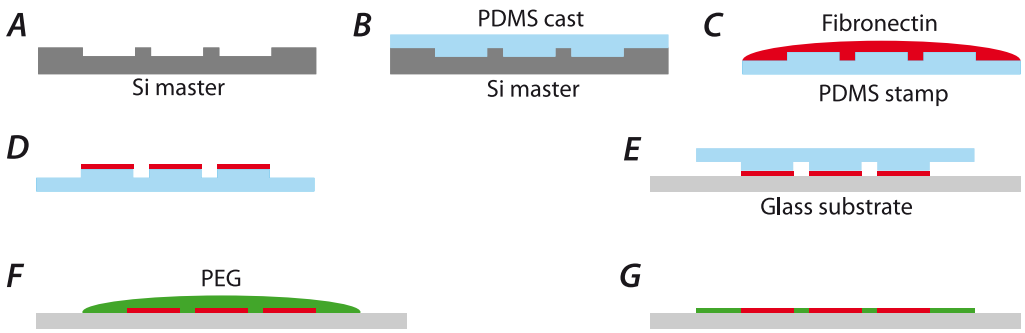

Figure 8.2: *Microcontact printing.* *A*-*G* show the different stages of the production of the stamp (*A*-*B*) and the actual steps involved in microcontact printing (*C*-*G*).

processes based on deep reactive ion etching (IMSAS, University of Bremen, Germany). The silicon master processed this way carried the negative of the structures for production of PDMS (Sylgard 184 silicone elastomere) stamps and could therefore serve as a mould for PDMS casting (Figure 8.2*B*).

8.4.2 Printing of Adhesive Protein Patches

For fibroblast cells, the extracellular matrix protein fibronectin serves as a signalling factor indicating cells the presence of connective tissue and thus suitable adhesion conditions [Hynes, 1992]. Fibronectin is therefore an ideal protein for microcontact printing of patterns for fibroblast adhesion and found application in this thesis.

Prior to the actual stamping glass substrates were treated using an argon-plasma generated in a Kinpen 1 plasma pen (Neoplas Control, Germany). This step serves the adhesion of the protein on glass surfaces by making the surface strongly hydrophilic. The surface of PDMS stamps carrying the negative patterns were then immersed in a drop of a 50 µg mL^{-1} fibronectin (Roche) solution and incubated for 20 min (Figure 8.2*C*). After removal of the drop a thin layer of fibronectin had deposited on the stamp and could be stamped on the glass surface (Figure 8.2*D*-*E*). Subsequent to fibronectin stamping the non-coated regions, where no cell adhesion was wanted, were exposed to poly-l-lysine-PolyEthylene Glucol (pll-PEG, SuSoS Surface Technology) solution for 20 min, resulting in fibronectin patches embedded in pll-PEG surroundings (Figure 8.2*F*-*G*). This resulted in repelling properties of the regions coated with pll-PEG. The printed substrates were then washed with and stored covered with PBS.

Before seeding of cells on printed substrates, the PBS covering the protein patterns was replaced with DMEM. The imaging dishes were then stored in an incubator at 37 °C for 30 min to prepare them towards physiological conditions. Cells were harvested at 70% confluency using trypsin/EDTA, centrifuged and re-suspended in fresh DMEM. For experiments with open imaging dishes, the cell suspension was diluted to 5×10^4 cells/mL, gently mixed, and then plated in a volume of 1 mL on the pre-warmed

imaging dishes. For experiments with Ibidi Sticky Slides the same protocol was followed, except that the density of cells was 8×10^4 cells/mL. Cells were allowed to adhere for 15 min and from that time point on checked in 5 min intervals for proper spreading under a microscope. Once the cells had settled at a sufficient density the sample was gently washed with 20 ml PBS and subsequently rinsed with 10 ml of DMEM to ensure that cells were covered with pure DMEM. When using flow channels non-adhered cells could simply be washed out using the microfluidic system described in Section 8.3.

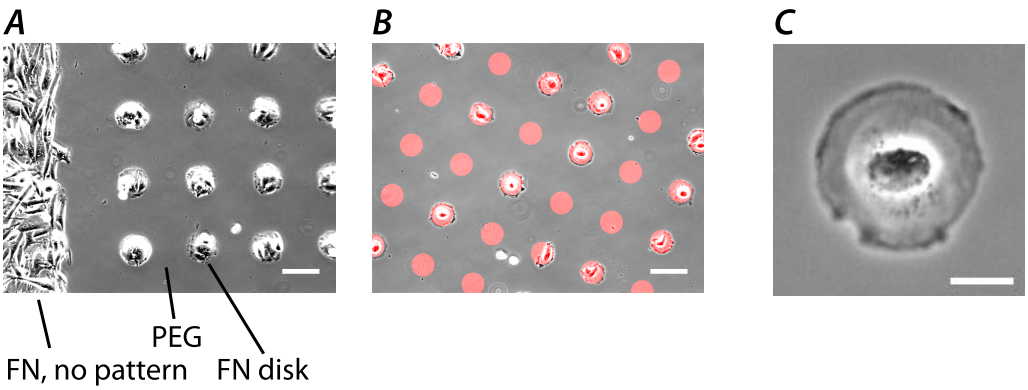

Figure 8.3: *Controlling cell shapes and positions with microcontact printing.* *A*: high cell density, *B*: typical density used in experiments. Red discs highlight patch positions. *C*: Enlarged ROI of a cell from *B*. Area of the discs: $3000\,(\mu m)^2$, Scale bars: *A*&*B*: $100\,\mu m$, *C*: $25\,\mu m$.

Figure 8.3 shows the controlled cell morphology and arrangement achieved via microncontact printed substrates. For the purpose of demonstration of cell arrangement, a large number of cells was plated on a patterned substrate. A region close to the edge of the stamp was imaged, showing the border between patterned and non-patterned substrate. Cell adhesion is totally prevented in PEG-coated regions, while fibronectin (FN)-coated regions are covered with cells. (Figure 8.3*A*).

For actual experiments lower cell numbers must be plated. Therefore in real experiments not every fibronectin patch was occupied by a cell Figure 8.3*B*. Typically up to ten percent of NIH 3T3 WT cells on $3000\,(\mu m)^2$-substrates had suitable morphology for imaging. In the remaining cases the positions were either empty, occupied by more than one cell, or by cells that were either too large or too small for the adhesion area offered.

8.5 Imaging

In this thesis various techniques of imaging were used to account for the diverse questions on the structure and dynamics of CDRs. Two different microscopes were used.

All live cell imaging was performed on an Axio Oberver.Z1 equipped with an AxioCam

Mag.	Type	Contrast	NA
2.5x	EC PlnN	BF	0.075
10x	Achro Pl	PH	0.25
40x	Pln Apo	PH, DIC	0.95
63x	EC PlnN Oil	PH, DIC	1.25
100x	α-Pln Apo Oil	DIC, TIRF	1.46

Table 8.2: *List of objectives that found application in this thesis.* BF: bright field, PH: phase contrast, DIC: differential interference contrast, TIRF: total internal reflection fluorescence, NA: numerical aperture.

MRm digital camera. Microscope and camera were controlled via the software AxioVision (Version 4.8.2.0). All components mentioned above were from Zeiss microscopy, Germany. The imaging system was controlled via a Fujitsu CELSIUS R650 high-end workstation with an Intel CPUQuad Core XEON 5430 2,66 GHz.

The objectives of the Axio Observer.Z1 that found application in this thesis are listed in Table 8.2. The 2.5x objective served for overview images of microfluidic channels and cell localisation. The 10x objective was extensively used for imaging of CDR dynamics. Its low resolution facilitated long-term imaging with minimal focus drift and its low magnification the imaging of several cells in parallel. The objectives with 40-100x and high resolution were used for experiments regarding the structure and substructure of CDRs and the actin distribution within CDRs. The microscope further allowed for additional magnification by a factor of 1.6 using an optovar lens. This lens was used in conjunction with the 10x objective for experiments on the contour dynamics of CDRs.

For fluorescence imaging samples were illuminated with a HXP120 mercury lamp (Zeiss microscopy, Germany), a 488 nm BrightLine HC filter (AHF Analysetechnik, Germany), and a 76 HE reflector filter set (Zeiss microscopy, Germany). For TIRF imaging a laser of 561 nm wavelength was used (part of a Zeiss TIRF system).

The Axio Oberver microscope was equipped with an incubation system consisting of Heating Unit XL S, Temp Module S and a Heating Insert P S1 allowing for heating of the whole microscope and the sample holder respectively. Physiological CO_2 conditions were achieved using the CO_2 Module S. All experiments were carried out at a temperature of 37 °C and 5% CO_2 (all incubation components: Pecon GmbH, Germany/Zeiss microscopy, Germany).

The second microscopy system for confocal imaging was a LSM 780 (Zeiss Microscopy, Germany) laser scanning microscope equipped with a Plan-Apochromat 63x (numerical aperture: 1.4) objective. Rhodamin dye was excited with a laser line of 561 nm and DAPI dye with 405 nm. The detector range of the spectral photomultiplier was set to 570-632 nm for Rhodamin and to 415-558 nm for the DAPI channel. The size of the pinhole was set to one Airy unit for each channel (141 µm for Rhodamin and 45 µm for DAPI).

8.6 Software

AxioVision (Version 4.8.2.0, Zeiss Microscopy, Germany) was used for control of the microscope for live cell imaging and image acquisition on the Axio Observer.Z1. On the LSM 780, ZEN System was used.

For viewing of imaging data ZEN 2012 lite found application (Carl Zeiss Microscopy).

Image processing was carried out using FIJI [Schindelin et al., 2012] and MATLAB2012b (The Mathworks) using mostly custom-written routines. Within Matlab, the image processing toolbox and the signal processing toolbox (Vers. 8.0.0.783, R2012b) were used.

Numerical integration of systems of partial differential equations was done in Matlab and XMDS2 [Dennis et al., 2013].

Statistical test were carried out in r (version 3.2.0) [R Development Core Team, 2008].

The drawing of the wafer layout for fabrication of stamps for microcontact printing was done in AutoCAD 2013 (Version G.55.M.208, Autodesk). Figure 3.9 was drawn and rendered in 3-d Studio Max by Sven Cordes.

Classification, filtering and archiving of data was done in Excel (Version 14.1.0, Microsoft).

The control software for the microfluidic system was written in C and Python programming language by Malte Ohmstede.

All plots were produced in Matlab. The figure layout was composed in Illustrator CS3 (Version 13.0.2, Adobe).

This thesis was written in LaTeXusing TexMaker 3.0.2.

8.7 Experimental Setups

In the following sections the experimental setups of the individual results chapters are summarized.

8.7.1 Experiments on the Structure of CDRs

Numerous different imaging strategies were used for the experiments on the substructure of CDRs, according to the diverse research questions. Each individual experiment is described separately in the following and in the order of appearance in the text flow.

The imaging of the substructure of CDRs via phase contrast, actin fluorescence, and DIC in Section 3.1.2 and Figure 3.4 was based on fixed cells. For this, NIH 3T3 X2 cells were fixed using 2% glutaraldehyde (5 min) in PBS, washed with PBS and then permeabilized with Triton X-100 (5 min). Cells were then stained with DAPI (Roche, Germany) for the cell nucleus and Rhodamin/Phalloidin (Biotium, USA) for f-actin (10 min each) according to the vendor's protocol. The samples were then washed and imaged with the Axio Observer.Z1 using the 63x objective from Table 8.2.

Imaging of actin dynamics (Figures 4.7 and 3.5) was based on cells that were transiently transfected with pLifeAct-TagGFP2 or pLifeAct-TagRFP (Ibidi, Germany) using Lipofectamin2000 (Invitrogen) and according to the manufacturer's protocols. The further sample preparation was as described in Section 8.7.2. For imaging, the Axio Observer.Z1 was used with physiological incubation conditions and with the 40x and the 63x objective from Table 8.2 at frame rates of 3 s.

For the following, we refer to the experiments described in Section 3.2. For TIRF imaging, resulting in data as shown in Figure 3.6, NIH 3T3 WT cells were stimulated with PDGF, fixed as described above and then imaged with the Axio Observer.Z1 and the 100x TIRF objective (Table 8.2). The laser angle was changed between epi and TIRF angle for the corresponding mode of illumination.

The sample preparation for confocal imaging resulting in Figure 3.7 were as follows. NIH 3T3 WT cells were stimulated with PDGF, fixed and stained for actin via Rhodamine/Phalloidin and for the nucleus with DAPI as described above and then imaged under the LSM with the setting given in Section 8.5. The z-spacing was set to 0.65 µm to get maximal vertical resolution at acceptable intensity loss due to photobleaching.

DIC optical sectioning resulting in z-stacks as shown in Figure 3.8 was performed on living NIH 3T3 X2 cells. The samples were prepared as described in 8.7.2. The Axio Observer.Z1 was incubated for physiological conditions set to DIC imaging mode with the 100x objective (Table 8.2). The sample was imaged in optical sectioning mode with a vertical spacing of 0.26 µm and at maximal possible frame rate (time between successive images < 0.1 second).

8.7.2 Long-Term Experiments Under Constant Biochemical Conditions

The results described in Section 3.1.1 and Chapter 4 were based on experiments under constant biochemical conditions. Except from Figure 4.7, in which fluorescence microscopy was used, all data were acquired with low-resolution phase contrast microscopy. In the following, the experimental procedure for preparation and conductance of long-term experiments under biochemical constant conditions is described.

One day prior to imaging, NIH 3T3 X2 cells were plated at intermediate confluency on plasma-treated glass bottom dishes (Zellkontakt, Germany). The next day, most cells were spatially isolated, i.e., they did not have contact to other cells. Directly before imaging, cells were washed with Phosphate Buffer Saline (PBS) and fresh DMEM containing 10% FBS was added to the dishes. The sample was then mounted into the incubator of the microscope (Axio Observer.Z1) and allowed to thermally adjust for 20 min before the imaging was stated. The microscope was pre-heated for several hours before the start of experiments to minimize focus drift.

For the observation of cells under constant physiological conditions NIH 3T3 X2 cells were imaged for 12-24 h in standard cell media. The temperature in the incubation unit was 37 °C and the CO_2 content of the humidified air was 5%. For imaging, the 10x phase contrast objective from Table 8.2 was used in conjunction with an optovar

lens providing an additional factor of 1.6 for the total magnification. With this setting, one pixel spacing in the image corresponded to a distance of $\Delta x = 0.4\,\mu\text{m}$ in real space. The low-resolution of this objective was sufficient to resolve CDRs and low enough to guarantee focus-stability for the total time course of long-term experiments. Test experiments and subsequent kymograph analyses revealed that during a typical life course of a CDR a maximal velocity of $v_{\max} = 0.13\,\mu\text{m}\,\text{s}^{-1}$ could be found for the normal wavefront displacement. Sampling intervals below $\Delta t = \frac{\Delta x}{v_{\max}} \approx 3\,\text{s}$ were thus not reasonable, because a CDR wavefront at high speeds would on average not move by a distance of one pixel in the computer image between two frames. Lower frame rates, on the other hand, would have led to displacements of more than one pixel on average for fast CDR wave fronts, which would have led to problems for the routines used for CDR contour tracking. Thus, the optimal frame rate of $\Delta t = 3\,\text{s}$ was chosen for long-term experiments.

8.7.3 Experiments with Disc-Shaped Cells

Ibidi Sticky-Slides allow to combine microcontact printing with the perfusion system described in Section 8.3. Therefore, all experiments on micro patterns were carried out in microfluidic flow chambers to achieve no-evaporation conditions. Fibronectin patterns were stamped onto the bottom slide of Ibidi Sticky-Slides as described in sections 8.4.2 and 8.3. For this the positions of the channels were outlined on the glass bottom with a marker. Protein patches were stamped into the marked areas and the bottom part was then mounted to the chamber. The incubation of the glass substrate with PEG and the succeeding washing steps were performed by introduction of the corresponding solutions into the flow channels.

Cells were plated on arrays of disc-shaped fibronectin patches and allowed to adhere and spread for 15-20 min. Non-adhered cells were washed out via the flow control system and the imaging was started. The xyz-coordinates of 8-12 different positions within the same dish were stored in the imaging software. A time-lapse recording was set up that would drive the xy-stage of the microscope repeatedly to all positions yielding time-lapse sequences of all positions simultaneously. Typically, 30 protein patches were visible in each field of view. However, not every position was occupied by exactly one cell; some positions remained empty while others were occupied by more than one cell (Figure 8.3*A* & *B*). Also, some cells were too big or too small for the available patch size of $3000\,(\mu\text{m})^2$. The nuclei of cells that were too big for a substrate covered almost the complete area, leaving no space for CDR formation. Cell that were too small for the substrates only partially covered the substrate and therefore had no disc-like morphologies. Typically one to two cells in each field of view exhibited rotating CDR dynamics.

The frame rates were typically 10-15 s. The time stamps of all images were stored and fed into the image processing routines to account for deviations in the time increment due to delays caused by the mechanical movement of the xy table.

8.8 Numerical Simulations

Numerical solutions of systems of coupled partial differential equations were carried out in Matlab and XMDS2. Within Matlab the solver *pdepe* was used for integration. XMDS2 was utilized for solving two-dimensional systems and those that included noise [Dennis et al., 2013]. For the latter, a semi-implicit Stratonovich integration scheme was used with fixed Wiener increments. Within XMDS2-routines spatial derivatives were calculated in Fourier space. A step-width of typically 10^{-4}-10^{-3} in dimensionless time was used in integration. The correct convergence of the solution was verified via comparison of the solutions to the results of an integration with half step size. To ensure reproducibility of results the seeds of the random number generators were saved and could then be used to replicate results.

8.9 Data Analysis

Time-lapse sequences of micrographs play a fundamental role in this thesis; virtually all results were obtained via microscopic imaging. In some cases the extraction of quantitative data from time-lapse sequences required extensive image processing. This holds especially true for the position detection of CDR wavefronts. In the following the methods for contour detection and the derivations of contour velocity and curvature are introduced, followed by a description of the analysis of kymographs via autocorrelation functions and Radon transformations.

8.9.1 Representation of CDRs as Contours

On disc-shaped cells the movement of CDRs was restricted two one-dimensional space and could therefore easily be described by circular kymographs. On cells of random shapes, however, CDR shapes and movement could be complex prohibiting the use of kymographs as a general tool for quantification of their dynamics. Therefore an alternative approach of the quantification of CDR morphodynamics was followed, which is the analysis of the contour evolution of CDRs. From contours quantities like, e.g., propagation velocities and geometrical features like curvatures can be calculated.

The representation of image features by curves or contours is a common approach in digital image processing and the strategies for curve or contour detection make up a whole field in computer vision. A prominent example is the problem of edge detection in which the contour of an object is the subject of interest [Gonzales et al., 2004, pp. 384] [Gonzales and Woods, 2008, pp 692] [Burger and Burge, 2010, pp. 120]. In the research of the morphodynamics of cells the concept of the representation of cells by its contours and the succeeding analysis of its dynamics has proven a highly fruitful approach [Dubin-Thaler et al., 2004, Machacek and Danuser, 2006, Dubin-Thaler et al., 2008, Machacek et al., 2009, Ryan et al., 2013].

Provided the whole object is visible in an image its contour is a closed and continuous curve. In contrast, CDRs are not objects in a classical sense. Rather, they are parts

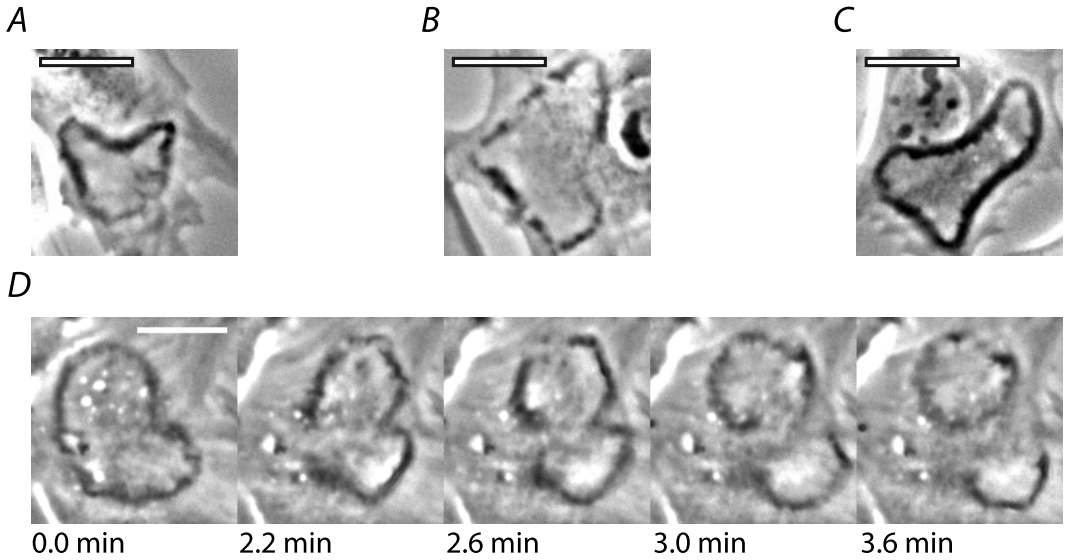

Figure 8.4: *Contour representation of CDRs. A-C*: CDRs of complex shapes that can be represented by contours. *D*: Time-lapse of a CDR that cannot be represented by a contour without ambiguousness. The CDR splits into one circular (upper part of the image) and one arc-shaped piece (lower part of the image). During the fission process, a new piece of contour is formed that makes up the lower part of the circular shape. All scale bars: $25\,\mu\mathrm{m}$

of the object cell, characterized by local maxima in actin concentration and vertically protruding cell membrane. Even though their name implies that CDRs are circular structures, in fact they can have complex geometries and do not necessarily have closed shapes. CDRs can even be observed to split and fuse. Figure 8.4 opposes CDRs that can be represented by contours with CDRs that cannot be represented by contours and therefore summarizes some characteristic behaviours that contradict a general contour description of CDRs. Therefore, the contour representation of CDRs can only proceed within certain limits and necessarily goes along with some assumptions regarding their properties. These assumptions are that CDRs are represented by a characteristic signals in images and that CDR shapes can be described as a continuous, parametrized function. With the use of phase contrast microscopy or fluorescence microscopy with stained actin, CDRs usually form strong contrast and correspond to dark or bright regions in images respectively. This means, the first assumption is met under appropriate imaging conditions. In Figure 8.5 images obtained on the same cell in phase contrast and fluorescence with stained actin are juxtaposed. The dark signature of the CDR in phase contrast is surrounded by two local maxima in intensity due to the formation of the characteristic halo with this imaging technique. The minima in phase contrast co-localizes with the maximum in actin fluorescence, the difference in position is $0.2\,\mu\mathrm{m}$ in this example, which is a typical value.

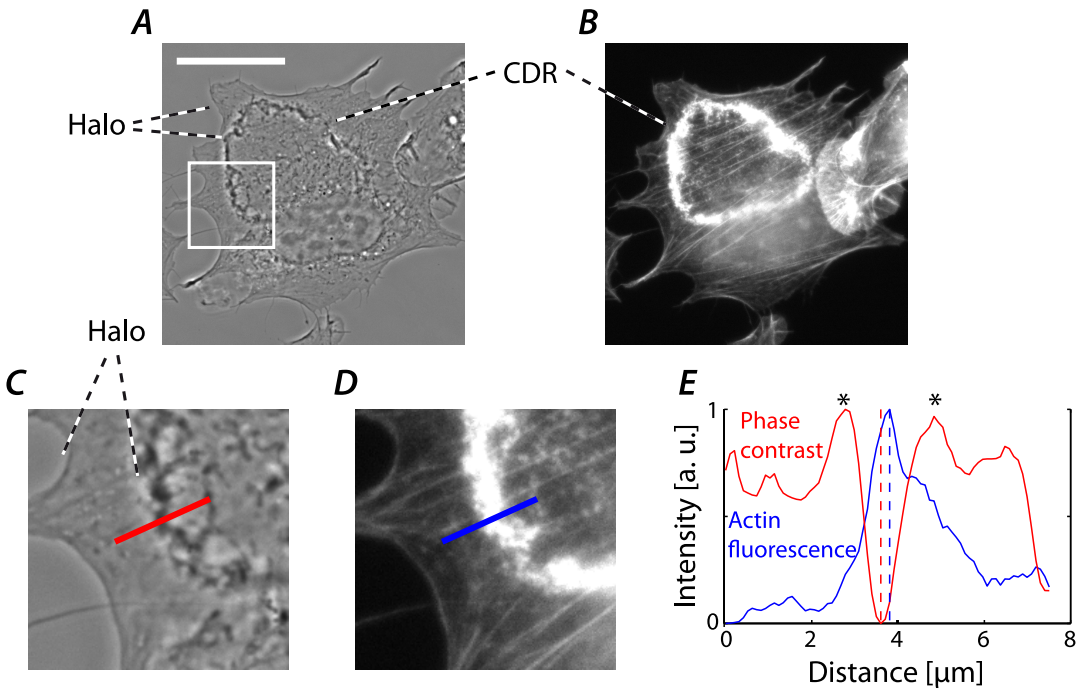

Figure 8.5: *Signature of CDRs in phase contrast and fluorescence imaging.* A CDR was imaged in phase contrast (*A*) and fluorescence microscopy with stained actin (*B*, pLifeAct-TagRFP stain). *C* and *D* are close up views of the ROI highlighted in *A*. CDRs are surrounded by halos in phase contrast images. *E*: normalized intensity profiles sampled at identical positions (lines in *C* and *D*). Maxima of fluorescence (dashed blue line) co-localize with minima in phase contrast (dashed red line). Scale bar: $25\,\mu\mathrm{m}$.

The second assumption, however, cannot be addressed technically. Instead, the analysis had to be restricted to CDRs of closed shapes.

In practice it proved optimal to use a two-step process for contour detection of CDRs. The first relies on active contours while the second is based on local fits for contour refinement. Both methods can be used iteratively in the sense that the estimated contour position by one run of the algorithms can be refined through additional iterations. This has the very useful consequence that it allows to track moving CDRs in time-lapse sequences. Doing so, the current position of a CDR can be used as the first estimate of its position in the next frame etc. Both methods are introduced in brief in the following together with the protocol of data processing that was followed for contour detection of the data presented in Section 4.1.

8.9.2 Active Contours

Active contours are curves that iteratively change their shape and position in an image based on the action of forces that can be calculated from the shape of the the curve and its position in the image. Image-derived ("external") forces are chosen in a way that contours are driven towards the features of interest of images that shall be represented by contours. The contour itself is modelled as an elastic object that tends to contract and resists strong deformations due to the action of "internal" forces. Internal and external forces are derived from their respective energies that describe the system in form of the Hamiltonian $\mathcal{H}$.

Active contour, or "snake", algorithms have a long history in digital image processing [Kass et al., 1988]. They allow fast convergence and only intermediate computational power, because they only require the processing of the pixels in the direct surrounding of a contour. Normally, this only makes up a small fraction of the total number of pixels in an image.

Internal energies usually correspond to the mechanical energies of a stretchable and bendable thin rod. These energies are therefore minimal when the curve is a short and straight object. This implies that high curvatures, such as sharp kinks and jumps, are energetically costly, which imposes an inherent smoothness constraint to active contours. It also implies that curves would tend to shrink to infinitely small size if they were only subject to internal energies. In fact, however, the aim is to attract active contours towards features of the image like, e.g., edges, or in the case of CDRs imaged in phase contrast, minima of image intensity. This is achieved via the external energies. These energies are chosen in a way that the image is transformed into a potential landscape that has local minima at positions that are the desired positions of the contour.

Feature localisation via active contours starts from an initial guess of the contour position. Considering their contractile properties, this initial guess is usually a contour surrounding the true position. Conformation and position are then changed iteratively until a minimum in energy is obtained. The contour position is then defined as the position where an active contour has minimal energy.

The implementation of active contour algorithms in this work is based on the following energy functional as described by [Xu and Prince, 1998]:

$$\mathcal{H} = \int F \mathrm{d}s = \int \left[\frac{\alpha}{2} \left| \frac{\partial \vec{r}}{\partial s} \right|^2 + \frac{\beta}{2} \left| \frac{\partial^2 \vec{r}}{\partial s^2} \right|^2 + E_{\mathrm{ext}}(\vec{r}(s)) \right] \mathrm{d}s. \tag{8.1}$$

This functional assigns an energy value to a contour, which depends on its shape and its position. The shape-induced energy is given by the term weighted with the parameter α, which corresponds to a tension, and a measure of its curvature, described by the term weighted with β. The position of the contour in the image results in the external energy $E_{\mathrm{ext}}(\vec{r}(s))$, which is the image intensity in our case. This results in active contours with an affinity to dark regions.

The position of the active contour at the true CDR contour corresponds to a minimum of the energy functional. This minimum is computationally found by iterative minimization of $\mathcal{H}$. The minimum of $\mathcal{H}$ fulfils the following Euler-Lagrange equation [Bronstein et al., 2008, p. 620]

$$\frac{\partial F}{\partial r_i} - \frac{\mathrm{d}}{\mathrm{d}s} \left(\frac{\partial F}{\partial r_i'} \right) + \frac{\mathrm{d}^2}{\mathrm{d}s^2} \left(\frac{\partial F}{\partial r_i''} \right) = 0.$$

Hence, a deviation from the minimum requires the contour to change position. This is achieved via an iterative minimization algorithm in which the contour performs steps of

$$v_i = \alpha r_i'' - \beta r_i'''' - \frac{\partial E_{\mathrm{ext}}}{\partial r_i} \tag{8.2}$$

$$\text{with } r_i'' = \frac{\partial^2 r_i}{\partial s^2} \text{ and } r_i'''' = \frac{\partial^4 r_i}{\partial s^4} \tag{8.3}$$

until an equilibrium is reached. Physically, this can be seen as the balance of the internal and external forces by a dissipative force resulting from the motion in, e.g., a viscous environment.

To prevent contour points to move in tangential direction, the movement was restricted to the local normal direction of a contour. Without this constraint, contour points tended to move tangentially along the contour and to assemble into global minima of image energies.

For numerical stabilization, the calculation of the external energy was subsequent to image smoothing via convolution with a Gaussian. The differentials of second and fourth order were realized using a finite difference scheme of the form

$$\frac{\mathrm{d}^2 f}{\mathrm{d}s^2} \approx f_{s-1} - 2f_s + f_{s+1}$$
$$\frac{\mathrm{d}^4 f}{\mathrm{d}s^4} \approx f_{s-2} - 4f_{s-1} + 6f_s - 4f_{s+1} + f_{s+2}.$$

The integration of the equation of motion was performed using an one-step explicit Runge-Kutta scheme with Matlab's *ode45* function.

8.9.3 Fit-Based Contour Detection

Using active contours, the true contour of CDRs could be approximated in a robust and computationally effective way. The resulting contours approximated the true position of CDRs well, although they were usually smoother than the true CDR contour. The reason for this was the impact of the mechanical properties of active contours that tended to favour smooth contours. Since the CDR contours should be analysed regarding their curvature in this work, the bias in smoothness as resulting from active contours was not acceptable. Therefore, the contours in every frame of the time-lapse sequence were re-positioned using a fit-based contour detection. For this contours were positioned to the minima of cubic fits to the local intensity profiles in local orthogonal direction. Since active contours converged close to the true position of CDRs, i.e., the local minima in phase contrast images, the length of profiles that were fitted had an extension of typically only 5 µm, which roughly corresponds to the CDR width. This contour relaxation step guaranteed that the contour curvature was not biased.

8.9.4 Protocol of Contour Detection

Due to the complex shapes of CDRs, their complicated dynamics, and the inherently inhomogeneous appearance of cells, localisation of CDRs by automated algorithms is a challenging task. Therefore, a software implementation was developed that allowed for user interactions for quality control of contours and, if necessary, their corrections. The corresponding program, called "Contouro", was implemented in Matlab and had a GUI that enabled the user to conveniently switch between the use of active contours or fit-based routines for CDR localisation. The program is introduced in more detail in Section 9.5 of the Appendix. All contour processing steps described in the following were carried out in Contouro.

One initial guess for each CDR was drawn manually. Contours were then located and tracked automatically using active contours with parameters chosen in favour of fast convergence. The spacing of contour points was set to 0.19 µm for the first CDR contour approximation and then refined to 0.08 µm once the rough position was found. Contours were then placed into the minima of cubic approximations of the intensity profile in local orthogonal direction. Smoothing with a Gaussian of $\sigma = 0.08$ µm yielded the final contour positions.

8.9.5 Contour Velocity

The algorithms for calculation of contour velocities were developed in my diploma thesis [Bernitt, 2010]. In the following, the principle is summarized.

The contour points that define the contour of a CDR at a given time point have normal distances Δr_i to the contour of the succeeding frame. This normal distance, divided by the time interval Δt between two frames, defines the contour normal velocity $v_{\mathrm{n,i}} = \frac{\Delta r_i}{\Delta t}$. The local normal direction of a contour c_t at a given contour point i was

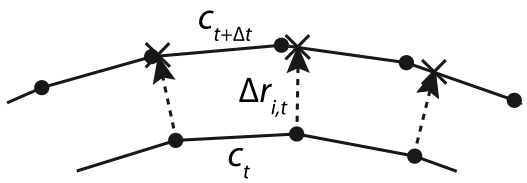

Figure 8.6: *Calculation of contour velocities.* The normal distance $\Delta r_{i,t}$ between the contour point i of the contour c_t and the contour $c_{t+\Delta t}$ determines the contour normal velocity. Filled dots mark contour points and crosses the intersections points between rays (dashed vectors) originating from contour points of contour c_t and contour c_{t+1}.

approximated by a local linear fit to the contour and subsequent calculation of the orthogonal direction. The intersection point of a line in normal direction originating from contour point i with the contour $c_{t+\Delta t}$ of the next frame was then calculated using a linear interpolation between contour points of contour $c_{t+\Delta t}$. The distance between contour point i and intersection point $r_{i,t}$ was defined as the normal distance between the two contours at position i. Figure 8.6 illustrates the working principle of the algorithm.

8.9.6 Contour Curvature

The curvature of a wavefront can, much like the contour velocity, easily be calculated from the contour representation of the wavefront. The curvature of a curve in parametric representation

$$x = x(s)$$
$$y = y(s)$$

is given by

$$K = \begin{vmatrix} x' & y' \\ x'' & y'' \end{vmatrix} \cdot \frac{1}{(x'^2 + y'^2)^{3/2}} \tag{8.4}$$

where dashes represent derivatives with respect to the parameter s [Bronstein et al., 2008, p 238]. The numerical calculation of derivatives is sensitive to noise. It is therefore favourable not to calculate these derivatives directly. An particularly robust method for calculation of derivatives of curves relies on their local approximation with cubic splines of the form

$$\begin{aligned} x(s) &= a_x s^3 + b_x s^2 + c_x s + d_x \\ y(s) &= a_y s^3 + b_y s^2 + c_y s + d_y \end{aligned} \tag{8.5}$$

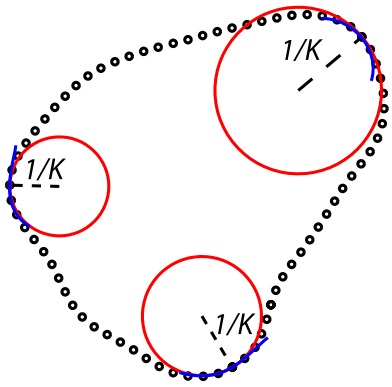

Figure 8.7: *Calculation of contour curvature.* The local curvature K of a contour was calculated at three contour points for demonstration. Blue lines represent the splines that approximate the contour locally according to (8.5). The red circles have a radius of $1/K$, i.e., the same curvature as the local contour pieces.

and subsequent analytical calculation of the derivatives

$$\begin{aligned} x'(s) &= 3a_x s^2 + 2b_x s + c_x \\ x''(s) &= 6a_x s + 2b_x \\ y'(s) &= 3a_y s^2 + 2b_y s + c_y \\ y''(s) &= 6a_y s + 2b_y. \end{aligned}$$

Figure 8.7 illustrates the process of curvature calculation by means of an example. The software implementation of this approach was designed to yield the local curvature at each point of a contour. The results of the velocity and curvature analysis of a contour can thus easily be compared.

8.9.7 Autocorrelation Function Analysis

Autocorrelation functions are convenient means to quantify data superimposed with noise with respect to characteristic lengths and periods. In this thesis, autocorrelation functions were used for the analysis of binarized kymographs. Binarization was performed based on visually determined gray value thresholds. In binarized kymographs, a value of $B_{s,t} = 1$ and $B_{s,t} = 0$ correspond to time and space coordinates with and without presence of CDRs respectively. Prior to the calculation of correlation functions I took advantage of the periodicity of kymographs in space by replication of the kymograph in negative and positive direction in space. The autocorrelation function was then

calculated according to

$$c_{\Delta s,\Delta t} = \frac{1}{N_s N_t - |\Delta s \Delta t|} \sum_{s=-(\frac{N_s}{2}-\Delta s-1)}^{+\frac{N_s}{2}-\Delta s-1} \sum_{t=0}^{N_t-\Delta t-1} \left(B_{s+\Delta s,t+\Delta t} - \bar{B}\right) \cdot \left(B_{s,t} - \bar{B}\right). \tag{8.6}$$

Here, N_t and N_s are the number of data points in spatial and temporal direction respectively. $\bar{B}$ is the mean value of the binarized kymograph. Note that the quantities propagation velocity and period of ruffling events do not depend on the gray value thresholds used for binarization.

8.9.8 Velocity Measurements using the Radon Transformation

The Radon transform is an integral transform that projects a function along straight lines. It was introduced by the Austrian mathematician Johann Radon in 1917 [Radon, 1917]. Nowadays, the Radon transform finds wide application in image processing, especially in the scope of tomographic imaging. In the scope of this thesis, the Radon transformation was used to identify the dominant velocity patterns in autocorrelation functions of kymographs.

In the following, the theory underlying the Radon transform is presented following Gonzales and Woods [Gonzales and Woods, 2008, pp. 368-373]. Let $I(x, y)$ be a two-dimensional image. Any line in the xy-plane of the image can be described by its normal representation

$$L(\Theta_k, \rho_j) : \{x, y | x \cos(\Theta_k) + y \sin(\Theta_k) = \rho_j\}, \tag{8.7}$$

where the angle Θ defines the orientation of this line with respect to the y-axis (see Figure 8.8). The Radon transform at (Θ_k, ρ_j) is then obtained by the projection of image $I(x, y)$ along the line $L(\Theta_k, \rho_j)$

$$g(\Theta_k, \rho_j) = \int_{-\infty}^{+\infty} \int_{-\infty}^{+\infty} I(x, y) \delta(x \cos(\Theta_k) + y \sin(\Theta_k) - \rho_j) \mathrm{d}x \mathrm{d}y. \tag{8.8}$$

Here, δ represents Dirac's distribution. Figure 8.8 illustrates the projection based on an example.

Images showing line patterns with orientation Θ_p with respect to the y-axis yield Radon transforms with strong variations at $g(\Theta = \Theta_\mathrm{p}, \rho)$. The Radon transform thus provides a convenient way to detect line patterns in images and to determine their orientation. Figure 8.9 illustrates this based on two artificial images of line patterns.

Since objects moving with constant velocity have a signature in form of lines in kymographs, the Radon transform can be used to quantify these velocities. In practice, it proved beneficial to calculate correlation functions of kymographs and to apply the Radon transform to these correlation functions (Figure 8.9). All velocity values were visually confirmed by plotting line grids with respective slopes into the original kymographs.

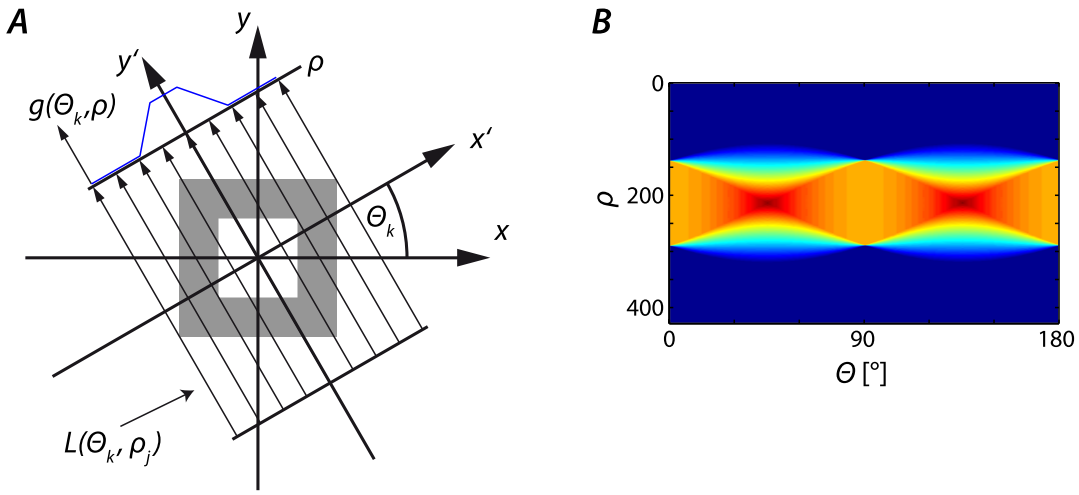

Figure 8.8: *Illustration of the projection integral for calculation of the Radon transformation.* *A*: The image (white square on gray ground) is projected on the ρ-axis along parallel rays $L(\Theta_k, \rho_j)$ orthogonal to ρ. The blue line shows the Radon transform $g(\Theta_k, \rho)$ obtained this way for a fixed angle Θ_k. *B*: The full radon transform $g(\Theta, \rho)$ of the white rectangle in *A* calculated on a $\Delta\rho = 1\,\mathrm{pix}$ and $\Delta\Theta = 1^\circ$ grid.

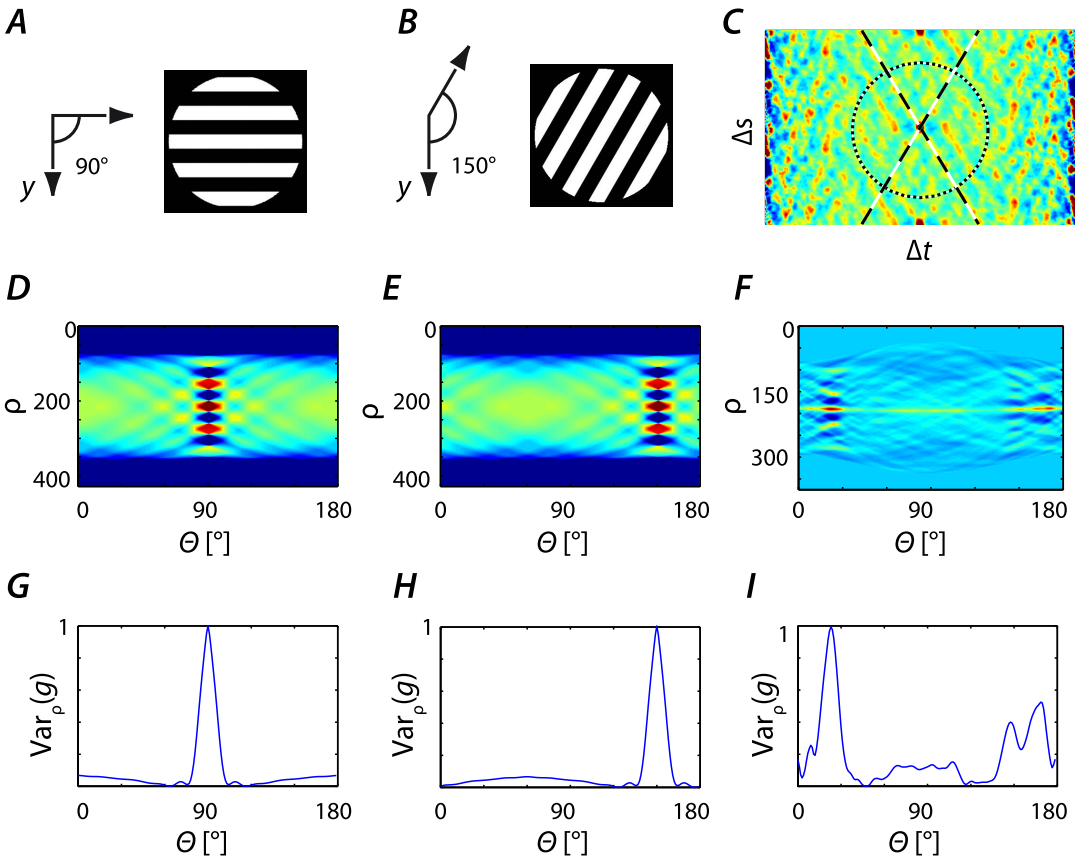

Figure 8.9: *Slope measurements using the Radon transformation.* *A* and *B*: line patterns with an angle of $90°$ and $150°$ with respect to the y-axis. *C*: a correlation function with a circular ROI (dotted line). Dashed lines visualize the slope as determined using the Radon transformation $g(\Theta, \rho')$. *D-F*: the Radon transform of images *A-B* and the ROI in *C* respectively. *G-I*: the position of the global maximum of the variance of R in $\rho'-$direction corresponds to the direction Θ_p of the dominant line pattern signal (*G*: $\Theta_p = 90°$, *H*: $\Theta_p = 150°$). The peak in *I* corresponds to the slope $v = \pm\frac{\Delta s}{\Delta t}$ of the kymograph *C* (dashed lines) and is the dominant velocity signal in this correlation function. The data in *G-I* have been normalized to unity.

Chapter 9

Appendix

9.1 Comparison of Spontaneously Formed and Induced CDRs

The test experiments described in this section served to check if the morphodynamical features of CDRs that form spontaneously or as a consequence of stimulation with growth factors were identical. These experiments were conducted for both, cells on non-structured substrates and for cells plated on microcontact printed substrates.

For non-structured substrates CDRs only formed rarely on NIH 3T3 WT cells. Therefore, NIH 3T3 X2 cells were used for experiments on spontaneous formation of CDRs. NIH 3T3 WT and NIH 3T3 X2 cells both formed CDRs as a response to growth factor stimulation with PDGF ($30\,\mathrm{ng\,l^{-1}}$). In Figure 9.1 time-lapse sequences of three experiments are shown on NIH 3T3 WT + PDGF (A), NIH 3T3 X2 + PDGF (B), and NIH 3T3 X2 without PDGF (C). The cell morphology of NIH 3T3 WT and NIH 3T3 X2 cells differs considerably, as NIH 3T3 X2 cells tend to take more spread shapes and also exceed NIH 3T3 WT cells in size. However, the morphodynamics of CDRs on both cell lines is identical. NIH 3T3 X2 cells do form CDRs with higher rates than NIH 3T3 WTs when stimulated with PDGF.

The results presented above have significance for the results presented in the chapters 3 and 4

For cells on disc-shaped substrates no stimulation with PDGF was required even for NIH 3T3 WT cells, as they formed CDRs at high rates spontaneously. It is the working hypothesis of this thesis, that the growth factors contained in the FBS of the cell culture cause the formation of CDRs on disc-shaped cells. In the absence of FBS no CDR formation was observed on disc-shaped cells. Addition of either FBS or PDGF, however, caused CDRs to form. This is demonstrated in Figure 9.2 in which NIH 3T3 WT cells in serum free medium were either exposed to FBS (10%) or PDGF ($1\,\mathrm{ng\,ml^{-1}}$). Again, the CDRs formed have identical morphodynamics properties. Interestingly, however, in most cases stimulation with PDGF only lead to formation of CDRs on a relatively low number of cells on disc-shaped fibronectin patters when compared to the impact

of PDGF on cells of random shapes. Most dish-shaped cells did, however, respond to PDGF stimulation with formation of transient, large and coherently protruding lamellipodia.

The results presented above are significant for all results on disc-shaped substrates (Chapter 5).

9.2 Correcting Projection Artefacts of Cluster Velocities

Motile clusters of polymerizing actin, as described in Section 3.1.2, are localized to the dorsal membrane, where their growth forms outward protrusions. The orientation of the growth direction can vary, as shown in the Figures 1.1 and 3.8. Therefore, the measurements of the velocity of actin clusters as presented in Figure 3.5 suffers from projection artefacts. In the following, the impact of projection on the velocity distribution is estimated.

The velocity v', that is measured in the xy-plane of time-lapse sequences of images, is a projection of the true cluster velocity v onto the xy-plane (Figure 9.3). With introduction of the angle Θ that is measured between the true growth direction and the xy-plane, the measured velocity reads

$$v'(v, \Theta) = v \cos(\Theta). \tag{9.1}$$

We assume that both, v and Θ follow probability density functions $p(v)$ and $p(\Theta)$. The distribution of the true velocity, $p(v)$, is the function of interest.

We further assume that Θ and v are independent variables and that all possible orientations are equally possible. With this, the expectation value of the measured velocity is

$$\begin{aligned} E(v') &= \int_0^{\pi/2} \int_0^{\infty} v' p(v) p(\Theta) \mathrm{d}v \mathrm{d}\Theta \\ &= \int_0^{\pi/2} \int_0^{\infty} v \cos(\Theta) p(v) \frac{1}{\pi/2} \mathrm{d}v \mathrm{d}\Theta \\ &= \frac{\pi}{2} E(v). \end{aligned} \tag{9.2}$$

Therefore, we assume that the distribution of the true velocity v is positively shifted by an increment of $E(v')(1 - \frac{\pi}{2})$ with respect to the measured velocity v'. The measured velocity has a mean of $\bar{v'} = 0.128 \pm 0.006\,\mu\mathrm{m\,s^{-1}}$. The estimate for the mean true velocity then becomes $\bar{v} = 0.175 \pm 0.009\,\mu\mathrm{m\,s^{-1}}$.

In fact, however, no velocities of clusters that appeared stationary were measured. Therefore, the actual distribution $p(\Theta)$ does not start at zero, as assumed here for simplicity. Thus, the estimation presented above yields an upper bound for the mean of the true velocity.

9.3 Time-Dependence of CDR Velocities on Disc-Shaped Cells

The first series of experiments on cells plated on microcontact-printed substrates after successful implementation of the microcontact printing protocol were performed in open imaging dishes. A detailed analysis of the propagation velocities of CDRs from these experiments, however, revealed that there was a trend of the velocity data to decrease with the runtime of experiments.

To demonstrate this effect semi-quantitatively the data were binned into time windows of a length of 15 min and the velocities were measured as described in Section 8.9.7-8.9.8. The data were then plotted against a time axis, which has units of the frame rate of experiments (typically: 12 s/frame). However, the frame rate was not identical in all experiments, as the number of positions imaged in an experiments and the distance between the positions determined the actual frame rate. Further, there is no well-defined time point for the start of experiments. Therefore, no exactly defined time unit was chosen for the plotting. Even though the plot in Figure 9.4 is, therefore, only half-quantitative the red trend line clearly highlights the decrease in the average velocity.

The reason for the change of propagation velocity of CDRs with experimental run time is not entirely clear at this stage. As no such trend occurred in experiments in flow chambers, it is obvious to think along the lines of changing medium conditions in experiments when using open containers. This could include, e.g., increasing osmolarity due to evaporation or non-constant pH-values. The result is still surprising as all necessary measures were taken to guarantee stable physiological conditions by use of the incubation unit described in Section 8.5. This includes a CO_2 concentration of 5% and humidification of air in the incubation unit.

To prevent the velocity distributions of data from cells on dish-shaped protein patches from being influenced by the bias of non-constant propagation velocities of CDRs as obtained when using open imaging dishes, all quantitative data from experiments involving the latter where discarded and not included in, e.g., velocity distributions, period distributions etc. Instead, all data presented in Chapter 5 where based on experiments with closed containers in the form of microfluidic flow chambers where no drifts in velocity data occurred.

Even though the reasons for the changing CDR speed in experiments performed with open imaging dishes are not entirely clear and remain speculative at this stage this observation deserves further attention in possible future experiments as the, e.g., the effect of changing osmolarity on CDR velocity might yield clues for a deeper understanding of the wave mechanism of CDRs. The use of microfluidic chambers allows for experiments with controlled variation in osmolarity.

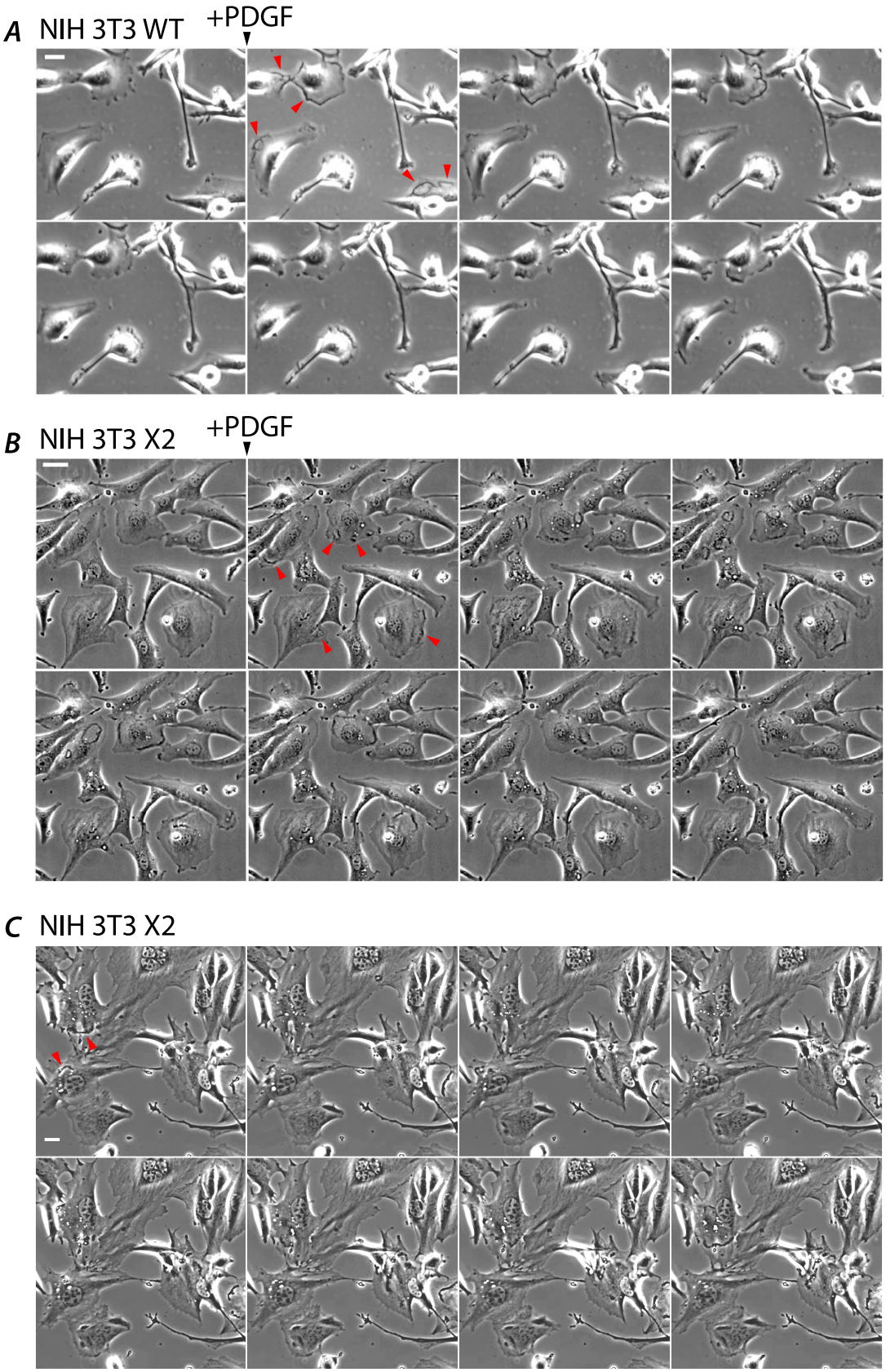

Figure 9.1: *Spontaneous and induced formation of CDRs. A*: NIH 3T3 WT cells stimulated with PDGF, *B*: NIH 3T3 X2 cells stimulated with PDGF, *C*: NIH 3T3 X2 cells without stimulation. Red arrow heads highlight the first CDR appearances. Time between frames: $5\,\mathrm{min}$, all scale bars: $25\,\mu\mathrm{m}$.

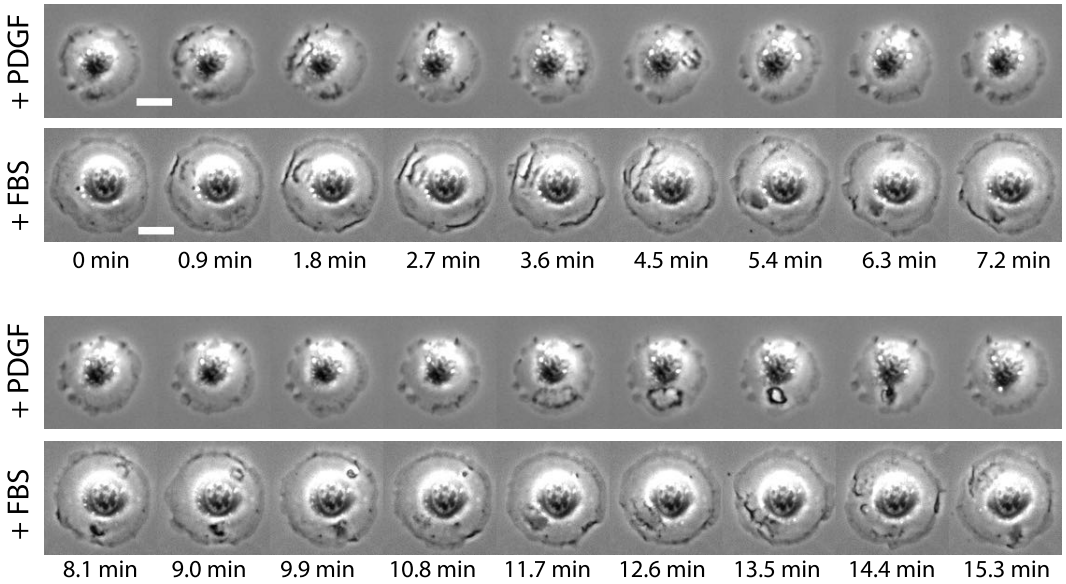

Figure 9.2: *Comparing the effect of PDGF and FBS on disc-shaped cells.* The CDRs formed due to either FBS or PDGF on cells on disc-shaped fibronectin patches exhibit identical wave dynamics. Scale bars: $25\,\mu\mathrm{m}$.

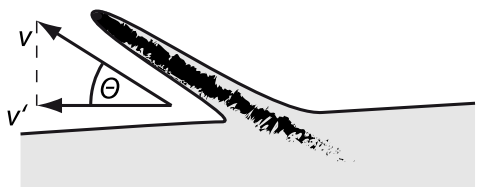

Figure 9.3: *Projection artefacts of cluster velocities.* The schematic diagram visualizes the trigonometric relations underlying the projection.

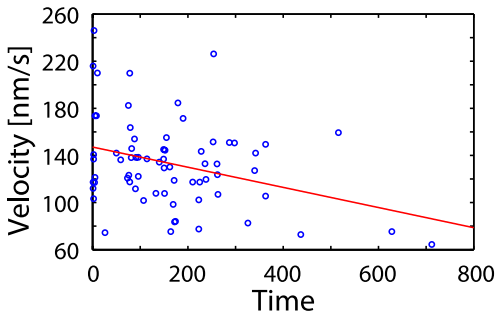

Figure 9.4: *CDR velocities on disc-shaped cells decrease with experiment run-time in open imaging dishes.* Blue dots are velocity values obtained in kymograph subframes of $15\,\mathrm{min}$ length. The trend line (red) highlights the velocity decrease. The time-axis has units of the frame interval of experiments and cannot serve exact quantitative purposes and has therefore no units in this figure.

9.4 Microcontact Printing

Figure 9.5*A*-*B* shows the wafer layout consisting of 52 fields of arrays of micro structures together with a close-up view of one of the fields. Figure 9.5*C* shows a photograph of the actual silicon master.

Besides of fields containing disk shapes, also square- and triangular-shaped patterns were included to allow for test experiments with different geometries (not reported in this thesis). Each pattern was realized with different sizes to allow flexible experiments on multiple cell lines and to study the effect of varying adhesion area as an experimental parameter.

The sizes of the patterns were chosen according to an experimentally determined cell size distribution. NIH 3T3 X2 cells adhering on plasma-treated homogeneous glass-bottom dishes were imaged under normal culture conditions and their adhesion area was measured by drawing their outline in AxioVision. The resulting distribution is shown in Figure 9.6. Even though there were some extremely large cells with adhesion areas of more than 20 000 $(\mu m)^2$, most cells had areas ranging from 3000 $(\mu m)^2$ to 12 000 $(\mu m)^2$.

An inspection of live imaging data showed that cells with adhesion areas below 3000 $(\mu m)^2$ usually showed no propagating CDRs. Therefore, the smallest patterns were realized with an area of 3000 $(\mu m)^2$. Cells with adhesion areas larger than 12 000 $(\mu m)^2$ were rare. Since investigations on the effect of pattern size on CDR propagation was one experimental aim, a large range of pattern sizes was chosen, with a maximal area of 13 000 $(\mu m)^2$. Sizes which were expected to yield most promising data were realized in up to three copies to facilitate the production of stamps of these sizes. An overview about the stamp sizes and shapes is given in Figure 9.5*D*.

9.5 An Interactive GUI for Contour Tracking

Figure 9.7 shows the layout of Contouro under the use of active contours and under the use of fit-based routines. In the following a brief descriptions of Contouro's functionality is presented. The order of the individual paragraphs follows the enumeration of the functional modules of Contouro as shown in Figure 9.7*B*.

1. **Loading and storing of data.** Contouro loads image stacks of the tif format. The user can either choose to load all frames in the memory of the computer or use a so-called "virtual stack". Using the latter, the computer reads all image meta information, but only the actual image data of the currently processed frame. Contouro can also read in the results of a previous image processing session in form of the MATLAB file format mat.

   Results of an image processing session using Contouro contain the contours that are created and several bits of meta information like the parameters that were used, the name of the processed image etc. in form of a comprehensive log file.

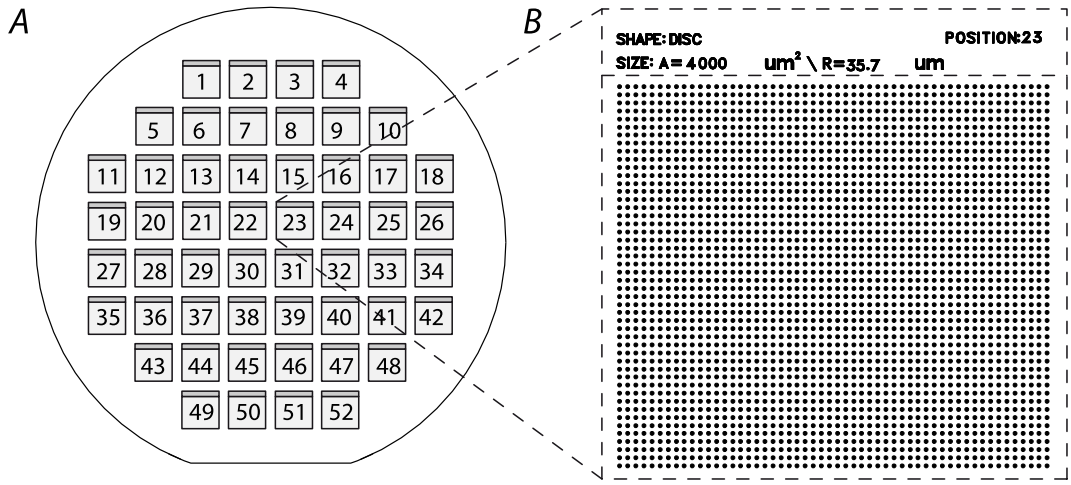

C

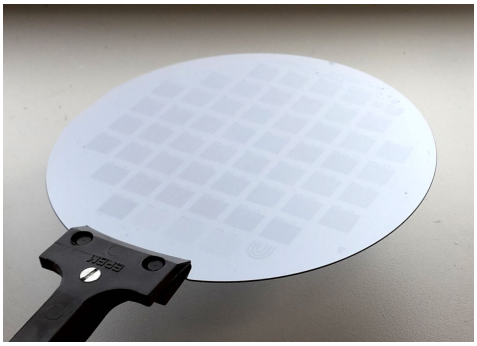

D

Size	Disc	Square	Triangle
3000	25	49	-
4000	23-24	48	-
5000	21-22	46-47	-
6000	19-20	44-45	-
7000	16-18	41-43	52
8000	13-15	38-40	-
9000	10-12	35-37	51
10000	7-9	32-34	-
11000	4-6	29-31	50
12000	2-3	27-28	-
13000	1	26	-

Figure 9.5: *Layout of the silicon master for production of micro stamps. A*: Overview of the layout with numbered fields. *B*: Close-up view on field 23, containing an array of discs with an area of $4000\,(\mu\mathrm{m})^2$. *C*: A photograph of the $10\,\mathrm{cm}$-wafer. Only the field positions can be seen with the bare eye. *D*: Table relating pattern area, shape and position. The numbers in the columns *Disc*, *Square* and *Triangle* correspond to the field positions.

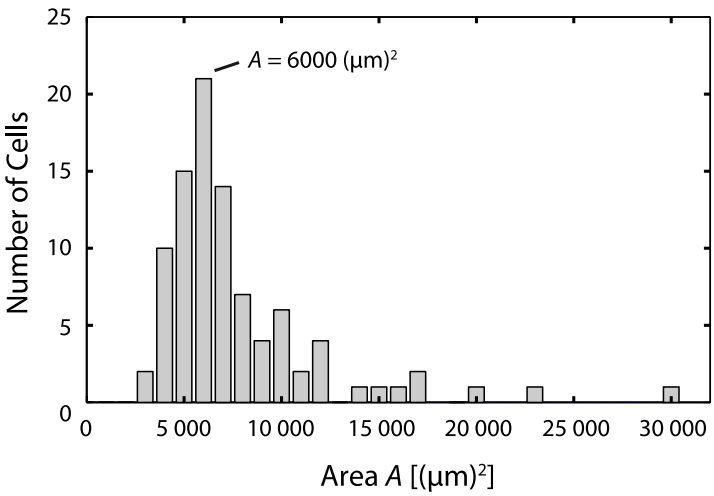

Figure 9.6: *Distribution of adhesion area of NIH 3T3 X2 cells.* Most cells had adhesion areas between $3000\,(\mu\mathrm{m})^2$ and $12\,000\,(\mu\mathrm{m})^2$. $A = 6000\,(\mu\mathrm{m})^2$ is the most frequently found value and median of the distribution.

2. **Image smoothing setting.** Smoothing of images is often a helpful step of preprocessing. It avoids, e.g., high local image energies when using active contours or erroneous fits of profiles of image intensity.

3. **Drawing of initial contour guesses.** Both, active contours and fit-based algorithms require initial contour estimates. These can be drawn by the user in form of polygons to which each mouse click successively adds new nodes. Initial contours can either be closed or open. After drawing, either a piece-wise linear contour interpolates the regions between points that were added via mouse clicks, or cubic splines are chosen for interpolation. Alternatively, the initial contour guess can be in form of a user-drawn ellipse. Existing contours can be corrected clicking a designated button. After button press, the contour takes the form of an editable polygon again, whose contour points can be shifted. This panel also allows to check all contours of the entire stack in form of a 3-d plot.

4. **Display of time-lapse frames and contours.** This main control panel shows the currently processed frame of time-lapse sequences with the overlaid contours. The current frame can either be chosen via a frame slider or an editable text box. Additionally, the zoom factor and the intensity mapping can be controlled.

5. **Contour properties.** A contour has some general properties like, e.g., the spacing between contour points that can be set in this panel. Since several routines require estimates of the local normal direction, the number of contour points that is used for these estimates can be set here. Further, the smoothness of contours can be controlled. A smoothness value of zero yields un-smoothed

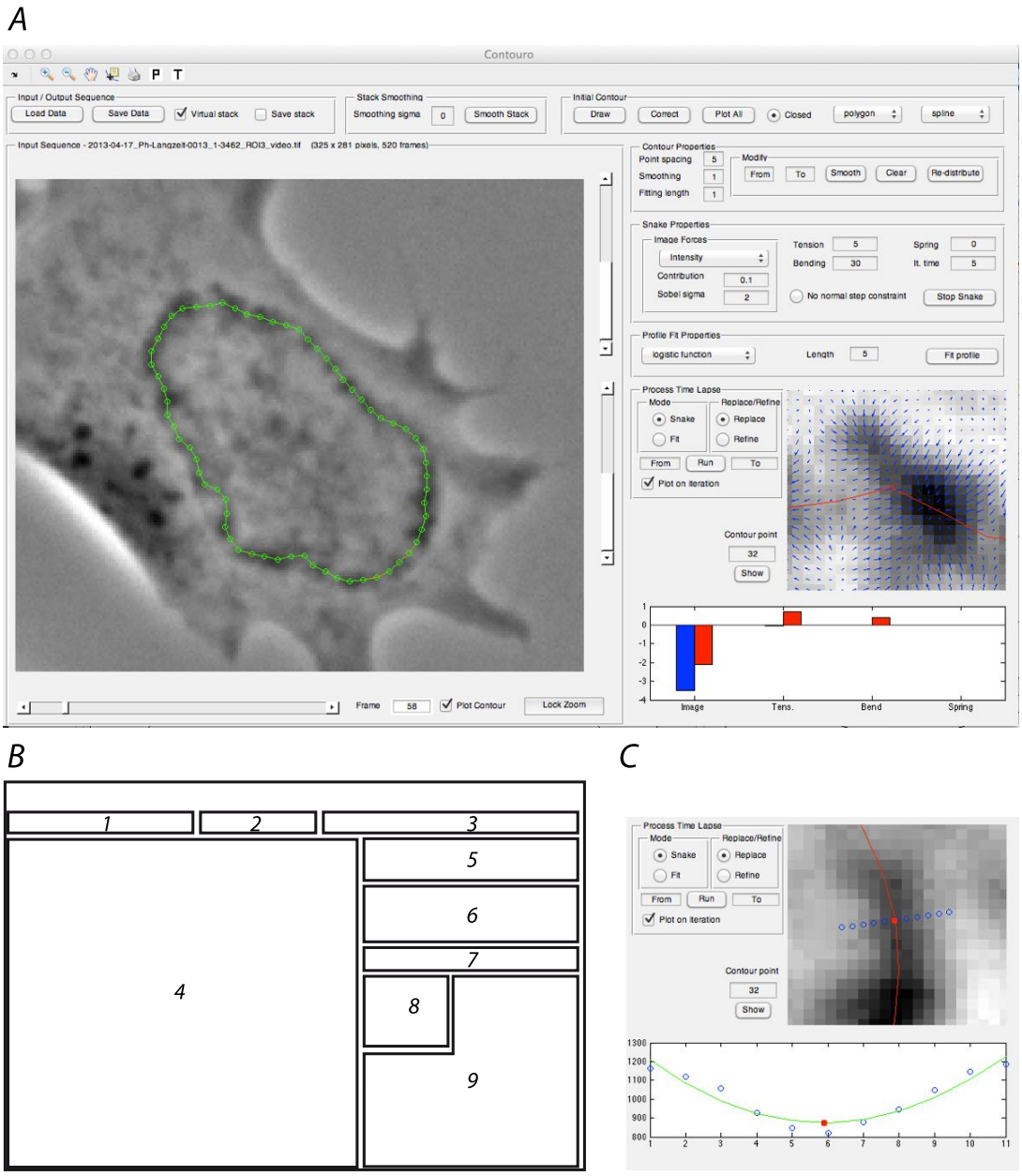

Figure 9.7: *The GUI of "Contouro".* In *A* the full GUI is shown in the active contour mode. (*B*) The layout of Contouro is divided into the following functional parts: (*1*) loading and storing of data, (*2*) image smoothing, (*3*) drawing of initial contour guess, (*4*) display of time-lapse frames and contours, (*5*) contour properties, (*6*) active contour properties, (*7*) Fitting properties, (*8*) Tracking settings, (*9*) Close-up view of image details with overlaid image force field or fitting profile, including a control plot showing either energy contributions on active contours or the local fits for estimation of contour positions. When using fit-based contour detection, panel *9* appears as shown in *C*.

contours. This panel also allows to clear contours.

6. **Snake properties.** In this panel, the parameters of active contours can be set. These cover the coefficients of external and internal energies. Furthermore, it can be chosen if the image energy should attract contours to extrema of intensity or to edges.

7. **Profile fit properties.** Here, the type of function can be selected that is used upon fit-based contour detection. The possible options comprise the logistic function, the error function, the Gauss curve, the derivative of a Gaussian, cubic functions and the local minimum and maximum. The latter two are no functions but simply the darkest or brightest pixels along a profile. For each fit function, the user has the possibility to choose whether minima or maxima are of interest, i.e., the sign of the fit function. The only parameter that needs to be specified for fit-based contour detection is the length of the profiles.

8. **Process time-lapse.** For the tracking of CDRs, the user can choose between the fit-based and the active contour method and select the time interval. The user can further decide whether previous contours should be replaced or refined. Using the replace option, contour detection routines take the contour of the last frame as an initial guess for the current frame. In the refinement mode, the contour of the actual frame is based on a previous guess of the contour in the actual frame, i.e., its position is refined. The latter option, of course, requires that the frame has been processed previously. In practise, a combined run has proven useful in which the replace option is chosen with parameters that let contours converge quickly to their approximate position, and this positions is refined with a more sensible parameter setting afterwards.

9. **Parameter control panel.** The accurate setting of parameters is checked easiest via the display of this panel. Depending on the contour detection mode of choice, it either shows the contributions of the individual energies acting on a pre-selected contour point, or the fitted intensity profile. In the active contour mode, the image force field is overlaid to a close-up view on the surrounding of the selected contour point. Upon fit-based contour detection, markers denote the points where image intensity was sampled for the profiles.

The typical contour detection process using Contouro proceeds in the following steps. The user loads a time-lapse sequence and selects a frame at which the CDR that shall be tracked has maximal extension. Under favourable conditions, the user has to roughly approximate the CDR contour manually only once. Then, the program finds the accurate CDR contour automatically and tracks it through the whole sequence. The contour data can then be kept and processed with other routines.

Chapter 10

Bibliography

[Abella et al., 2010] Abella, J. V., Vaillancourt, R., Frigault, M. M., Ponzo, M. G., Zuo, D., VeenaSangwan, Larose, L., and Park, M. (2010). The gab1 scaffold regulates rtk-dependent dorsal ruffle formation through the adaptor nck. *J. Cell Sci.*, 123(8):1306 – 1319.

[Abercrombie, 1978] Abercrombie, M. (1978). The croonian lecture, 1978: The crawling movement of metazoan cells. *Proc. Roy. Soc. London*, 207(1167):129 – 147.

[Abercrombie et al., 1970a] Abercrombie, M., Heaysman, J. E., and Pegrum, S. M. (1970a). The locomotion of fibroblasts in culture I. movements of the leading edge. *Exp. Cell Res.*, 59(3):393 – 398.

[Abercrombie et al., 1971] Abercrombie, M., Heaysman, J. E., and Pegrum, S. M. (1971). The locomotion of fibroblasts in culture: IV. electron microscopy of the leading lamella. *Exp. Cell Res.*, 67(2):359 – 367.

[Abercrombie et al., 1970b] Abercrombie, M., Joan, E., Heaysman, M., and Pegrum, S. M. (1970b). The locomotion of fibroblasts in culture: II. "ruffling". *Exp. Cell Res.*, 60(3):437 – 444.

[Alberts et al., 2005] Alberts, B., Bray, D., Hopkin, K., Johnson, A., Lewis, J., Raff, M., Roberts, K., and Walter, P. (2005). *Lehrbuch der Molekularen Zellbiologie.* Wiley-VCH.

[Alberts et al., 2014] Alberts, B., Johnson, A., Lewis, J., Morgan, D., Raff, M., Roberts, K., and Walter, P. (2014). *Molecular Biology of the Cell.* Garland Publishing, 6 edition.

[Aliev and Panfilov, 1996] Aliev, R. R. and Panfilov, A. V. (1996). A simple two-variable model of cardiac excitation. *Chaos Soliton. Fract.*, 7(3):293 – 301.

[Allard and Mogilner, 2013] Allard, J. and Mogilner, A. (2013). Traveling waves in actin dynamics and cell motility. *Curr. Opin. Cell Biol.*, 25(1):107 – 115.

[Allen et al., 1969] Allen, R. D., David, G. B., and Normarski, G. (1969). The zeiss-normarski differential intereference equipment for transmitted-light microscopy. *Zeitschrift für wissenschaftliche Mikroskopie und mikroskopische Technik*, 69(4):193 – 220.

[Ambros et al., 1975] Ambros, V. R., Chen, L. B., and Buchanan, J. M. (1975). Surface ruffles as markers for studies of cell transformation by rous sarcoma virus. *Proc. Natl. Acad. Sci.*, 72(8):3144 – 3148.

[Argentina et al., 2000] Argentina, M., Coullet, P., and Krinsky, V. (2000). Head-on collisions of waves in an excitable fitzhugh–nagumo system: a transition from wave annihilation to classical wave behavior. *J. Theor. Biol.*, 205(1):47 – 52.

[Asano et al., 2009] Asano, Y., Liverpool, A. J.-D. T., Marchetti, M., Giomi, L., Kiger, A., Duke, T., and Baum, B. (2009). Pak3 inhibits local actin filament formation to regulate global cell polarity. *HFSP Journal*, 3(3):194 – 203.

[Azimifar et al., 2012] Azimifar, S. B., Böttcher, R. T., Zanivan, S., Grashoff, C., Krüger, M., Legate, K. R., Mann, M., and Fässler, R. (2012). Induction of membrane circular dorsal ruffles requires co-signalling of integrin–ilk-complex and egf receptor. *J. Cell Sci.*, 125(2):435 – 448.

[Azioune et al., 2010] Azioune, A., Carpi, N., Tseng, Q., Théry, M., and Piel, M. (2010). Chapter 8 - protein micropatterns: A direct printing protocol using deep uvs. In Cassimeris, L. and Tran, P., editors, *Microtubules: in vivo*, volume 97 of *Methods in Cell Biology*, pages 133 – 146. Academic Press.

[Bak et al., 1990] Bak, P., Chen, K., and Tang, C. (1990). A forest-fire model and some thoughts on turbulence. *Phys. Lett. A*, 147(5-6):297 – 300.

[Bamburg et al., 1999] Bamburg, J. R., McGough, A., and Ono, S. (1999). Putting a new twist on actin: Adf/cofilins modulate actin dynamics. *Trends Cell Biol.*, 9(9):364 – 370.

[Berenfeld and Abboud, 1996] Berenfeld, O. and Abboud, S. (1996). Simulation of cardiac activity and the ECG using a heart model with a reaction-diffusion action potential. *Med. Eng. Phys.*, 18(8):615 – 625.

[Bernitt, 2010] Bernitt, E. (2010). Quantitative investigation of lamellipodia protrusion velocities during isotropic cell spreading of two fibroblast cell lines. German diploma thesis, University of Bremen.

[Berre et al., 2014] Berre, M. L., Zlotek-Zlotkiewicz, E., Bonazzi, D., Lautenschlaeger, F., and Piel, M. (2014). Chapter 14 - methods for two-dimensional cell confinement. In Piel, M. and Théry, M., editors, *Micropatterning in Cell Biology Part C*, volume 121 of *Methods in Cell Biology*, pages 213 – 229. Academic Press.

[Blanchoin et al., 2014] Blanchoin, L., Boujemaa-Paterski, R., Sykes, C., and Plastino, J. (2014). Actin dynamics, architecture, and mechanics in cell motility. *Physiol. Rev.*, 94(1):235 – 263.

[Bonny et al., 2013] Bonny, M., Fischer-Friedrich, E., Loose, M., Schwille, P., and Kruse, K. (2013). Membrane binding of mine allows for a comprehensive description of min-protein pattern formation. *PLoS Comput. Biol.*, 12(12):e1003347.

[Borisy and Svitkina, 2000] Borisy, G. G. and Svitkina, T. M. (2000). Actin machinery: pushing the envelope. *Curr. Opin. Cell Biol.*, 12(1):104 – 112.

[Borm et al., 2005] Borm, B., Requardt, R. P., Herzog, V., and Kirfel, G. (2005). Membrane ruffles in cell migration: indicators of inefficient lamellipodia adhesion and compartments of actin filament reorganization. *Exp. Cell Res.*, 302(1):83 – 95.

[Bray, 2001] Bray, D. (2001). *Cell Movements, Second Edition.* Garland Publishing.

[Bretschneider et al., 2009] Bretschneider, T., Anderson, K., Ecke, M., Müller-Taubenberger, A., Schroth-Diez, B., Ishikawa-Ankerhold, H. C., and Gerisch, G. (2009). The three-dimensional dynamics of actin waves, a model of cytoskeletal self-organization. *Biophys. J.*, 96(7):2888 – 2900.

[Bronstein et al., 2008] Bronstein, I. N., Semendjajew, K. A., Musiol, G., and Mühlig, H. (2008). *Taschenbuch der Mathmatik.* Verlag Harri Deutsch, 7th edition.

[Buccione et al., 2004] Buccione, R., Orth, J. D., and A.McNiven, M. (2004). Foot and mouth: Podosomes, invadopodia and circular dorsal ruffles. *Nat. Rev. Mol. Cell Biol.*, 5(8):647 – 657.

[Burger and Burge, 2010] Burger, W. and Burge, M. J. (2010). *Digital Image Processing.* Springer.

[Burnette et al., 2011] Burnette, D. T., Manley, S., Sengupta, P., Sougrat, R., Davidson, M. W., Kachar, B., and Lippincott-Schwartz, J. (2011). A role for actin arcs in the leading-edge advance of migrating cells. *Nat. Cell Biol.*, 13(4):371 – 382.

[Burnette et al., 2007] Burnette, D. T., Schaefer, A. W., Ji, L., Danuser, G., and Forscher, P. (2007). Filopodial actin bundles are not necessary for microtubule advance into the peripheral domain of aplysia neuronal growth cones. *Nat. Cell Biol.*, 9(12):1360 – 1369.

[Burridge and Wennerberg, 2004] Burridge, K. and Wennerberg, K. (2004). Rho and rac take center stage. *Cell*, 116(2):167 – 179.

[Cameron et al., 2000] Cameron, L. A., Giardini, P. A., Soo, F. S., and Theriot, J. A. (2000). Secrets of actin-based motility revealed by a bacterial pathogen. *Nat. Rev. Molec. Cell Biol.*, 1(2):110 – 119.

[Camley et al., 2014] Camley, B. A., Zhang, Y., Zhao, Y., Li, B., Ben-Jacob, E., Levine, H., and Rappel, W.-J. (2014). Polarity mechanisms such as contact inhibition of locomotion regulate persistent rotational motion of mammalian cells on micropatterns. *Proc. Natl. Acad. Sci.*, 111(41):14770 – 75.

[Carlier et al., 1999] Carlier, M.-F., Loisel, T. P., Boujemaa, R., and Pantaloni, D. (1999). Reconstitution of actin-based motility of listeria and shigella using pure proteins. *Nature*, 401(6753):613 – 616.

[Carlsson, 2010] Carlsson, A. E. (2010). Dendritic actin filament nucleation causes traveling waves and patches. *Phys. Rev. Lett.*, 104(22):228102.

[Cavagna et al., 2010] Cavagna, A., Cimarelli, A., Giardina, I., Parisi, G., Santagati, R., Stefanini, F., and Viale, M. (2010). Scale-free correlations in starling flocks. *Proc. Natl. Acad. Sci.*, 107(26):11865 – 70.

[Chen et al., 2009] Chen, C.-H., Tsai, F.-C., Wang, C.-C., and Lee, C.-H. (2009). Three-dimensional characterization of active membranewaves on living cells. *Phys. Rev. Lett.*, 103(23):238101 – 4.

[Chen et al., 2010] Chen, W. W., Niepel, M., and Sorger, P. K. (2010). Classic and contemporary approaches to modeling biochemical reactions. *Gene. Dev.*, 24(17):1861 – 75.

[Chinkers et al., 1979] Chinkers, M., McKanna, J. A., and Cohen, S. (1979). Rapid induction of morphological changes in human carcinoma cells a-431 by epidermal growth factor. *J. Cell Biol.*, 83(1):260 – 265.

[Chou et al., 2001] Chou, T., Kim, K. S., and Oster, G. (2001). Statistical thermodynamics of membrane bending-mediated protein-protein attractions. *Biophys. J.*, 80(3):1075 – 87.

[Comtois et al., 2005] Comtois, P., Kneller, J., and Nattel, S. (2005). Of circles and spirals: Bridging the gap between the leading circle and spiral wave concepts of cardiac reentry. *EP Europace*, 7(s2):S10 – S20.

[Cortesio et al., 2010] Cortesio, C. L., Perrin, B. J., Bennin, D. A., and Huttenlocher, A. (2010). Actin-binding protein-1 interacts with wasp-interacting protein to regulate growth factor-induced dorsal ruffle formation. *Mol. Biol. Cell*, 21(1):186 – 197.

[Couzin and Krause, 2003] Couzin, I. D. and Krause, J. (2003). Self-organization and collective behaviour in vertebrates. *Adv. Stud. Behav.*, 32(1):1 – 75.

[Cox and Lowengrub, 2015] Cox, G. and Lowengrub, J. (2015). The effect of spontaneous curvature on a two-phase vesicle. *Nonlinearity*, 28(3):773 – 793.

[Danuser et al., 2013] Danuser, G., Allard, J., and Mogilner, A. (2013). Mathematical modeling of eukaryotic cell migration: Insights beyond experiments. *Annu. Rev. Cell Dev. Biol.*, 29(1):501 – 528.

[Dennis et al., 2013] Dennis, G. R., Hope, J. J., and Johnsson, M. T. (2013). Xmds2: Fast, scalable simulation of coupled stochastic partial differential equations. *Comput. Phys. Commun.*, 184(1):201 – 208.

[Döbereiner et al., 2006] Döbereiner, H.-G., Dubin-Thaler, B. J., Hofman, J. M., Xenias, H. S., Sims, T. N., Giannone, G., Dustin, M. L., Wiggins, C. H., and Sheetz, M. P. (2006). Lateral membrane waves constitute a universal dynamic pattern of motile cells. *Phys. Rev. Lett.*, 97(3):038102.

[Doherty and McMahon, 2009] Doherty, G. J. and McMahon, H. T. (2009). Mechanisms of endocytosis. *Ann. Rev. Biochem.*, 78(1):857 – 902.

[Dos Remedios et al., 2003] Dos Remedios, C. G., Chhabra, D., Kekic, M., Dedova, I. V., Tsubakihara, M., Berry, D. A., and Nosworthy, N. J. (2003). Actin binding proteins: Regulation of cytoskeletal microfilaments. *Physiol. Rev.*, 83(2):433 – 473.

[Doubrovinski and Kruse, 2008] Doubrovinski, K. and Kruse, K. (2008). Cytoskeletal waves in the absence of molecular motors. *Europhys. Lett.*, 83(1):18003.

[Doubrovinski and Kruse, 2011] Doubrovinski, K. and Kruse, K. (2011). Cell motility resulting from spontaneous polymerization waves. *Phys. Rev. Lett.*, 107(25):258103.

[Dowrick et al., 1993] Dowrick, P., Kenworthy, P., McCann, B., and Warn, R. (1993). Circular ruffle formation and closure lead to macropinocytosis in hepatocyte growth factor/scatter factor-treated cells. *Eur. J. Cell Biol.*, 61(1):44 – 53.

[Dreher et al., 2014] Dreher, A., Aranson, I. S., and Kruse, K. (2014). Spiral actin-polymerization waves can generate amoeboidal cell crawling. *New J. Phys.*, 16(1):055007.

[Driscoll et al., 2012] Driscoll, M. K., McCann, C., Kopace, R., Homan, T., Fourkas, J. T., Parent, C., and Losert, W. (2012). Cell shape dynamics: From waves to migration. *PLoS Comput. Biol.*, 8(3):e1002392.

[Dubin-Thaler et al., 2004] Dubin-Thaler, B. J., Giannone, G., Döbereiner, H.-G., and Sheetz, M. P. (2004). Nanometer analysis of cell spreading on matrix-coated surfaces reveals two distinct cell states and steps. *Biophys. J.*, 86(3):1794 – 1806.

[Dubin-Thaler et al., 2008] Dubin-Thaler, B. J., Hofman, J. M., Cai, Y., Xenias, H., Spielman, I., Shneidman, A. V., David, L. A., Döbereiner, H.-G., Wiggins, C. H., and Sheetz, M. P. (2008). Quantification of cell edge velocities and traction forces reveals distinct motility modules during cell spreading. *PLoS ONE*, 3(11):e3735.

[Döbereiner et al., 2006] Döbereiner, H.-G., Dubin-Thaler, B. J., Hofman, J. M., Xenias, H. S., Sims, T. N., Giannone, G., Dustin, M. L., Wiggins, C. H., , and Sheetz, M. P. (2006). Lateral membrane waves constitute a universal dynamic pattern of motile cells. *Phys. Rev. Lett.*, 97(3):038102.

[Edelstein-Keshet, 1988] Edelstein-Keshet, L. (1988). *Mathematical Models in Biology.* Siam.

[Edgar and Bennett, 1997] Edgar, A. and Bennett, J. (1997). Circular ruffle formation in rat basophilic leukemia cells in response to antigen stimulation. *Eur. J. Cell Biol.*, 73(2):132 – 140.

[Enculescu et al., 2010] Enculescu, M., Sabouri-Ghomi, M., Danuser, G., and Falcke, M. (2010). Modeling of protrusion phenotypes driven by the actin-membrane interaction. *Biophys. J.*, 98(8):1571 – 81.

[Etienne-Manneville and Hall, 2002] Etienne-Manneville, S. and Hall, A. (2002). Rho gtpases in cell biology. *Nature*, 420(6916):629 – 635.

[Figard and Sokac, 2014] Figard, L. and Sokac, A. M. (2014). A membrane reservoir at the cell surface. *BioArchitecture*, 4(2):39 – 46.

[FitzHugh, 1961] FitzHugh, R. (1961). Impulses and physiological states in theoretical models of nerve membrane. *Biophys. J.*, 1(6):445 – 446.

[FitzHugh, 1968] FitzHugh, R. (1968). Motion picture of nerve impulse propagation using computer animation. *J. Appl. Physiol.*, 25(5):628 – 630.

[FitzHugh, 1969] FitzHugh, R. (1969). *Biological Engineering.* McGraw-Hill.

[Fließbach, 2005] Fließbach, T. (2005). *Elektrodynamik - Lehrbuch zur Theoretischen Physik II.* Elsevier.

[Folch and Toner, 2000] Folch, A. and Toner, M. (2000). Microengineering of cellular interactions. *Annu. Rev. Biomed. Eng.*, 2(1):227 – 256.

[Gauthier et al., 2011] Gauthier, N. C., Fardin, M. A., Roca-Cusachs, P., and Sheetz, M. P. (2011). Temporary increase in plasma membrane tension coordinates the activation of exocytosis and contraction during cell spreading. *Proc. Natl. Acad. Sci. U. S. A.*, 108(35):14467 – 72.

[Gauthier et al., 2012] Gauthier, N. C., Masters, T. A., and Sheetz, M. P. (2012). Mechanical feedback between membrane tension and dynamics. *Trends Cell Biol.*, 22(10):527 – 535.

[Gauthier et al., 2009] Gauthier, N. C., Rossier, O. M., Mathur, A., Hone, J. C., and Sheetz, M. P. (2009). Plasma membrane area increases with spread area by exocytosis of a gpi-anchored protein compartment. *Mol. Biol. Cell*, 20(14):3261 – 72.

[Geiger et al., 2001] Geiger, B., Bershadsky, A., Pankov, R., and Yamada, K. M. (2001). Transmembrane crosstalk between the extracellular matrix-cytoskeleton crosstalk. *Nat. Rev. Mol. Cell Biol.*, 2(11):793 – 805.

[Gerhardt et al., 2014] Gerhardt, M., Ecke, M., Walz, M., Stengl, A., Beta, C., and Gerisch, G. (2014). Actin and pip3 waves in giant cells reveal the inherent length scale of an excited state. *J. Cell Sci.*, 127(1):4507 – 17.

[Gerisch, 2010] Gerisch, G. (2010). Self-organizing actin waves that stimulate phygocytotic cup structures. *PMC Biophysics*, 3(7).

[Gerisch et al., 2004] Gerisch, G., Bretschneider, T., Müller-Taubenberger, A., Simmeth, E., Ecke, M., Diez, S., and Anderson, K. (2004). Mobile actin clusters and traveling waves in cells recovering from actin depolymerization. *Biophys. J.*, 87(5):3493 – 3503.

[Gerisch et al., 2012] Gerisch, G., Schroth-Diez, B., Müller-Taubenberger, A., and Ecke, M. (2012). Pip3 waves and pten dynamics in the emergence of cell polarity. *Biophys. J.*, 103(6):1170 – 78.

[Gholami et al., 2012] Gholami, A., Enculescu, M., and Falcke, M. (2012). Membrane waves driven by forces from actin filaments. *New J. of Phys.*, 14(11):115002.

[Ginelli et al., 2010] Ginelli, F., Peruani, F., Bär, M., and Chaté, H. (2010). Large-scale collective properties of self-propelled rods. *Phys. Rev. Lett.*, 104:184502.

[Gonzales and Woods, 2008] Gonzales, R. C. and Woods, R. E. (2008). *Digital Image Processing*. Pearson Prentice Hall, 3rd edition.

[Gonzales et al., 2004] Gonzales, R. C., Woods, R. E., and Eddins, S. L. (2004). *Digital Image Processing using Matlab*. Pearson Prentice Hall.

[Gonzalez-Perez et al., 2014] Gonzalez-Perez, A., Budvytyte, R., Mosgaard, L. D., Nissen, S., and Heimburg, T. (2014). Penetration of action potentials during collision in the median and lateral giant axons of invertebrates. *Phys. Rev. X*, 4(3):031047.

[Goodsell, 2001] Goodsell, D. (2001). Actin - protein data bank. Accessed Oct. 11th 2015.

[Grosheva et al., 2006] Grosheva, I., Vittitow, J. L., Goichberg, P., Gabelt, B. A. T., Kaufman, P. L., Borrás, T., Geiger, B., and Bershadsky, A. D. (2006). Caldesmon effects on the actin cytoskeleton and cell adhesion in cultured htm cells. *Exp. Eye Res.*, 82(6):945 – 958.

[Gu et al., 2011] Gu, Z., Noss, E. H., Hsu, V. W., and Brenner, M. B. (2011). Integrins traffic rapidly via circular dorsal ruffles and macropinocytosis during stimulated cell migration. *J. Cell Biol.*, 193(1):61 – 70.

[Guerriero and Weisz, 2007] Guerriero, C. J. and Weisz, O. A. (2007). N-wasp inhibitor wiskostatin nonselectively perturbs membrane transport by decreasing cellular atp levels. *Am. J. Phys. Cell Phys.*, 292(4):C1562 – C1566.

[Guilluy et al., 2011] Guilluy, C., Garcia-Mata, R., and Burridge, K. (2011). Rho protein crosstalk: another social network? *Trends Cell Biol.*, 21(12):718 – 726.

[Hasegawa et al., 2011] Hasegawa, J., Tokuda, E., Tenno, T., Tsujita, K., Sawai, H., Hiroaki, H., Takenawa, T., and Itoh, T. (2011). Sh3yl1 regulates dorsal ruffle formation by a novel phosphoinositide-binding domain. *J. Cell Biol.*, 193(5):901 – 916.

[Hasegawa et al., 2012] Hasegawa, J., Tsujita, K., Takenawa, T., and Itoh, T. (2012). Arap1 regulates the ring size of circular dorsal ruffles through arf1 and arf5. *Mol. Biol. Cell*, 23(13):2481 – 89.

[Heath and Insall, 2008] Heath, R. J. and Insall, R. H. (2008). F-bar domains: multifunctional regulators of membrane curvature. *J. Cell Sci.*, 121(12):1951 – 54.

[Helfrich, 1973] Helfrich, W. (1973). Elastic properties of lipid bilayers: Theory and possible experiments. *Z. Naturforsch*, 28(11):693 – 703.

[Hoch and Soriano, 2003] Hoch, R. V. and Soriano, P. (2003). Roles of pdgf in animal development. *Development*, 130(20):4769 – 84.

[Hodgkin and Huxley, 1952] Hodgkin, A. L. and Huxley, A. F. (1952). A quantitative description of membrane current and its application to conduction and excitation in nerve. *J. Phys.*, 117(4):500 – 544.

[Holmes et al., 2012] Holmes, W. R., Carlsson, A. E., and Edelstein-Keshet, L. (2012). Regimes of wave type patterning driven by refractory actin feedback: transition from static polarization to dynamic wave behaviour. *Phys. Biol.*, 9(4):046005–16.

[Hoon et al., 2012] Hoon, J.-L., Wong, W.-K., and Koh, C.-G. (2012). Functions and regulation of circular dorsal ruffles. *Mol. Cell. Biol.*, 32(21):4246 – 57.

[Hynes, 1992] Hynes, R. O. (1992). Integrins: Versatility, modulation, and signaling in cell adhesion. *Cell*, 69(1):11 – 25.

[Itoh and Hasegawa, 2012] Itoh, T. and Hasegawa, J. (2012). Mechanistic insights into the regulation of circular dorsal ruffle formation. *J. Biochem*, 153(1):21 – 29.

[Jin et al., 2008] Jin, Q., Wei, G., Lin, Z., Sugai, J. V., Lynch, S. E., Ma, P. X., and Giannobile, W. V. (2008). Nanofibrous scaffolds incorporating pdgf-bb microspheres induce chemokine expression and tissue neogenesis *In Vivo*. *PLoS One*, 3(3):e1729.

[Joanny et al., 2007] Joanny, J. F., Jülicher, F., Kruse, K., and Prost, J. (2007). Hydrodynamic theory for multi-component active polar gels. *New J. Phys.*, 9(11):422.

[Jung and Mayer-Kress, 1995] Jung, P. and Mayer-Kress, G. (1995). Spatiotemporal stochastic resonance in excitable media. *Phys. Rev. Lett.*, 74(11):2130 – 33.

[Kam, 1998] Kam, Z. (1998). Microscopic differential interference contrast image processing by line integration (lid) and deconvolution. *Bioimaging*, 6(4):166 – 176.

[Kass et al., 1988] Kass, M., Witkin, A., and Terzopoulos, D. (1988). Snakes: Active contour models. *Int. J. Comput. Vis.*, 1(4):321 – 331.

[Keener, 1986] Keener, J. P. (1986). A geometrical theory for spiral waves in excitable media. *Siam J. Appl. Math.*, 46(6):1039 – 56.

[Keener, 1991] Keener, J. P. (1991). An eikonal-curvature equation for action potential propagation in myocardium. *J. Math. Biol.*, 29(7):629 – 651.

[Keren, 2011] Keren, K. (2011). Cell motility: the integrating role of the plasma membrane. *Eur. Biophys. J.*, 40(9):1013 – 27.

[Kessler and Levine, 1993] Kessler, D. A. and Levine, H. (1993). Pattern formation in dictyostelium via the dynamics of cooperative biological entities. *Phys. Rev. E*, 48(6):4801 – 04.

[Khamviwath et al., 2013] Khamviwath, V., Hu, J., and Othmer, H. G. (2013). A continuum model of actin waves in dictyostelium discoideum. *PLoS ONE*, 8(5):e64272.

[Killich et al., 1994] Killich, T., Plath, P. J., Haß, E.-C., Xiang, W., Bultmann, H., Rensing, L., and Vicker, M. G. (1994). Cell movement and shape are non-random and determined by intracellular, oscillatory rotating waves in dictyostelium amoebae. *Biosystems*, 33(2):75 – 87.

[Kogan et al., 1991] Kogan, B. Y., Karplus, W. J., Billett, B. S., and Pang, A. T. (1991). The simplified fitzhugh-nagumo model with action potential duration restitution: Effects on 2d wave propagation. *Physica D*, 50(3):327 – 340.

[Koh et al., 2002] Koh, C., Tan, E., Manser, E., and Lim, L. (2002). The p21-activated kinase pak is negatively regulated by popx1 and popx2, a pair of serine/threonine phosphatases of the pp2c family. *Curr. Biol.*, (4):317 – 21.

[Krueger et al., 2003] Krueger, E. W., Orth, J. D., Cao, H., and McNiven, M. A. (2003). A dynamin-cortactin-arp2/3 complex mediates actin reorganization in growth factor-stimulated cells. *Mol. Biol. Cell*, 14(3):1085 – 96.

[Kruse et al., 2005] Kruse, K., Joanny, J. F., Jülicher, F., Prost, J., and Sekimoto, K. (2005). Generic theory of active polar gels: a paradigm for cytoskeletal dynamics. *Eur. Phys. J. E*, 16(1):5 – 16.

[Kruse and Jülicher, 2003] Kruse, K. and Jülicher, F. (2003). Self-organization and mechanical properties of active filament bundles. *Phys. Rev. E*, 67(5):051913.

[Kruse et al., 2003] Kruse, K., Zumdieck, A., and Jülicher, F. (2003). Continuum theory of contractile fibres. *Europhys. Lett.*, 64(5):716 – 722.

[Kádár et al., 1998] Kádár, S., Wang, J., and Showalter, K. (1998). Noise-supported travelling waves in sub-excitablemedia. *Nature*, 391(6669):770 – 772.

[Landau and Lifshitz, 1989] Landau, L. D. and Lifshitz, E. M. (1989). *Lehrbuch der Theoretischen Physik, VII Ealstizitätstheorie*. Akademie-Verlag, 6th edition.

[Landau and Lifshitz, 1991] Landau, L. D. and Lifshitz, E. M. (1991). *Lehrbuch der Theoretischen Physik, VI Hydrodynamik*. Akademie-Verlag, 5th edition.

[Legg et al., 2007] Legg, J. A., Bompard, G., Dawson, J., Morris, H. L., Andrew, N., Cooper, L., Johnston, S. A., Tramountanis, G., and Machesky, L. M. (2007). N-wasp involvement in dorsal ruffle formation in mouse embryonic fibroblasts. *Mol. Biol. Cell*, 18(2):678 – 687.

[Leibler and Andelman, 1987] Leibler, S. and Andelman, D. (1987). Ordered and curved meso-structures in membranes and amphiphilic films. *Journal de Physique*, 48(11):2013 – 18.

[Levoy, 1988] Levoy, M. (1988). Display of surfaces from volume data. *IEEE Computer Graphics and Applications*, 8(3):29 – 37.

[Machacek and Danuser, 2006] Machacek, M. and Danuser, G. (2006). Morphodynamic profiling of protrusion phenotypes. *Biophys. J.*, 90(4):1439 – 52.

[Machacek et al., 2009] Machacek, M., Hodgson, L., Welch, C., Elliott, H., Pertz, O., Nalbant, P., Abell, A., Johnson, G. L., Hahn, K. M., and Danuser, G. (2009). Coordination of rho gtpase activities during cell protrusion. *Nature*, 461(7260):99 – 103.

[Marchetti et al., 2013] Marchetti, M. C., Joanny, J. F., Ramaswamy, S., Liverpool, T. B., Prost, J., Rao, M., and Simha, R. A. (2013). Hydrodynamics of soft active matter. *Rev. Mod. Phys.*, 85(3):1143 – 89.

[Mata et al., 2013] Mata, M. A., Dutot, M., Edelstein-Keshet, L., and Holmes, W. R. (2013). A model for intracellular actin waves explored by nonlinear local perturbation analysis. *J. Theo. Biol.*, 334(1):149 – 161.

[Meinhardt, 2012] Meinhardt, H. (2012). Turing's theory of morphogenesis of 1952 and the subsequent discovery of the crucial role of local self-enhancement and long-range inhibition. *Interface Focus*, 2(4):407 – 416.

[Meinhardt et al., 1998] Meinhardt, H., Koch, A.-J., and Bernasconi, G. (1998). *Symmetry in Plants*. World Scientific Publishing.

[Mellström et al., 1983] Mellström, K., Höglund, A.-S., Nistér, M., Heldin, C.-H., Westermark, B., and Lindberg, U. (1983). The effect of platelet-derived growth factor on morphology and motility of human glial cells. *J. Muscle Res. Cell Motil.*, 4(5):589 – 609.

[Mercer and Helenius, 2009] Mercer, J. and Helenius, A. (2009). Virus entry by macropinocytosis. *Nat. Cell Biol.*, 11(5):510 – 520.

[Michaelis and Menten, 1913] Michaelis, L. and Menten, M. L. (1913). Die kinetik der invertinwirkung. *Biochem. Z.*, 49(1):333 – 369.

[Millius et al., 2009] Millius, A., Dandekar, S. N., Houk, A. R., and Weiner, O. D. (2009). Neutrophils establish rapid and robust WAVE complex polarity in an actin-dependent fashion. *Curr. Biol.*, 19(3):253 – 259.

[Mitchison and Cramer, 1996] Mitchison, T. and Cramer, L. (1996). Actin-based cell motility and cell locomotion. *Cell*, 84(3):371 – 379.

[Mogilner and Oster, 1996] Mogilner, A. and Oster, G. (1996). Cell motility driven by actin polymerization. *Biophys. J.*, 71(6):3030 – 45.

[Mogilner and Oster, 2003] Mogilner, A. and Oster, G. (2003). Force generation by actin polymerization II: The elastic ratchet and tethered filaments. *Biophys. J.*, 84(3):1591 – 1605.

[Mori et al., 2008] Mori, Y., Jilkine, A., and Edelstein-Keshet, L. (2008). Wave-pinning and cell polarity from a bistable reaction-diffusion system. *Biophys. J.*, 94(9):3684 – 97.

[Mulholland and Gomatam, 1996] Mulholland, A. J. and Gomatam, J. (1996). The eikonal approximation to excitable reaction-diffusion systems: travelling non-planar wave fronts on the plane. *Physica D*, 89(3-4):329 – 345.

[Murphy and Davidson, 2013] Murphy, D. B. and Davidson, M. W. (2013). *Fundamentals of Light Microscopy and Electronic Imaging.* Wiley-Blackwell, 2nd edition.

[Murray, 2004a] Murray, J. D. (2004a). *Mathematical Biology I: An Introduction.* Springer, 3rd edition.

[Murray, 2004b] Murray, J. D. (2004b). *Mathematical Biology II: Spatial Models and Biomedical Applications.* Springer, 3rd edition.

[Mäntele, 2012] Mäntele, W. (2012). *Biophysik.* Verlag Eugen Ulmer Stuttgart.

[Nagumo et al., 1962] Nagumo, J., Arimoto, S., and Yoshizawa, S. (1962). An active pulse transmission line simulating the nerve axon. *Proceedings of the IRE*, 50(10):2061 – 70.

[Nelson, 2004] Nelson, P. (2004). *Biological Physics*. Freeman.

[Ohmstede, 2015] Ohmstede, M. (2015). Master's thesis, Universität Bremen. In preparation.

[Orth et al., 2006] Orth, J. D., Krueger, E. W., Weller, S. G., and McNiven, M. A. (2006). A novel endocytic mechanism of epidermal growth factor receptor sequestration and internalization. *Cancer Res.*, 66(7):3606 – 10.

[Orth and McNiven, 2006] Orth, J. D. and McNiven, M. A. (2006). Get off my back! rapid receptor internalization through circular dorsal ruffles. *Cancer Res.*, 66(23):11094 – 96.

[Page et al., 2005] Page, K. M., Maini, P. K., and Monk, N. A. (2005). Complex pattern formation in reaction–diffusion systems with spatially varying parameters. *Physica D*, 202(1–2):95 – 115.

[Panfilov and Keener, 1995] Panfilov, A. and Keener, J. (1995). Re-entry in an anatomical model of the heart. *Chaos Soliton. Fract.*, 5(3–4):681 – 689. Nonlinear Phenomena in Excitable Physiological Systems.

[Park et al., 2010] Park, H., Chan, M. M., and Iritani, B. M. (2010). Hem-1: Putting the "wave" into actin polymerization during an immune response. *FEBS Lett.*, 584(24):4923 – 32.

[Patel and Galán, 2005] Patel, J. C. and Galán, J. E. (2005). Manipulation of the host actin cytoskeleton by salmonella — all in the name of entry. *Curr. Opin. Microbiol.*, 8(1):10 – 15.

[Payne et al., 2014] Payne, L. J., Eves, R. L., Jia, L., and Mak, A. S. (2014). p53 down regulates pdgf-induced formation of circular dorsal ruffles in rat aortic smooth muscle cells. *PLoS ONE*, 9(9):e108257.

[Peleg et al., 2011] Peleg, B., Disanza, A., Scita, G., and Gov, N. (2011). Propagating cell-membrane waves driven by curved activators of actin polymerization. *PLoS ONE*, 6(4):e18635.

[Pikovsky and Kurths, 1997] Pikovsky, A. S. and Kurths, J. (1997). Coherence resonance in a noise-driven excitable system. *Phys. Rev. Lett.*, 78:775 – 778.

[Pollard et al., 2000] Pollard, T. D., Blanchoin, L., and Mullins, R. D. (2000). Molecular mechanisms controlling actin filament dynamics in nonmuscle cells. *Annu. Rev. Biophys. Biomol. Struct.*, 29:545–76.

[Pollard and Borisy, 2003] Pollard, T. D. and Borisy, G. G. (2003). Cellular motility driven by assembly and disassembly of actin filaments. *Cell*, 112(4):453 – 465.

[Pollitt and Insall, 2009] Pollitt, A. Y. and Insall, R. H. (2009). Wasp and scar/wave proteins: the drivers of actin assembly. *J. Cell Sci.*, 122(1):2575 – 78.

[Pálsson and Cox, 1996] Pálsson, E. and Cox, E. C. (1996). Origin and evolution of circular waves and spirals in dictyostelium discoideum territories. *Proc. Natl. Acad. Sci. U. S. A.*, 93(3):1151 – 55.

[Qu et al., 2014] Qu, Z., Hu, G., Garfinkel, A., and Weiss, J. N. (2014). Nonlinear and stochastic dynamics in the heart. *Phys. Rep.*, 543(2):61 – 162.

[Qualmann et al., 2011] Qualmann, B., Koch, D., and Kessels, M. M. (2011). Let's go bananas: revisiting the endocytic bar code. *The EMBO journal*, 30(17):3501 – 15.

[R Development Core Team, 2008] R Development Core Team (2008). *R: A Language and Environment for Statistical Computing*. R Foundation for Statistical Computing, Vienna, Austria. ISBN 3-900051-07-0.

[Radon, 1917] Radon, J. (1917). Über die bestimmung von funktionen durch ihre integralwerte längs gewisser mannigfaltigkeiten. *Akad. Wiss.*, 69(1):262 – 277.

[Ramaswamy et al., 2000] Ramaswamy, S., Toner, J., and Prost, J. (2000). Nonequilibrium fluctuations, traveling waves, and instabilities in active membranes. *Phys. Rev. Lett.*, 84(15):3494 – 97.

[Ridley and Hall, 1992] Ridley, A. J. and Hall, A. (1992). The small gtp-binding protein rho regulates the assembly of focal adhesions and actin stress fibers in response to growth factors. *Cell*, 70(3):389 – 399.

[Ridley et al., 1992] Ridley, A. J., Paterson, H. F., Johnston, C. L., Diekmann, D., and Hall, A. (1992). The small gtp-binding protein rac regulates growth factor-induced membrane ruffling. *Cell*, 70(3):401 – 410.

[Ross et al., 1974] Ross, R., Glomset, J., Kariya, B., and Harker, L. (1974). A platelet-dependent serum factor that stimulates the proliferation of arterial smooth muscle cells in vitro. *Proc. Natl. Acad. Sci.*, 71(4):1207 – 10.

[Ryan et al., 2013] Ryan, G. L., Watanabe, N., , and Vavylonis, D. (2013). Image analysis tools to quantify cell shape and protein dynamics near the leading edge. *Cell Struct. Funct.*, 38(1):1 – 7.

[Sackmann and Merkel, 2000] Sackmann, E. and Merkel, R. (2000). *Lehrbuch der Biophysik*. Wiley-VCH.

[Schindelin et al., 2012] Schindelin, J., Arganda-Carreras, I., Frise, E., Kaynig, V., Longair, M., Pietzsch, T., Preibisch, S., Rueden, C., Saalfeld, S., Schmid, B., Tinevez, J.-Y., White, D. J., Hartenstein, V., Eliceiri, K., Tomancak, P., and Cardona, A. (2012). Fiji: an open-source platform for biological-image analysis. *Nat. Methods*, 9(1):676 – 682.

[Schreiber et al., 2009] Schreiber, G., Haran, G., and Zhou, H.-X. (2009). Fundamental aspects of protein-protein association kinetics. *Chem. Rev.*, 109(3):839 – 859.

[Schroth-Diez et al., 2009] Schroth-Diez, B., Gerwig, S., Ecke, M., Hegerl, R., Diez, S., and Gerisch, G. (2009). Propagating waves separate two states of actin organization in living cells. *HFSP J.*, 6(6):412 – 427.

[Schünemann, 2005] Schünemann, V. (2005). *Biophysik*. Springer.

[Seifert, 1993] Seifert, U. (1993). Curvature-induced lateral phase segregation in two-component vesicles. *Phys. Rev. Lett.*, 70(9):1335 – 38.

[Shlomovitz and Gov, 2007] Shlomovitz, R. and Gov, N. S. (2007). Membrane waves driven by actin and myosin. *Phys. Rev. Lett.*, 98(16):168103.

[Shutova et al., 2012] Shutova, M., Yang, C., Vasiliev, J. M., and Svitkina, T. (2012). Functions of nonmuscle myosin ii in assembly of the cellular contractile system. *PLoS One*, 7(7):e40814.

[Singh et al., 2011] Singh, P., Gan, C. S., Guo, T., Phang, H.-Q., Sze, S. K., and Koh, C. G. (2011). Investigation of popx2 phosphatase functions by comparative phosphoproteomic analysis. *Proteomics*, 11(14):2891 – 2900.

[Smolka et al., 2005] Smolka, L. B., Marts, B., and Lin, A. L. (2005). Effect of inhomogeneities on spiral wave dynamics in the belousov-zhabotinsky reaction. *Phys. Rev. E*, 72(5 Pt. 2):056205.

[Spector et al., 1989] Spector, I., Shochet, N. R., Blasberger, D., and Kashman, Y. (1989). Latrunculins-novel marine macrolides that disrupt microfilament organization and affect cell growth: I. comparison with cytochalasin d. *Cell Motil. Cytoskeleton*, 13(3):127 – 144.

[Strogatz, 2007] Strogatz, S. H. (2007). *Nonlinear Dynamics and Chaos*. Levant Books.

[Strübig et al., 2015] Strübig, J., Bernitt, E., and Döbereiner, H.-G. (2015). Dynamics of filopodia in fibroblasts on microcontact printed substrates. - *in preparation* -.

[Stukalin and Kolomeisky, 2006] Stukalin, E. B. and Kolomeisky, A. B. (2006). ATP hydrolysis stimulates large length fluctuations in single actin filaments. *Biophys. J.*, 90(8):2673 – 85.

[Susila et al., 2010] Susila, A., Chan, H., Loh, A., Phang, H., Wong, E., Tergaonkar, V., and Koh, C. (2010). The popx2 phosphatase regulates cancer cell motility and invasiveness. *Cell Cycle*, 9(1):179 – 187.

[Swanson and Watts, 1995] Swanson, J. A. and Watts, C. (1995). Macropinocytosis. *Trends Cell Biol.*, 5(11):424 – 428.

[Tallquist and Kazlauskas, 2004] Tallquist, M. and Kazlauskas, A. (2004). Pdgf signaling in cells and mice. *Cytokine Growth F. R.*, 15(4):205 – 213. Platelet-derived Growth Factor.

[Théry and Piel, 2009] Théry, M. and Piel, M. (2009). Adhesive micropatterns for cells: A microcontact printing protocol. *Cold Spring Harb. Protoc.*, 4(7):pdb.prot5255.

[Théry et al., 2006] Théry, M., Racine, V., Piel, M., Pépin, A., andJean Baptiste Sibarita, A. D. Y. C., and Bornens, M. (2006). Anisotropy of cell adhesive microenvironment governs cell internal organization and orientation of polarity. *Proc. Natl. Acad. Sci. U. S. A.*, 103(52):19771 – 76.

[Tomchik and Devreotes, 1981] Tomchik, K. J. and Devreotes, P. N. (1981). Adenosine 3',5'-monophosphate waves in dictyostelium discoideum: a demonstration by isotope dilution-fluorography. *Science*, 212(4493):443 – 446.

[Troy, 1985] Troy, W. C. (1985). *Oscillations and Traveling Waves in Chemical Systems.* Wiley.

[Tsekouras et al., 2011] Tsekouras, K., Lacoste, D., Mallick, K., and Joanny, J.-F. (2011). Condensation of actin filaments pushing against a barrier. *New J. Phys.*, 13(10):103032.

[Tsimring, 2014] Tsimring, L. S. (2014). Noise in biology. *Reports on Progress in Physics*, 77(2):026601.

[Turing, 1952] Turing, A. M. (1952). The chemical basis of morphogenesis. *Philos. Trans. Roy. Soc. London*, 237(641):37 – 72.

[Tyson and Murray, 1989] Tyson, J. J. and Murray, J. D. (1989). Cyclic amp waves during aggregation of dictyostelium amoebae. *Development*, 106(3):421 – 426.

[Upadhyaya and van Oudenaarden, 2003] Upadhyaya, A. and van Oudenaarden, A. (2003). Biomimetic systems for studying actin-based motility. *Curr. Biol.*, 13(18):R734 – R744.

[Van Aelst and D'Souza-Schorey, 1997] Van Aelst, L. and D'Souza-Schorey, C. (1997). Rho gtpases and signaling networks. *Gene. Develop.*, 11(18):2295 – 2322.

[Vasiev, 2004] Vasiev, B. N. (2004). Classification of patterns in excitable systems with lateral inhibition. *Phys. Lett. A*, 323(3–4):194 – 203.

[Vicker, 2000] Vicker, M. G. (2000). Reaction-diffusion waves of actin filament polymerization/depolymerization in *Dictyostelium* pseudopod extension and cell locomotion. *Biophys. Chem.*, 84(3):87 – 98.

[Vicsek et al., 1995] Vicsek, T., Czirók, A., Ben-Jacob, E., Cohen, I., and Shochet, O. (1995). Novel type of phase transition in a system of self-driven particles. *Phys. Rev. Lett.*, 75:1226 – 1229.

[Wasnik and Mukhopadhyay, 2014] Wasnik, V. and Mukhopadhyay, R. (2014). Modeling the dynamics of dendritic actin waves in living cells. *Phys. Rev. E*, 90(5):052707.

[Weber et al., 2015] Weber, C. A., Suzuki, R., Schaller, V., Aranson, I. S., Bausch, A. R., and Frey, E. (2015). Random bursts determine dynamics of active filaments. *Proc. Natl. Acad. Sci.*, 112(34):10703 – 07.

[Weibel et al., 2007] Weibel, D. B., DiLuzio, W. R., and Whitesides, G. M. (2007). Microfabrication meets microbiology. *Nat. Rev. Micro.*, 5(3):209 – 218.

[Weiner et al., 2007] Weiner, O. D., Marganski, W. A., Wu, L. F., Altschuler, S. J., and Kirschner, M. W. (2007). An actin-based wave generator organizes cell motility. *PLoS Biol.*, 5(9):e221.

[Westendorf et al., 2013] Westendorf, C., Negrete, J., Bae, J. A. J., Sandmann, R., Bodenschatz, E., and Beta, C. (2013). Actin cytoskeleton of chemotactic amoebae operates close to the onset of oscillations. *Proc. Natl. Acad. Sci. U. S. A.*, 110(10):3853 – 58.

[Whitelam et al., 2009] Whitelam, S., Bretschneider, T., and Burroughs, N. J. (2009). Transformation from spots to waves in a model of actin pattern formation. *Phys. Rev. Lett.*, 102(19):198103 – 4.

[Wordinger and Clark, 2008] Wordinger, R. J. and Clark, A. F. (2008). *Ocular Therapeutics: Eye on new Discoveries, Chap. 5.* 1st edition.

[Xu and Prince, 1998] Xu, C. and Prince, J. L. (1998). Generalized gradient vector flow external forces for active contours. *Signal Process.*, 71(2):131 – 139.

[Yarmola et al., 2000] Yarmola, E. G., Somasundaram, T., Boring, T. A., Spector, I., and Bubb, M. R. (2000). Actin-latrunculin a structure and function: Differential modulation of actin-binding protein function by latrunculin a. *J. Biol. Chem.*, 275(36):28120 – 27.

[Zaikin and Zhabotinsky, 1970] Zaikin, A. and Zhabotinsky, A. (1970). Concentration wave propagation in two-dimensional liquid-phase self-oscillating system. *Nature*, 225(5232):535 – 537.

[Zeng et al., 2011] Zeng, Y., Lai, T., Koh, C. G., LeDuc, P. R., and Chiam, K.-H. (2011). Investigating circular dorsal ruffles through varying substrate stiffness and mathematical modeling. *Biophys. J.*, 101(9):2122 – 30.